



Universiteit Gent
Faculteit Wetenschappen
Vakgroep Fysica en Sterrenkunde

² No title yet

³ No sub-title neither, obviously...

⁴ Alexis Fagot

5



Thesis to obtain the degree of
Doctor of Philosophy in Physics
Academic years 2012-2017



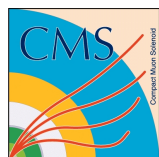


Universiteit Gent
Faculteit Wetenschappen
Vakgroep Fysica en Sterrenkunde

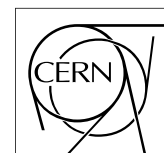
Promotoren: Dr. Michael Tytgat
Prof. Dr. Dirk Ryckbosch

Universiteit Gent
Faculteit Wetenschappen
Vakgroep Fysica en Sterrenkunde
Proeftuinstraat 86, B-9000 Gent, België
Tel.: +32 9 264.65.28
Fax.: +32 9 264.66.97

17



Thesis to obtain the degree of
Doctor of Philosophy in Physics
Academic years 2012-2017



Acknowledgements

¹⁹ Ici on remerciera tous les gens que j'ai pu croiser durant cette aventure et qui m'ont permis de passer
²⁰ un bon moment

²¹ *Gent, ici la super date de la mort qui tue de la fin d'écriture*
²² *Alexis Fagot*

Table of Contents

24	Acknowledgements	i
25	Nederlandse samenvatting	vii
26	English summary	ix
27	1 Introduction	1-1
28	1.1 A story of High Energy Physics	1-1
29	1.2 Organisation of this study	1-1
30	2 Investigating the TeV scale	2-1
31	2.1 The Standard Model of Particle Physics	2-2
32	2.1.1 A history of particle physics	2-2
33	2.1.2 Construction and test of the model	2-11
34	2.1.3 Investigating the TeV scale	2-12
35	2.2 The Large Hadron Collider & the Compact Muon Solenoid	2-14
36	2.2.1 LHC, the most powerful particle accelerator	2-14
37	2.2.1.1 Particle acceleration	2-15
38	2.2.2 CMS, a multipurpose experiment	2-18
39	2.2.2.1 The silicon tracker, core of CMS	2-20
40	2.2.2.2 The calorimeters, measurement of particle's energy	2-20
41	2.2.2.3 The muon system, corner stone of CMS	2-22
42	3 Muon Phase-II Upgrade	3-1
43	3.1 High Luminosity LHC and muon system requirements	3-2
44	3.2 Necessity for improved electronics	3-5
45	3.3 New detectors and increased acceptance	3-8
46	3.3.1 Improved forward resistive plate chambers	3-9
47	3.3.2 Gas electron multipliers	3-12
48	3.3.3 Installation schedule	3-19
49	3.4 Implications of the different upgrades on the Level-1 Trigger. Improvement of physics performance.	3-20
50	3.5 Ecofriendly gas studies	3-24
51	3.5.1 Status of the studies and potential candidates	3-24
52	3.5.2 Implications in case of no suitable ecofriendly mixture	3-24
53		
54	4 Physics of Resistive plate chambers	4-1
55	4.1 Principle	4-1
56	4.1.1 Electron drift velocity	4-4
57	4.2 Rate capability and time resolution of Resistive Plate Chambers	4-4
58	4.2.1 Operation modes	4-4

59	4.2.2	Detector designs and performance	4-6
60	4.2.2.1	Double-gap RPC	4-7
61	4.2.2.2	Multigap RPC (MRPC)	4-8
62	4.2.2.3	Charge distribution and performance limitations	4-9
63	4.3	Signal formation	4-12
64	4.4	Gas transport parameters	4-12
65	5	Longevity studies and Consolidation of the present CMS RPC subsystem	5-1
66	5.1	Resistive Plate Chambers at CMS	5-1
67	5.1.1	Overview	5-1
68	5.1.2	The present RPC system	5-2
69	5.1.3	Pulse processing of CMS RPCs	5-3
70	5.2	Testing detectors under extreme conditions	5-4
71	5.2.1	The Gamma Irradiation Facilities	5-6
72	5.2.1.1	GIF	5-6
73	5.2.1.2	GIF++	5-8
74	5.3	Preliminary tests at GIF	5-10
75	5.3.1	Resistive Plate Chamber test setup	5-10
76	5.3.2	Data Acquisition	5-12
77	5.3.3	Geometrical acceptance of the setup layout to cosmic muons	5-12
78	5.3.3.1	Description of the simulation layout	5-13
79	5.3.3.2	Simulation procedure	5-15
80	5.3.3.3	Results	5-16
81	5.3.4	Photon flux at GIF	5-16
82	5.3.4.1	Expectations from simulations	5-16
83	5.3.4.2	Dose measurements	5-21
84	5.3.5	Results and discussions	5-22
85	5.4	Longevity tests at GIF++	5-23
86	5.4.1	Description of the Data Acquisition	5-26
87	5.4.2	RPC current, environmental and operation parameter monitoring	5-27
88	5.4.3	Measurement procedure	5-28
89	5.4.4	Longevity studies results	5-28
90	6	Investigation on high rate RPCs	6-1
91	6.1	Rate limitations and ageing of RPCs	6-1
92	6.1.1	Low resistivity electrodes	6-1
93	6.1.2	Low noise front-end electronics	6-1
94	6.2	Construction of prototypes	6-1
95	6.3	Results and discussions	6-1
96	7	Conclusions and outlooks	7-1
97	7.1	Conclusions	7-1
98	7.2	Outlooks	7-1
99	A	A data acquisition software for CAEN VME TDCs	A-1
100	A.1	GIF++ DAQ file tree	A-1
101	A.2	Usage of the DAQ	A-2
102	A.3	Description of the readout setup	A-3
103	A.4	Data read-out	A-3
104	A.4.1	V1190A TDCs	A-4

105	A.4.2 DataReader	A-6
106	A.4.3 Data quality flag	A-10
107	A.5 Communications	A-12
108	A.5.1 V1718 USB Bridge	A-13
109	A.5.2 Configuration file	A-13
110	A.5.3 WebDCS/DAQ intercommunication	A-17
111	A.5.4 Example of inter-process communication cycle	A-18
112	A.6 Software export	A-18
113	B Details on the offline analysis package	B-1
114	B.1 GIF++ Offline Analysis file tree	B-1
115	B.2 Usage of the Offline Analysis	B-2
116	B.2.1 Output of the offline tool	B-3
117	B.2.1.1 ROOT file	B-3
118	B.2.1.2 CSV files	B-5
119	B.3 Analysis inputs and information handling	B-6
120	B.3.1 Dimensions file and IniFile parser	B-6
121	B.3.2 TDC to RPC link file and Mapping	B-7
122	B.4 Description of GIF++ setup within the Offline Analysis tool	B-9
123	B.4.1 RPC objects	B-9
124	B.4.2 Trolley objects	B-10
125	B.4.3 Infrastructure object	B-11
126	B.5 Handeling of data	B-12
127	B.5.1 RPC hits	B-13
128	B.5.2 Clusters of hits	B-14
129	B.6 DAQ data Analysis	B-15
130	B.6.1 Determination of the run type	B-16
131	B.6.2 Beam time window calculation for efficiency runs	B-17
132	B.6.3 Data loop and histogram filling	B-18
133	B.6.4 Results calculation	B-19
134	B.6.4.1 Rate normalisation	B-19
135	B.6.4.2 Rate and activity	B-21
136	B.6.4.3 Strip masking tool	B-23
137	B.6.4.4 Output CSV files filling	B-25
138	B.7 Current data Analysis	B-29

139

Nederlandse samenvatting –Summary in Dutch–

140

141 Le resume en Neerlandais (j'aurais peut-être pu apprendre la langue juste pour ça...).

English summary

¹⁴³ Le meme résume mais en Anglais (on commencera par la hein!).

List of Figures

144

145	2.1	Through the gold foil experiment Rutherford could show that most of the mass of atoms was contained in a positively charged nucleus and could then propose a more accurate atomic model than that of Thomson.	2-3
146	2.2	Figure 2.2a: Meson octet. Figure 2.2b: Baryon octet. Figure 2.2c: Baryon decuplet.	2-8
147	2.3	The elementary particles of the Standard Model are showed along with their names and properties. Their interactions with the strong, weak and electromagnetic forces have been explicated using color squares. In the left column, the scalar higgs boson is depicted, while the central is focused on the matter particles, the fermions, and the right on the force carriers, the gauge bosons. The role of the Higgs boson in electroweak symmetry breaking is highlighted, and the corresponding way properties of the various particles differ in the (high-energy) symmetric phase (top) and the (low-energy) broken-symmetry phase (bottom) are showed.	2-11
148	2.4	CERN accelerator complex.	2-15
149	2.5	Pictures of the different accelerators. From top to bottom: first the LINAC 2 and the <i>Pb</i> source of LINAC 3. Then the Booster and the LEIR. Finally, the PS, the SPS and the LHC.	2-16
150	2.6	Figure 2.6a: schematics of the LHC cryodipoles. 1: Superconducting Coils, 2: Beam pipe, 3: Heat exchanger Pipe, 4: Helium-II Vessel, 5: Superconducting Bus-bar, 6: Iron Yoke, 7: Non-Magnetic Collars, 8: Vacuum Vessel, 9: Radiation Screen, 10: Thermal Shield, 11: Auxiliary Bus-bar Tube, 12: Instrumentation Feed Throughs, 13: Protection Diode, 14: Quadrupole Bus-bars, 15: Spool Piece Bus-bars. Figure 2.6b: magnetic field and resulting motion force applied on the beam particles.	2-17
151	2.7	Figure 2.7a: picture of the LHC quadrupoles. Figure 2.7b: magnetic fields and resulting focussing force applied on the beam by 2 consecutive quadrupoles.	2-18
152	2.8	Picture of the CMS barrel. The red outer layer is the muon system hosted into the red iron return yokes. The calorimeters are the blue cylinder inside in magnet solenoid and the tracker is the inner yellow cylinder built around the beam pipe.	2-19
153	2.9	View of the CMS apparatus and of its different components.	2-19
154	2.10	Slice showing CMS sub-detectors and how particles interact with them.	2-20
155	2.11	CMS tracker.	2-20
156	2.12	Figure 2.12a: picture of the ECAL. Figure 2.12b: picture of the lead tungstate crystals composing the ECAL.	2-21
157	2.13	CMS hadron calorimeter barrel.	2-21
158	2.14	A quadrant of the muon system, showing DTs (yellow), RPCs (blue), and CSCs (green).	2-22
159	2.15	Figure 2.15a: Barrel wheel with its detector rings and return yokes. Figure 2.15b: CSC endcap disk with the 2 CSC stations. The outer station is made of 10 deg detectors while the inner station is made of 20 deg detectors. Figure 2.15c: RPC endcap disk. The inner station is not equipped and the inner CSC station can be seen.	2-23
160			
161			
162			
163			
164			
165			
166			
167			
168			
169			
170			
171			
172			
173			
174			
175			
176			
177			
178			
179			
180			
181			
182			
183			

- 184 2.16 Figure 2.16a: Cross section of a DT module showing the two superlayers measur-
 185 ing the ϕ coordinate, perpendicular to the cross section plane, and the superlayer
 186 measuring the η coordinate, placed in between the two others with honeycomb and
 187 parallel to the cross section plane. The DT detector is sandwiched in between 2
 188 RPCs whose readout strips are perpendicular to the cross section plane, measuring
 189 the ϕ coordinate. Figure 2.16b: A DT cell is shown together with its electric field.
 190 The path of a muon through a superlayer is shown. 2-23
- 191 2.17 Figure 2.17a: cathode strips and anode wire layout of a CSC panel. Figure 2.17b
 192 avalanche development and charge collection by anode wires and induction on cath-
 193 ode strips inside of a CSC panel. 2-24
- 194 2.18 Muon track reconstruction through the 6 panels of a CMS CSC using the infor-
 195 mation of anode wire groups and cathode strip charge distribution combined with
 196 comparator bits to decide on which half strip the muon is more likely to have passed. 2-24
- 197 2.19 Double gap layout of CMS RPCs. Muons passing through the gas volumes will cre-
 198 ate electron-ions pairs by ionising the gas. this ionisation will immediately translate
 199 into a developing avalanche. 2-25
- 200 3.1 Detailed timeline projection of for LHC and HL-LHC operation until 2039 show-
 201 ing the evolution of the instantaneous and integrated luminosity as designed (Fig-
 202 ure 3.1a) and in the ultimate case where the instantaneous luminosity is increased to
 203 $7.5 \times 10^{34} \text{ cm}^{-2}\text{s}^{-1}$ (Figure 3.1b) [20, 22]. 3-2
- 204 3.2 Absorbed dose in the CMS cavern after an integrated luminosity of 3000 fb. Using
 205 the interaction point as reference, R is the transverse distance from the beamline and
 206 Z is the distance along the beamline. 3-3
- 207 3.3 A quadrant of the muon system, showing DTs (yellow), RPCs (blue), and CSCs
 208 (green). The locations of new forward muon detectors for Phase-II are contained
 209 within the dashed box and indicated in red for GEM stations (ME0, GE1/1, and
 210 GE2/1) and dark blue for improved RPC (iRPC) stations (RE3/1 and RE4/1). 3-4
- 211 3.4 Figure 3.4a: Extrapolated fraction of failing channels of the present DT MiC1 elec-
 212 tronics as a function of the integrated luminosity for different scenari until LS4. Fig-
 213 ure 3.4b: Comparison of the current (left) and upgraded (right) DT data processing.
 214 So far, the data is sent to service cavern of CMS facility via copper-to-optical-fiber
 215 translators (CuOF) by each MiC1. There, data including RPCs and outer hadron
 216 calorimeter is combined into trigger primitives (TPG) and transmitted by the Twin-
 217 Mux system to CMS Track Finder. The time-to-digital converter (TDC) data is col-
 218 lected and sent to the CMS data acquisition system (DAQ) by the micro read-out
 219 server (μ ROS). After the upgrade, the TDC data will be sent via optical links to
 220 a patch panel inside the experimental cavern by each MiC2, and transferred to the
 221 back-end, where triggering and event building will be performed. 3-6
- 222 3.5 Figure 3.5a: The event loss fractions as a function of the instantaneous luminosity is
 223 compared for CFEBs (Phase-1) and DCFEBs (Phase-II) at different CSC locations.
 224 HL-LHC luminosity is marked with the dashed brown line. Figure 3.5b: Comparison
 225 of the current (left) and upgraded (right) CSC data processing. A part of the con-
 226 nections in between ALCTs and DCFEBs, and the trigger mother boards (TMBs)
 227 and data acquisition mother boards (DMBs) will be upgraded toward optical data
 228 transfer. The detector dependent units (DDUs) used as interface in between CSCs'
 229 front-end electronics and the CMS DAQ will be replaced by new FED boards. 3-7
- 230 3.6 Comparison of the simulated time residuals in between reconstructed and true muon
 231 times without (blue) and with (red) the upgraded RPC link system. 3-8

232	3.7	RMS of the multiple scattering displacement as a function of muon p_T for the proposed forward muon stations. All of the electromagnetic processes such as bremsstrahlung and magnetic field effect are included in the simulation.	3-9
233			
234			
235	3.8	Simulation of the impact of RPC hit inclusion onto the local trigger primitive efficiency in station 3 (left) and station 4 (right). The contribution of iRPC starts above $ \eta = 1.8$	3-9
236			
237			
238	3.9	Expected hit rate due to neutrons, photons, electrons and positrons at HL-HLC instantaneous luminosity of $5 \times 10^{34} \text{ cm}^{-2}\text{s}^{-1}$ in RE3/1 and RE4/1 chambers. The sensitivities of iRPCs used in the simulation for each particle are reported and differ from one endcap disk to another as the energies of the considered particles varies with the increasing distance from the interaction point.	3-10
239			
240			
241			
242			
243	3.10	Measured average charge per avalanche as a function of the effective electric field for different gas gap thickness in double gap RPCs using HPL electrodes.	3-11
244			
245	3.11	The PETIROC time jitter as a function of the input signal amplitude, measured with and without internal clocks.	3-12
246			
247	3.12	Schematics of a GEM showing the cathode on top, the GEM foil separating the gas volume into the drift region, in between the cathode and foil, and the induction region, in between the GEM foil and the anode, and the anode on which a 2D readout is installed. A negative voltage is applied on the cathode while the anode is connected to the ground.	3-13
248			
249			
250			
251			
252	3.13	Left: Picture of a CMS GEM foil provided by a scanning electron microscope. Right: Representation of the electric field lines in a GEM hole and of the amplification that electrons and ions undergo in the hole's volume due to the very intense electric field.	3-14
253			
254			
255	3.14	Schematic representation of CMS triple GEMs. The gas volume is divided into 4 areas. The drift area is the region where the primary electrons are created before being amplified a first time while passing through the first GEM foil. Then the process of drift and amplification is repeated twice in following two transfer areas and GEM foils. Finally, the charges have been amplified enough to induce current in the read-out strips while in the last drift area. The dimensions, potentials and electric fields are provided.	3-14
256			
257			
258			
259			
260			
261			
262	3.15	Simulated efficiency and rate of the standalone Level-1 muon trigger using tracks reconstructed in CSCs and all GEM stations compared with Phase-I values in the case where only CSCs are used or CSCs+GE1/1. The zones of inefficiency of the CSC subsystem are compensated by the addition of GEMs during Phase-II and the trigger rates is kept from increasing due to the high luminosity.	3-15
263			
264			
265			
266			
267	3.16	Figure 3.16a: Simulated resolution of the muon direction measurement $\Delta\phi$ with Phase-II conditions. In the second endcap station, the resolution is compared in the case of CSCs (ME2/1) alone and CSCs+GEMs (GE2/1+ME2/1) while a similar resolution measurement is given in the case of the first station (GE1/1+ME1/1). Figure 3.16b: The addition of GEM detectors on stations 1 and 2 (ME0 is considered to contribute to station station 1) as redundant system to CSCs allows to improve the muon momentum improvement through a more accurate measurement of the local bending angles ϕ_1 and ϕ_2	3-16
268			
269			
270			
271			
272			
273			
274			
275	3.17	Schematics of the data communication chain for DAQ of the GEM subsystems. The sending of trigger data via optical links to the CSC OTMBs is only done for GE1/1 and GE2/1 to match the data with ME1/1 and ME2/1.	3-16
276			
277			

278	3.18	Figure 3.18a: Energy spectrum of GIF++ ^{137}Cs source as measured by the GE1/1 279 detector installed in GIF++. Figure 3.18b: Evolution of the normalized gain of the 280 GE1/1 detector installed at in GIF++ as a function of the integrated charge per unit 281 area. The first part of the study, up to a charge of 55 mC/cm^2 had been done in the 282 former Gamma Irradiation Facility (GIF) that has now been dismantled following 283 the construction of GIF++. No variation of the normalized gain can be observed 284 after an accumulation of 110 mC/cm^2	3-17
285	3.19	Figure 3.19a: Comparison of the gas gain as a function of the divider voltage before 286 and after the irradiation of a triple-GEM by neutrons in CHARM. Figure 3.19b: 287 Comparison of the gas gain as a function of the divider voltage before and after the 288 irradiation of a triple-GEM by alpha particles.	3-18
289	3.20	Data flow of the Level-1 Trigger during Phase-II operations.	3-20
290	3.21	Comparison of Phase-II DT trigger primitives algorithmic efficiency for segments 291 obtained with 2 super-layers (quality $\geq 6/8$) and 1 super-layer only (quality = 4/4). 292 The simulation was done by generating 2×10^6 muons. The candidate tracks with 293 correct time identification is showed with open symbols.	3-21
294	3.22	Simulated spatial (3.22a) and angular (3.22b) resolution of the algorithm using 8 295 aligned hits in both super-layers (quality = 8/8) and 4 aligned hits in only one super- 296 layer (quality = 4/4). The contribution of intermediate quality tracks (6 aligned hits) 297 is negligible in the angular range shown. [Be careful to update this caption as it 298 uses a text to close to the published one.]	3-21
299	3.23	Efficiency of the L1 trigger in the endcap region after Phase-II upgrade in the case 300 CSC/GEM/RPC hits are requested in at least 2 stations out of four (3.23a) and in all 301 four stations (3.23b).	3-22
302	3.24	Resolution of the LCT ambiguous events thanks to the combination of CSC and 303 iRPC readout data. Using CSCs only, 2 pairs of hits are possible.	3-23
304	3.25	The angular resolution on reconstructed muon tracks in the GEM overlap region 305 $2.0 < \eta < 2.15$ is compared for Phase-II conditions in the case CSC are alone 306 (Figure 3.25a) and in the case the GEMs' data, including ME0, is combined to which 307 of CSCs (Figure 3.25b).	3-23
308	3.26	Comparison of L1 trigger performances for prompt muons with and without the 309 addition of GEMs in the region $2.1 < \eta < 2.4$ at Phase-II conditions. GEMs would 310 allow a reduction of the trigger accept rate by an order of magnitude (Figure 3.26a) 311 while increasing the trigger efficiency (Figure 3.26b).	3-24
312	4.1	Different phases of the avalanche development in the RPC gas volume subjected to 313 a constant electric field E_0 . a) An avalanche is initiated by the primary ionisation 314 caused by the passage of a charged particle through the gas volume. b) Due to 315 its growing size, the avalanche starts to locally influence the electric field. c) The 316 electrons, lighter than the cations reach the anode first. d) The ions reach the cathode. 317 While the charges have not recombined, the electric field in the small region around 318 the avalanche stays affected and locally blind the detector.	4-2
319	4.2	Effeciency (circles and stars with 30 mV and 100 mV thresholds respectively) and 320 streamer probability (opened circles) as function of the operating voltatge of a 2 mm 321 single gap HPL RPC flushed with a gas mixture containing (a) 5%, (b) 2%, (c) 1% 322 and (d) no SF_6 [41].	4-3

323	4.3	Movement of the charge carriers in an RPC. Figure 4.3a: Voltage across an RPC whose electrode have a relative permittivity of 5 at the moment the tension s applied. Figure 4.3b: After the charge carriers moved, the electrodes are charged and there is no voltage drop over the electrodes anymore. The full potential is applied on the gas gap only. Figure 4.3c: The streamer discharge initiated by a charged particle transports electrons and cations towards the anode and cathode respectively.	4-5
329	4.4	Typical oscilloscope pulses in streamer mode (Figure 4.4a) and avalanche mode(Figure 4.4b). In the case of streamer mode, the very small avalanche signal is visible.	4-5
331	4.5	Rate capability comparison for the streamer and avalanche mode of operation. An order of magnitude in rate capability for a maximal efficiency drop of 10% is gained by using the avalanche mode over the streamer mode.	4-6
334	4.6	Possible double-gap RPC layouts: a) "standard" 1D double-gap RPC, as used in CMS experiment, where the anodes are facing each other and a 1D read-out plane is sandwiched in between them, b) double read-out double-gap RPC as used in AT-LAS experiment, where the cathodes are facing each other and 2 read-out planes are used on the outer surfaces. This last layout can offer the possibility to use a 2D reconstruction by using orthogonal read-out planes.	4-7
340	4.7	Comparison of performance of CMS double and single gap RPCs using cosmic muons [52]. Figure 4.7a: Comparison of efficiency sigmoids. Figure 4.7b: Voltage distribution at 95% of maximum efficiency. Figure 4.7c: $\Delta_{10\%}^{90\%}$ distribution. . . .	4-7
343	4.8	Presentation of ALICE MRPC using 250 μm gas gaps, 620 μm outer glass electrodes and 550 μm inner floating electrodes. More details on the labels are given in [53]. . .	4-8
345	4.9	Particle identification applied to electrons in the STAR experiment. The identification is performed combining ToF and dE/dx measurements [58].	4-9
347	4.10	Comparison of the detector performance of ALICE ToF MRPC [59] at fixed applied voltage (in blue) and at fixed effective voltage (in red). The effective voltage is kept fixed by increasing the applied voltage accordingly to the current drawn by the detector.	4-9
350	4.11	Ratio between total induced and drifting charge have been simulated for single gap, double-gap and multigap layouts [60]. The total induced charge for a double-gap RPC is a factor 2 higher than for a multigap.	4-10
353	4.12	Charge spectra have been simulated for single gap, double-gap and multigap layouts [60]. It appears that when single gap shows a decreasing spectrum, double and multigap layouts exhibit a spectrum whose peak is detached from the origin. The detachment gets stronger as the number of gaps increases.	4-11
357	4.13	The maximal theoretical efficiency is simulated for single gap, double-gap and multi-gap layouts [60] at a constant gap thickness of 2 mm and using an effective Townsend coefficient of 9 mm^{-1}	4-11
360	5.1	Signals from the RPC strips are shaped by the FEE described on Figure 5.1a. Output LVDS signals are then read-out by a TDC module connected to a computer or converted into NIM and sent to scalers. Figure 5.1b describes how these converted signals are put in coincidence with the trigger.	5-3

364	5.2	Description of the principle of a CFD. A comparison of threshold triggering (left) and constant fraction triggering (right) is shown in Figure 5.2a. Constant fraction triggering is obtained thanks to zero-crossing technique as explained in Figure 5.2b. The signal arriving at the input of the CFD is split into three components. A first one is delayed and connected to the inverting input of a first comparator. A second component is connected to the noninverting input of this first comparator. A third component is connected to the noninverting input of another comparator along with a threshold value connected to the inverting input. Finally, the output of both comparators is fed through an AND gate.	5-4
373	5.3	Figure 5.3a: The integrated charge per region (Barrel, Endcap) is extrapolated to HL-LHC integrated luminosity (3000 fb^{-1}) using the data accumulated in 2016 in every HV channels. Figure 5.3b: The hit rate per region (Barrel, Endcap) is linearly extrapolated to HL-LHC highest instantaneous luminosity ($5 \times 10^{34} \text{ cm}^{-2}\text{s}^{-1}$) using the rate as a function of instantaneous luminosity recorded by RPCs in 2017 showing a linear dependence.	5-5
379	5.4	Background Fluka simulation compared to 2016 Data at $L = 10^{34} \text{ cm}^{-2}\text{s}^{-1}$ in the fourth endcap disk region. A mismatch in between simulation and data can be observed. [To be understood.]	5-6
382	5.5	Layout of the test beam zone called X5c GIF at CERN. Photons from the radioactive source produce a sustained high rate of random hits over the whole area. The zone is surrounded by 8 m high and 80 cm thick concrete walls. Access is possible through three entry points. Two access doors for personnel and one large gate for material. A crane allows installation of heavy equipment in the area.	5-7
387	5.6	^{137}Cs decays by β^- emission to the ground state of ^{137}Ba (BR = 5.64%) and via the 662 keV isomeric level of ^{137}Ba (BR = 94.36%) whose half-life is 2.55 min.	5-8
389	5.7	Floor plan of the GIF++ facility. When the facility downstream of the GIF++ takes electron beam, a beam pipe is installed along the beam line (z-axis). The irradiator can be displaced laterally (its center moves from $x = 0.65 \text{ m}$ to 2.15 m), to increase the distance to the beam pipe.	5-8
393	5.8	Simulated unattenuated current of photons in the xz plane (Figure 5.8a) and yz plane (Figure 5.8b) through the source at $x = 0.65 \text{ m}$ and $y = 0 \text{ m}$. With angular correction filters, the current of 662 keV photons is made uniform in xy planes.	5-9
396	5.9	Description of the RPC setup. Dimensions are given in mm. A tent containing RPCs is placed at 1720 mm from the source container. The source is situated in the center of the container. RE-4-2-BARC-161 chamber is 160 mm inside the tent. This way, the distance between the source and the chambers plan is 2060 mm. Figure 5.9a provides a side view of the setup in the xz plane while Figure 5.9b shows a top view in the yz plane.	5-10
402	5.10	RE-4-2-BARC-161 chamber is inside the tent as described in Figure 5.9. In the top right, the two scintillators used as trigger can be seen. This trigger system has an inclination of 10° relative to horizontal and is placed above half-partition B2 of the RPCs. PMT electronics are shielded thanks to lead blocks placed in order to protect them without stopping photons from going through the scintillators and the chamber.	5-11

407	5.11 Hit distributions over all 3 partitions of RE-4-2-BARC-161 chamber is showed on these plots. Top, middle and bottom figures respectively correspond to partitions A, B, and C. These plots show that some events still occur in other half-partitions than B2, which corresponds to strips 49 to 64, in front of which the trigger is placed, contributing to the inefficiency of detection of cosmic muons. In the case of partitions A and C, the very low amount of data can be interpreted as noise. On the other hand, it is clear that a little portion of muons reach the half-partition B1, corresponding to strips 33 to 48.	5-12
415	5.12 Results are derived from data taken on half-partition B2 only. On the 18 th of June 2014, data has been taken on chamber RE-2-BARC-161 at building 904 (Prevessin Site) with cosmic muons providing us a reference efficiency plateau of $(97.54 \pm 0.15)\%$ represented by a black curve. A similar measurement has been done at GIF on the 21 st of July with the same chamber giving a plateau of $(78.52 \pm 0.94)\%$ represented by a red curve.	5-13
421	5.13 Representation of the layout used for the simulations of the test setup. The RPC is represented as a yellow trapezoid while the two scintillators as blue cuboids looking at the sky. A green plane corresponds to the muon generation plane within the simulation. Figure 5.9a shows a global view of the simulated setup. Figure 5.9b shows a zommed view that allows to see the 2 scintillators as well as the full RPC plane.	5-14
426	5.14 γ flux $F(D)$ is plot using values from table 5.1. As expected, the plot shows similar attenuation behaviours with increasing distance for each absorption factors.	5-17
428	5.15 Figure 5.15a shows the linear approximation fit done via formulae 5.7 on data from table 5.2. Figure 5.15b shows a comparison of this model with the simulated flux using a and b given in figure 5.15a in formulae 5.4 and the reference value $D_0 = 50\text{cm}$ and the associated flux for each absorption factor F_0^{ABS} from table 5.1	5-19
432	5.16 Dose measurements has been done in a plane corresponding to the tents front side. This plan is 1900 mm away from the source. As explained in the first chapter, a lens-shaped lead filter provides a uniform photon flux in the vertical plan orthogonal to the beam direction. If the second line of measured fluxes is not taken into account because of lower values due to experimental equipments in the way between the source and the tent, the uniformity of the flux is well showed by the results.	5-21
438	5.17	5-22
439	5.18 Evolution of the maximum efficiency for RE2 (5.18a) and RE4 (5.18b) chambers with increasing extrapolated γ rate per unit area at working point. Both irradiated (blue) and non irradiated (red) chambers are shown.	5-24
442	5.19 Evolution of the working point for RE2 (5.19a) and RE4 (5.19b) with increasing extrapolated γ rate per unit area at working point. Both irradiated (blue) and non irradiated (red) chambers are shown.	5-24
445	5.20 Evolution of the maximum efficiency at HL-LHC conditions, i.e. a background hit rate per unit area of 300 Hz/cm ² , with increasing integrated charge for RE2 (5.20a) and RE4 (5.20b) detectors. Both irradiated (blue) and non irradiated (red) chambers are shown. The integrated charge for non irradiated detectors is recorded during test beam periods and stays small with respect to the charge accumulated in irradiated chambers.	5-25
451	5.21 Comparison of the efficiency sigmoid before (triangles) and after (circles) irradiation for RE2 (5.21a) and RE4 (5.21b) detectors. Both irradiated (blue) and non irradiated (red) chambers are shown.	5-25
454	5.22 Evolution of the Bakelite resistivity for RE2 (5.22a) and RE4 (5.22b) detectors. Both irradiated (blue) and non irradiated (red) chambers are shown.	5-26

456	5.23 Evolution of the noise rate per unit area for the irradiated chamber RE2-2-BARC-9 only.	5-26
457		
458	A.1 (A.1a) View of the front panel of a V1190A TDC module [66]. (A.1b) View of the front panel of a V1718 Bridge module [67]. (A.1c) View of the front panel of a 6U 6021 VME crate [68].	A-3
459		
460		
461	A.2 Module V1190A <i>Trigger Matching Mode</i> timing diagram [66].	A-4
462		
463	A.3 Structure of the ROOT output file generated by the DAQ. The 5 branches (<code>EventNumber</code> , <code>number_of_hits</code> , <code>Quality_flag</code> , <code>TDC_channel</code> and <code>TDC_TimeStamp</code>) are visible on the left panel of the ROOT browser. On the right panel is visible the histogram cor- responding to the variable <code>nHits</code> . In this specific example, there were approximately 50k events recorded to measure the gamma irradiation rate on the detectors. Each event is stored as a single entry in the <code>TTree</code>	A-10
464		
465		
466		
467		
468	A.4 The effect of the quality flag is explained by presenting the content of <code>TBranch</code> <code>number_of_hits</code> of a data file without <code>Quality_flag</code> in Figure A.4a and the con- tent of the same <code>TBranch</code> for data corresponding to a <code>Quality_flag</code> where all TDCs were labelled as <code>GOOD</code> in Figure A.4b taken with similar conditions. It can be noted that the number of entries in Figure A.4b is slightly lower then in Figure A.4a due to the excluded events.	A-12
469		
470		
471		
472		
473		
474	A.5 Using the same data as previously showed in Figure A.4, the effect of the quality flag is explained by presenting the reconstructed hit multiplicity of a data file with- out <code>Quality_flag</code> in Figure A.5a and the reconstructed content of the same RPC partition for data corresponding to a <code>Quality_flag</code> where all TDCs were labelled as <code>GOOD</code> in Figure A.5b taken with similar conditions. The artificial high content of bin 0 is completely suppressed.	A-12
475		
476		
477		
478		
479		
480	A.6 WebDCS DAQ scan page. On this page, shifters need to choose the type of scan (Rate, Efficiency or Noise Reference scan), the gamma source configuration at the moment of data taking, the beam configuration, and the trigger mode. These in- formation will be stored in the DAQ ROOT output. Are also given the minimal measurement time and waiting time after ramping up of the detectors is over before starting the data acquisition. Then, the list of HV points to scan and the number of triggers for each run of the scan are given in the table underneath.	A-14
481		
482		
483		
484		
485		
486		
487	B.1 Example of expected hit time distributions in the cases of efficiency (Figure B.1a) and noise/gamma rate per unit area (Figure B.1b) measurements as extracted from the raw ROOT files. The unit along the x-axis corresponds to ns. The fact that "the" muon peak is not well defined in Figure B.1a is due to the contribution of all the RPCs being tested at the same time that don't necessarily have the same signal arrival time. Each individual peak can have an offset with the ones of other detectors. The inconsistancy in the first 100 ns of both time distributions is an artefact of the TDCs and are systematically rejected during the analysis.	B-16
488		
489		
490		
491		
492		
493		
494		
495	B.2 The effect of the quality flag is explained by presenting the reconstructed hit multi- plicity of a data file without <code>Quality_flag</code> . The artificial high content of bin 0 is the effect of corrupted data.	B-19
496		
497		

List of Tables

506

507	4.1	Properties of the most used electrode materials for RPCs.	4-4
508	5.1	Total photon flux ($E\gamma \leq 662$ keV) with statistical error predicted considering a ^{137}Cs activity of 740 GBq at different values of the distance D to the source along the x-axis of irradiation field [63].	5-16
509	5.2	Correction factor c is computed thanks to formulae 5.5 taking as reference $D_0 = 50$ cm and the associated flux F_0^{ABS} for each absorption factor available in table 5.1.	5-18
510	5.3	The data at D_0 in 1997 is taken from [63]. In a second step, using Equations 5.8 and 5.9, the flux at D can be estimated in 1997. Then, taking into account the attenuation of the source activity, the flux at D can be estimated at the time of the tests in GIF in 2014. Finally, assuming a sensitivity of the RPC to γ $s = 2 \cdot 10^{-3}$, an estimation of the hit rate per unit area is obtained.	5-20
511	A.1	Inter-process communication cycles in between the webDCS and the DAQ through file string signals.	A-19
512			
513			
514			
515			
516			
517			
518			
519			

List of Acronyms

520

521

522

523

A

524

526

AFL
ALCTs

Almost Full Level
anode local charged track boards

528

529

B

530

BARC
BLT
BMTF
BNL
BR

Bhabha Atomic Research Centre
Block Transfer
Barrel Muon Track Finder
Brookhaven National Laboratory
Branching Ratio

537

538

C

539

CAEN
CERN
CFD
CFEBs
CMB
CMS
CSC
CuOF

Costruzioni Apparecchiature Elettroniche Nucleari S.p.A.
European Organization for Nuclear Research
Constant Fraction Discriminator
cathode front-end boards
Cosmic Microwave Background
Compact Muon Solenoid
Cathode Strip Chamber
copper-to-optical-fiber translators

549

550

D

551

DAQ
DCS
DQM

Data Acquisition
Detector Control Software
Data Quality Monitoring

556	DT	Drift Tube
557		
558	E	
559		
560		
561	ECAL	electromagnetic calorimeter
562	EMTF	Endcap Muon Track Finder
563		
564	F	
565		
566		
567	FCC	Future Circular Collider
568	FEE	Front-End Electronics
569	FEB	Front-End Board
570		
571	G	
572		
573		
574	GE-/-	Find a good description
575	GE1/1	Find a good description
576	GE2/1	Find a good description
577	GEANT	GEometry ANd Tracking - a series of software toolkit platforms developed by CERN
578		
579	GEB	GEM Electronics board
580	GEM	Gas Electron Multiplier
581	GIF	Gamma Irradiation Facility
582	GIF++	new Gamma Irradiation Facility
583		
584	H	
585		
586		
587	HCAL	hadron calorimeter
588	HL-LHC	High Luminosity LHC
589	HPL	High-pressure laminate
590	HV	High Voltage
591		
592	I	
593		
594		
595	iRPC	improved RPC
596	IRQ	Interrupt Request
597	ISR	Intersecting Storage Rings

598

599

L

600

601

602	LEIR	Low Energy Ion Ring
603	LEP	Large Electron-Positron
604	LHC	Large Hadron Collider
605	LS1	First Long Shutdown
606	LS2	Second Long Shutdown
607	LS3	Third Long Shutdown
608	LV	Low Voltage
609	LVDS	Low-Voltage Differential Signaling

610

611

M

612

613

614	MiC1	first version of Minicrate electronics
615	MC	Monte Carlo
616	MCNP	Monte Carlo N-Particle
617	ME-/	Find good description
618	ME0	Find good description
619	MRPC	Multigap RPC

620

621

N

622

623

624	NIM	Nuclear Instrumentation Module logic signals
-----	-----	--

625

626

O

627

628

629	OH	Optohybrid Board
630	OMTF	Overlap Muon Track Finder

631

632

P

633

634

635	PMT	PhotoMultiplier Tube
636	PS	Proton Synchrotron
637	PU	pile-up

638

639

Q

640

641

642	QCD	Quantum Chromodynamics
643	QED	Quantum Electrodynamics
644		
645		
646	R	
647		
648	RE/-	Find a good description
649	RE2/2	Find a good description
650	RE3/1	Find a good description
651	RE3/2	Find a good description
652	RE4/1	Find a good description
653	RE4/2	Find a good description
654	RE4/3	Find a good description
655	RMS	Root Mean Square
656	ROOT	a framework for data processing born at CERN
657	RPC	Resistive Plate Chamber
658		
659		
660	S	
661		
662	SC	Synchrocyclotron
663	SLAC	Stanford Linear Accelerator Center
664	SM	Standard Model
665	SPS	Super Proton Synchrotron
666	SUSY	supersymmetry
667		
668		
669	T	
670		
671	TDC	Time-to-Digital Converter
672	TDR	Technical Design Report
673	ToF	Time-of-flight
674	TPG	trigger primitives
675		
676		
677	W	
678		
679	webDCS	Web Detector Control System
680		
681		
682	Y	
683		
684	YETS	Year End Technical Stop

1

Introduction

685

686

⁶⁸⁷ **1.1 A story of High Energy Physics**

⁶⁸⁸ **1.2 Organisation of this study**

2

689

690

Investigating the TeV scale

691 „We may regard the present state of the universe as the effect of the
692 past and the cause of the future. An intellect which at any given mo-
693 ment knew all of the forces that animate nature and the mutual posi-
694 tions of the beings that compose it, if this intellect were vast enough
695 to submit the data to analysis, could condense into a single formula
696 the movement of the greatest bodies of the universe and that of the
697 lightest atom; for such an intellect nothing could be uncertain and
698 the future just like the past would be present before its eyes.”

699

700 - Pierre Simon de Laplace, *A Philosophical Essay on Probabilities*, 1814

Throughout history, physics experiment became more and more powerful in order to investigate finer details of nature and helped understanding the elementary blocks of matter and the fundamental interactions that bond them in the microscopic world. Nowadays, the Standard Model (SM) of particle physics is the most accurate theory designed to explain the behaviour of particles and was able to make very precise predictions that are constantly verified, although some hints of new physics are visible as bricks are still missing to have a global comprehension of the Universe.

To highlight the limits of the SM and test the different alternative theories, ever more powerful machines are needed. This is in this context that the Large Hadron Collider (LHC) has been thought and built to accelerate and collide particles at energies exceeding anything that had been done before. Higher collision energies and high pile-up imply the use of enormous detectors to measure the properties of the interaction products. The Compact Muon Solenoid (CMS) is a multipurpose experiment that have been designed to study the proton-proton collisions of the LHC and give answers on various high energy physics scenari. Nevertheless, the luminosity delivered by the collider will in the future be increased to levels beyond the original plans to improve its discovery potential giving no choice to experiments such as CMS to upgrade their technologies to cope with the increased radiation levels and detection rates.

2.1 The Standard Model of Particle Physics

In this early 21st century it is now widely accepted that matter is made of elementary blocks referred to as *elementary particles*. The physics theory that classifies and describes the best the behaviour and interaction of such elementary particles is the so called Standard Model that formalizes 3 of the 4 fundamental interactions (electromagnetic, weak and strong interactions). It's development took place during the 20th century thanks to a strong collaboration in between the theoretical and experimental physicists.

2.1.1 A history of particle physics

The idea that nature is composed of elementary bricks, called *atomism*, is not contemporary as it was already discussed by Indian or Greek philosophers during antiquity. In Greece, atomism has been rejected by Aristotelianism as the existance of *atoms* would imply the existance of a void that would violate the physical principles of Aristotle philosophy. Aristotelianism has been considered as a reference in the european area until the 15th century and the italian *Rinascimento* where antic text and history started to be more deeply studied. The re-discovery of Platon's philosophy would allow to open the door to alternative theories and give a new approach to natural sciences where experimentation would become central. A new era of knowledge was starting. By the begining of the 17th century, atomism was re-discovered by philosophers and the very first attempt to estimate an *atom* size would be provided by Magnetus in 1646. Although his *atoms* correspond to what would nowadays be called *molecules*, Magnetus achieved feats by calculating that the number of molecules in a grain of incense would be of the order of 10^{18} simply by considering the time necessary to smell it everywhere in a large church after the stick was lit on. It is now known that this number only falls short by 1 order of magnitude.

An alternative philosophy to atomism popularized by Descartes was corpuscularianism. Built on ever divisible corpuscles, contrary to atoms, it's principles would be mainly used by alchemists like Newton who would later develop a corpuscular theory of light. Boyle would combine together ideas of both atomism or corpuscularianism leading to mechanical philosophy. The 18th century have

743 seen the development of engineering providing philosophical thought experiments with repeatable
 744 demonstration and a new point of view to explain the composition of matter and Lavoisier would
 745 greatly contribute to chemistry and atomism by publishing in 1789 a list of 33 chemical elements
 746 corresponding to what is now called *atoms*. In the early 19th century Dalton would summarize the
 747 knowledge on composition of matter and Fraunhofer would invent the spectrometer and discover
 748 the spectral lines. The rise of atomic physics, chemistry and mathematical formalism would unravel
 749 the different atomic elements and ultimately, the 20th century would see the very first sub-atomic
 750 particles.

751 **Discovery of the inner structure of the atom**

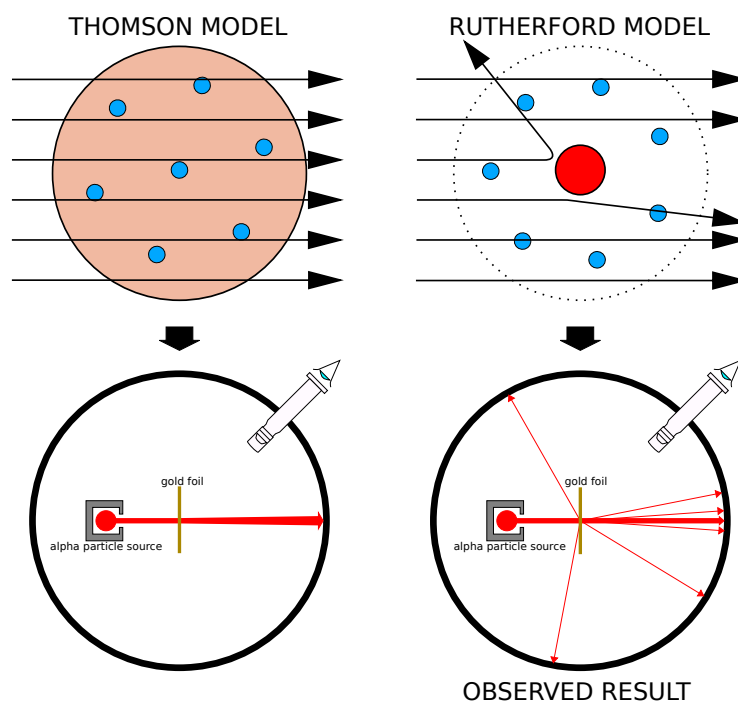


Figure 2.1: Through the gold foil experiment Rutherford could show that most of the mass of atoms was contained in a positively charged nucleus and could then propose a more accurate atomic model than that of Thomson.

752 The negative *electron* would be the first to be discovered in 1897 by Thomson after 3 decades of
 753 research on cathode rays by proving that the electrification observed in an electroscope, as reported
 754 by Perrin, was due to the rays themselves and that they had to be composed of electrically charged
 755 particles. In 1900, Becquerel would show the *beta rays* emitted by radium had the same charge over
 756 mass ratio than what measured by Thomson for cathode rays, pointing to electrons as a constituent
 757 of atoms. In 1907, Rutherford and Royds showed that *alpha* particles, once captured in a tube
 758 and subjected to an electric spark causing an electron avalanche, where helium ions as they could
 759 combine with 2 electrons to form a ${}^4\text{He}$. This discovery was directly followed by the constraint of
 760 the atom structure in 1909 through the gold foil experiment in which the deflection angle of alpha
 761 particles fired at a very thin gold foil was measured and highlighted atoms where mainly empty with

762 nearly all its mass contained into a tiny positively charged *nucleus*. With these two observations,
 763 he could formulate the Rutherford model of the atom in 1911, shown together with the Thomson
 764 plum pudding model in Figure 2.1. The link in between atomic number and number of positive and
 765 negative charges contained into the atoms would fast be understood and the different kind of element
 766 transmutation appeared to be purely nuclear processes making clear that the electromagnetic nature
 767 of chemical transformation could not possibly change nuclei. Thus a new branch in physics appeared
 768 to study nuclei exclusively: the nuclear physics.

769 Moreover, in 1913 quantum physics would be introduced into the atomic model by Bohr based
 770 on the assumptions of Plank to explain spectral lines, and other observed quantum effects. The same
 771 year, Moseley would confirm Bohr's model and Debye would extend it by introducing elliptical
 772 orbits.

773 By studying alpha emission and the product of their interaction with nitrogen gas, Rutherford
 774 reported in 1919 the very first nuclear reaction leading to the discovery that the hydrogen nucleus was
 775 composed of a single positively charged particle that was later baptised *proton*. This idea came from
 776 1815 Prout's hypothesis proposing that all atoms are composed of "*protyles*" (i.e. hydrogen atoms).
 777 By using scintillation detectors, Rutherford could highlight typical hydrogen nuclei signature and
 778 understand that the impact of alpha particles with nitrogen would knock out an hydrogen nucleus
 779 and produce an oxygen 17, as explicated in Formula 2.1 and would then postulate that protons are
 780 building bricks of all elements.



781 With this assumption and the discovery of isotopes together with Aston, elements with identical
 782 atomic number but different masses, Rutherford would propose that all elements' nuclei but hydrogen's are composed of both charged particles, protons, and of chargeless particles, which he called
 783 *neutrons*, and that these neutral particles would help maintaining nuclei as one, as charged protons
 784 were likely to electrostatically repulse each other, and introduced the idea of a new force, a *nuclear*
 785 force. Though the first idea concerning neutrons was a bond state of protons and electrons as it was
 786 known that the beta decay, emitting electrons, was taking place in the nucleus, it was then showed
 787 that such a model would hardly be possible due to Heisenberg's uncertainty principle and by the
 788 recently measured *spin* of both protons and electrons. The spin, discovered through the study of
 789 the emission spectrum of alkali metals, would be understood as a "two-valued quantum degree of
 790 freedom" and formalized by Pauli and extended by Dirac, to take the relativist case into account.
 791 Measured to be $\frac{1}{2}\hbar$ for both, it was impossible to arrange an odd number of half integer spins and
 792 obtain a global nucleus spin that would be integer. Finally, in 1932, following the discovery of a new
 793 neutral radiation, Chadwick could discover the neutron as an uncharged particle with a mass similar
 794 to that of the proton whose half integer spin would reveal to be the solution to explain the nuclear
 795 spin.

797 Development of the Quantum Electrodynamics

798 Historically, the development of the quantum theory revolved around the question of emission and
 799 absorption of discrete amount of energy through light. Einstein used the initial intuition of Plank
 800 about the black-body radiation to develop in 1905 a model to explain the photoelectric effect in
 801 which light was described by discrete quanta now called *photons*. For this model, Einstein introduced
 802 the concept of wave-particle duality as classical theory was not able to describe the phenomenon.
 803 With the new understanding of atoms and of their structure, classical theories also proved unable

804 to explain atoms stability. Indeed, using classical mechanics, electrons orbiting around a nucleus
 805 should radiate an energy proportional to their angular momentum and thus lose energy through
 806 time and the spectrum of energy emission should then be continuous, but it was known since the
 807 19th century and the discovery of spectral lines that the emission spectrum of material was discrete.

808 This was Bohr who first suggested that a quantum description of the atom was necessary in 1913.
 809 Using the correspondence principle stating that at large enough numbers the quantum calculations
 810 should give the same results than the classical theory, he proposed the very first quantum model
 811 of the hydrogen atom explaining the line spectrum by introducing the principal quantum number
 812 n describing the electron shell. This model would then be improved by Sommerfeld that would
 813 quantize the z-component of the angular momentum, leading to the second and third quantum
 814 numbers, or azimuthal and magnetic quantum number, l and m defining for the second the orbital
 815 angular momentum of the electrons on their shells and thus, the shape of the orbital, and for the third
 816 the available orbital on the subshell for each electron. Nevertheless, although the model was not only
 817 limited to spherical orbitals anymore, making the atom more realistic, the Zeeman effect couldn't be
 818 completely explained by just using n , l and m . A solution would be brought after the discovery of
 819 Pauli in 1924, as Uhlenbeck, Goudsmit, and Kramers proposed in 1925 the idea of intrinsic rotation
 820 of the electron, introducing a new angular momentum vector associated to the particle itself, and
 821 not to the orbital, and associated to a new quantic number s , the *spin* projection quantum number
 822 explaining the lift of degeneracy to an even number of energy levels.

823 The introduction of the *spin* happened 1 year after another attempt of improvement of the theory
 824 was made by De Broglie in his PhD thesis. The original formulation of the quantum theory only
 825 considered photons as energy quanta behaving as both waves and particles. De Broglie proposed
 826 that all matter are described by waves and that their momentum is proportional to the oscillation of
 827 quantized electromagnetic field oscillators. This interpretation was able to reproduce the previous
 828 version of the quantum energy levels by showing that the quantum condition involves an integer
 829 multiple of 2π , as shown by Formula 2.2.

$$p = \hbar k \Leftrightarrow \int pdx = \hbar \int kdx = 2\pi\hbar n \quad (2.2)$$

830 Although the intuition of De Broglie about the wave-particle duality of all matter, his interpretation
 831 was semiclassical and it's in 1926 that the first fully quantum mechanical wave-equation would
 832 be introduced by Schrödinger to describe electron-like particles, reproducing the previous semiclassical
 833 formulation without inconsistencies. This complexe equation describes the evolution of the
 834 wave function Ψ of the quantum system, defined by its position vector \mathbf{r} and time t as an energy
 835 conservation law, in which the hamiltonian of the system \hat{H} is explicit, by solving the Equation 2.3.

$$i\hbar \frac{\partial}{\partial t} |\Psi(\mathbf{r}, t)\rangle = \hat{H} |\Psi(\mathbf{r}, t)\rangle \quad (2.3)$$

836 In 1927, Dirac would go further in his paper about emission and absorption of radiation by
 837 proposing a second quantization not only of the physical process at play but also of the electromagnetic
 838 field, providing the ingredients to the first formulation of *Quantum Electrodynamics (QED)*
 839 and the description of photon emission by electrons dropping into a lower energy state in which the
 840 final number of particles is different than the initial one. To complete this model to the many-body
 841 wave functions of identical particles, Jordan included creation and annihilation operators for fields
 842 obeying Fermi-Dirac statistics leading to a model describing particles that would be referred to as
 843 *fermions*. Nevertheless, in order to properly treat electromagnetism, the incorporation of the relativ-

844 ity theory developed by Einstein. Including gravity into quantum physics still is a challenge nowa-
 845 days, but in 1928 Pauli and Jordan would show that special relativity's coordinate transformations
 846 could be applied to quantum fields as the field commutators were Lorentz invariant. Finally derived
 847 the same year, the Dirac equation, shown as Equation 2.4, similarly to Schrödinger's equation, is a
 848 single-particle equation but it incorporates special relativity in addition to quantum mechanics rules.
 849 It features the 4×4 gamma matrices γ^μ built using 2×2 Pauli matrices and unitary matrix, the
 850 4-gradient ∂_μ , the rest mass m of any half integer spin massive particle described by the wave func-
 851 tion $\psi(x, t)$, also called a Dirac spinor, and the speed of light c . In addition to perfectly reproduce
 852 the results obtained with quantum mechanics so far, it also provided with *negative-energy solutions*
 853 that would later be interpreted as a new form of matter, *antimatter* and give a theoretical justifica-
 854 tion to the Pauli equation that was phenomenologically constructed to account for the spin as in the
 855 non-relativistic limit, the Dirac equation is similar.

$$i\hbar\gamma^\mu\partial_\mu\psi - mc\psi = 0 \quad (2.4)$$

856 The successes of the QED was soon followed with theoretical problems as computations of any
 857 physical process involving photons and charged particles were showed to be only reliable at the first
 858 order of perturbation theory. At higher order of the theory, divergent contributions were appearing
 859 giving nonsensical results. Only two effects were contributing to these infinities.

- 860 • The self-energy of the electron (or positron), the energy that the particle has due its own
 861 interaction with its environment.
- 862 • The vacuum polarization, virtual electron–positron pairs produced by a background electro-
 863 magnetic field in the vacuum which is not an "empty" space. These virtual pairs affect the
 864 charge and current distributions generated by the original electromagnetic field.

865 Solving this apparent problem was done by carefully defining the concepts of each observables,
 866 for example mass or charge, as these quantities are understood within the context of a non-interacting
 867 field equation, and that from the experiment point of view, they are abstractions as what is measured
 868 are "renormalized observables" shifted from there "bare" value by the interaction taking place in
 869 the measuring process. The infinities needed to be connected to corrections of mass and charge
 870 as those are fixed to finite values by experiment. This was the intuition of Bethe in 1947 who
 871 successfully computed the effect of such *renormalization* in the non-relativist case. Fully covariant
 872 formulations of QED including renormalization was achieved by 1949 by Tomonaga, Schwinger,
 873 Feynman and Dyson and Feynman is now famous for his association of diagrams to the term of
 874 the scattering matrix, greatly simplifying the representation and computation of interactions as the
 875 diagrams directly corresponded the measurable physical processes and would then be used in every
 876 quantum field theories. With the resolution of infinities, QED had mostly reached its final form,
 877 being still today the most accurate physical theory and would serve as a model to build all other
 878 quantum field theories.

879 Development of the quark model and Quantum Chromodynamics

880 To explain the nuclear force that holds *nucleons* (protons and neutrons) together, Yukawa theoreti-
 881 cally proposed in 1934 the existence of a force carrier called *meson* due to it's predicted mass in
 882 the range in between the electron and nucleon masses. Discovered in 1936 by Anderson and Ned-
 883 dermeyer, and confirmed using bubble chambers in 1937 by Street and Stevenson, a first meson

884 candidate was observed in the decay products of cosmic rays. Assuming it had the same electric
 885 charge than electrons and protons, this particle was observed to have a curvature due to magnetic
 886 field that was sharper than protons but smoother than electrons resulting in a mass in between that
 887 of electrons and protons. But its properties were not compatible with Yukawa's theory, which was
 888 emphasized by the discovery of a new candidate in 1947, again in cosmic ray products using photo-
 889 graphic emulsions.

890 This new candidate, although it had a similar mass than the already believed *meson*, would rather
 891 decay into it. For distinction, the first candidate would then be renamed "*mu meson*" when the second
 892 would be the "*pi meson*". The *mu meson* was behaving like a heavy electron and didn't participate
 893 in the strong interaction whereas the pion was believed to be the carrier of the nuclear interaction.
 894 This lead to classify the *mu* in a new category of particles called *leptons* together with the electron
 895 that shared similar properties and *the neutrino*, and be renamed *muon*. The *pi meson* was finally
 896 found to be a triplet of particles: a positively charged, a negatively charged, and a neutral particle.
 897 The neutral *pi meson* has been more difficult to identify as it wouldn't leave tracks on emulsions nor
 898 on bubble chambers and needed to be studied via it's decay products. It was ultimately identified in
 899 University of California's cyclotron in 1950 through the observation of its decay into 2 photons.

900 Also discovered in 1947 but in cloud chamber photographs, the *K meson* as also been an im-
 901 portant step towards the establishment of the Standard Model. A triplet of particle, 2 charged and a
 902 neutral, with a mass roughly half that of a proton, were reported. These particles were baptised *K*
 903 *meson* in contrast to the "light" *pi* and *mu* "L-mesons". The particularity of the *K* were there very
 904 slow decays with a typical lifetime of the order of 10^{-10} s much greater than the 10^{-23} s of *pi*-proton
 905 reactions. The concept of *strangeness*, a new quantum number was then introduced by Pais as an
 906 attempt to explain this phenomenon as *strange* particles appeared as a pair production of a strange
 907 and anti-strange particle.

908 With the development of synchrotrons, the particle *zoo* would grow to several dozens during the
 909 1950s as higher energies were reachable through acceleration. In 1961, a first classification system,
 910 called Eightfold Way, was proposed by Gell-Mann and finding its roots in the Gell-Mann–Nishijima
 911 formula, which relates the electric charge Q , the third component of the isospin I_3 , the *baryon*
 912 number B and the strangeness S , as explicitated in Formula 2.5. The isospin was a quantum number
 913 introduced in 1932 to explain symmetries of the newly discovered neutron using representation
 914 theory of SU(2). The baryon number, was introduced by Nishijima as a quantum number for baryons,
 915 i.e. particles of the same family as nucleons. The mesons were classified in an octet and baryons of
 916 spin $\pm \frac{1}{2}$ and $\pm \frac{3}{2}$ were respectively classified into an octet and a decuplet, as shown in Figure 2.2. To
 917 complete the baryon decuplet, Gell-Mann predicted the existance of baryon Ω^- which would later
 918 be discovered in 1964.

$$Q = I_3 + \frac{1}{2}(B + S) \quad (2.5)$$

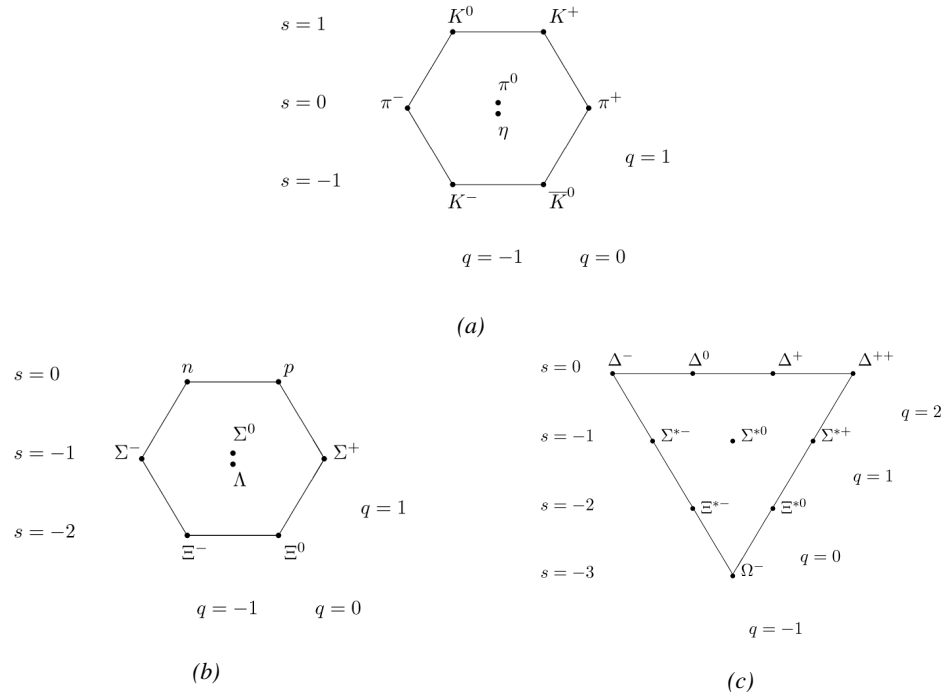


Figure 2.2: Figure 2.2a: Meson octet. Figure 2.2b: Baryon octet. Figure 2.2c: Baryon decuplet.

Strong of this classification using an SU(3) flavor symmetry, Gell-Mann, and independently Zweig, would propose a full theoretical model in which *hadrons* (strongly interacting particles, i.e. mesons and baryons) were not elementary particles anymore. They would rather be composed with 3 flavors of particles called *quarks* and there anti-particles. The 3 flavors were called *up*, *down* and *strange*. *Up* and *down* would be used to explain the nucleons and non-strange mesons, while *strange* would come into the composition of hadrons showing strangeness. *Up* and *down* flavors would be discovered in 1968 thanks to the deep inelastic scattering experiments conducted at the Stanford Linear Accelerator Center (SLAC), and *strange* could only be indirectly validated even though it provided a robust explanation to *kaon* (K) and *pion* (π). However, in the decade following the Gell-Mann-Zweig quark model proposition, several improvement to the model were brought, first by Glashow and Bjorken the same year that predicted the existence of a fourth quark flavor, the *charm*, that would equalize the then known number of quarks and leptons and finally in 1973 by Kobayashi and Maskawa that would increase the number of quarks to 6 to explain the experimental observation of CP violation. These two quarks would be referred to as *top* and *bottom* for the first time in 1975. It's only after these additions to the quark model that finally the *charm* would be discovered in 1974 at both SLAC and Brookhaven National Laboratory (BNL). A meson where the *charm* was bound with an *anti-charm*, called J/ψ , would help convince the physics community of the validity of the model. The *top* would be discovered soon after in 1977 in Fermilab and indicate the existence of the *bottom* that would resist to discovery until Fermilab's experiments CDF and D \emptyset in 1995 due its very large mass and the energy needed to produce it.

As remarked by Struminsky, the original quark model proposal composed of 3 quarks should possess an additional quantum number due to mesons such as Ω^- or Δ^{++} . Indeed, these mesons are composed of 3 identical quarks, respectively 3 *strange* and *up* quark, with parallel spins, which

should be forbidden by the exclusion principle. Independentle, Greenberg and Han-Nambu proposed an additional SU(3) degree of freedom possessed by the quarks, that would later be refered to as *color charge gauge*, that could interact through *gluons*, the gauge boson octet corresponding to this degree of freedom. Nevertheless, as observing free quarks proved to be impossible, two visions of the quarks were argued mainly due to the failures to observe these particles free to prove their existence. On one side, Gell-Mann proposed to see quarks as mathematical construct instead of real particles, as they are always confined, implying that quantum field theory would not describe entirely the strong interaction. Opposed to this vision, Feynman on the contrary argued that quarks were real particles, that he would call *partons*, that should be described as all other particles by a distribution of position and momentum. The implications of quarks as point-like particles would be verified at SLAC and the concept of *color* would be added to the quark model in 1973 by Fritzsch and Leutwyler together with Gell-Mann to propose a description of the strong interaction through the theory of Quantum Chromodynamics (QCD). The discovery the same year of asymptotic freedom within the QCD by Groos, Politzer and Wilczek, allowed for very precise predictions thanks to the perturbation theory. Nowadays, the confinement of quarks is studied in experiments such as ALICE, through exploration of the quark-gluon plasma.

958 The Weak interaction, spontaneous symmetry breaking, the Higgs mechanism and the Elec- 959 troweak unification

The weak interaction is the process that causes radioactive decays. Thanks to the neutron discovery, Fermi could explain in 1934 the beta radiations through the beta decay process in which the neutron decays into a proton by emitting an electron. Though the missing energy observed during this process triggered a huge debate about the apparent non conservation of energy, momentum and spin of the process, Fermi, as Pauli before him, proposed that the missing energy was due to a neutral not yet discovered particle that would then be baptised *neutrino*. The impossibility to detect such a particle would leave some members of the scientific community sceptical, but hints of energy conservation and of the existence of the neutrino were provided by measuring the energy spectrum of electrons emitted through beta decay, as there was a strict limit on their energy. It's only 30 years later in 1953 that it would be discovered by the team of Cowan and Reines using the principle of inverse beta decay described through Formula 2.6. The experiment consisted in placing water tanks sandwiched in between liquid scintillators near a nuclear reactor with an estimated neutrino flux of $5 \times 10^{13} \text{ s}^{-1} \text{ cm}^{-2}$. However, in order to explain the absence of some reactions in the experiment of Cowan and Reines, and constraint the beta decay theory of Fermi and extend it to the case of the muon, Konopinski and Mahmoud proposed in 1953 that the muon decay would eject a particle similar to the neutrino and thus predicted the existence of a muon neutrino that would be different than the one involved in the beta decay, related to the electron. With this, the idea of lepton number would arise. The muon neutrino would successfully be detected in 1962 by Lederman, Schwartz and Steinberger.

$$\bar{\nu} + p \rightarrow n + e^+ \quad (2.6)$$

The theory could not be valid though as the probability of interaction, called cross-section, would have been increasing without bond with the square of the energy. Fermi assumed in a two vector current coupling but Lee and Yang noted that an axial current could appear and would violate parity. The experiment of Wu in 1956 would confirm the parity violation and Gamow and Teller would try to account for it by describing Fermi's interaction through allowed (parity-violating) and superallowed

984 (parity-conserving) decays. But the success of QED as a quantum field theory would spark the
985 development of such a theory to describe the weak interaction.

986 As previously discussed, the great success of QED was built on an underlying symmetry, inter-
987 preted as a gauge invariance so that the effect of the force is the same in all space-time coordinates,
988 and of the possibility to renormalize it in order to absorb the infinities. Independently in 1958,
989 Glashow, and Salam and Ward used 1957 Schwinger ideas about vector intermediary for the decay
990 processes, could find a way to unite both the electromagnetic and weak interaction into a gauge
991 theory involving 4 gauge bosons, 3 of which were massive and carried out the weak interaction and
992 a massless boson carrying the electromagnetic interaction. Among the 3 massive bosons, 2 were
993 charged and 1 was neutral, similarly to the previously theorized *pi meson* vector of the Yukawa
994 model and all have a mass much greater than nucleons and thus a very short life time implying a
995 finite very short range contrary to the contact interaction originally proposed by Fermi.

996 Breakthrough in other fields of physics contributed in giving theoretical support and interpreta-
997 tion to the unified electroweak theory. The stepping stone would be the use of spontaneous symmetry
998 breaking that was inspired to Nambu at the end of the 1950s following the development of the BCS
999 superconductivity mechanism in 1957. Cooper had shown that BCS pairs, pairs of electrons bound
1000 together at low temperature, could have lower energy than the Fermi energy and where responsi-
1001 ble for superconductivity. This lead to the discovery of Goldstone-Nambu bosons as a result of the
1002 spontaneous breaking of the chiral symmetry in a theory describing nucleons and mesons devel-
1003 opped by Nambu and Jona-Lasinio in 1961, and now understood as a low-energy approximation of
1004 QCD. Similarly to mechanism of energy gap appearance in superconductivity, the nucleon mass
1005 is suggested to the result of a self-energy of a fermion field and is studied through a four-fermion
1006 interaction in which, as a consequence of the symmetry, bound states of nucleon-antinucleon pairs
1007 appear and can be regarded as virtual pions. Though the symmetry is maintained in the equations,
1008 the ground state is not preserved. Goldstone would later the same year show that the bound states
1009 corresponds to spinless bosons with zero mass.

1010 Although the model in itself didn't revolutionize particle physics, spontaneous symmetry break-
1011 ing would be generalized to quantum field theories. As all fundamental interactions are described
1012 using gauge theories based on underlying symmetries, processes such as the chiral symmetry break-
1013 ing would be introduced soon after the publication of Nambu and Jona-Lasinio. In 1962, Anderson,
1014 following an idea of Schwinger who suggested that zero-mass vector bosons were not necessarily
1015 required to describe the conservation of baryons contrary to the bosons emerging from chiral sym-
1016 metry breaking, discussed the implications of spontaneous symmetry breaking in particles physics.
1017 A model was finally independently built in 1964 by Brout and Englert, Higgs, and Guralnik, Hagen,
1018 and Kibble, who discovered that combining an additional field into a gauge theory in order to break
1019 the symmetry, the resulting gauge bosons acquire a nonzero mass. Moreover, Higgs stated that this
1020 implied the existence of at least one new massive, i.e. self-interacting, scalar boson, that are now
1021 known as *Higgs bosons* corresponding to this additional field. The Higgs mechanism today specific-
1022 ally refers to the process through which the gauge bosons of the weak interaction acquire mass. In
1023 1968, Weinberg could point to the Higgs mechanism to integrate a Higgs field into a new version
1024 of the electroweak theory in which the spontaneous symmetry breaking mechanism of the Higgs
1025 field would explicitly explain the masses of the weak interaction gauge bosons and the zero-mass
1026 of photons.

1027 2.1.2 Construction and test of the model

1028 The Standard Model of particle physics was built in the middle of the 1970s after the experimental
 1029 confirmation of the existence of quarks. It is based on the assembly of the models previously introduced
 1030 and describing the fundamental interactions, except for gravitation, and their gauge bosons
 1031 as well as the way elementary "matter" particles interact with the fields associated with these force
 1032 carriers. In this sense, the development of QED and the unification of the electroweak interaction,
 1033 of the Yukawa interaction and of QCD, and of the Higgs mechanism made it possible to explain most
 1034 of contemporary physics.

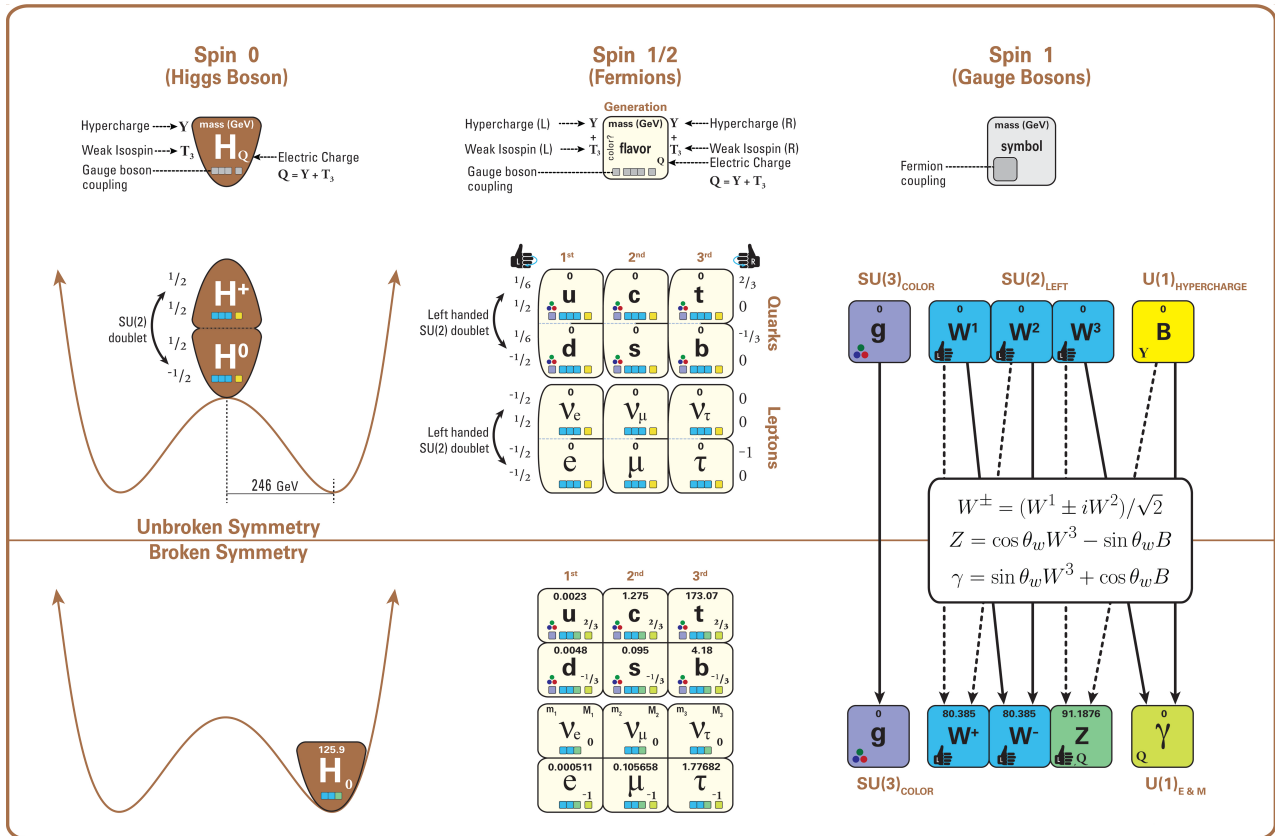


Figure 2.3: The elementary particles of the Standard Model are showed along with their names and properties. Their interactions with the strong, weak and electromagnetic forces have been explicited using color squares. In the left column, the scalar higgs boson is depicted, while the central is focused on the matter particles, the fermions, and the right on the force carriers, the gauge bosons. The role of the Higgs boson in electroweak symmetry breaking is highlighted, and the corresponding way properties of the various particles differ in the (high-energy) symmetric phase (top) and the (low-energy) broken-symmetry phase (bottom) are showed.

1035 In the SM, "matter" particles, are described by 12 fermion fields of spin $\frac{1}{2}$ obeying the Fermi-
 1036 Dirac statistics, i.e. subjected to the Pauli exclusion principle. To each fermion is associated its
 1037 corresponding antiparticle. The fermions are classified according to the way they interact and, thus,
 1038 according to the charges they carry. 6 of them are classified as quarks (u, d, c, s, t , and b) and
 1039 are subjected to all interactions and the 6 others as leptons ($e^-, \mu^-, \tau^-, \nu_e, \nu_\mu$, and ν_τ). Leptons

1040 are not subjected to the strong interaction and among them, the 3 neutrinos only interact weakly as
 1041 they are neutral particles, which explains why they are so difficult to detect. The gauge boson fields
 1042 are the gluons g for the strong interaction, the photon γ for the electromagnetic interaction and the
 1043 weak bosons W^+ , W^- , and Z^0 for the weak interaction. Finally, the Higgs field H^0 is responsible,
 1044 through the spontaneous symmetry breaking, of the mixing of the massless electroweak boson fields
 1045 W_1 , W_2 , W_3 , and B leading to the observable states γ , W^+ , W^- , and Z^0 that can gain mass while
 1046 interacting with the Higgs field. This picture of the SM is summarized through Figure 2.3 where the
 1047 antifermions are not showed.

1048 When the model was first finalized, the existence of the weak gauge bosons, of the charm, of the
 1049 third quark generation composed of top and bottom quarks to explain the observed CP violation was
 1050 not proven but the predictions were measured with good precision in the years following. First, the
 1051 charm quark would be discovered in 1974, followed by the bottom quark in 1977. The weak bosons
 1052 would be discovered during the next decade in 1983. The top quark would resist until 1995 due to
 1053 its very large mass but would offer the last piece of the elementary QCD particles. The very last
 1054 predicted elementary particle of the model that was not observed yet would prove to be very difficult
 1055 to observe. The Higgs boson needed the start of the LHC to finally be observed in 2012. A few years
 1056 more of tests were necessary to measure its properties to confirm the observation of a scalar boson
 1057 compatible with the predicted Higgs boson H^0 . Even though only quark-antiquark (mesons) and 3
 1058 quark states (baryons) were observed, exotic hadrons were not forbidden by QCD and no limit of
 1059 quark is imposed by the theory. Moreover, gluons could form bond states by themselves and with
 1060 quarks. These two types of states are called *glueballs* and *hybrid hadrons*. For decades, experi-
 1061 ments have been conducted without confirmation of such possible states existing. Nevertheless, in
 1062 2014, tetraquarks were observed by LHCb, one of LHC's main experiments, and in 2015, the same
 1063 experiment reported the discovery of pentaquarks making the SM one of the best tested theories of
 1064 physics.

1065 2.1.3 Investigating the TeV scale

1066 Even though the SM is a well tested theory, several hints of physics going beyond its scope have
 1067 been observed. First of all, gravity is not explained through this model and huge difficulties are en-
 1068 countered when trying to include gravitation. The strength of gravitational interaction is expected to
 1069 be negligible at the scale of elementary particles, nevertheless, adding gravitation in the perspective
 1070 of developing a "theory of everything" leads to divergent integrals that could not be fixed through
 1071 renormalization.

1072 Moreover, the SM considers neutrinos to be massless but it was shown in the late 1960s by the
 1073 Homestake experiment that the flux of solar neutrinos (i.e. ν_e) measured didn't match the predicted
 1074 values due to neutrino oscillations, confirmed in the early 2000s by the Sudbury Neutrino Obser-
 1075 vatory. This oscillation implies that neutrinos that can be observed are a superposition of massive
 1076 neutrino states. The research on neutrino oscillation is already quite advanced with experiments
 1077 looking at atmospheric, reactor or beam neutrinos in order to determine the elements of the mixing
 1078 matrix similar to the CKM matrix describing the mixing of quarks. Nevertheless, no answer to the
 1079 origin of neutrino mass is provided.

1080 Another intriguing fact is that the universe is dominated by matter. However, the SM predicted
 1081 that matter and antimatter should have been created in equal amounts and no mechanism is able to
 1082 explain this matter-antimatter asymmetry. Although this asymmetry is seen from the visible uni-
 1083 verse, it may be possible that other unknown regions of the Universe are dominated by antimatter.

1084 Another possibility to explain the apparent asymmetry would be the existence of a electric dipole
1085 in any fundamental particle that would permit matter and antimatter particles to decay at different
1086 rates.

1087 The discrepancy of velocity dispersion of stars in galaxies with respect to the visible mass they
1088 contain is known since the end of the 19th century where Kelvin proposed that this problem could
1089 be solved if a "*great majority of [the stars] would be dark bodies*". Throughout the 20th century,
1090 physicists like Kapteyn, Zwicky, showed the first hints of a "*dark matter*" by studying star veloc-
1091 ities and galactic clusters, followed by robust measurements of galaxy rotation curves by Babcock
1092 which suggested that the mass-to-luminosity ratio was different from what would be expected from
1093 watching the visible light. Later in the 1970s, Rubin and Ford from direct light observations and
1094 Rogstad and Shostak from radio measurements showed that the radial velocity of visible objects in
1095 galaxies was increasing with increasing distance to the center of the galaxy. Finally observation of
1096 lensing effect by galaxy clusters, temperature distribution of hot gas in galaxies and clusters, and
1097 the anisotropies in the Cosmic Microwave Background (CMB) kept on pointing to a "*dark matter*".
1098 From all the data accumulated, the visible matter would only account to no more than 5% of the total
1099 content on the visible universe. Alternative theories have tried to investigate modified versions of
1100 the General Relativity as this theory is only well tested at the scale of the solar system but is not suf-
1101 ficiently tested on wider ranges or even theories in which gravitation is not a fundamental force but
1102 rather an emergent one, but so far, such theories have difficulties to reproduce all the experimental
1103 observations as easily as through dark matter.

1104 A possible theory to offer dark matter candidates would be supersymmetry (SUSY) which pro-
1105 poses a relationship in between bosons and fermions. In this model, each elementary particle,
1106 through a spontaneous spacetime symmetry breaking mechanism would have a *super partner* from
1107 the other family of particles. On top of providing heavy dark matter candidates, supersymmetry
1108 could also help solving the *Hierarchy problem*, the very large scale difference in between the weak
1109 interaction and gravity, although, as mentioned before, in the case gravity is found not to be a fun-
1110 damental force, this problem would automatically fade.

1111
1112 All these different aspects of physics beyond the Standard Model of particle physics and the
1113 Standard model itself can be tested through the use of very energetic and intense hadron and ion col-
1114 liders. The LHC at CERN is a perfect tool to seek answers to these open questions except maybe for
1115 the gravity as gravity is extremely weak at particles level. For example, one of LHCb experiment's
1116 goal is to investigate CP-violation and thus baryonic asymmetry. In 2017, the collaboration has an-
1117 nounced to have so far a 3.3σ statistical significance over a CP-violation through the study of the
1118 decays of Λ_b^0 and $\overline{\Lambda}_b^0$ into a proton (or antiproton) and 3 pions. Many analysis teams are also working
1119 hard on supersymmetry both in ATLAS and CMS collaborations, the two multipurpose experiments
1120 of LHC, even though no evidence of a supersymmetrical theory was seen, the few hint having the
1121 tendency to confirm the standard model. These experiments also have the possibility to investigate
1122 ways to explain Majorana neutrino mass through Yukawa interactions of scalar particles.

1123 The higher the center-of-mass energy, the smaller details the experiments will be able to see, the
1124 heavier the potential particle creation barrier will be, the stronger the cross-section of certain rare
1125 decay channels will be. As a comparison, with collisions happening at 14 TeV, the LHC is approxi-
1126 mately 2 orders of magnitude more sensitive to the Higgs than the Tevatron was with its already very
1127 powerful 2 TeV. All these advantages eventually lead to new discoveries and deeper understanding
1128 of the models describing our Universe. But the LHC only is a step forward to gather more precise
1129 tests of the Standard Model and new knowledge about the physics beyond it. A successful physics

1130 campaign will probably serve to justify the building of new accelerators with even greater discovery
1131 potential like for example the Future Circular Collider (FCC) that would push even further the study
1132 of the unanswered questions of contemporary physics.

1133 2.2 The Large Hadron Collider & the Compact Muon Solenoid

1134 Throughout its history, CERN has played a leading role in high energy particle physics. Large re-
1135 gional facilities such as CERN were thought after the second world war in an attempt to increase
1136 international scientific collaboration and allows scientists to share the forever increasing costs of
1137 experiment facilities required due to the need for increasing the energy in the center of mass to
1138 deeper probe matter. The construction of the first accelerators at the end of the 50s, the Synchro-
1139 cyclotron (SC) and the Proton Synchrotron (PS), was directly followed by the first observation of
1140 antinuclei in 1965 [1]. Strong from the experience of the Intersecting Storage Rings (ISR), the very
1141 first proton-proton collider that showed hints that protons are not elementary particles, the Super
1142 Proton Synchrotron (SPS) was built in the 70s to investigate the structure of protons, the preference
1143 for matter over antimatter, the state of matter in the early universe or exotic particles, and lead to
1144 the discovery in 1983 of the W and Z bosons [2–5]. These newly discovered particles and the elec-
1145 troweak interaction would then be studied in details by the Large Electron-Positron (LEP) collider
1146 that will help to prove in 1989 that there only are three generations of elementary particles [6]. The
1147 LEP would then be dismantled in 2000 to allow for the LHC to be constructed in the existing tunnel.

1148 2.2.1 LHC, the most powerful particle accelerator

1149 The LHC has always been considered as an option to the future of CERN. At the moment of the
1150 construction of the LEP beneath the border between France and Switzerland, the tunnel was built in
1151 order to accomodate what would be a Large Hadron Collider with a dipole field of 10 T and a beam
1152 energy in between 8 and 9 TeV [7] directly followed in 1985 with the creation of a 'Working Group
1153 on the Scientific and Technological Future of CERN' to investigate such a collider [8]. The decision
1154 was finally taken almost 10 years later, in 1994, to construct the LHC in the LEP tunnel [9] and the
1155 approval of the 4 main experiments that would take place at the 4 interaction points would come in
1156 1997 [10] and 1998 [11]:

- 1157 • ALICE [12] has been designed in the purpose of studying quark-gluon plasma that is believed
1158 to have been a state of matter that existed in the very first moment of the universe.
- 1159 • ATLAS [13] and CMS [14] are general purpose experiments that have been designed with
1160 the goal of continuing the exploration of the Standard Model and investigate new physics.
- 1161 • LHCb [15] has been designed to investigate the preference of matter over antimatter in the
1162 universe through the CP violation.

1163 These large scale experiments, as well as the full CERN accelerator complex, are displayed on
1164 Figure 2.4. The LHC is a 27 km long hadron collider and the most powerful accelerator used for
1165 particle physics since 2008 [16]. The LHC was originally designed to collide protons at a center-
1166 of-mass energy of 14 TeV and luminosity of $10^{34} \text{ cm}^{-2}\text{s}^{-1}$, as well as Pb ions at a center-of-mass
1167 energy of 2.8 TeV/A with a peak luminosity of $10^{27} \text{ cm}^{-2}\text{s}^{-1}$. Run 1 of LHC, when the center-of-
1168 mass energy only was half of the nominal LHC energy, was enough for both CMS and ATLAS to

discover the Higgs boson [17] and for LHCb to discover pentaquarks [18] and confirm the existance of tetraquarks [19]. Nevertheless, after the Third Long Shutdown (LS3) (2024-2026), the accelerator will be in the so called High Luminosity LHC (HL-LHC) configuration [20], increasing its instantaneous luminosity to $10^{35} \text{ cm}^{-2}\text{s}^{-1}$ for pp collisions and to $4.5 \times 10^{27} \text{ cm}^{-2}\text{s}^{-1}$, boosting the discovery potential of the LHC. The HL-LHC phase should last at least another 10 years depending on the breakthrough this machine would lead to. Already a new accelerating device, the FCC, as been proposed to prepare the future of high energy physics after the LHC.

CERN's Accelerator Complex

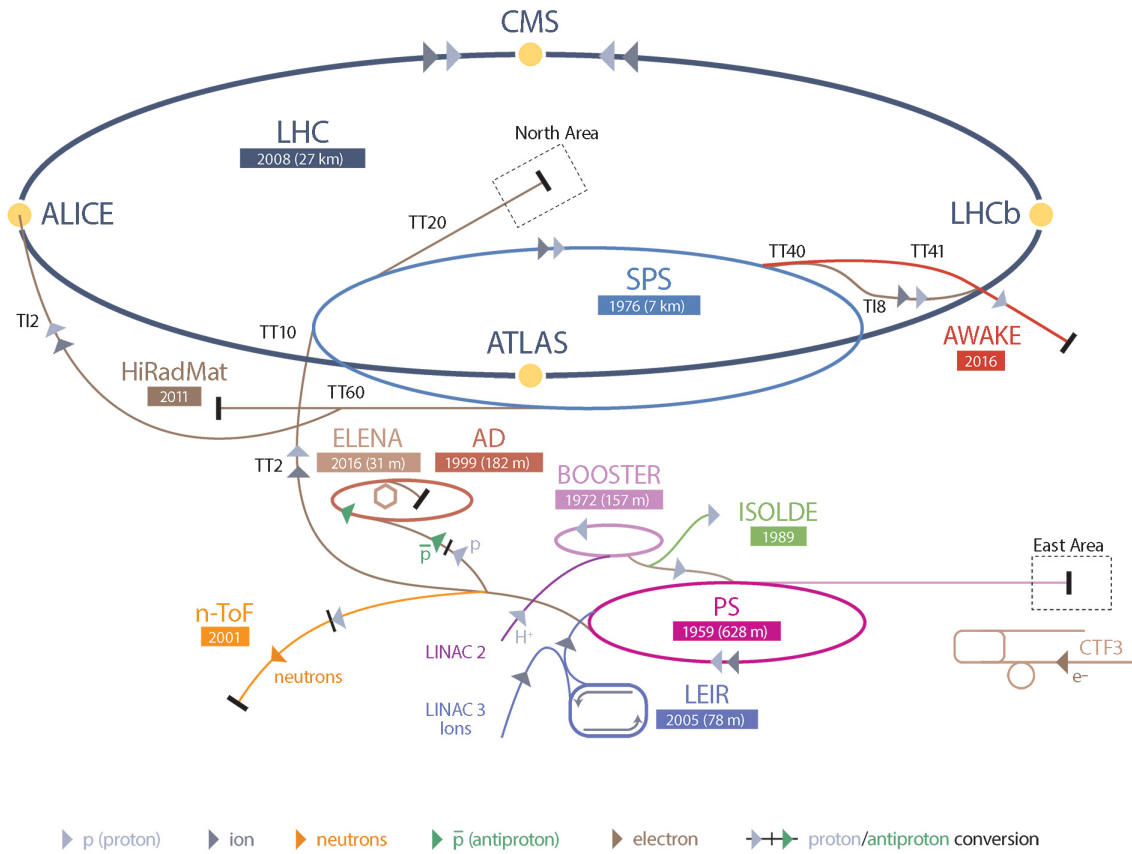


Figure 2.4: CERN accelerator complex.

2.2.1.1 Particle acceleration

The LHC is the last of a long series of accelerating devices. Before being accelerated by the LHC, the particles need to pass through different acceleration stages. All these acceleration stages are visible on Figure 2.4 and pictures of the accelerators are showed in Figure 2.5.

The story of accelerated protons at CERN starts with a bottle of hydrogen gas injected into the source chamber of the linear particle accelerator *LINAC 2* in which a strong electric field strips the

1183 electron off the hydrogen molecules only to keep their nuclei, the protons. The cylindrical conductors,
 1184 alternatively positively or negatively charged by radiofrequency cavities, accelerate protons by
 1185 pushing them from behind and pulling them from the front and ultimately give them an energy of
 1186 50 MeV, increasing their mass by 5% in the process.

1187

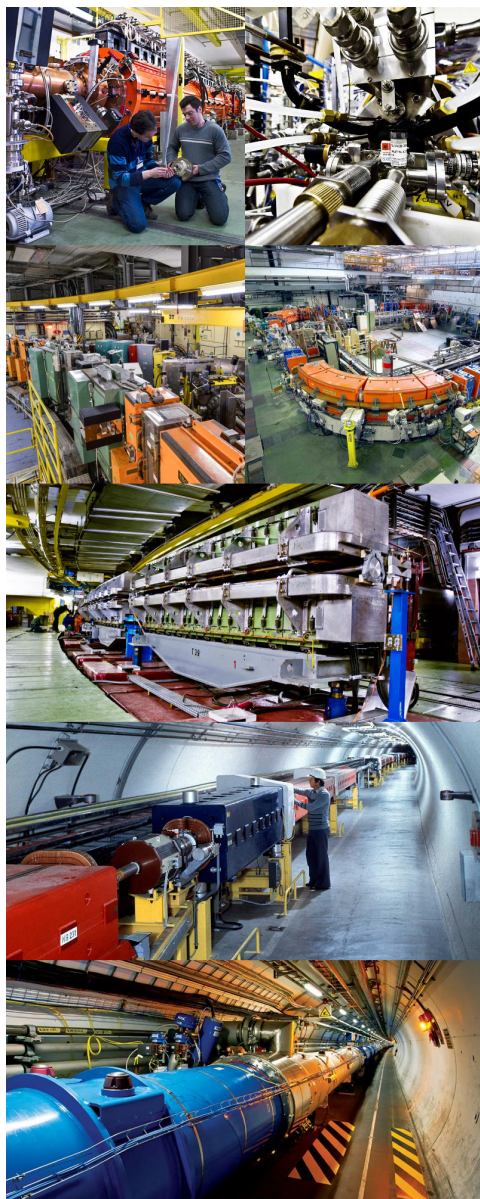


Figure 2.5: Pictures of the different accelerators. From top to bottom: first the LINAC 2 and the Pb source of LINAC 3. Then the Booster and the LEIR. Finally, the PS, the SPS and the LHC.

1188 When exiting the LINAC 2, the protons are divided into 4 bunches and injected into the 4 su-
 1189 perimposed synchrotron rings of the *Booster* where they are then accelerated to reach an energy of

1190 1.4 GeV before being injected into the PS. Before the Booster was operational in 1972, the protons
 1191 were directly injected into the PS from the LINAC 2 but the low injection energy limited the amount
 1192 of protons that could be accelerated at once by the PS. With the Booster, the PS accepts approxi-
 1193 mately 100 times more particles.

1194

1195 The 4 proton bunches are thus sent as one to the PS where their energy eventually reaches
 1196 26 GeV. Since the 70s, the main goal of this 628 m circumference synchrotron has been to sup-
 1197 ply other machines with accelerated particles. Nowadays, not only the PS accelerates protons, it also
 1198 accelerates heavy ions from the *Low Energy Ion Ring (LEIR)*. Indeed, the LHC experiments are not
 1199 only designed to study *pp*-collisions but also *Pb*-collisions. Lead is first injected into the dedicated
 1200 linear collider *LINAC 3*, that accelerate the ions using the same principle than LINAC 2. Electrons
 1201 are striped off the lead ions all along the acceleration process and eventually, only bare nuclei are
 1202 injected in the LEIR whose goal is to transform the long ion pulses received into short dense bunches
 1203 for LHC. Ions injected and stored in the PS were aceelerated by the LEIR from 4.2 MeV to 72 MeV.

1204

1205 Directly following the PS, is finally the last acceleration stage before the LHC, the 7 km long
 1206 *SPS*. The SPS accelerates the protons to 450 GeV and inject proton in both LHC accelerator rings
 1207 that will increase their energy up to 7 TeV. When the LHC runs with heavy lead ions for ALICE
 1208 and LHCb, ions are injected and accelerated to reach the energy of 2.8 TeV/A.

1209

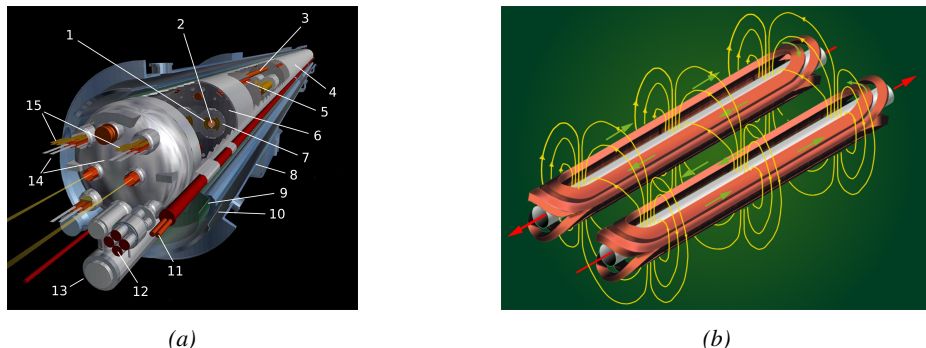


Figure 2.6: Figure 2.6a: schematics of the LHC cryodipoles. 1: Superconducting Coils, 2: Beam pipe, 3: Heat exchanger Pipe, 4: Helium-II Vessel, 5: Superconducting Bus-bar, 6: Iron Yoke, 7: Non-Magnetic Collars, 8: Vacuum Vessel, 9: Radiation Screen, 10: Thermal Shield, 11: Auxiliary Bus-bar Tube, 12: Instrumentation Feed Throughs, 13: Protection Diode, 14: Quadrupole Bus-bars, 15: Spool Piece Bus-bars. Figure 2.6b: magnetic field and resulting motion force applied on the beam particles.

1210

1211 The LHC beams are not continuous and are rather organised in bunch of paticles. When in *pp*-
 1212 collision mode, the beams are composed of 2808 bunches of 1.15×10^{11} protons separated by 25 ns.
 1213 When in *Pb* collision mode, the 592 *Pb* bunches are on the contrary composed of 2.2×10^8 ions
 1214 separated by 100 ns. The two parrallel proton beams of the LHC are contained in a single twin-
 1215 bore magnet due to the space restriction in the LEP tunnel. Indeed, building 2 completely separate
 1216 accelerator rings next to each other was impossible. The dipoles of the 1232 twin-bore magnets are
 1217 showed in Figure 2.6 alongside the magnetic field generated along the dipole section to accelerate the
 1218 particles. The dipoles generate a nominal field of 8.33 T, needed to give protons and lead nucleons
 their nominal energy. Some 392 quadrupoles, presented in Figure 2.7, are also used to focus to the

1219 beams, as well as other multipoles to correct smaller imperfections.

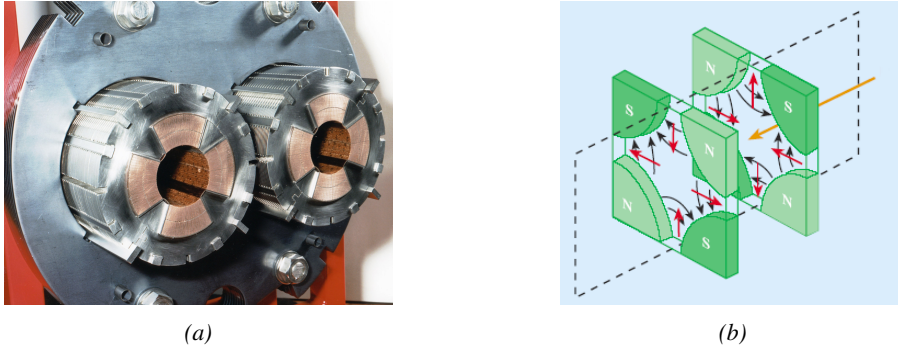


Figure 2.7: Figure 2.7a: picture of the LHC quadrupoles. Figure 2.7b: magnetic fields and resulting focussing force applied on the beam by 2 consecutive quadrupoles.

1220 2.2.2 CMS, a multipurpose experiment

1221 Among the four main LHC experiments is the Compact Muon Solenoid used as a multipurpose tool to
1222 investigate the SM and physics beyond its scope. Proposed through a letter of intention in 1992 [14],
1223 and as its name suggests, this very compact detector's uses the muons as a clear tag of most of SM
1224 and new physics interesting channels. In the original 1997 Technical Design Report (TDR) [21], the
1225 very first sentences were stating that "*Muons are an unmistakable signature of most of the physics*
1226 *LHC is designed to explore. The ability to trigger on and reconstruct muons at the highest lumi-*
1227 *nosities is central to the concept of CMS, the Compact Muon Solenoid.*" CMS participated in the
1228 discovery of the Higgs boson and the measurement of its properties and couplings together with
1229 ATLAS and is also actively involved in the search for SUSY and heavy ion collisions. Other exotic
1230 physics are also being investigated using the data collected by CMS.

1231 The CMS apparatus in itself is the heaviest detector ever built starring a SI15m diameter and a
1232 29 m length for a total weight of 14 kT. A thick 4 T solenoid magnet located at the beam interaction
1233 point hosts trackers and calorimeters. Extending in all directions around the magnet, heavy iron
1234 return yokes are installed to extend the magnetic field and support a muon system. The apparatus
1235 consists of a barrel, referring to the magnet and the detectors contained in it and the part of the muon
1236 system built directly in the cylinder around the magnet, and of 2 endcaps in the forward and back-
1237 ward region of the detector that closes the apparatus and complete the detection coverage along the
1238 beam line. A front view on the barrel is provided in Figure 2.8 while a detailed view of the apparatus
1239 is given in Figure 2.9.

1240

1241 In order to efficiently detect all long leaving particles and measure their properties with good
1242 precision, the CMS detector uses an onion like layout around of the interaction point in order to
1243 maximize the covered solid angle. As detailed in Figure 2.10, in the innermost region of the detector,
1244 closest to the interaction point, the silicon tracker records the trajectory of charged particles. Around
1245 it, the electromagnetic calorimeter (ECAL) stops and measure the energy deposition of electrons
1246 and photons. In the next layer, the hadron calorimeter (HCAL), hadrons are stopped and their energy
1247 measured. These layers are contained inside of the magnet of CMS, the superconducting solenoid.
1248 Outside of the magnet are the muon chambers embedded into iron return yokes used to control the

1249 magnetic field and gives muons, the only particles traveling completely through the whole detector, a
 1250 double bending helping in reconstructing their energy and trajectory. Note that photons and neutral
 1251 hadrons are differentiated from electrons and charged hadrons in the calorimeters by the fact that
 1252 don't interact with the silicon tracker and that they are not influenced by the magnetic field.

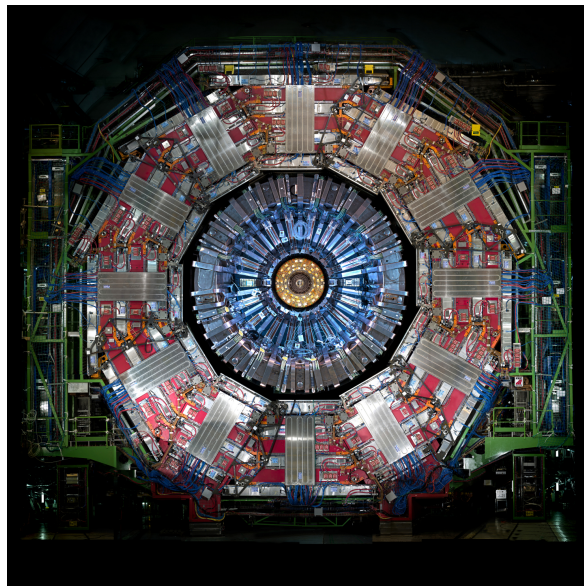


Figure 2.8: Picture of the CMS barrel. The red outer layer is the muon system hosted into the red iron return yokes. The calorimeters are the blue cylinder inside in magnet solenoid and the tracker is the inner yellow cylinder built around the beam pipe.

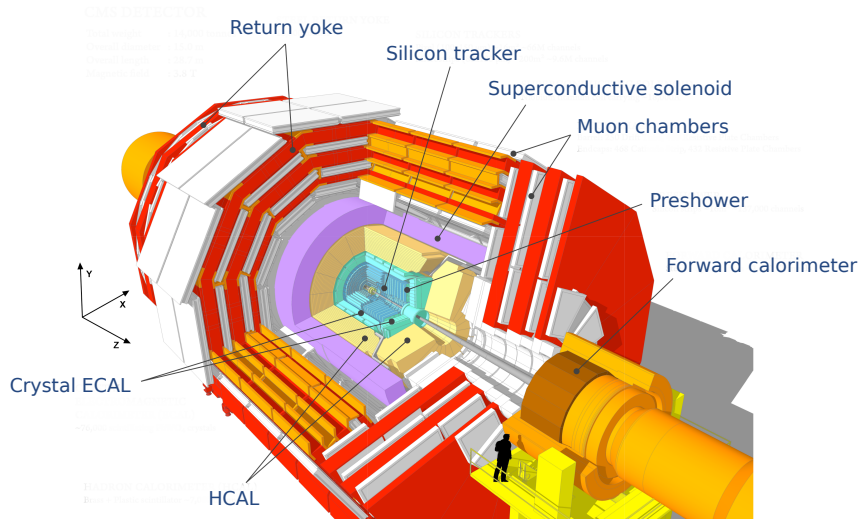


Figure 2.9: View of the CMS apparatus and of its different components.

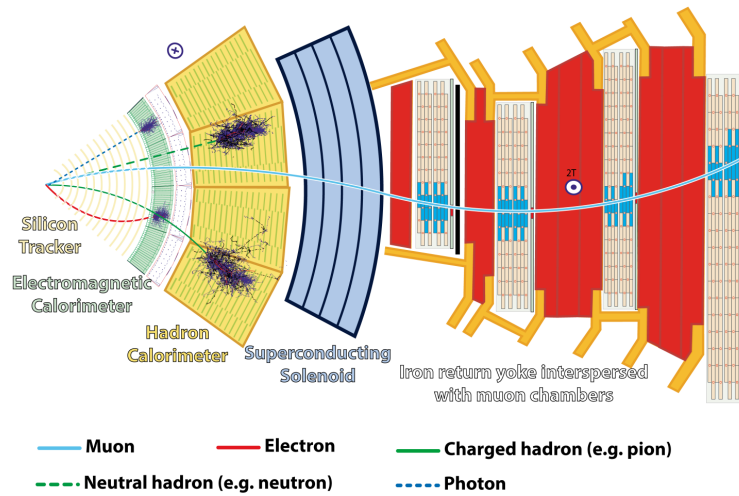


Figure 2.10: Slice showing CMS sub-detectors and how particles interact with them.

2.2.2.1 The silicon tracker, core of CMS

The silicon tracker visible on Figure 2.11 is divided into 2 different sub-systems: the *pixel detector* at the very core and the *microstrip detector* around it. This system is composed of 75 million individual readout channels with up to 6000 channels per squared centimeter for the pixels making it the world's biggest silicon detector. This density allows for measurements of the particle tracks with a precision of the order of $10\ \mu\text{m}$. This is necessary to reconstruct all the different interaction vertices with precision and have a precise measure of the curvature of the charged particles traveling through the magnetic field to estimate their charge and momentum.

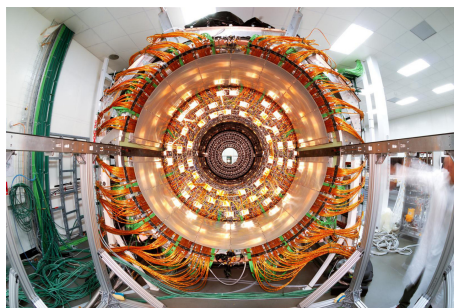


Figure 2.11: CMS tracker.

2.2.2.2 The calorimeters, measurement of particle's energy

The ECAL directly surrounding the tracker is composed of crystals of lead tungstate, PbWO_4 , a very dense but optically transparent material used to stop high energy electrons and photons. These crystal blocks basically are extremely dense scintillators which scintillate in fast, short light bursts proportionally to the energy deposition. The light is yielded rapidly and contained at 80% in the corresponding 25 ns lasting bunch crossing. Each crystal is isolated from the other by the carbon fiber matrix they are embedded in. It is composed of a barrel containing more than 60,000 crystals

and of closing endcaps containing another 15,000 crystals. In front of the ECAL endcap is installed a preshower detector made out of two layers of lead and silicon strip detectors to increase the spatial resolution close to the beam line for pion-photon and single-double photon discrimination purposes. Figure 2.12 shows the calorimeter inside of the magnet and the crystals.

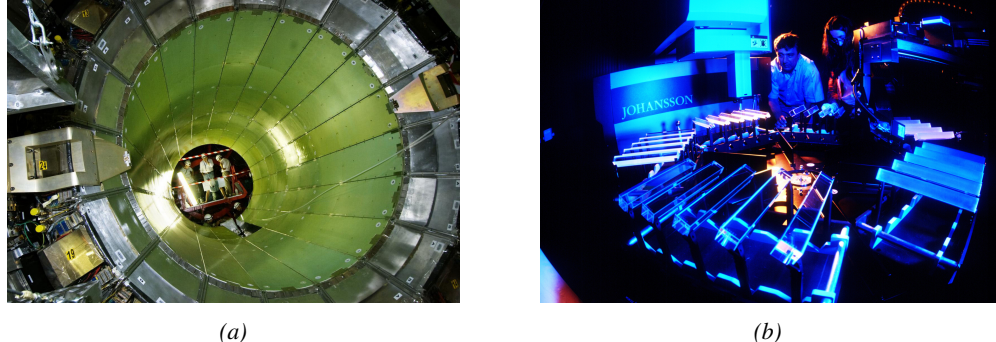


Figure 2.12: Figure 2.12a: picture of the ECAL. Figure 2.12b: picture of the lead tungstate crystals composing the ECAL.

The next layer is the HCAL measuring the hadrons momentum and providing indirect hints of non interacting neutral particles, such as neutrinos, as missing transverse momentum. Several layers of brass or steel are interleaved with plastic scintillators readout by photodiodes using wavelength-shifting fibers. The HCAL is also composed of a barrel, showed in Figure 2.13 and of endcaps. It also features forward calorimeters on both sides of CMS in the region very close to the beam line at high pseudorapidity ($3.0 < |\eta| < 5.0$). The role of these forward calorimeters, made using steel and quartz fibers, is to measure very energetic hadrons.



Figure 2.13: CMS hadron calorimeter barrel.

Finally, in the outer region of the apparatus, a muon system is used to trigger on potentially interesting event by identifying muons. Indeed, the muon system is a very important part of the CMS trigger infrastructure designed to efficiently select data from the enormous data flow received by the detectors as the LHC delivers collisions at a rate of 40 MHz with a pile-ip of 20 to 30 collisions per bunch crossing during Phase-I and up to 200 during Phase-II, representing billions of interactions per second among which a large quantity are low energy collisions that are not likely to produce new reactions, and which is physically impossible for nowadays technologies to cope with. Working at a maximum rate of 100 kHz, the trigger system is able to select the 100,000 more interesting events

by looking at the energy distribution of the interaction products and clear signatures like muons reconstructed by the muon system. the vast majority of these events will not finally be stored after physics tests are applied.

2.2.2.3 The muon system, corner stone of CMS

The challenge for the muon system is to provide a robust and fast measurement of muons. Three different subsystems, and soon 4 after LS2, compose the muon system as showed in Figure 2.14 in which a quadrant of the CMS detector focused on muon system. Drift Tube (DT) are found in the barrel region covering the low pseudorapidity region where particles transverse momentum is lower and Cathode Strip Chamber (CSC) are found in the endcap region covering higher pseudorapidity region closer to beam line where particles have a stronger momentum. The redundancy of the system is insured by Resistive Plate Chamber (RPC) in both the barrel and endcap region. Nevertheless, the region closest to the beam line ($|\eta| > 1.8$) was not equipped with RPCs. This lack of redundancy in the high pseudo rapidity region will be solved during LS2, the following Year End Technical Stop (YETS) in 2021 and 2022, and LS3 where the necessary services, detectors and Link System, that collects the data and synchronizes them, will be installed.

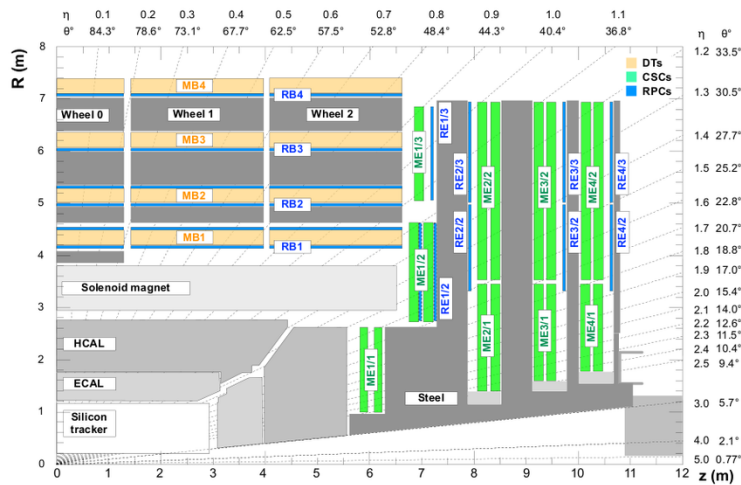


Figure 2.14: A quadrant of the muon system, showing DTs (yellow), RPCs (blue), and CSCs (green).

The barrel region is divided into 5 *wheels* made out of 4 *rings* of detectors with iron return yokes in between them whereas the endcaps are made out of 4 disks, each divided into pseudorapidity stations, 2 for CSCs (except for the first disk where 3 stations are equipped) and 3 for RPCs, although only 2 RPCs stations are equipped at present. The wheels and disks are showed in Figure 2.15. So far, each subsystem was dedicated to a particular task. DTs, in the barrel, and CSCs, in the endcaps, are used mainly for their spatial resolution. Indeed, DTs' resolution is of the order of 100 μm along both the $(r - \phi)$ and $(r - z)$ components while the resolution of CSCs is similar but varies in a range from 50 μm to 140 μm depending on the distance to the beamline. On the other hand, RPCs are used for their time resolution as they can deliver an information on the muon tracks within 1.5 ns.

The 250 CMS DTs, found in the barrel covering the pseudorapidity region $0 < |\eta| < 1.2$ and whose structure is shown in Figure 2.16, are composed of 3 *superlayers* of DT cells. Two of these superlayers are dedicated to measuring the ϕ coordinate of the muons and while the last one

measures the η (or z) coordinate. Each superlayer consists on 4 layers of 60 to 70 DT cells arranged in quincunx to allow for a precise reconstruction of the muon path through the DT layers. Each DT cell is a rectangular aluminium gas volume with a central anode wire. Cathode strips are placed on the narrow surface of the cells and electrode strips are placed on the wide surface to help shaping the electric field to ensure a consistent drift velocity of electrons in the drift volume. These detectors are operated using a 85/15 mixture of Ar and CO_2 .

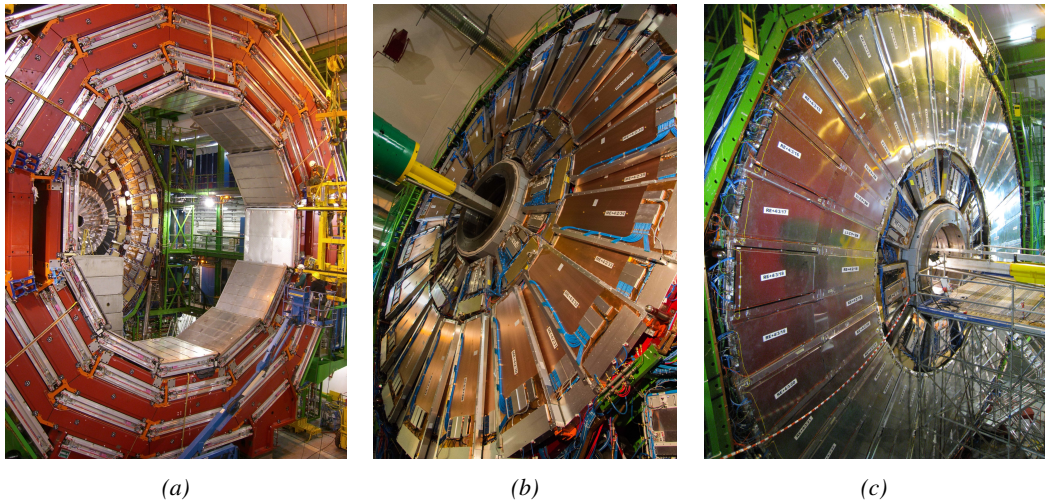


Figure 2.15: Figure 2.15a: Barrel wheel with its detector rings and return yokes. Figure 2.15b: CSC endcap disk with the 2 CSC stations. The outer station is made of 10 deg detectors while the inner station is made of 20 deg detectors. Figure 2.15c: RPC endcap disk. The inner station is not equipped and the inner CSC station can be seen.

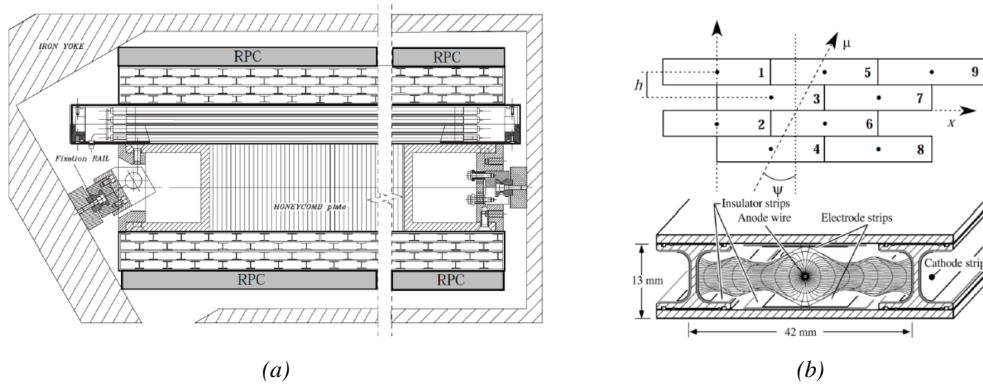


Figure 2.16: Figure 2.16a: Cross section of a DT module showing the two superlayers measuring the ϕ coordinate, perpendicular to the cross section plane, and the superlayer measuring the η coordinate, placed in between the two others with honeycomb and parallel to the cross section plane. The DT detector is sandwiched in between 2 RPCs whose readout strips are perpendicular to the cross section plane, measuring the ϕ coordinate. Figure 2.16b: A DT cell is shown together with its electric field. The path of a muon through a superlayer is shown.

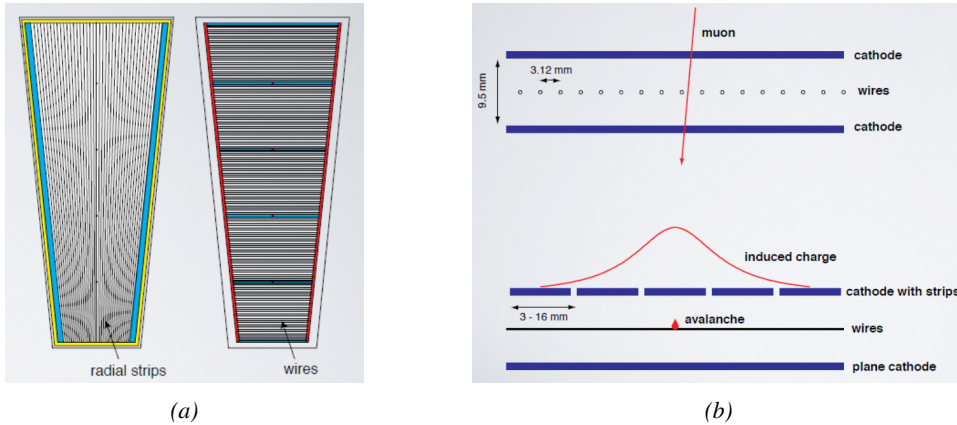


Figure 2.17: Figure 2.17a: cathode strips and anode wire layout of a CSC panel. Figure 2.17b avalanche development and charge collection by anode wires and induction on cathode strips inside of a CSC panel.

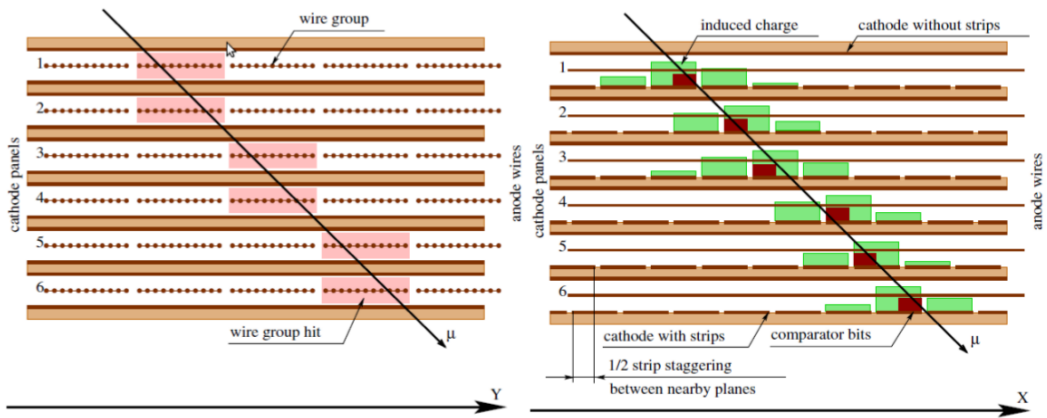


Figure 2.18: Muon track reconstruction through the 6 panels of a CMS CSC using the information of anode wire groups and cathode strip charge distribution combined with comparator bits to decide on which half strip the muon is more likely to have passed.

The 540 CMS CSCs, found in the endcaps covering the pseudorapidity region $0.9 < |\eta| < 2.5$ and described through Figure 2.17, are composed of 6 panels of CSC, each panel consisting in a wide gas volume of 9.5 mm (7 mm in the case of ME1/1 station) containing anode wires and whose surfaces are cathodes. The top cathode is a wide copper plane of the size of the gas volume. The bottom cathode is divided into thin trapezoidal copper strips radially arranged to measure the azimuthal coordinate ϕ with a pitch ranging from 8 to 16 mm. The $0.50 \mu\text{m}$ anode wires are placed perpendicularly to the strips to measure radial coordinate r and are grouped by 10 to 15 with a wire to wire space of 3.2 mm. In the specific case of ME1/1 placed against the HCAL endcap, the $0.30 \mu\text{m}$ anode wires have a wire to wire distance of 2.5 mm and are not disposed perpendicularly to the strips but slightly tilted by an angle of 29 deg to compensate for the lorentz force due to the very strong local magnetic field of 4 T. These detectors are operated with a 40/50/10 mixture of Ar, CO₂ and CF₄. Combining the information of the multiple CSC panels, the detectors achieve a very precise measurement of the muon track.

Despite their excellent spatial resolution, the wire chambers (DTs and CSCs) are limited in terms of time resolution by the fact that the charge needs to drift towards the anode wire and be collected before having the confirmation that a particle was detected as the drift volume is not used to develop avalanches. Indeed, the stronger electric field close to the anode wire triggers the avalanche and the gain of the detector. Due to the drift, the time resolution is thus limited at best to approximately 2 to 3 ns. In addition, even though the intrinsic time resolution of the tracking chambers is rather good compared to the 25 ns in between successive collisions, the processing time of the trigger system doesn't allow for very fast triggering as it provides a time precision of only 12.5 ns. Thus, detectors fully dedicated to timing measurement have been installed as a redundant system. These detectors are RPCs, also gaseous detectors but that use current induction instead of charge collection allowing for a time resolution of the order of 1.5 ns only. Theoretically, depending on the design used, RPCs could reach a time resolution of the order of 10 ps but in the context of LHC where bunch crossing happen every 25 ns, a time resolution of 1.5 ns is sufficient to accurately assign the right bunch crossing to each detected muon.

The 1056 RPCs equipping the CMS muon system both in the barrel and endcap regions and covering the pseudorapidity region $0 < |\eta| < 1.6$ are composed of two layers of RPC *gaps* as described in Figure 2.19. Each gap consists in two resistive electrodes made out of 2 mm thick Bakelite enclosing a 2 mm thick gas volume containing a 95.2/4.5/0.3 mixture of $C_2H_2F_4$, $i - C_4H_{10}$ and SF_6 . Due to this geometry, the electric field inside of a gap is homogeneous and linear at every point in the gas translating into a uniform development of avalanches in the gas volume as soon as a passing muon ionises the gas. The two gaps sandwich a readout copper strip plane. A negative voltage is applied on the outer electrodes, used as cathodes, and the inner electrodes, the anodes, are simply connected to the ground as well as the readout panel that picks up the current induced by the accumulated charge of the growing avalanches in one or both of the gas gaps. This OR system allows for a lower gain (i.e. a lower electric field) on both gaps to reach the maximal efficiency of such a detector.

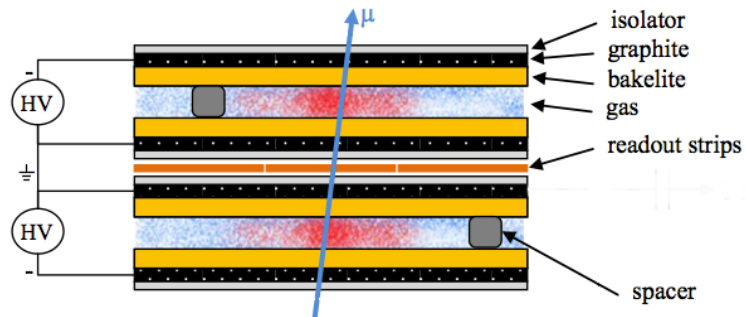


Figure 2.19: Double gap layout of CMS RPCs. Muons passing through the gas volumes will create electron-ion pairs by ionising the gas. this ionisation will immediately translate into a developing avalanche.

3

1359

1360

Muon Phase-II Upgrade

1361 The very first proton beam successfully circulated in the LHC in September 2008 directly followed
1362 by an incident leading to mechanical damage that would delay the LHC program for a year until
1363 November 2009, the very first collisions at a center-of-mass energy of 7 TeV taking place in March
1364 2010. The energy of the beam would be increased after a First Long Shutdown (LS1) starting early
1365 2013 after less than 3 years of data taking. Nevertheless, this first data taking period at only 7 TeV
1366 was sufficient to claim the discovery of a new particle compatible with the Higgs boson in July 2012.
1367 During the 2 years of shutdown, the upgrade of the accelerator allowed for several maintainances
1368 along the beam pipes, repair and consolidation of magnet connection and high-current splices. But
1369 not only the LHC was upgraded. Indeed, the experiments at the 4 collision points also took the
1370 advantage of this time to upgrade their system in prevision of the next LHC run (Run-II) until
1371 2018 and the Second Long Shutdown (LS2) as the luminosity and energy of the beam would be
1372 continuously increasing. By the end of Run-II, the luminosity will have reached twice its nominal
1373 value when the center-of-mass energy has already got close to its nominal value by reaching an
1374 historical 13 TeV for the first time in 2017.

1375 The next long shutdown will occur at the end of this year and will again be the occasion for sim-
1376 ilar maintenance and consolidation in prevision of Run-III and the future upgrade of LS3. Still, the
1377 main occupation of LS2 on LHC side will be the upgrade of LHC injectors. On the experiments side,
1378 LHCb and ALICE will, in a very tight schedule, implement major upgrades while ATLAS and CMS
1379 will wait until LS3 to upgrade their detectors in prevision of high luminosity *LHC-Phase-II*. ALICE
1380 main challenge is an upgrade of their apparatus to cope with the 50 kHz $Pb - Pb$ collisions. Simi-
1381 larly, LHCb will upgrade their frontend readout electronics to cope with the full 40 MHz collisions
1382 delivered by LHC. ATLAS will perform standard maintenance and CMS will focus on the urgent up-
1383 grade of the pixel detector and on the installation of new muon detectors in order to take profit of LS2
1384 time to mitigate the upgrade of detectors foreseen during LS3. Run-III will start in 2021 with the LHC
1385 at its nominal center-of-mass energy and will bring LHC-Phase-I to an end at the end of 2023. By
1386 then the luminosity will only increase to reach 2.5 times the nominal luminosity but during these 3
1387 years of run, the LHC will deliver as much integrated luminosity as what what brought during the al-

most 7 years of both Run-I and II of data taking. Phase-I will end with an overall 300 fb^{-1} delivered.

1389

3.1 High Luminosity LHC and muon system requirements

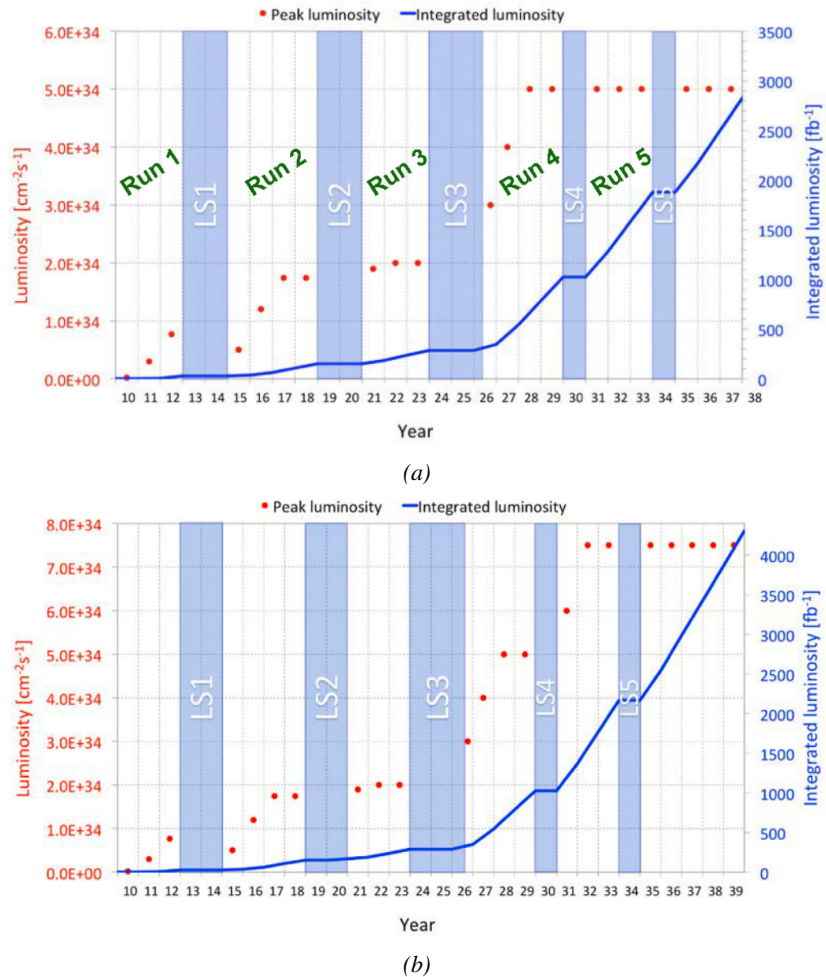


Figure 3.1: Detailed timeline projection of for LHC and HL-LHC operation until 2039 showing the evolution of the instantaneous and integrated luminosity as designed (Figure 3.1a) and in the ultimate case where the instantaneous luminosity is increased to $7.5 \times 10^{34} \text{ cm}^{-2}\text{s}^{-1}$ (Figure 3.1b) [20, 22].

After approximately 15 years of operation, the LHC will undergo a new series of upgrade during the LS3 in order to boost its discovery potential as showed in Figure 3.1. This moment onward is what is referred to HL-LHC or Phase-II. The goal is to aim for a luminosity 5 to 7 times stronger than the nominal one trying to reach even 10 times this value if possible. Increasing the luminosity means that the beam size at the collision points needs to be reduced to boost the number of collisions per bunch crossing. For this purpose, new focusing and bending magnets, and collimators will be installed at the collision points as well as newly developed "crab cavities" that will tilt the particle

1391

1392

1393

1394

1395

1396

1397

1398

1399

1400

1401

1402

1403

1404

1405

1406

1407

1408

1409

1410

1411

1412

1413

1414

1415

1416

1417

1418

1419

1420

1421

1422

1423

1424

1425

1426

1427

1428

1429

1430

1431

1432

1433

1434

1435

1436

1437

1438

1439

1440

1441

1442

1443

1444

1445

1446

1447

1448

1449

1450

1451

1452

1453

1454

1455

1456

1457

1458

1459

1460

1461

1462

1463

1464

1465

1466

1467

1468

1469

1470

1471

1472

1473

1474

1475

1476

1477

1478

1479

1480

1481

1482

1483

1484

1485

1486

1487

1488

1489

1490

1491

1492

1493

1494

1495

1496

1497

1498

1499

1500

1501

1502

1503

1504

1505

1506

1507

1508

1509

1510

1511

1512

1513

1514

1515

1516

1517

1518

1519

1520

1521

1522

1523

1524

1525

1526

1527

1528

1529

1530

1531

1532

1533

1534

1535

1536

1537

1538

1539

1540

1541

1542

1543

1544

1545

1546

1547

1548

1549

1550

1551

1552

1553

1554

1555

1556

1557

1558

1559

1560

1561

1562

1563

1564

1565

1566

1567

1568

1569

1570

1571

1572

1573

1574

1575

1576

1577

1578

1579

1580

1581

1582

1583

1584

1585

1586

1587

1588

1589

1590

1591

1592

1593

1594

1595

1596

1597

1598

1599

1600

1601

1602

1603

1604

1605

1606

1607

1608

1609

1610

1611

1612

1613

1614

1615

1616

1617

1618

1619

1620

1621

1622

1623

1624

1625

1626

1627

1628

1629

1630

1398 bunched just prior to the collisions by giving them transverse momentum and thus increasing their
 1399 meeting area. In addition, the full proton injection line will be upgraded.

1400 Over its full lifetime, the HL-LHC is expected to deliver an outstanding integrated luminosity of
 1401 3000 fb^{-1} leading, in the case of Higgs studies to measuring the couplings of the boson to a precision
 1402 of 2 to 5% thanks to the estimated 15 millions of Higgs created every year providing a more precise
 1403 measurement of potential deviations from the theoretical predictions. SUSY and heavy gauge boson
 1404 studies would also see their mass range limits pushed away by at least 1 TeV and could lead to a new
 1405 breakthrough. SUSY is a particularly important topic as it could give an answer to why the Higgs
 1406 boson can stay so light while coupled to heavy particles by introducing the contributions of the super
 1407 partners on top of providing dark matter candidates. Finally, the increase of luminosity will give the
 1408 possibility to investigate "exotic" mode like for example the models introducing extra dimensions to
 1409 explain the hierarchy problem.

1410 On the experiments side, the pile-up (PU) will be increased up to 150 to 200 interactions per
 1411 bunch crossing in ATLAS and CMS, making necessary an strong upgrade of the trigger system and
 1412 of the inner trackers and of the calorimeters. Both ATLAS and CMS will also need to upgrade
 1413 the muon trigger at the level of the endcaps mainly focusing on the coverage near the beam line in
 1414 order to increase the detection acceptance and event selection. Moreover, the increased luminosity
 1415 will also lead to an increased background rate and a faster ageing of the detectors. This PhD work
 1416 takes place into this very specific context of muon detector consolidation and certification for the
 1417 HL-LHC period in order to provide the CMS experiment with robust new detectors and confirm that
 1418 the present system will survive through the next 20 years of HL-LHC.

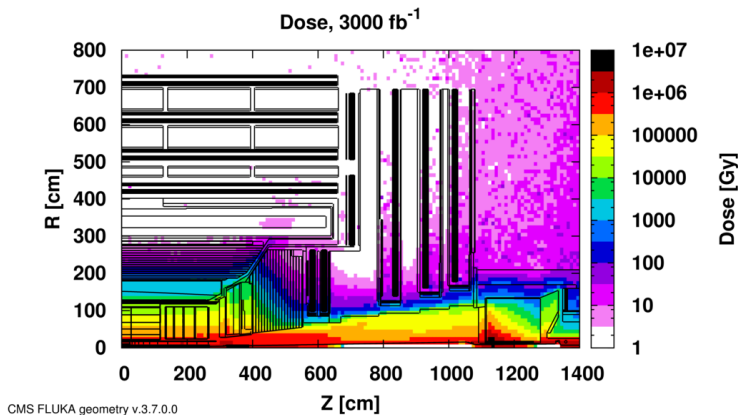


Figure 3.2: Absorbed dose in the CMS cavern after an integrated luminosity of 3000 fb^{-1} . Using the interaction point as reference, R is the transverse distance from the beamline and Z is the distance along the beamline.

1419 The end of 2018 will mark the beginning of LS2 and the start of Phase-II upgrade activities.
 1420 From the HL-LHC period onwards, i.e. past LS3, the performance degradation due to integrated
 1421 radiation as well as the average number of inelastic collisions per bunch crossing, seen as pile-up
 1422 into the detectors' readout that far exceeds this of the original LHC plans, will rise substantially and
 1423 become a major challenge for all of the LHC experiments, like CMS, that were forced to address
 1424 an upgrade program for Phase-II [23]. Dealing with the data from the muon detectors will force
 1425 to upgrade the detectors and electronics towards the most recent technologies. Simultaneously, this
 1426 will push new latency requirements onto the Level-1 trigger and the Data Acquisition (DAQ) that

will only be fulfilled by upgrading the system with electronics having deeper buffering and faster processing. Simulations of the expected distribution of absorbed dose in the CMS detector under HL-LHC conditions show, in Figure 3.2, that detectors placed close to the beam line will have to withstand high irradiation, the radiation dose being of the order of a few tens of Gy.

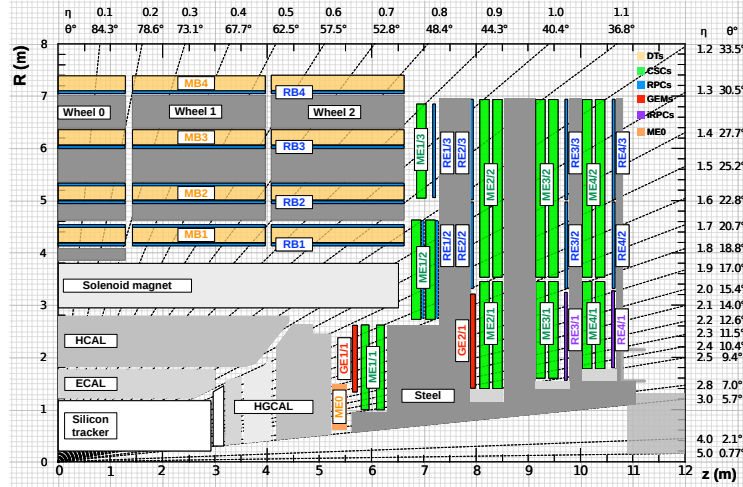


Figure 3.3: A quadrant of the muon system, showing DTs (yellow), RPCs (blue), and CSCs (green). The locations of new forward muon detectors for Phase-II are contained within the dashed box and indicated in red for GEM stations (ME0, GE1/1, and GE2/1) and dark blue for improved RPC (iRPC) stations (RE3/I and RE4/I).

The increase of irradiation close to the beam line will affect the background rate seen by the muon detectors in this area and tracking muons will prove to be difficult as this region is not yet equipped with all the detectors that were already foreseen for Phase-I. Improving this situation will come with the increase of hit numbers recorded along the particle track to reduce the ambiguity on muon versus background detection. Moreover, the measurement of small production cross-section and/or decay branching ratio processes, such as the Higgs boson coupling to charge leptons, and in particular to muons, or the $B_s \rightarrow \mu^+ \mu^-$ decay, is of major interest and specific upgrades in the forward regions of the detector will be required to maximize the physics acceptance to the largest possible solid angle.

To ensure proper trigger performance within the present coverage, the muon system will be completed with new chambers and the electronics of the present system will need to be upgraded to ensure an efficient triggering. Figure 3.3 shows the addition of Gas Electron Multiplier (GEM) and improved RPC (iRPC) in the pseudo-rapidity region $1.6 < |\eta| < 2.4$ to complete the redundancy of the already existing CSCs as originally scheduled in the CMS Technical Proposal [24]. A first step into this direction will be taken by installing GEMs on the first endcap disk in position GE1/1 during LS2, during which preparations for the future installation of more GEMs and RPCs will take place by installing the needed services. During the YETS following LS2, iRPCs will be installed on the third and fourth endcap disks in position RE3/I and RE4/I, and more GEMs will equip the second endcap in position GE2/1 and the inner layer, closest to the HCAL endcap called ME0 during LS3, finally completing the redundant coverage of the muon system and extending it a little by extending the reach to $|\eta| = 2.8$, the redundancy in the region $2.4 < |\eta| < 2.8$ being maintained by the 6 GEM layers contained in each ME0 detector that provide enough tracking points to efficiently reject

1453 neutron-induced background.

1454 Nevertheless, the region beyond $|\eta| > 2.8$ and extending to $|\eta| = 5.0$ only is covered by the
 1455 forward HCAL detectors and lack redundant muon detector coverage. Extensions of the tracker in
 1456 the context of HL-LHC will increase its coverage up to $|\eta| = 4.0$ but the identification of muons and
 1457 measurement of their energy with reasonable precision only using the tracker is nearly impossible.
 1458 Thus, this increased tracker coverage range needs to be put in parallel with a matching muon detector
 1459 and will open doors to multi-lepton final states in which leptons are likely to have a low transverse
 1460 momentum and to be found near the beam line.

1461

1462 Finally, as the muon system is composed only of gaseous detectors, strong environmental con-
 1463 cerns have risen over the last years as the European directives will restrict the use of fluorine based
 1464 gas mixtures. Both the CSC and RPC subsystems, using CF_4 , $C_2H_2F_4$, or SF_6 , will need to adapt
 1465 their working gas in order to strongly reduce the greenhouse potential of the mixtures released into
 1466 the atmosphere due to gas leaks.

1467 3.2 Necessity for improved electronics

1468 Drift Tubes and Cathode Strip Chambers are important components used to identify and measure
 1469 muons, especially thanks to their spatial resolution of the order of $100\text{ }\mu\text{m}$. Nevertheless, the lumi-
 1470 nosity and irradiation during HL-LHC will cause serious event loss and ageing on the electronics of
 1471 these subsystems that will comprise the triggering and data transferring needs of CMS. Thus, elec-
 1472 tronics upgrade are foreseen to address these expected problems. While only the RPCs' electronic
 1473 system is able to operate under Phase-II requirements, DTs and CSCs will need to improve their
 1474 trigger accept rate and latency to ensure that Level-1 trigger threshold stays at the same level [25],
 1475 and DAQ data transfer rate, that respectively need to achieve a minimum of 500 kHz , get down to
 1476 $12.5\text{ }\mu\text{s}$ [26], and increase to 1082 Gbit/s DTs and to 1026 Gbit/s for CSCs. As of today, the Level-
 1477 1 trigger accept rate of DTs doesn't reach 300 kHz while this of CSCs is below 250 kHz but the
 1478 foreseen upgrades are expected to increase the rate way beyond the requirement in the of DTs and
 1479 up to 4 MHz for CSCs [23].

1480 The first version of Minicrate electronics (MiC1) used by DTs don't allow for high enough
 1481 trigger rate. In addition to this problem, it was showed that these electronics contain components
 1482 that are not radiation hard enough to sustain HL-LHC conditions and thus, a too large number of
 1483 channels may fail due to radiations. Considering the most optimistic scenario, at least 19% of the
 1484 channels could have failed by LS4, as explicitated in Figure 3.4, far before the end of the HL-LHC
 1485 campain. The MiC1 will be replaced on each detector by an improved version referred to as MiC2
 1486 while front-end electronics and high-voltage modules will not need any replacement. On the other
 1487 hand, CSCs showed that there electronics would be able to live through the 10 years of Phase-II but
 1488 the limited buffer depth might cause memory overflows and readout inefficiencies with a fraction
 1489 of event loss ranging from 5 to more than 10% at an instantaneous luminosity similar to which of
 1490 HL-LHC depending on the expected background, as showed on Figure 3.5 through the different
 1491 detector positions. Thus the replacement of CSCs' cathode front-end boards (CFEBs) by digital
 1492 ones, DCFEBS, with deeper buffer would permit to make event loss negligible and satisfy HL-LHC
 1493 requirements [23].

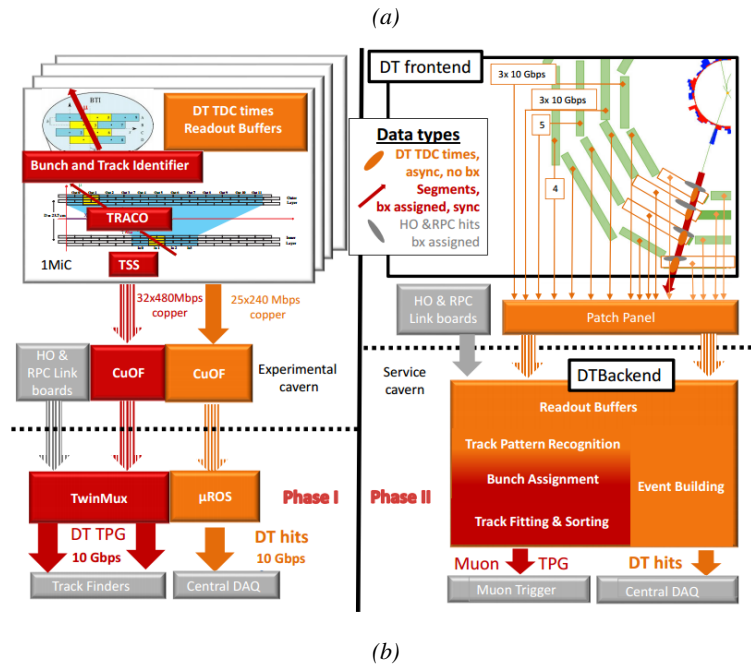
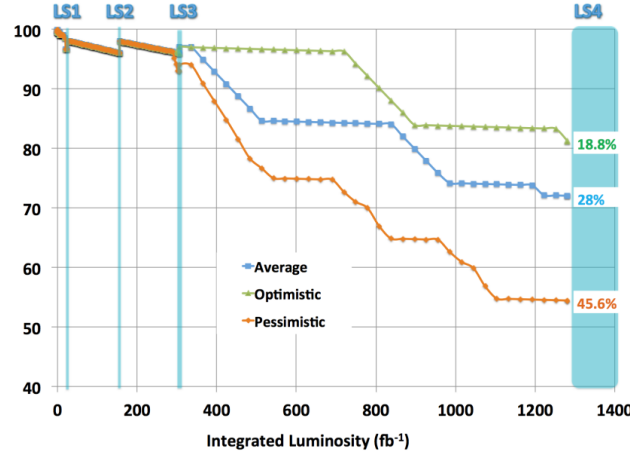


Figure 3.4: Figure 3.4a: Extrapolated fraction of failing channels of the present DT MiC1 electronics as a function of the integrated luminosity for different scenari until LS4. Figure 3.4b: Comparison of the current (left) and upgraded (right) DT data processing. So far, the data is sent to service cavern of CMS facility via copper-to-optical-fiber translators (CuOF) by each MiC1. There, data including RPCs and outer hadron calorimeter is combined into trigger primitives (TPG) and transmitted by the TwinMux system to CMS Track Finder. The time-to-digital converter (TDC) data is collected and sent to the CMS data acquisition system (DAQ) by the micro read-out server (μ ROS). After the upgrade, the TDC data will be sent via optical links to a patch panel inside the experimental cavern by each MiC2, and transferred to the back-end, where triggering and event building will be performed.

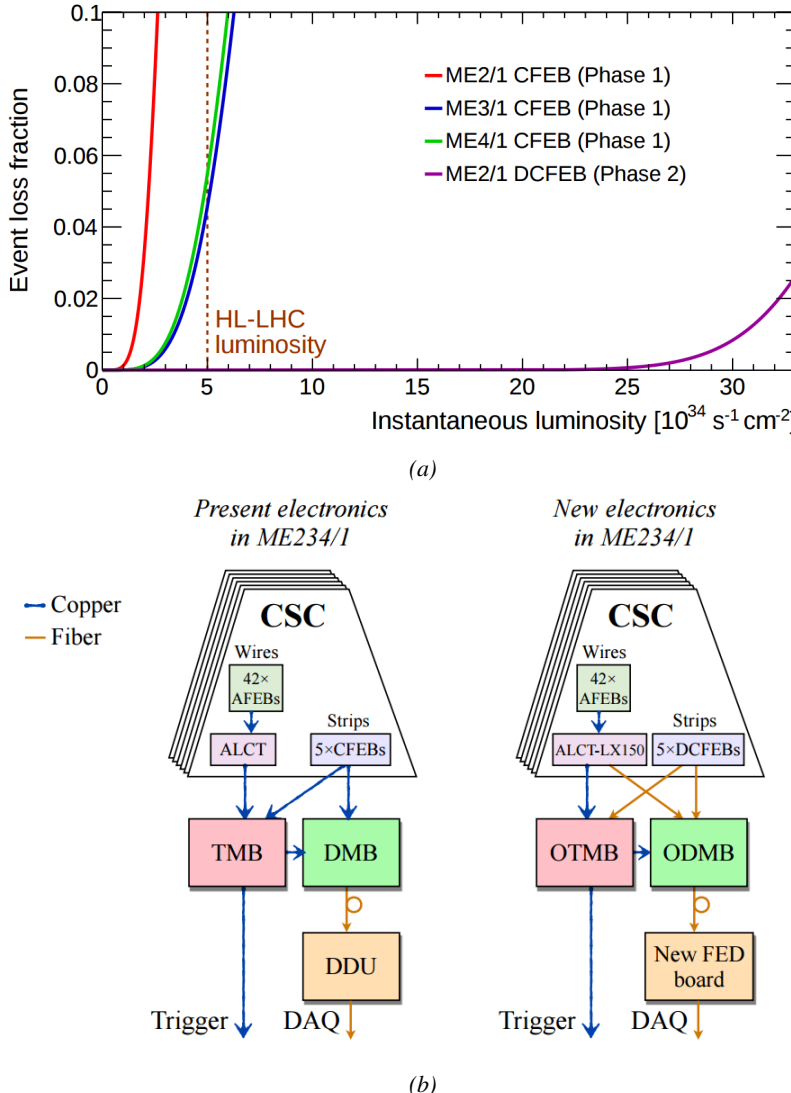


Figure 3.5: Figure 3.5a: The event loss fractions as a function of the instantaneous luminosity is compared for CFEBs (Phase-1) and DCFEBs (Phase-II) at different CSC locations. HL-LHC luminosity is marked with the dashed brown line. Figure 3.5b: Comparison of the current (left) and upgraded (right) CSC data processing. A part of the connections in between ALCTs and DCFEBs, and the trigger mother boards (TMBs) and data acquisition mother boards (DMBs) will be upgraded toward optical data transfer. The detector dependent units (DDUs) used as interface in between CSCs' front-end electronics and the CMS DAQ will be replaced by new FED boards.

All these new DT and CSC electronics will be connected to the trigger electronics via optical links to ensure a faster communication. The main change will come from the new DT minicrate modules which will not anymore be responsible for trigger and event building logic which will be transferred to the back-end electronics instead located in the service cavern via the patch pannels to which the Time-to-Digital Converter (TDC) data will be sent. The trigger and data transfer logic will barely change for CSCs. The existing copper cable connections of cathode and anode FEBs (CFEBs,

1500 and AFEBs which data is transmitted through the ALCTs) toward the trigger and data mother boards
 1501 (TMBs and DMBs) will simply be replaced by optical fibers and the TMBs and DMBs upgraded with
 1502 optical versions (OTMBS and ODMBs). As a new feature, the full anode wire data from ALCTs
 1503 will be sent to the ODMBs causing a lack of FPGA memory resources in these ALCT boards that
 1504 will thus need replacement.

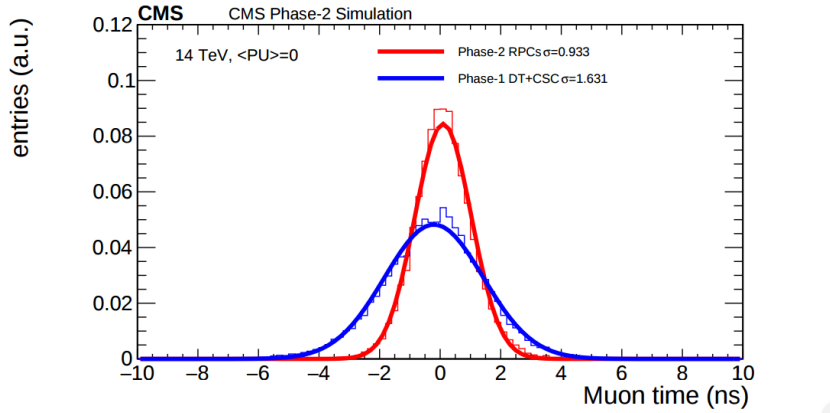


Figure 3.6: Comparison of the simulated time residuals in between reconstructed and true muon times without (blue) and with (red) the upgraded RPC link system.

1505 The upgrade on the side of Resistive Plate Chambers will then not come from their on-board
 1506 electronics but from the Link System located in the service cavern of CMS and that connects the
 1507 front-end electronics data of RPCs into CMS trigger processors. The main motivation for such an
 1508 upgrade is that the electronic board composing the link system are built using obsolete components
 1509 and weak components that can easily suffer from the electromagnetic noise. These components may
 1510 be the source of failing channels throughout Phase-II. Moreover, these link boards were originally
 1511 designed only to match RPC digitized signals with the corresponding bunch crossing. Due to this
 1512 feature, the time resolution of the full RPC chain is thus limited to 25 ns and does not exploit the full
 1513 time resolution of the detectors. This would make the synchronization of the RPC system easier and
 1514 allow to have a finer offline background removal within the 25 ns in between bunch crossings thanks
 1515 to the order of magnitude gained in terms of time resolution.

1516 Upgrading RPC link system will require the installation of 1376 new link boards and 216 control
 1517 boards. The new boards will make use of the recent progress made with fast FPGAs and will be a
 1518 great improvement to the ASICs formerly used as they will be able to process signals from several
 1519 detectors in parallel. The benefit from using the full RPC time resolution thanks to the upgraded
 1520 link system can be seen through Figure 3.6 where the resolution of the RPC system itself is better
 1521 than that of DTs and CSCs that was used until now.

1522 **3.3 New detectors and increased acceptance**

1523 In the present muon system, the redundancy was assured by RPCs used for their good timing per-
 1524 formances. The extension of the muon system towards higher pseudo-rapidity in order to complete
 1525 the redundancy in this very region and to contribute to the precision of muon momentum measure-
 1526 ments will require muon chambers with a spatial resolution less or comparable to the contribution

1527 muon of multiple scattering through the detector volume [21]. Most of the plausible physics is
 1528 covered only considering muons with $p_T < 100$ GeV thus, in order to match CMS requirements,
 1529 a spatial resolution of $\mathcal{O}(\text{few mm})$ will be necessary for the proposed new RPC stations while the
 1530 GEMs will need a resolution better than 1 mm, as showed by the simulation in Figure 3.7.

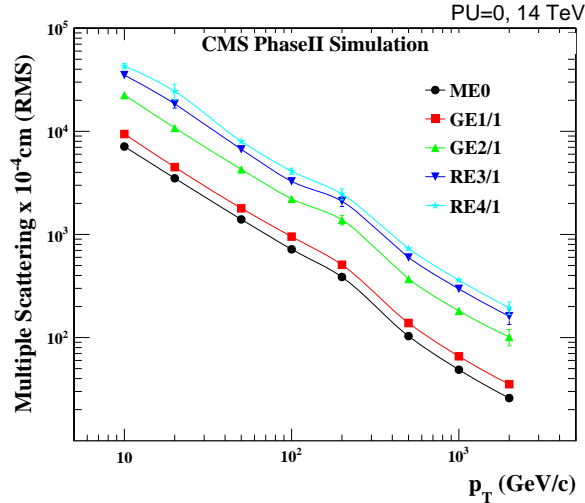


Figure 3.7: RMS of the multiple scattering displacement as a function of muon p_T for the proposed forward muon stations. All of the electromagnetic processes such as bremsstrahlung and magnetic field effect are included in the simulation.

1531 3.3.1 Improved forward resistive plate chambers

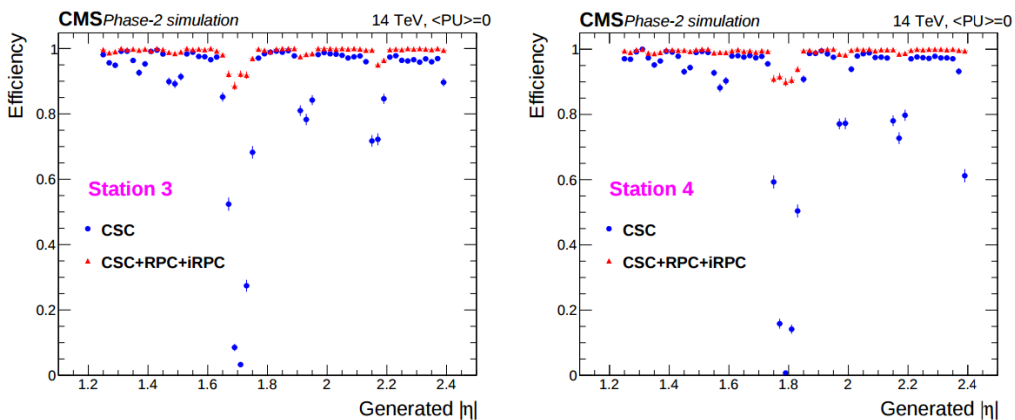


Figure 3.8: Simulation of the impact of RPC hit inclusion onto the local trigger primitive efficiency in station 3 (left) and station 4 (right). The contribution of iRPC starts above $|\eta| = 1.8$.

1532 Figure 3.3 shows that the iRPCs that will equip the third and fourth endcap disks in position RE3/1
 1533 and RE4/1 will finally be the partners of the CSCs in position ME3/1 and ME4/1 and complete
 1534 Phase-I plans but bringing the needed upgrades in the scope of Phase-II as the older chambers are

not suitable to equip the forward region of CMS due to HL-LHC rates and charge deposition. By completing the redundancy, more track along the muon trajectory will be available and the lever arm will be improved. The benefits from extending the redundancy of the muon system with iRPCs to the forward most region is showed in Figure 3.8 in which the trigger efficiency is showed with and without RPCs in which it is possible to see that the efficiency of CMS trigger with the complete redundancy is improved is above 95% in the region $|\eta| > 1.8$ as the iRPCs help filling the holes in the CSC system.

1542

The detectors that will be installed in the coming years will be similar to the already existing RPC system. 18 of the new chambers, each spanning 20° in φ around the beam axis with 96 radially oriented trapezoidal read-out strips, will cover each muon endcap disk leading to the production of 72 iRPCs. The main difference with the old RPC chambers is that these detectors will not have readout strips segmented in η as by using fast front-end electronics the strips will be read-out on both sides allowing for a radial spatial resolution of the order of 2 cm in order to contribute to the better reconstruction of muon in the forward region where the bending of muons by the magnetic field is low. This is motivated by the fact that, in the case a η segmentation was used, at least 5 pseudorapidity partitions would have been necessary to reach the minimal radial spatial resolution (≈ 20 cm). Having only one strip read-out from both along the chamber reduces by 60% the total number of channels and the necessary cabling and allows for a better spatial resolution. The strip pitch will range from 6.0 mm (5.9 mm) on the high pseudo-rapidity end to 12.3 mm (10.9 mm) on the low one on position RE3/1 (RE4/1). The spatial resolution in the direction perpendicular to the strips should reach approximately 3 mm, better than the minimal needed resolution (Figure 3.7), and the overall time resolution of the new installation will be equally 1.5 ns, as for the present due to the same link system being used.

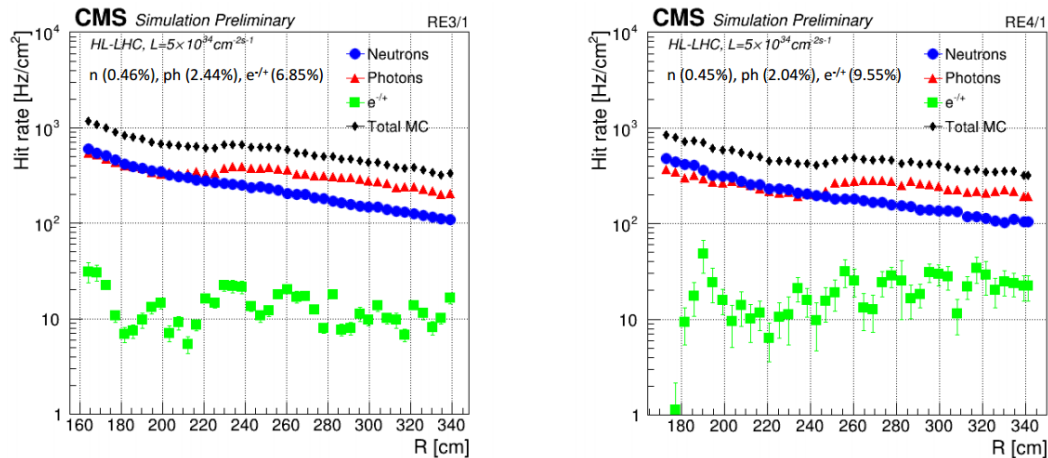


Figure 3.9: Expected hit rate due to neutrons, photons, electrons and positrons at HL-HLC instantaneous luminosity of $5 \times 10^{34} \text{ cm}^{-2}\text{s}^{-1}$ in RE3/1 and RE4/1 chambers. The sensitivities of iRPCs used in the simulation for each particle are reported and differ from one endcap disk to another as the energies of the considered particles varies with the increasing distance from the interaction point.

Nevertheless, having only a single strip instead of pseudo-rapidity segmentation will increase the probability of double hits in the same channel. This probability was estimated to be low enough

as it shouldn't exceed 0.7%. This estimation was made assuming an average hit rate per unit area of 600 Hz/cm² in the iRPCs (see Figure 3.9), a cluster size (average number of strips fired per muon) of 2, a strip active area of 158.4 × 0.87 cm² and a safety factor 3 leading to an estimated rate per strip of 380 kHz corresponding to an average time interval of 2600 ns in between 2 consecutive hits. The time for a signal to go through the full strip length is about 10 ns to which can be added 1 ns of dead time and 2 TDC clock cycles of 2.5 ns for a minimal time interval of 16 ns necessary to avoid ambiguities. The probability of having ambiguous double hits in a strip in then the ratio in between this minimal time interval in between 2 consecutive hits and the average time interval estimated from the rate the detectors are subjected to.

The instantaneous luminosity at HL-LHC being very high, the rates at the level of the new chambers needed to be simulated in order to understand the necessary requirements for these detectors. The simulated results for different background components (neutrons, photons, electrons and positrons) are showed in Figure 3.9 assuming known sensitivities to these particles. It is showed that on average over the iRPC areas the rates would be of the order of 600 Hz/cm² (600 Hz/cm² seen in RE3/1 and 480 Hz/cm² in RE4/1) [27]. Thus, taking into account a safety factor of about 3, it was decided that improved RPCs should at least be certified for rates reaching 2 kHz/cm² which would be achieved thanks to several improvements on the design and on the electronics. The detectors design will be based on the existing RPC design as they will be double gaps. Similarly to the existing RPC system, the electrode material will be HPL although the thickness of the electrodes and of the gas gap will be reduced to 1.4 mm as a thinner gas gap leads to a decrease of deposited charge per avalanche as showed in Figure 3.10. The smaller the gas gap, the more the detector becomes sensitive to gap non-uniformities across the electrode planes making a gap of 1.4 mm a good compromise in between these two competing factors.

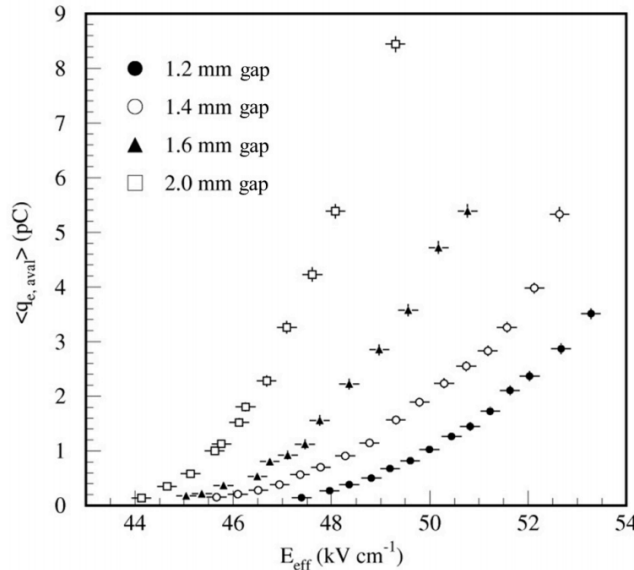


Figure 3.10: Measured average charge per avalanche as a function of the effective electric field for different gas gap thickness in double gap RPCs using HPL electrodes.

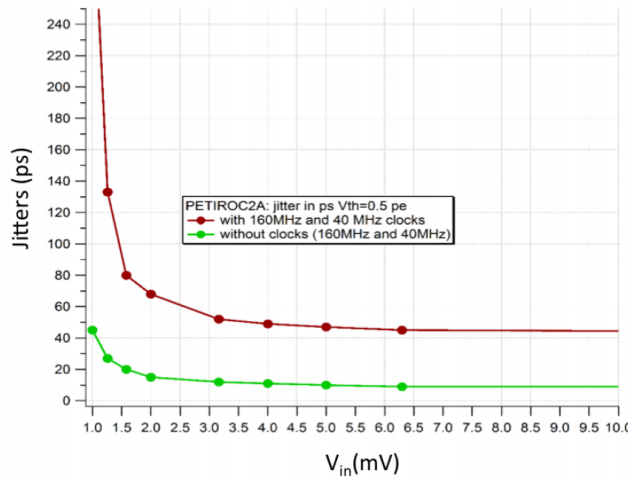


Figure 3.11: The PETIROC time jitter as a function of the input signal amplitude, measured with and without internal clocks.

1584 A lower charge deposition inside of the detector volume means a slower ageing and a longer life-
 1585 time for detectors subjected to high irradiation. But, in order to take advantage of the lower detector
 1586 gain, more sensitive electronics are required so that the part of gain that was formerly done in the gas
 1587 volume can be moved to the electronics. Achieving this with the technology developed more than
 1588 10 years ago for the present system is not possible as the signal over noise ratio of such electronics
 1589 doesn't allow to detect charges as low as 10 fC. Moreover, the new front-end electronics will need
 1590 to be radiation hard to survive to more than 10 years of HL-LHC conditions. The new technology
 1591 that has been chosen is based on the PETIROC ASIC manufactured by OMEGA and is a 64-channel
 1592 ASIC called CMS RPCROC on which the original SiGe technology will be replaced by CMOS to
 1593 increase its radiation hardness while keeping fast pre-amplification and discrimination with a very
 1594 low jitter that can reach less than 20 ps if no internal clock is used, as can be seen from Figure 3.11.
 1595 The ASIC is associated with an FPGA which purpose is to measure time thanks to a TDC with a
 1596 time resolution of 50-100 ps developed by Tsinghua University and that will provide a measurement
 1597 of the signal position along the strip with a precision of a few cm by measuring the signal timing
 1598 on both ends of the strips. In order to read-out all 96 strips, 3 ASICs and 3 TDCs, each having 64
 1599 channels, are hosted on a front-end board attached to the chamber.

1600

1601 [Wait for the analysis of 2018 GIF++ data to add interesting information about the time and
 1602 spatial resolution measured during test beam periods.]

1603

1604 3.3.2 Gas electron multipliers

1605 In the region closer to the interaction point where the spatial resolution is requested to be better
 1606 than 1 mm for the new detectors (at least for GE1/1 and ME0, GE2/1 being in the same order of
 1607 requested spatial resolution than the new iRPCs that will equip the third and fourth endcaps), the
 1608 choice has been made to use triple GEMs, micro pattern gaseous detectors, in the place of RPCs.
 1609 The GE1/1 project had been the first to be approved and demonstrators had been installed in CMS

already during LS1. The rest of the detectors will be installed during LS2 while the GE2/1 and ME0 projects are still under development. ME0, GE1/1 and GE2/1 will be installed respectively next to the HCAL endcap, on the first and on the second muon endcap disks as can be seen from Figure 3.3.

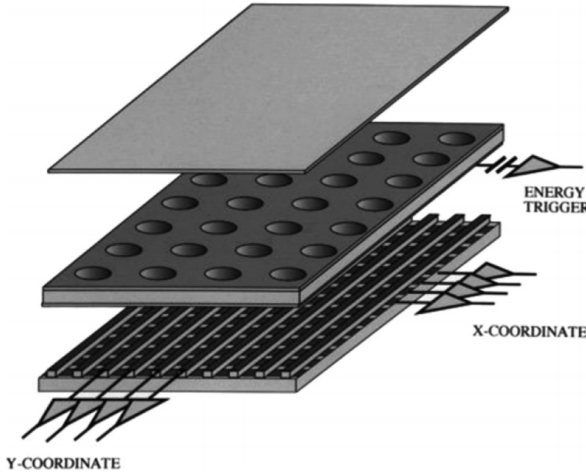


Figure 3.12: Schematics of a GEM showing the cathode on top, the GEM foil separating the gas volume into the drift region, in between the cathode and foil, and the induction region, in between the GEM foil and the anode, and the anode on which a 2D read-out is installed. A negative voltage is applied on the cathode while the anode is connected to the ground.

Gas Electron multipliers are gaseous detectors [28] which gas volume is confined in between 2 planar electrodes, the anode serving as read-out panel. The gas volume is divided in 2 or more regions by a single or multiple *GEM foils* as showed in Figure 3.12. These foils are very thin, of the order of a few tens of μm , and are pierced with holes as can be seen in Figure 3.13. Both surfaces of the GEM foils are clad with copper in order to apply a strong electric field in between each side that will generate very strong potentials in the holes. The gas region contained in between the cathode and the GEM foil is called the drift region as the electric field is not strong enough to cause avalanches and thus start an amplification. The primary electrons drift toward the foil and are accelerated and amplify by the very high potential within the holes, as showed in Figure 3.13. Then the electrons reach the second drift region in which they will induce signal on the read-out located on the anode. By restraining the amplification process at the level of the holes, the electrons can stay in a very confined space and thus induce a very localized current, providing the GEMs with a very good spatial resolution.

In order to achieve a stronger amplification, the amplification process can be repeated several times in a row. The GEMs that will be used in CMS are triple GEM detectors operated with a 70/30 gas mixture of Ar/CO_2 . They contain 3 GEM foils and thus 3 electron amplifications, as can be seen in Figure 3.14. The GEM foils used in CMS are 50 μm foils clad with 5 μm of copper on each side. The foils are pierced with double-canonical holes which inner and outer diameters are respectively 50 and 70 μm which are placed 140 μm from each other in an hexagonal pattern, as showed in Figure 3.13. These detectors have a time resolution better than 10 ns and reach very good spatial resolutions of less than 200 μrad as indeed the position of the hits is not measured along the strips but following the azimuthal angle granularity of the radially organized trapezoidal strips.

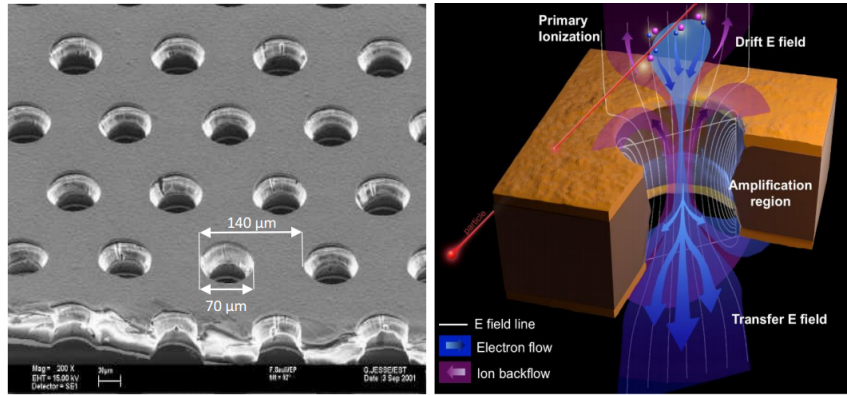


Figure 3.13: Left: Picture of a CMS GEM foil provided by a scanning electron microscope. Right: Representation of the electric field lines in a GEM hole and of the amplification that electrons and ions undergo in the hole's volume due to the very intense electric field.

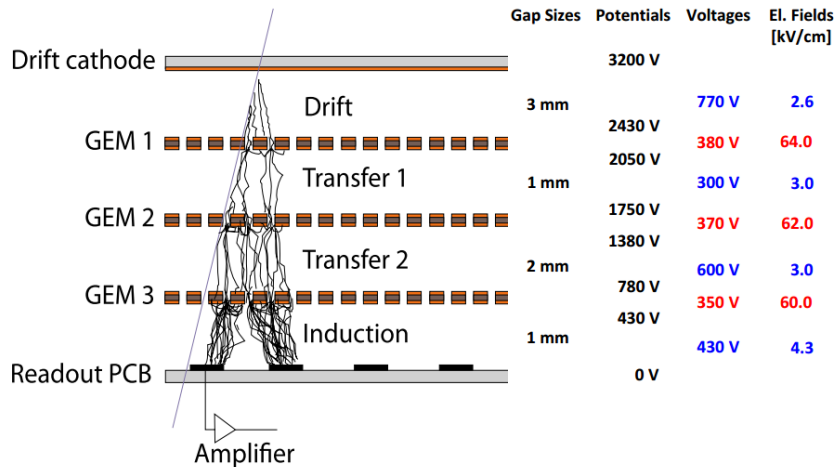


Figure 3.14: Schematic representation of CMS triple GEMs. The gas volume is divided into 4 areas. The drift area is the region where the primary electrons are created before being amplified a first time while passing through the first GEM foil. Then the process of drift and amplification is repeated twice in following two transfer areas and GEM foils. Finally, the charges have been amplified enough to induce current in the read-out strips while in the last drift area. The dimensions, potentials and electric fields are provided.

1635 The GEM Upgrade is divided into 3 subsystems as GE1/1 was the first approved project [29]
 1636 and that the detectors will already be installed during LS2. GE2/1 and ME0, on the other hand,
 1637 will profit of the R&D knowledge and skills developed for GE1/1 while the requirements for each
 1638 subsystem are different as they are not placed at the same distance from the interaction point. In this
 1639 very forward region, a different position with respect to the center of the detector can change dra-
 1640 matically the conditions in which the detectors will have to be operated. In terms of rate capability,
 1641 GE2/1, which is the furthest, is required to withstand 2.1 kHz/cm^2 while GE1/1 needs to be better
 1642 than 10 kHz/cm^2 and ME0, better than 150 kHz/cm^2 . In terms of ageing with respect to charge
 1643 deposition, ME0 needs to be certified to 840 mC/cm^2 , GE1/1 to 200 mC/cm^2 and GE2/1 only to

1644 9 mC/cm². All 3 detectors need to have a time resolution better than 10 ns and an angular resolution
 1645 better than 500 µrad.

1646 On each GE1/1 ring, 36 super chambers, consisting of 2 single GEM layers and spanning 10°,
 1647 will be installed covering the pseudo-rapidity region $1.6 < |\eta| < 2.2$ together with ME1/1 CSCs and
 1648 the reach of the muon system will be improved thanks to the GE2/1 that will overlap with the GE1/1
 1649 and cover a region from $|\eta| > 1.6$ to $|\eta| < 2.4$ and complete the redundancy of ME2/1. The super
 1650 chambers, built with 2 triple GEM layers each consisting of 4 single GEM modules due to the rather
 1651 large surface of the GE2/1 chambers, that will be installed on the first ring of the second endcap will
 1652 span 20° each, hence, a total of 72 chambers will be assembled to equip the muon system. Finally,
 1653 the ME0 installed near the HCAL endcap will cover the region $2.0 < |\eta| < 2.8$ and this subsystem
 1654 will consist in super modules of 6 layers of triple GEM detectors covering an azimuthal angle of 20°
 1655 leading to the construction of 216 single detectors.

1656 All these new GEM detectors will be using a similar internal layout which is described in Figure
 1657 3.14. The incoming muons will create detectable electron-ion pairs in the 3 mm thick drift
 1658 volume in which an electric field of 2.6 kV/cm is applied for the electrons to drift to the first GEM
 1659 foil on which a very intense field of 64 kV/cm is applied over a distance of only 60 µm which allows
 1660 for an average electronic gain of 20 to 25. After the first amplification stage, the electrons drift over
 1661 the 1 mm separating the 2 first GEM foils thanks to an electric field of 3.0 kV/cm and are again
 1662 amplified by a factor 20 to 25 while going through the second GEM foil to which is applied an elec-
 1663 tric field of 62 kV/cm. The electron drift another 2 mm towards the last GEM foil through a field
 1664 of 3.0 kV/cm and are multiplied one last time from a similar factor passing through the 60 kV/cm
 1665 of the last GEM foil holes. Finally, they drift along the 1 mm of the induction volume in a field of
 1666 4.3 kV/cm to reach the trapezoidal strips on the read-out PCB used as anode. The total detector
 1667 gain is approximately of the order of 10^4 and the resulting output signal is both due to the induction
 1668 of moving charges in the induction volume and of charge pic-up once they read the read-out strips.

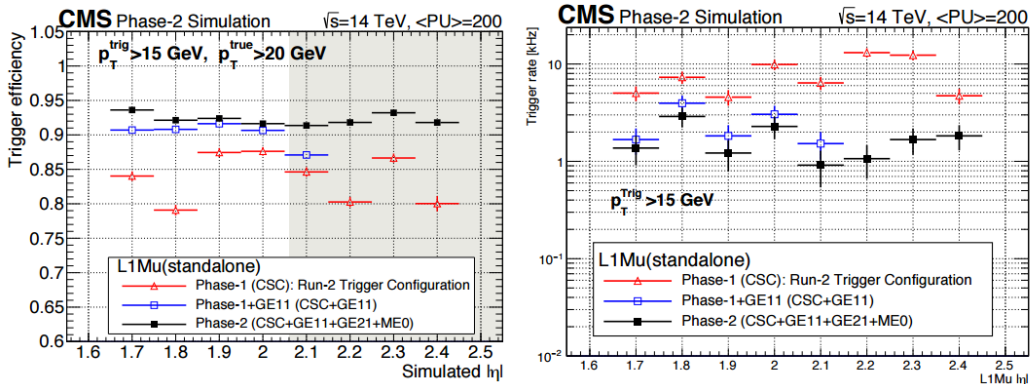


Figure 3.15: Simulated efficiency and rate of the standalone Level-1 muon trigger using tracks reconstructed in CSCs and all GEM stations compared with Phase-I values in the case where only CSCs are used or CSCs+GE1/1. The zones of inefficiency of the CSC subsystem are compensated by the addition of GEMs during Phase-II and the trigger rates is kept from increasing due to the high luminosity.

1669 Adding the GEMs into the forward region of the muon system will allow to strongly enhance
 1670 the Level-1 Trigger performance by reducing the inefficiency regions and the trigger rate as showed
 1671 in Figure 3.15. Moreover, benefiting from the good spatial and angular resolution of the GEMs, the

¹⁶⁷² precision into the muon measurement will also be greatly improved by the addition of GEMs as can
¹⁶⁷³ be seen from the simulation presented in Figure 3.16.

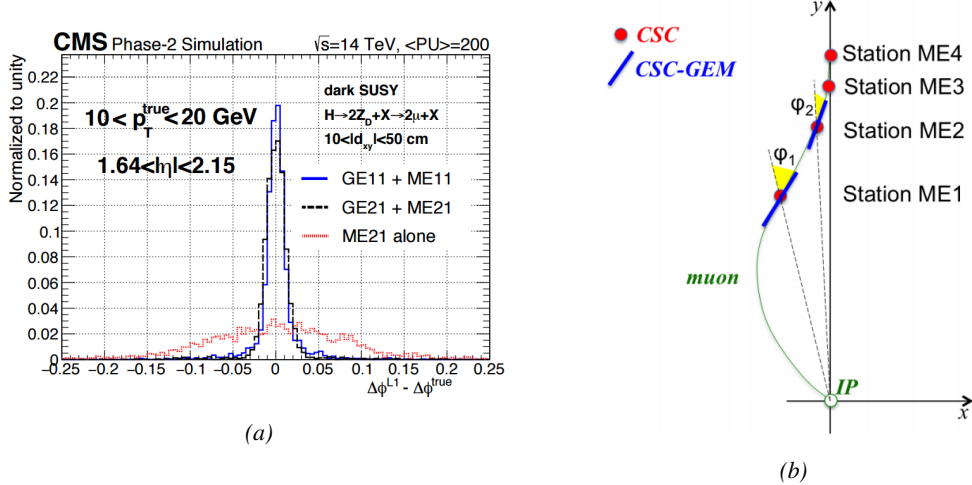


Figure 3.16: Figure 3.16a: Simulated resolution of the muon direction measurement $\Delta\phi$ with Phase-II conditions. In the second endcap station, the resolution is compared in the case of CSCs (ME2/I) alone and CSCs+GEMs (GE2/I+ME2/I) while a similar resolution measurement is given in the case of the first station (GE1/I+ME1/I). Figure 3.16b: The addition of GEM detectors on stations 1 and 2 (ME0 is considered to contribute to station station 1) as redundant system to CSCs allows to improve the muon momentum improvement through a more accurate measurement of the local bending angles ϕ_1 and ϕ_2 .

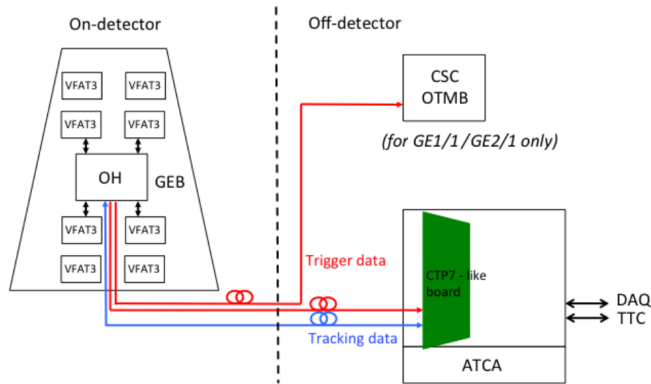


Figure 3.17: Schematics of the data communication chain for DAQ of the GEM subsystems. The sending of trigger data via optical links to the CSC OTMBs is only done for GE1/I and GE2/I to match the data with ME1/I and ME2/I.

¹⁶⁷⁴ The read-out of GEMs will use the same technology. The anode planes used as read-out PCBs
¹⁶⁷⁵ and referred to as GEM Electronics board (GEB) host on their outer surface VFAT3 ASICs that
¹⁶⁷⁶ connect to a total of 128 strips for a very fine angular granularity. Along the endcap radius, the strips are
¹⁶⁷⁷ divided into 8 pseudo-rapidity partitions. In the case of GE1/I and ME0, each η -partition consist in
¹⁶⁷⁸ 384 read-out strips connected into 3 VFAT3 ASICs and offering a while the large GE2/I partitions

1679 contain twice as many channels. Both GE1/1 and GE2/1 strips have an angular pitch of $474\text{ }\mu\text{m}$
 1680 while this of ME0 is twice larger due to its proximity with the interaction point. The VFAT3 ASICs
 1681 allow for a latency better than the $12.5\text{ }\mu\text{s}$ required by CMS Level-1 Trigger and there frequencies
 1682 goes up to 1 MHz. They are connected into the Optohybrid Board (OH) and this full ensemble
 1683 (GEB+VAT3+OH) constitute the on-chamber electronics. The OH is then sending the data to the
 1684 modules constituting the DAQ of the GEM system via optical fibers. These back-end electronics
 1685 modules are located in the service cavern of CMS and host CMS communication devices, used to
 1686 have a common clock, and control and links to the Endcap Muon Track Finder (EMTF) system.
 1687 Moreover, GE1/1 and GE2/1 also have links with the CSC OTMBs as the OH of these 2 subsystems
 1688 send data into these boards. This communication chain can be seen in Figure 3.17.

1689

1690 The detectors that will placed in CMS will have to live through Phase-II without significant
 1691 performance degradation to ensure an efficient data taking and the possibility to investigate more
 1692 exotic physics. As the 3 GEM subsystems will be using the same detector technology, the choice
 1693 was made to certify the GEMs in the worst of the 3 environments, i.e. the ME0 station located right
 1694 behind the HCAL. According to FLUKA simulation, including all the latest foreseen upgrades into
 1695 the CMS detector geometry, it was shown that the maximal hit rate expected in ME0 would be of
 1696 the order of 50 kHz/cm^2 with contributions of neutrons (6 kHz/cm^2), photons (35 kHz/cm^2), and
 1697 electrons and positrons (8 kHz/cm^2) resulting in a charge deposition a little lower than 300 mC/cm^2
 1698 after 10 years of HL-LHC [23]. It is necessary to understand the classical ageing effects on the GEMs
 1699 but also premature ageing due to contaminants in the gas mixture leading to polymerization on the
 1700 surface of the GEM foils during operation and the effect of discharges on the detector operations if
 1701 they have to happen during their lifetime.

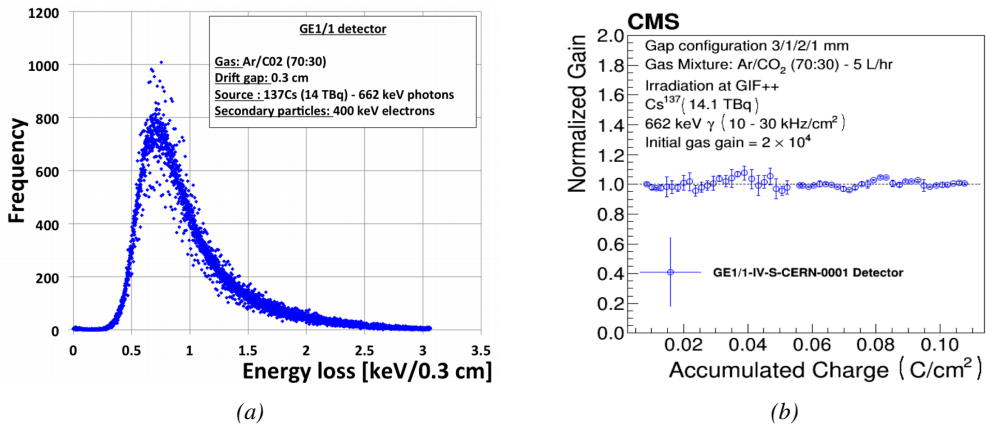


Figure 3.18: Figure 3.18a: Energy spectrum of GIF++ ^{137}Cs source as measured by the GE1/1 detector installed in GIF++. Figure 3.18b: Evolution of the normalized gain of the GE1/1 detector installed at in GIF++ as a function of the integrated charge per unit area. The first part of the study, up to a charge of 55 mC/cm^2 had been done in the former Gamma Irradiation Facility (GIF) that has now been dismantled following the construction of GIF++. No variation of the normalized gain can be observed after an accumulation of 110 mC/cm^2 .

1702

To characterize the classical ageing effects, a campaign is being conducted in the new Gamma Irradiation Facility (GIF++) of CERN where a GE1/1 detector operated at its nominal gain is placed 50 cm from the facility's 14 TBq ^{137}Cs source which emits gammas at an energy of 662 keV. In

order to spot any ageing of the detector, the effective gain is kept monitored, as can be seen in Figure 3.18b, as its variations gives clues about different aspects of the detector such as the geometry of the holes, the electric field configuration or the gas composition. The monitoring of the gamma energy distribution, showed on Figure 3.18a, can give an idea on the evolution of the performance of the chamber and finally, the evolution of the currents through time also is a good indicator of the appearance of dark current in the detector that would be due to the emission of electrons by thin insulating layers of the detector subjected to a long lasting irradiation known as Malter effect. At the time the Technical Design Report (TDR) for the Phase-II upgrade of the muon system was written [23], the GEM group had reported a total integrated charge of 110 mC/cm^2 which, if compared with 10 years of HL-LHC operation, represents a safety factor of 18 for the GE1/1 subsystem and a factor 37 for the GE2/1 subsystem but only 39% of the total expected ME0 integrated charge. It is estimated that reaching the total integrated charge necessary to certify the detectors for Phase-II operation will take another 2 to 3 years. Nevertheless, the present status of the longevity study shows no degradation of the performance of the detector installed in GIF++ as can be seen through Figure 3.18.

Aside of the classical ageing tests, outgassing of the different materials composing the GEMs have been conducted by placing the different materials to be tested into an outgassing box that consists in a stainless steel cylinder through which the CMS GEM 70/30 gas mixture of Ar/CO_2 with the possible contaminants is flowed while the detector is exposed to the continuous irradiation of a radioactive source and the heat is raised to enhance the outgassing. From the detector that was placed into this outgassing box, only one component was identified to cause loss of performance due to outgassing. This component was the polyurethane *Cell-Pack* used to coat the internal frame of the GEMs and the polymerization on its surface caused a 20% decrease of the gas gain. this polyurethane was replaced with a new one for which no outgassing effect causing a loss of performance was reported.

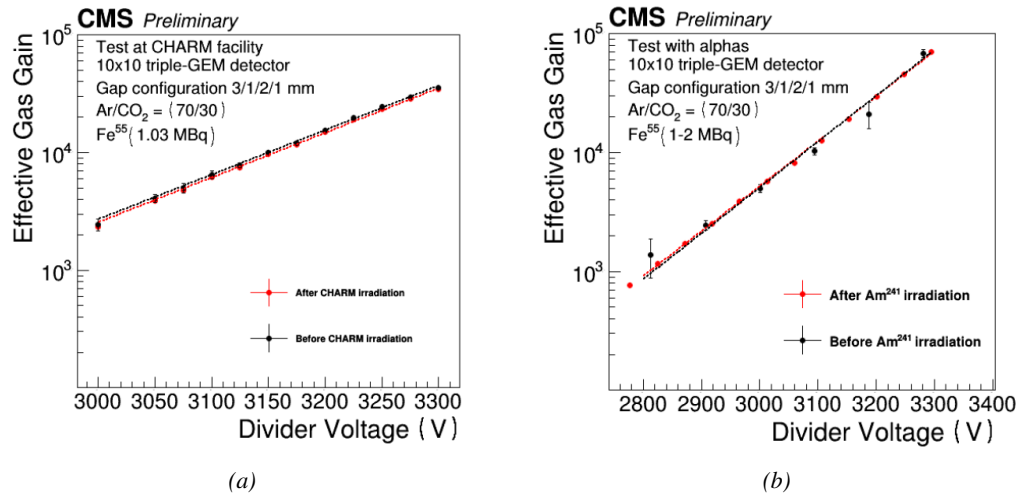


Figure 3.19: Figure 3.19a: Comparison of the gas gain as a function of the divider voltage before and after the irradiation of a triple-GEM by neutrons in CHARM. Figure 3.19b: Comparison of the gas gain as a function of the divider voltage before and after the irradiation of a triple-GEM by alpha particles.

Finally, even though the triple-GEM technology makes the detectors safe of discharges thanks to

its several amplification stages that allow to reach high gas gain using a relatively low electric field applied on the foils and to the distance separating the last foil from the read-out panel that is high enough to prevent discharging from developing all the way to the read-out, and hence, be stopped before it can cause any harm, it is important to have a good understanding of the discharge probability to ensure a safe operation over long periods. In order to further prevent discharges to develop in the detector volume, the GEM foils' power supply have been sectorized and protection resistors have been installed to limit the energy available for the discharge development. To reproduce the high-energy neutron background conditions of CMS, a GE1/1 detector have been placed in the CHARM facility of CERN. This facility allows to irradiate the detectors with a neutron fluence as high as $2.5 \times 10^8 / \text{cm}^2$. The detectors were operated with a slightly higher gain of 3.5×10^4 . It was measured that the discharge probability for a GEM operated under CMS conditions was of 2.85×10^{-9} per heavily ionizing particle with a 95% confidence level that would correspond to 225 discharges per cm^2 in ME0, 17 in GE1/1 and 12 in GE2/1 during the full HL-LHC period. According to Figure 3.19a, no degradation of the performance was observed after the irradiation at CHARM were 24 discharges per unit area were reported. Nevertheless, another test were the detector was exposed to a 5.5 MeV alpha source and were 450 discharges per unit area were reported didn't show any drop of performances either, as can be seen in Figure 3.19b.

3.3.3 Installation schedule

The previous discussion on the different upgrade projects makes it clear that a lot of work is scheduled for CMS to be ready at the end of LS3 for HL-LHC. Conducting all the upgrades of the muon system together with upgrades of the other subsystems like the replacement of the Tracker and of part of the ECAL, will prove to be very difficult as the opening of CMS to access the Barrel will be done by fully opening the endcaps leaving only the first disk to be accessible. Thus, most subsystems have planned early installation over LS2, and the following YETS until LS3 in order to give more space to LS3 schedule.

First of all, LS2 will see the installation of GE1/1 detectors, all the on-detector schedule of CSCs and the installation of the necessary services for the improved RPCs to be installed later, such as the HV and LV power supply lines, the gas and cooling lines or signal cables. CSCs will have a huge work to do during LS2 as they will need to extract all of their detectors to refurbish them with upgraded DCFEB and ALCT mezzanine boards. The GE1/1 services were installed during LS1 together with a few demonstrator and only the detectors needs to be integrated into the first endcap disk. The detectors are presently being built and tested at the different assembly site to prepare for a smooth LS2 work.

The work of GEMs will be continued during the following YETS during which is planned the installation of the GE2/1 stations to only leave the ME0 to be installed during LS3. The iRPC program will follow a similar path as the new detectors will be installed during the YETS preceding LS3 in prevision of the fact that the endcap disks will not be accessible during LS3. This way, all the subsystems, but DTs, made great effort on planning their installation and integration within CMS only to have to deal with off-detector issues during the LS3 period, such as the replacement of ODMBs and HV system in the case of CSCs or the upgrade of the RPC Link System. Finally, during LS3 are scheduled the replacement of DT minicrates electronics and the installation and integration of ME0 GEMs together with the HGCAL.

3.4 Implications of the different upgrades on the Level-1 Trigger. Improvement of physics performance.

The upgrades of the different subsystems will have a subsequent impact on the Level-1 Trigger. Indeed, although its main scheme will not be affected, the efficiency of the trigger in identifying muons and provide the DAQ with good and fast trigger that can cope with HL-LHC instantaneous luminosity is a major improvement. In addition to the upgrade of the muon system in terms of trigger accept rate and latency, the Level-1 Trigger will get extra information in including the Tracker Trigger into its Muon Track Finder logic and combine the L1 Muon Trigger with Tracker and Calorimeter Triggers to generate a Global L1 Trigger with a much better momentum resolution, as showed in Figure 3.20.

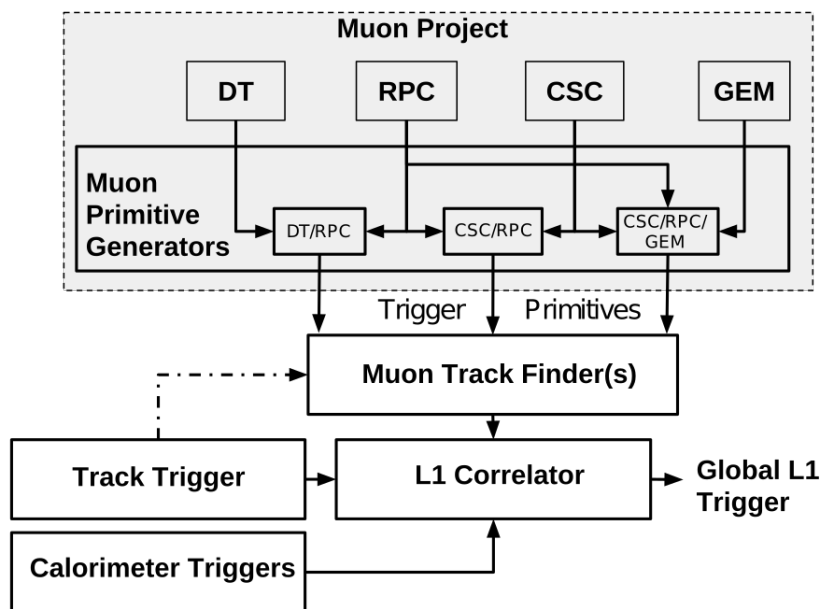


Figure 3.20: Data flow of the Level-1 Trigger during Phase-II operations.

In terms of muon trigger, 3 regions are considered due to their different track finding logic: the Barrel Muon Track Finder (BMTF), the Endcap Muon Track Finder (EMTF) for both the barrel and endcap regions, and finally the Overlap Muon Track Finder (OMTF) which concerns the pseudo-rapidity region in which there is a common coverage by both the barrel and endcap muon systems. This region can be seen in Figure 3.3 for $0.9 < |\eta| < 1.2$ and requires a specific more complex logic to provide with an efficient reconstruction of the muons due to the different orientation of the detectors and of the more complex magnetic field of this region that needs to be taken into account. The benefits of the upgrade for each of these track finders will be coming from different improvements and will be detailed sector by sector.

The main contribution to the improvement of the BMTF is the time resolution improvement of RPC link systems that will allow to take profit of the full 1.5 ns resolution of the detectors. From the perspective of RPCs only, this improvement will help reducing the neutron induced background and

slightly improve the bunch crossing assignment. The upgrade of DT electronics is also to take into account as the trigger primitive generator will be renewed through the use of TDCs that will send the digitized signals directly to the back-end electronics instead of having an on-detector trigger logic as it will be the case until the end of Phase-I. The front data of both DTs and RPCs will be sent to the same back-end electronics. These upgrades were detailed in section 3.2 and will lead to a more robust operation of the trigger in the barrel region. Indeed, the combination of RPC hits together with DT primitives will bring improvement in the bunch crossing assignment and improve the efficiency of the trigger in between the wheels where the quality of DT primitives is the poorest. Moreover, having a redundant information is important in the case of failure and loss of efficiency of one of either subsystems.

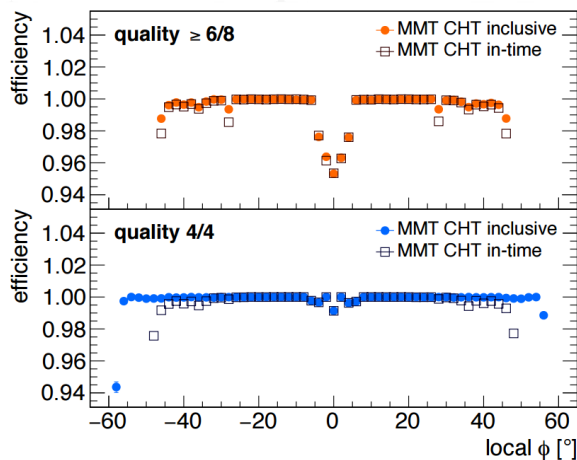


Figure 3.21: Comparison of Phase-II DT trigger primitives algorithmic efficiency for segments obtained with 2 super-layers ($\text{quality} \geq 6/8$) and 1 super-layer only ($\text{quality} = 4/4$). The simulation was done by generating 2×10^6 muons. The candidate tracks with correct time identification is showed with open symbols.

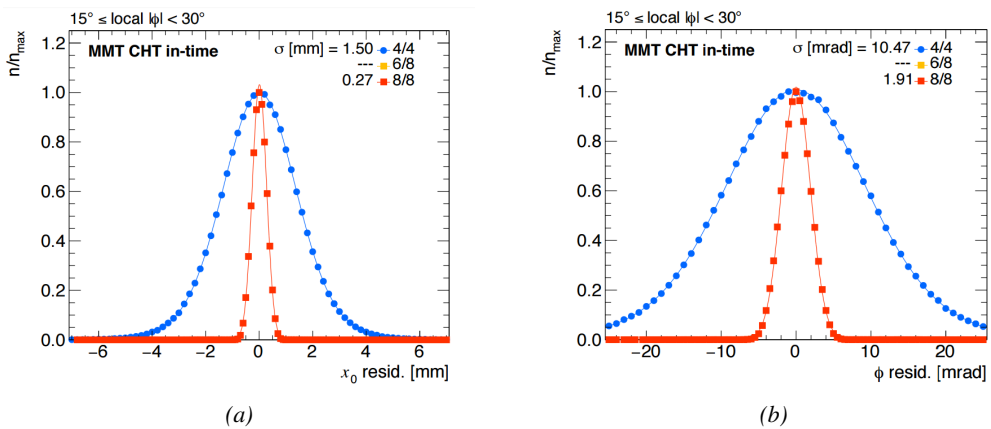


Figure 3.22: Simulated spatial (3.22a) and angular (3.22b) resolution of the algorithm using 8 aligned hits in both super-layers ($\text{quality} = 8/8$) and 4 aligned hits in only one super-layer ($\text{quality} = 4/4$). The contribution of intermediate quality tracks (6 aligned hits) is negligible in the angular range shown. [Be careful to update this caption as it uses a text to close to the published one.]

1807 The loss of single hit efficiency of DTs due to ageing will also force the DT to change the algo-
 1808 rithm use to identify tracks. So far, the identification was only performed at the level of a single DT
 1809 super-layer, which is composed of 4 single DT layers. In the perspective the single efficiency drops,
 1810 this will require to be upgraded to try to combine the data of more than a single super-layer to keep
 1811 a high muon track identification efficiency. In addition to this change in trigger primitive candidate
 1812 quality, new algorithms with higher efficiency are being developed. According to Figure 3.21, the
 1813 efficiency of the new algorithm, both in the cases using 1 or 2 super-layers, is higher than with the
 1814 current system [30]. Moreover, the overall efficiency of an algorithm requesting at least a muon
 1815 detected in 6 DT layers out of the 8 composing the 2 super-layers of a DT module would stay com-
 1816 parable to the 4 DT layers out of 4 algorithm within the local bending angle range. On the other
 1817 hand, despite the slight loss of efficiency in the low angle range, the algorithm using more DT layers
 1818 achieves both higher spatial and angular resolution according to Figure 3.22.

1819

1820 With new detectors to cover the very forward region and the upgrade of RPC Link System,
 1821 the EMTF will be greatly improved. The current EMTF already use more sophisticated algorithms
 1822 by combining together RPC hits and CSC primitives and will also benefit from the improved time
 1823 resolution of the RPC system. The GEMs, in stations 1 and 2, and the iRPCs, in stations 3 and 4,
 1824 will be added into the EMTF algorithm. Both these contributions will help increasing the efficiency
 1825 of the L1 trigger in the endcap region in one hand, and help lowering the L1 trigger rate in the other
 1826 hand, especially in the most forward region. The improvement of the efficiency will come both from
 1827 the better time resolution of RPC link boards and from the addition of more hits along the muon
 1828 tracks and also a contribution from the GEMs to the lever arm of each track thanks to their high
 1829 angular resolution.

1830

1831 The rate will be partly reduced in the forward region thanks to the better spatial resolution of
 1832 iRPCs, with respect to the current RPC system, that will reduce the ambiguity brought by multiple
 1833 local charged tracks in CSCs, as explained through Figure 3.24. Indeed, as the rates will increase,
 1834 the probability to record more than a single local charged track will greatly increase. This is due to
 1835 the fact that the trigger algorithm uses information from 3 consecutive bunch crossings to find muon
 1836 tracks. It is estimated that with iRPCs operated at 95% efficiency the resolution of ambiguous events
 would be of the order of 99.7%.

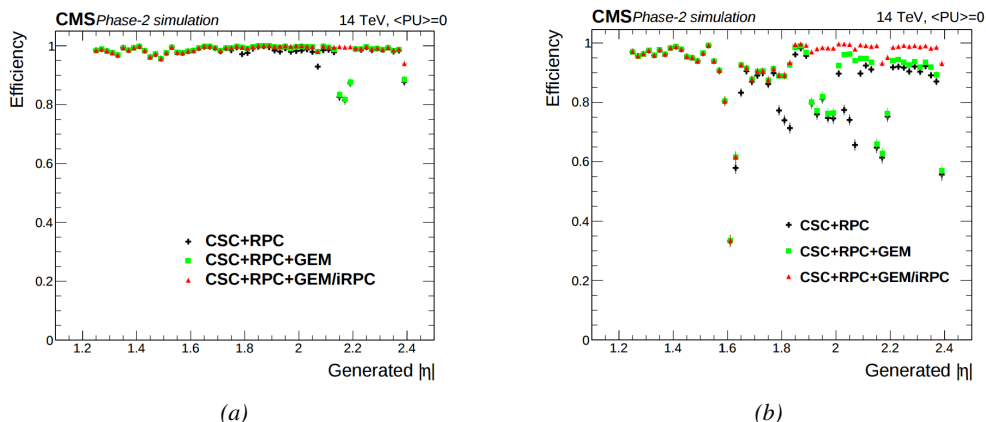


Figure 3.23: Efficiency of the L1 trigger in the endcap region after Phase-II upgrade in the case CSC/GEM/RPC hits are requested in at least 2 stations out of four (3.23a) and in all four stations (3.23b).

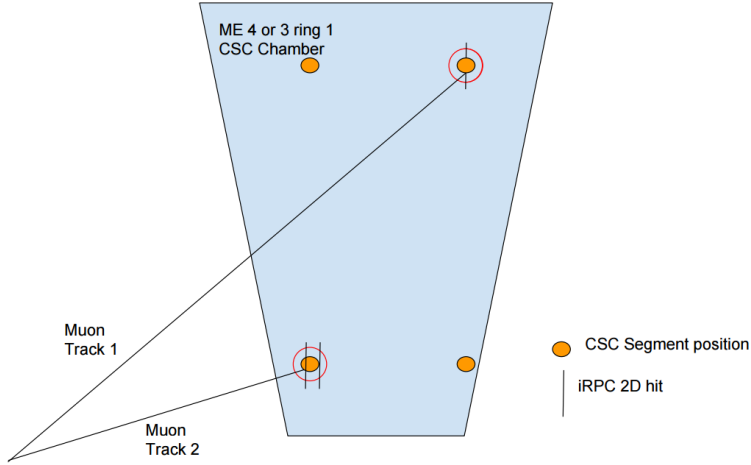


Figure 3.24: Resolution of the LCT ambiguous events thanks to the combination of CSC and iRPC readout data. Using CSCs only, 2 pairs of hits are possible.

The addition of GEMs will improve greatly the measured muon momentum resolution by improving the global resolution of the direction of muon tracks, as can be seen in Figure 3.25, which will contribute to lowering the trigger rate and increase the efficiency, as can be seen from Figure 3.26 that focuses especially in the most challenging pseudo-rapidity region. Data from both CSCs and GEMs are combined into the OTMB to build on each station, GEM/CSC primitives matching space and time information from both subsystems.

Finally, the development of a track finder specific to the overlap region was already achieved during the Phase-I upgrade of the L1-Trigger [31]. Nevertheless, the improvements of DT spatial resolution and RPC timing will be carried and implemented into the OMTF.

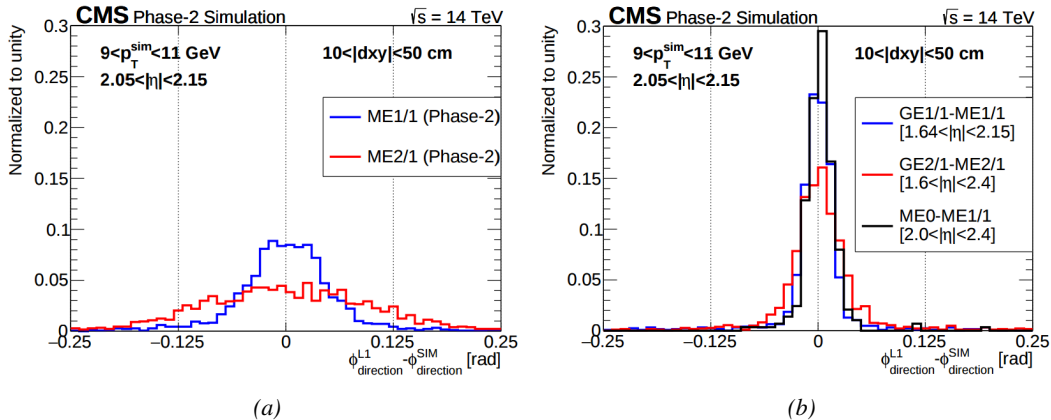


Figure 3.25: The angular resolution on reconstructed muon tracks in the GEM overlap region $2.0 < |\eta| < 2.15$ is compared for Phase-II conditions in the case CSC are alone (Figure 3.25a) and in the case the GEMs' data, including ME0, is combined to which of CSCs (Figure 3.25b).

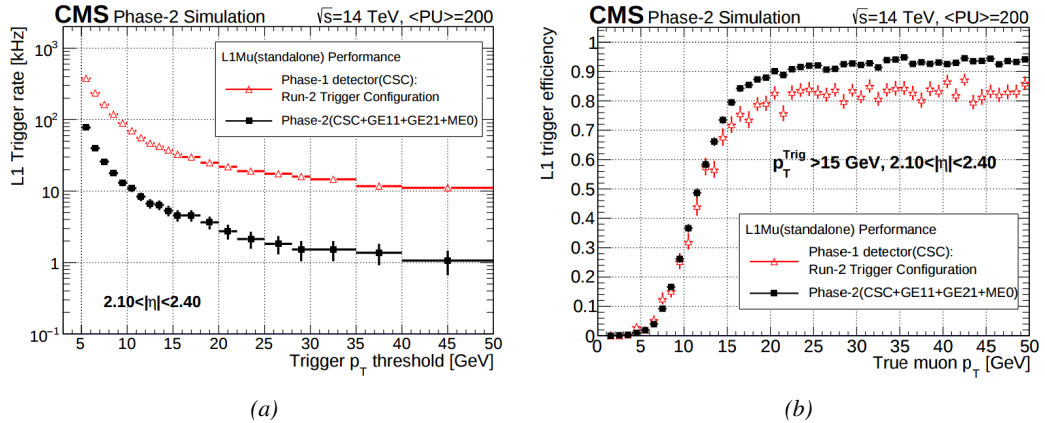


Figure 3.26: Comparison of L1 trigger performances for prompt muons with and without the addition of GEMs in the region $2.1 < |\eta| < 2.4$ at Phase-II conditions. GEMs would allow a reduction of the trigger accept rate by an order of magnitude (Figure 3.26a) while increasing the trigger efficiency (Figure 3.26b).

1846 3.5 Ecofriendly gas studies

1847 3.5.1 Status of the studies and potential candidates

1848 3.5.2 Implications in case of no suitable ecofriendly mixture

4

1849

1850

Physics of Resistive plate chambers

1851 A Resistive Plate Chamber (RPC) is a gaseous detector using the same physical processes described
1852 in Chapter 3. It has been developed in 1981 by Santonico and Cardarelli [32], under the name of
1853 *Resistive Plate Counter*, as an alternative to the local-discharge spark counters proposed in 1978
1854 by Pestov and Fedotovich [33, 34]. Working with spark chambers implied using high-pressure gas
1855 and high mechanical precision which the RPC simplified by formerly using a gas mixture of argon
1856 and butane flowed at atmospheric pressure and a constant and uniform electric field propagated
1857 in between two parallel electrode plates. Moreover, a significant increase in rate capability was
1858 introduced by the use of electrode plate material with high bulk resistivity, preventing the discharge
1859 from growing throughout the whole gas gap. Indeed, the effect of using resistive electrodes is that
1860 the constant electric field is locally canceled out by the development of the discharge, limiting its
1861 growth.

1862 Through its development history, different operating modes [35–37] and new detector designs [38–
1863 40] have been discovered, leading to further improvement of the rate capability of such a detector.
1864 Moreover, the addition of SF_6 into the gas mix improved the stability of operation of the RPC [41,
1865 42].

1866 The low developing costs and easily achievable large detection areas offered by RPCs, as well as
1867 the wide range of possible designs, made them a natural choice to as muon chambers and/or trigger
1868 detectors in multipurpose experiments such as CMS [21] or ATLAS [43], time-of-flight detectors in
1869 ALICE [44], calorimeter with CALICE [45] or even detectors for volcanic muography with ToMu-
1870 Vol [46].

1871 4.1 Principle

1872 RPCs are ionisation detectors composed of two parallel resistive plate electrodes in between which
1873 a constant electric field is set. The space in between the electrodes, referred as *gap*, is filled with a
1874 dense gas that is used to generate primary ionization into the gas volume. The free charge carriers
1875 (electrons and cations) created by the ionization of the gas molecules are then accelerated towards

¹⁸⁷⁶ the electrodes by the electric field, as shown in Figure 4.1 [47].

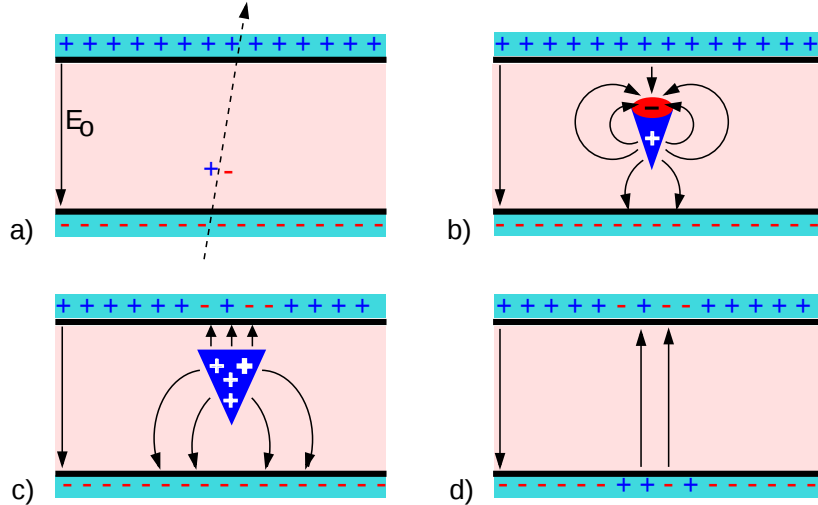


Figure 4.1: Different phases of the avalanche development in the RPC gas volume subjected to a constant electric field E_0 . a) An avalanche is initiated by the primary ionisation caused by the passage of a charged particle through the gas volume. b) Due to its growing size, the avalanche starts to locally influence the electric field. c) The electrons, lighter than the cations reach the anode first. d) The ions reach the cathode. While the charges have not recombined, the electric field in the small region around the avalanche stays affected and locally blind the detector.

¹⁸⁷⁷ RPCs being passive detectors, a current on pick-up copper read-out placed outside of the gas
¹⁸⁷⁸ volume is induced by the charge accumulation during the growth of the avalanche. As a result,
¹⁸⁷⁹ the time resolution of the detector is substantially increased as the output signal is generated while
¹⁸⁸⁰ the electrons are still in movement. The advantage of a constant electric field, over multi-wire
¹⁸⁸¹ proportional chambers, is that the electrons are being fully accelerated from the moment charge
¹⁸⁸² carriers are freed and feel the full strength of the electric field that doesn't depend on the distance to
¹⁸⁸³ the readout and that the output signal doesn't need for the electrons to be physically collected.

¹⁸⁸⁴ The typical gas mixture RPCs are operated with is generally composed of 3 gas compounds.

- ¹⁸⁸⁵ • Tetrafluoroethane ($C_2F_4H_2$), also referred to as *Freon*, is the principal compound of the RPC
¹⁸⁸⁶ gas mixtures, with a typical fraction above 90%. It is used for it's high effective Townsend
¹⁸⁸⁷ coefficient and the great average fast charge that allows to operate the detector with a high
¹⁸⁸⁸ threshold with respect to argon, for example, that has similar effective Townsend coefficient
¹⁸⁸⁹ but suffers from a lower fast charge. To operate with similar conditions, argon would require a
¹⁸⁹⁰ higher electric field leading to a higher fraction of streamers, thus limiting the rate capability
¹⁸⁹¹ of the detector [48].
- ¹⁸⁹² • Isobutane (i- C_4H_{10}), only present in a few percent in the gas mixtures, is used for its UV
¹⁸⁹³ quenching properties [49] helping to prevent streamers due to UV photon emission during the
¹⁸⁹⁴ avalanche growth.
- ¹⁸⁹⁵ • Sulfur hexafluoride, (SF_6), referred to simply as *SF6*, is used in very little quantities for its
¹⁸⁹⁶ high electronegativity. Excess of electrons are being absorbed by the compound and streamers

1897 are suppressed [42]. Nevertheless, a fraction of SF_6 higher than 1% will not bring any extra
 1898 benefit in terms of streamer cancelation power but will lead to higher operating voltage [41],
 1899 as can be understood through Figure 4.2.

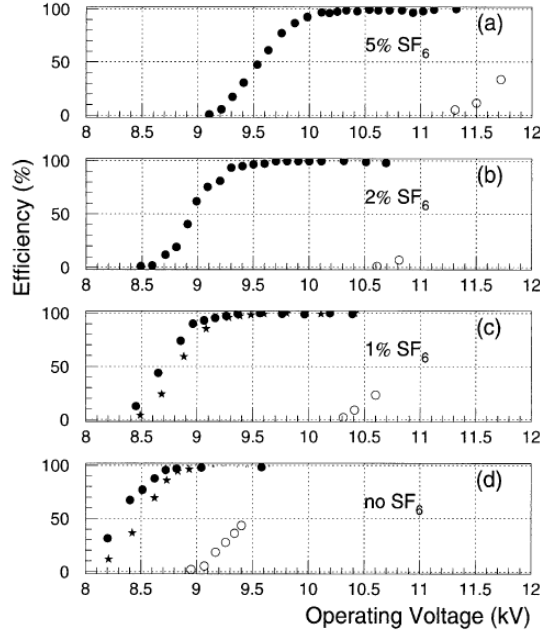


Figure 4.2: Effeciency (circles and stars with 30 mV and 100 mV thresholds respectively) and streamer probability (opened circles) as function of the operating voltatge of a 2 mm single gap HPL RPC flushed with a gas mixture containing (a) 5%, (b) 2%, (c) 1% and (d) no SF_6 [41].

1900 After an avalanche developed in the gas, a time long compared to the development of a discharge
 1901 is needed to recombine the charge carriers in the electrode material due to their resistivity. This
 1902 property has the advantage of affecting the local electric field and avoiding sparks in the detector
 1903 but, on the other hand, the rate capability is intrinsically limited by the time constant τ_{RPC} of the
 1904 detector. Using a quasi-static approximation of Maxwell's equations for weakly conducting media,
 1905 it can be shown that the time constant τ_{RPC} necessary to the charge recombination at the interface
 1906 in between the electrode and the gas volume is given by the Formula 4.1 [50].

$$\tau_{RPC} = \frac{\epsilon_{electrode} + \epsilon_{gas}}{\sigma_{electrode} + \sigma_{gas}} \quad (4.1)$$

1907 A gas can be assimilated to vacuum, leading to $\epsilon_{gas} = \epsilon_0$ and $\sigma_{gas} = 0$, and the electrodes
 1908 permittivity and conductivity can be written as $\epsilon_{electrode} = \epsilon_r \epsilon_0$ and $\sigma_{electrode} = 1/\rho_{electrode}$,
 1909 showing the strong dependence of the time constant to the electrodes resistivity in Formula 4.2.

$$\tau_{RPC} = (\epsilon_r + 1)\epsilon_0 \times \rho_{electrode} \quad (4.2)$$

1910 Very few materials with a low enough resistivity exist in nature. The resistivity targeted to build
 1911 RPCs ranges from 10^9 to $10^{12} \Omega \cdot \text{cm}$. The most common RPC electrode materials are displayed in
 1912 Table 4.1. When the doped glass and ceramics can offer short time constants of the order of 1 ms,

¹⁹¹³ the developing cost of such materials is quite high due to the very low demand. Thus, High-pressure
¹⁹¹⁴ laminate (HPL) is often the choice for high rate experiments using very large RPC detection areas.
¹⁹¹⁵ Other experiments working at cosmic muon fluxes can safely operate with ordinary float glass.

Material	$\rho_{electrode}$ ($\Omega \cdot \text{cm}$)	ϵ_r	τ_{RPC} (ms)
Float glass	10^{12}	~ 7	~ 700
High-pressure laminate	10^{10} to 10^{12}	~ 6	~ 6 to 600
Doped glass (LR S)	10^9 to 10^{11}	~ 10	~ 1 to 100
Doped ceramics (SiN/SiC)	10^9	~ 8.5	~ 1
Doped ceramics (Ferrite)	10^8 to 10^{12}	~ 20	~ 0.2 to 2000

Table 4.1: Properties of the most used electrode materials for RPCs.

¹⁹¹⁶ 4.1.1 Electron drift velocity

¹⁹¹⁷ Talk about the electron drift velocity and mention the time resolution of RPCs.

¹⁹¹⁸ 4.2 Rate capability and time resolution of Resistive Plate Chambers

¹⁹²⁰ As already previously discussed, the electrode material plays a key role in the max intrinsic rate
¹⁹²¹ capability of RPCs. R&D is being done to develop at always cheaper costs material with lower
¹⁹²² resistivity. Nevertheless, the amount of charge released, i.e. the size of the discharge, if reduced
¹⁹²³ leads to a smaller blind area in the detector, increasing the rate capability of the detector.

¹⁹²⁴ 4.2.1 Operation modes

¹⁹²⁵ RPCs where developed early 1980s. At that time it was using an operating mode now referred to
¹⁹²⁶ as *streamer mode*. Streamers are large discharges that develop in between the 2 electrodes enough
¹⁹²⁷ to locally discharge the electrodes. If the electric field inside of the gas volume is strong enough,
¹⁹²⁸ with electrons being fast compared to ions, a large and dense cloud of positive ions will develop
¹⁹²⁹ nearby the anode and extend toward the cathode while the electrons are being collected, eventually
¹⁹³⁰ leading to a streamer discharge due to the increase of field seen at the cathode. the field is then strong
¹⁹³¹ enough so that electrons are pulled out of the cathode. Electrodes, though they are a unique volume
¹⁹³² of resistive material, can be assimilated to capacitors. At the moment an electric field is applied in
¹⁹³³ between their outer surfaces, the charge carriers inside of the volume will start moving leading to
¹⁹³⁴ a situation where there is no voltage across the electrodes and a higher density of negative charges,
¹⁹³⁵ i.e. electrons, on the inner surface of the cathode. Finally, when a streamer discharge occurs, these
¹⁹³⁶ electrons are partially released in the gas volume contributing to increase the discharge strength until
¹⁹³⁷ the formation of a conductive plasma, the streamer. This can be understood through Figure 4.3 [35].
¹⁹³⁸ Streamer signals are very convenient in terms of read-out as no amplification is required with output
¹⁹³⁹ pulses amplitudes of the order of a few tens to few hundreds of mV as can be seen on Figure 4.4.

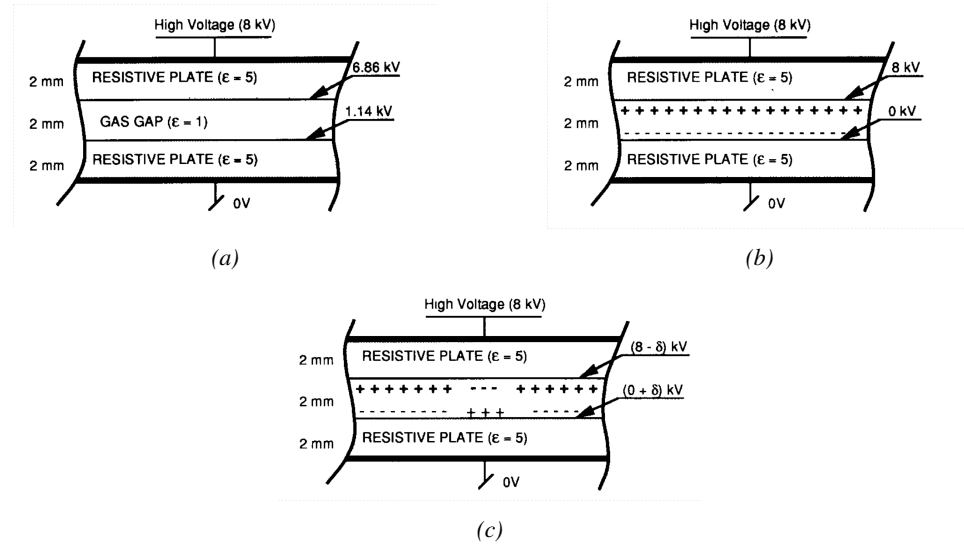


Figure 4.3: Movement of the charge carriers in an RPC. Figure 4.3a: Voltage across an RPC whose electrode have a relative permittivity of 5 at the moment the tension is applied. Figure 4.3b: After the charge carriers moved, the electrodes are charged and there is no voltage drop over the electrodes anymore. The full potential is applied on the gas gap only. Figure 4.3c: The streamer discharge initiated by a charged particle transports electrons and cations towards the anode and cathode respectively.

When the electric field is reduced though, the electronic gain is small until the electrons get close enough to the anode and the positive ion cloud is much smaller. The electric field cannot rise to the point a field emission of electrons on the cathode is possible. The resulting signal is weak, of the order of a few mv as shown on Figure 4.4, and requires amplification. This is the *avalanche mode* of RPC operation.

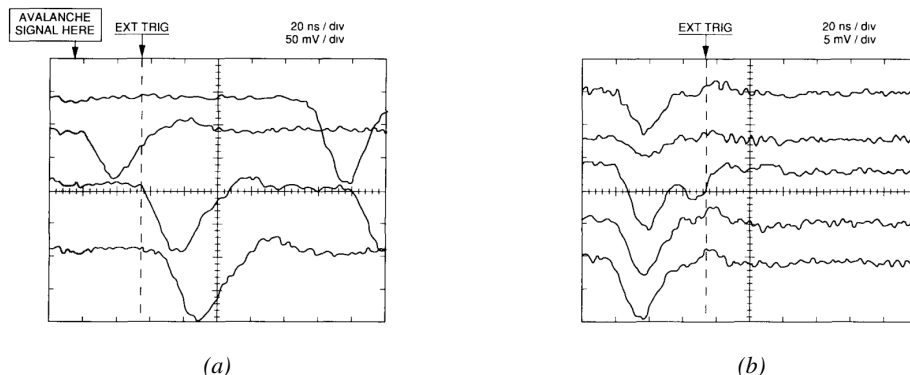


Figure 4.4: Typical oscilloscope pulses in streamer mode (Figure 4.4a) and avalanche mode (Figure 4.4b). In the case of streamer mode, the very small avalanche signal is visible.

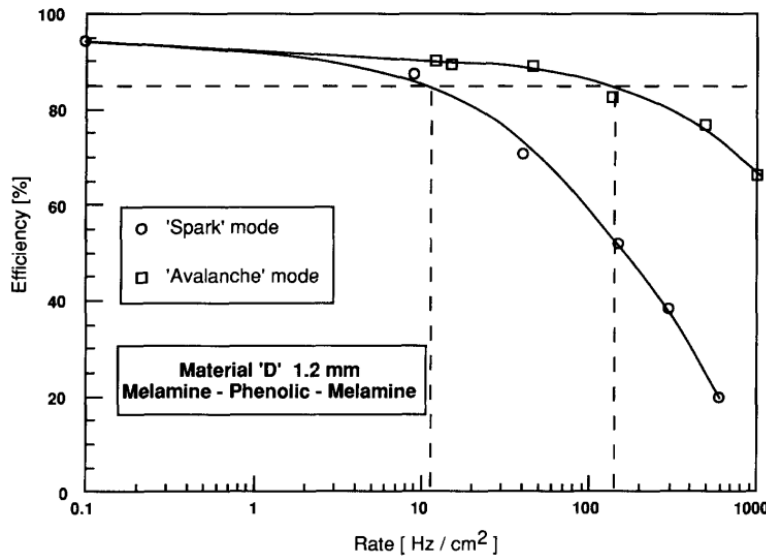


Figure 4.5: Rate capability comparison for the streamer and avalanche mode of operation. An order of magnitude in rate capability for a maximal efficiency drop of 10% is gained by using the avalanche mode over the streamer mode.

1945 This mode offers a higher rate capability by providing smaller discharges that don't affect the
 1946 electrodes charge and are more locally contained in the gas volume as was demonstrated by Crotty
 1947 with Figure 4.5 [35]. The detector only stays locally blind the time the charge carriers are recom-
 1948 bined and there is no need for electrode recharge which is a long process affecting a large portion
 1949 of the detector. Another advantage of avalanche signals over streamer is the great time consistency.
 1950 Figure 4.4 shows very clearly that avalanche signals have a very small time jitter. This is a natural
 1951 choice for high rate experiments.

1952 4.2.2 Detector designs and performance

1953 Different RPC design have been used and each of them present its own advantages. Historically,
 1954 the first type of RPC to have been developed is what is referred now to *narrow gap* RPC [32, 51].
 1955 After the avalanche mode has been discovered [35], it has been proven that increasing the width
 1956 of the gas gap lead to higher rate capability, due to lower charge deposition per avalanche, and
 1957 lower power dissipation [51]. Nevertheless, by increasing the gas gap width, the time resolution of
 1958 the detector decreases. This is a natural result if the increase of active gas volume in the detector is
 1959 taken into account. Indeed, for a given threshold, only the small fraction of gas closest to the cathode
 1960 will provide enough gain to have a detectable signal. In the case of a wider gas volume, the active
 1961 region is then larger and a larger time jitter is introduced with the variation of starting position of the
 1962 avalanche, as discussed in [38]. To solve improve both the time resolution and the rate capability,
 1963 different methods were used trying to get advantages of both narrow and wide gap RPCs.

1964 **4.2.2.1 Double-gap RPC**

1965 Double-gap RPCs are made out of 2 narrow RPC detectors. The 2 RPC gaps are stacked on top of
 1966 each other as shown in Figure 4.6. This detector layout, popularized by the two multipurpose experiments
 1967 CMS [21] and ATLAS [43] at LHC, can be used as an OR system in which each individual
 1968 chamber participates in the output signal. The gain of such a detector is greatly reduced with respect
 1969 to single-gap RPCs with an efficiency plateau reached at lower voltage, as visible on Figure 4.7.

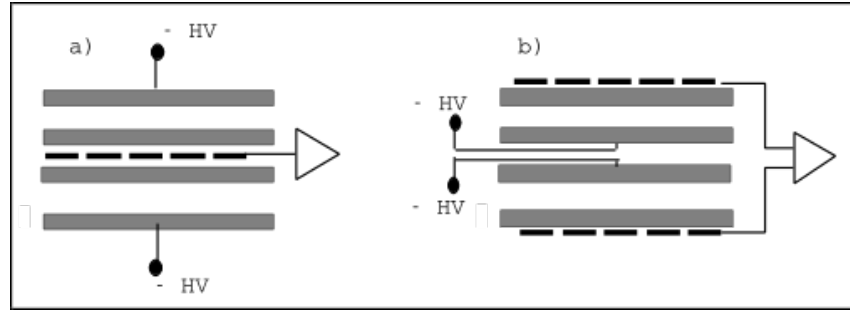


Figure 4.6: Possible double-gap RPC layouts: a) "standard" 1D double-gap RPC, as used in CMS experiment, where the anodes are facing each other and a 1D read-out plane is sandwiched in between them, b) double read-out double-gap RPC as used in ATLAS experiment, where the cathodes are facing each other and 2 read-out planes are used on the outer surfaces. This last layout can offer the possibility to use a 2D reconstruction by using orthogonal read-out planes.

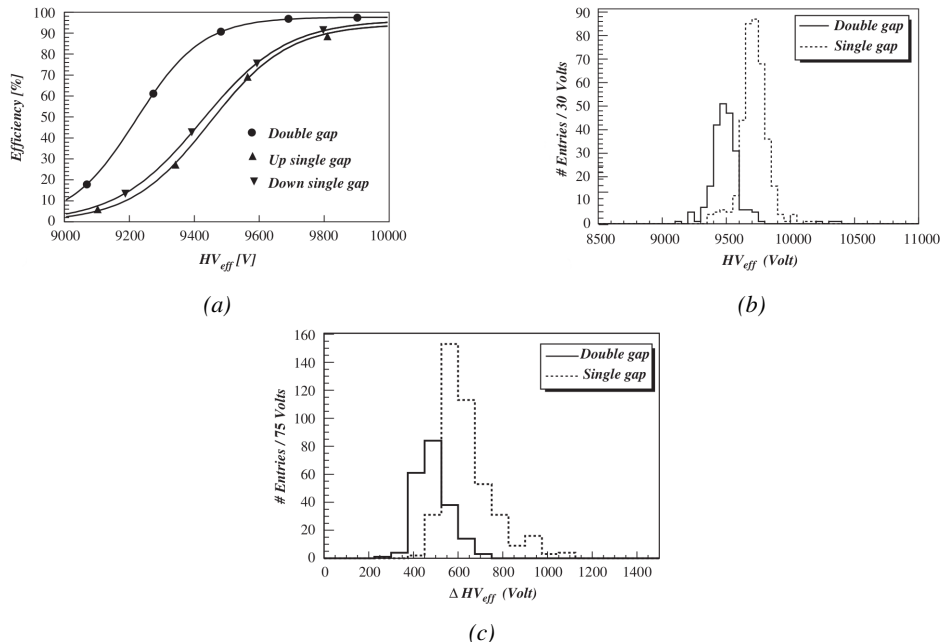


Figure 4.7: Comparison of performance of CMS double and single gap RPCs using cosmic muons [52]. Figure 4.7a: Comparison of efficiency sigmoids. Figure 4.7b: Voltage distribution at 95% of maximum efficiency. Figure 4.7c: $\Delta_{10\%}^{90\%}$ distribution.

4.2.2.2 Multigap RPC (MRPC)

MRPCs are layouts in which floating sub electrode plates are placed into a wide gap RPC to divide the gas volume and create a sum of narrow gaps [38, 39]. The time resolution of such a detector can reach of few tens of ps, with gas gaps of the order of a few hundred μm as shown in Figure 4.8 representing ALICE Time-of-flight (ToF) MRPCs.

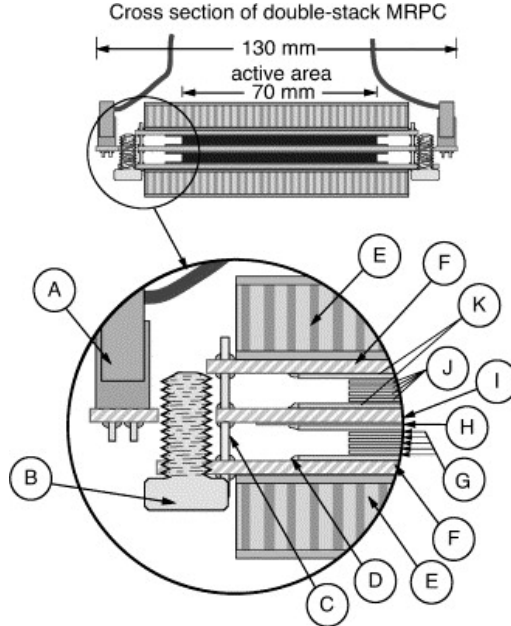


Figure 4.8: Presentation of ALICE MRPC using 250 μm gas gaps, 620 μm outer glass electrodes and 550 μm inner floating electrodes. More details on the labels are given in [53].

Sometimes used as a double multigap RPC, taking advantage of the OR of double gap RPCs, the MRPC is mainly used as ToF detector [53–57] due to its excellent timing properties that allow to perform particle identification as explained by Williams in [58]. The principle of particle identification using ToF is simply the measurement of the velocity of a particle. Indeed, particles are defined by their mass (for the parameter of interest here, their electric charge being measured using the bending angle of the particles traveling through a magnetic field) and this mass can be calculated by measuring the velocity β and momentum of the particle:

$$\beta = \frac{p}{\sqrt{p^2 + m^2}} \quad (4.3)$$

Intuitively, it is trivial to understand that 2 different particles having the same momentum will have a different velocity due to the mass difference and thus a different flight time T_1 and T_2 through the detector and this is used to separate and identify particles. The better the time resolution of the ToF system used, the stronger will the separation be:

$$T = \frac{L}{v} = \frac{L}{c \cdot \beta}, \quad \Delta T = T_1 - T_2 = \frac{L}{c} \left(\sqrt{1 + m_1^2/p^2} - \sqrt{1 + m_2^2/p^2} \right) \cong (m_1^2 - m_2^2) \frac{L}{2cp^2} \quad (4.4)$$

¹⁹⁸⁶ An example of particle identification is given for the case of STAR experiment in Figure 4.9.

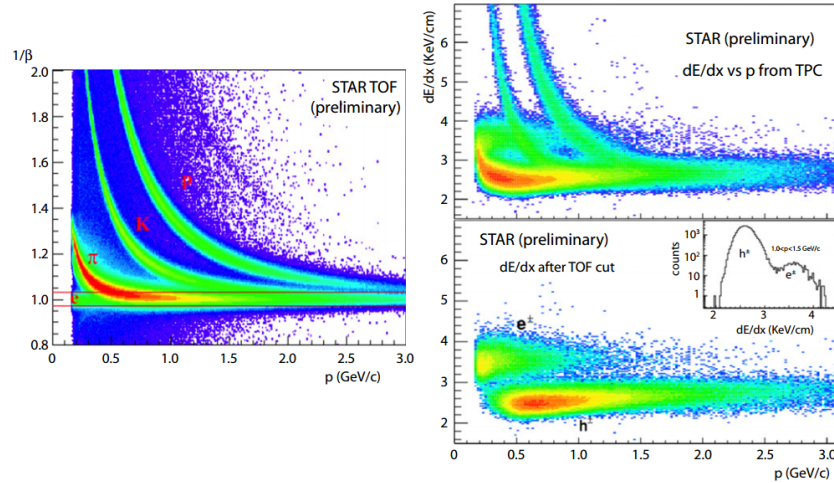


Figure 4.9: Particle identification applied to electrons in the STAR experiment. The identification is performed combining ToF and dE/dx measurements [58].

¹⁹⁸⁷ Another benefice of using such small gas gaps is the strong reduction of the average avalanche volume and thus of the blind spot on MRPCs leading to an improved rate capability. Multigaps can sustain backgrounds of several kHz/cm² as demonstrated in Figure 4.10.

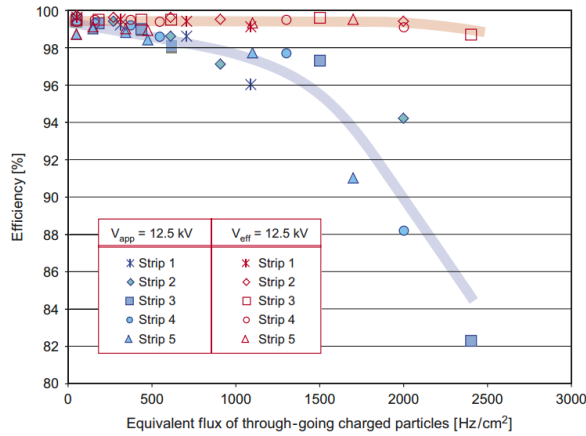


Figure 4.10: Comparison of the detector performance of ALICE ToF MRPC [59] at fixed applied voltage (in blue) and at fixed effective voltage (in red). The effective voltage is kept fixed by increasing the applied voltage accordingly to the current drawn by the detector.

¹⁹⁹⁰ 4.2.2.3 Charge distribution and performance limitations

¹⁹⁹¹ The direct consequence of the different RPC layouts is a variation of intrinsic time resolution of the ¹⁹⁹² RPC as the gap size decreases. An advantage is given to multigaps whose design use sub-millimeter ¹⁹⁹³ gas volumes providing very consistent signals.

1994 On the charge spectrum point of view, each layout has its own advantages. When the double-gap
 1995 has the highest induced over drifting charge ratio, as seen in Figure 4.11, the multigap has a charge
 1996 spectrum strongly detached from the origin, as visible in Figure 4.12. A high induced over drifting
 1997 charge ratio means that the double gap can be safely operated at high threshold or that at similar
 1998 threshold it can be operated with a twice smaller drifting charge, meaning a higher rate capability.
 1999 On the other hand, the strong detachment of the charge spectrum from the origin in the MRPC case
 2000 allows to reach a higher efficiency with increasing threshold as most of the induced charge is not low
 2001 due to the convolution of several single gap spectra. The range of stable efficiency increases with
 2002 the number of gap, as presented in Figure 4.13.

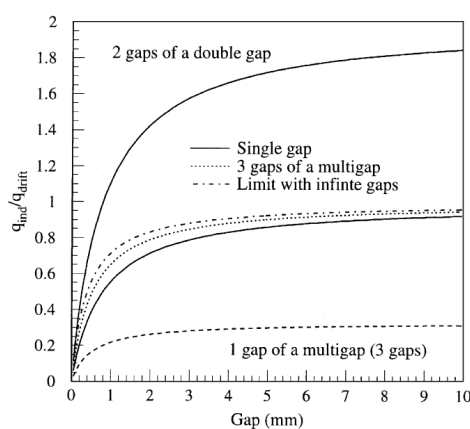


Figure 4.11: Ratio between total induced and drifting charge have been simulated for single gap, double-gap and multigap layouts [60]. The total induced charge for a double-gap RPC is a factor 2 higher than for a multigap.

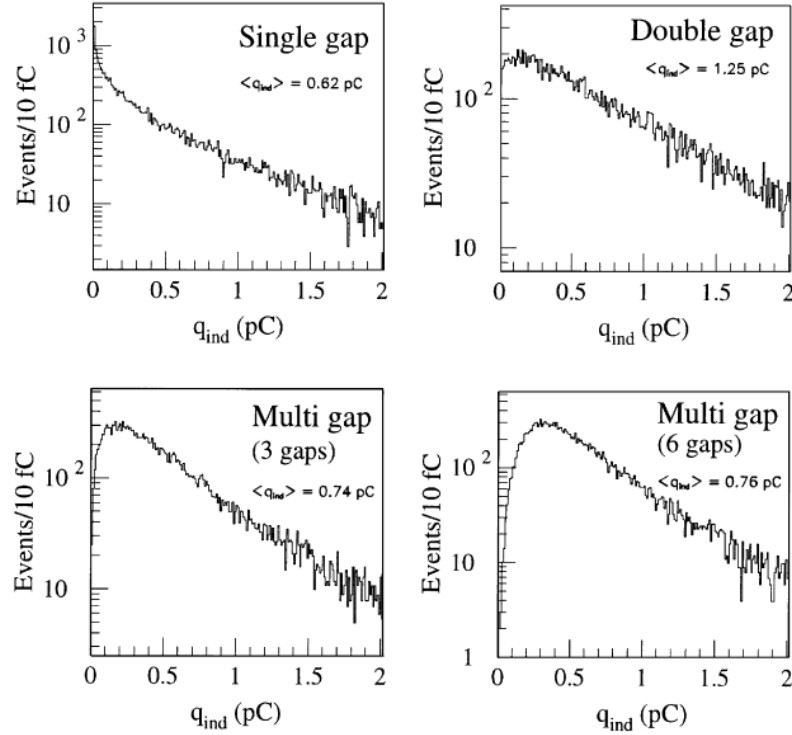


Figure 4.12: Charge spectra have been simulated for single gap, double-gap and multigap layouts [60]. It appears that when single gap shows a decreasing spectrum, double and multigap layouts exhibit a spectrum whose peak is detached from the origin. The detachment gets stronger as the number of gaps increases.

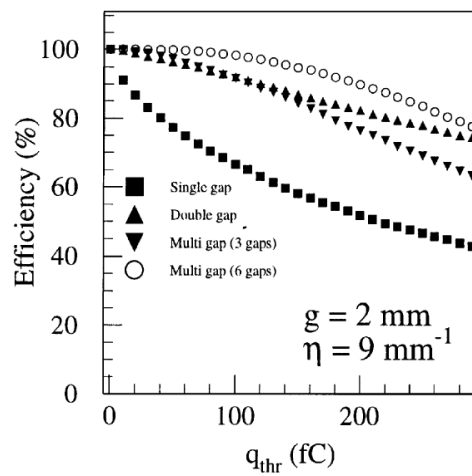


Figure 4.13: The maximal theoretical efficiency is simulated for single gap, double-gap and multigap layouts [60] at a constant gap thickness of 2 mm and using an effective Townsend coefficient of 9 mm^{-1} .

₂₀₀₃ **4.3 Signal formation**

₂₀₀₄ **4.4 Gas transport parameters**

5

2005

2006

2007

Longevity studies and Consolidation of the present CMS RPC subsystem

2008 5.1 Resistive Plate Chambers at CMS

2009 5.1.1 Overview

2010 The Resistive Plate Chambers (RPC) system, located in both barrel and endcap regions, provides a
2011 fast, independent muon trigger with a looser p_T threshold over a large portion of the pseudorapidity
2012 range ($|\eta| < 1.6$) [add reconstruction].

2013

2014 During High-Luminosity LHC (HL-LHC) operations the expected conditions in terms of back-
2015 ground and pile-up will make the identification and correct P_T assignment a challenge for the Muon
2016 system. The goal of RPC upgrade is to provide additional hits to the Muon system with precise tim-
2017 ing. All these informations will be elaborated by the trigger system in a global way enhancing the
2018 performance of the trigger in terms of efficiency and rate control. The RPC Upgrade is based on two
2019 projects: an improved Link Board System and the extension of the RPC coverage up to $|\eta| = 2.4$.
2020 [FIXME 2.4 or 2.5?]

2021 The Link Board system, that will be described in section xxx, is responsible to process, syn-
2022 chronize and zero-suppress the signals coming from the RPC front end boards. The Link Board
2023 components have been produced between 2006 and 2007 and will be subjected to aging and failure
2024 in the long term. The upgraded Link Board system will overcome the aging problems described in
2025 section xxx and will allow for a more precise timing information to the RPC hits from 25 to 1 ns [ref
2026 section xxx].

2027 The extension of the RPC system up to $|\eta| = 2.1$ was already planned in the CMS TDR [ref
2028 cmstdr] and staged because of budget limitations and expected background rates higher than the rate
2029 capability of the present CMS RPCs in that region. An extensive R&D program has been done in
2030 order to develop an improved RPC that fulfills the CMS requirements. Two new RPC layers in the
2031 innermost ring of stations 3 and 4 will be added with benefits to the neutron-induced background

2032 reduction and efficiency improvement for both trigger and offline reconstruction.

2033 5.1.2 The present RPC system

2034 The RPC system is organized in 4 stations called RB1 to RB4 in the barrel region, and RE1 to RE4
 2035 in the endcap region. The innermost barrel stations, RB1 and RB2, are instrumented with 2 layers
 2036 of RPCs facing the innermost (RB1in and RB2in) and outermost (RB1out and RB2out) sides of the
 2037 DT chambers. Every chamber is then divided from the read-out point of view into 2 or 3 η partitions
 2038 called “rolls”. The RPC system consist of 480 barrel chambers and 576 endcap chambers. Details
 2039 on the geometry are discussed in the paper [ref to geo paper].

2040 The CMS RPC chamber is a double-gap, operated in avalanche mode to ensure reliable operation
 2041 at high rates. Each RPC gap consists of two 2-mm-thick resistive High-Pressure Laminate (HPL)
 2042 plates separated by a 2-mm-thick gas gap. The outer surface of the HPL plates is coated with a thin
 2043 conductive graphite layer, and a voltage is applied. The RPCs are operated with a 3-component,
 2044 non-flammable gas mixture consisting of 95.2% freon ($C_2H_2F_4$, known as R134a), 4.5% isobutane
 2045 ($i-C_4H_{10}$), and 0.3% sulphur hexafluoride (SF_6) with a relative humidity of 40% - 50%. Readout
 2046 strips are aligned in η between the 2 gas gaps. [\[Add a sentence on FEBs.\]](#)

2047 The discriminated signals coming from the Front End boards feed via twisted cables (10 to 20 m
 2048 long) the Link Board System located in UXC on the balconies around the detector. The Link System
 2049 consist of the 1376 Link Boards (LBs) and the 216 Control Boards (CBs), placed in 108 Link Boxes.
 2050 The Link Box is a custom crate (6U high) with 20 slots (for two CBs and eighteen LBs). The Link
 2051 Box contains custom backplane to which the cables from the chambers are connected, as well as the
 2052 cables providing the LBs and CBs power supply and the cables for the RPC FEBs control with use
 2053 of the I2C protocol (trough the CB). The backplane itself contains only connectors (and no any other
 2054 electronic devices).

2055 The Link Board has 96 input channels (one channel corresponds to one RPC strip). The input
 2056 signals are the ~ 100 ns binary pulses which are synchronous to the RPC hits, but not to the LHC
 2057 clock (which drives the entire CMS electronics). Thus the first step of the FEB signals processing
 2058 is synchronization, i.e. assignment of the signals to the BXes (25 ns periods). Then the data are
 2059 compressed with a simple zero-suppressing algorithm (the input channels are grouped into 8 bit
 2060 partitions, only the partitions with at least one nonzero bit are selected for each BX). Next, the non-
 2061 empty partitions are time-multiplexed i.e. if there are more than one such partition in a given BX,
 2062 they are sent one-by-one in consecutive BXes. The data from 3 neighbouring LBs are concentrated
 2063 by the middle LB which contains the optical transmitter for sending them to the USC over a fiber at
 2064 1.6 Gbps.

2065 The Control Boards provide the communication of the control software with the LBs via the
 2066 FEC/CCU system. The CBs are connected into token rings, each ring consists of 12 CBs of one
 2067 detector tower and a FEC mezzanine board placed on the CCS board located in the VME crate in
 2068 the USC. In total, there are 18 rings in the entire Link System. The CBs also perform automatic
 2069 reloading of the LB's firmware which is needed in order to avoid accumulation of the radiation
 2070 induced SEUs in the LBs firmware.

2071 Both LBs and CB are based on the Xilinx Spartan III FPGAs, the CB additionally contains
 2072 radiation-tolerant (FLASH based) FPGA Actel ProAsicPlus.

2073 The High Voltage power system is located in USC, not exposed to radiation and easily accessible
 2074 for any reparation. A single HV channel powers 2 RPC chambers both in the barrel and endcap
 2075 regions. The Low Voltage boards are located in UXC on the balconies and provide the voltage to the

2076 front end electronics.

2077 5.1.3 Pulse processing of CMS RPCs

2078 Signals induced by cosmic particle in the RPC strips are shaped by standard CMS RPC Front-End
2079 Electronics (FEE) following the scheme of Figure 5.1. On a first stage, analogic signals are amplified
2080 and then sent to the Constant Fraction Discriminator (CFD) described in Figure 5.2. At the end of
2081 the chain, 100 ns long pulses are sent in the LVDS output. These output signal are sent on one side to
2082 a V1190A Time-to-Digital Converter (TDC) module from CAEN and on the other to an OR module
2083 to count the number of detected signals. Trigger and hit coïncidences are monitored using scalers.
2084 The TDC is used to store the data into ROOT files. These files are thus analysed to understand the
2085 detectors performance.

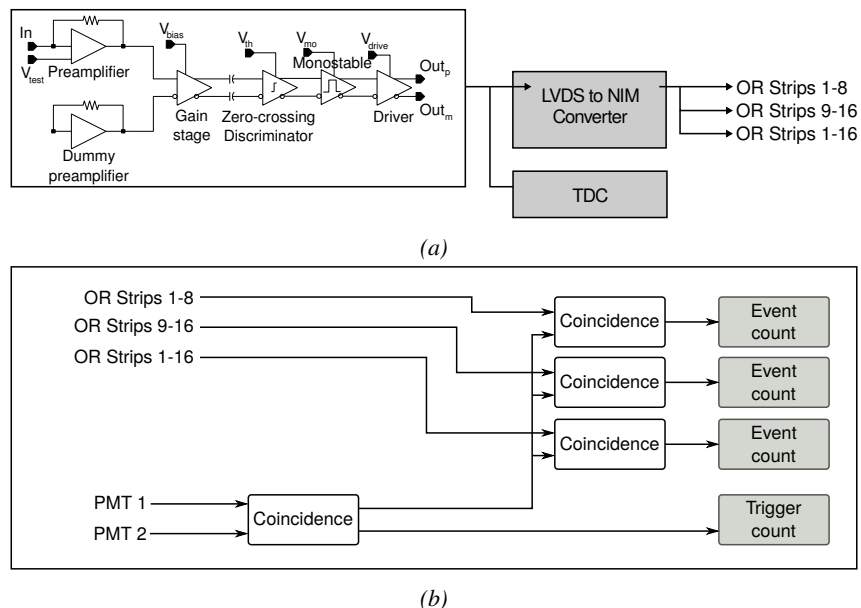


Figure 5.1: Signals from the RPC strips are shaped by the FEE described on Figure 5.1a. Output LVDS signals are then read-out by a TDC module connected to a computer or converted into NIM and sent to scalers. Figure 5.1b describes how these converted signals are put in coincidence with the trigger.

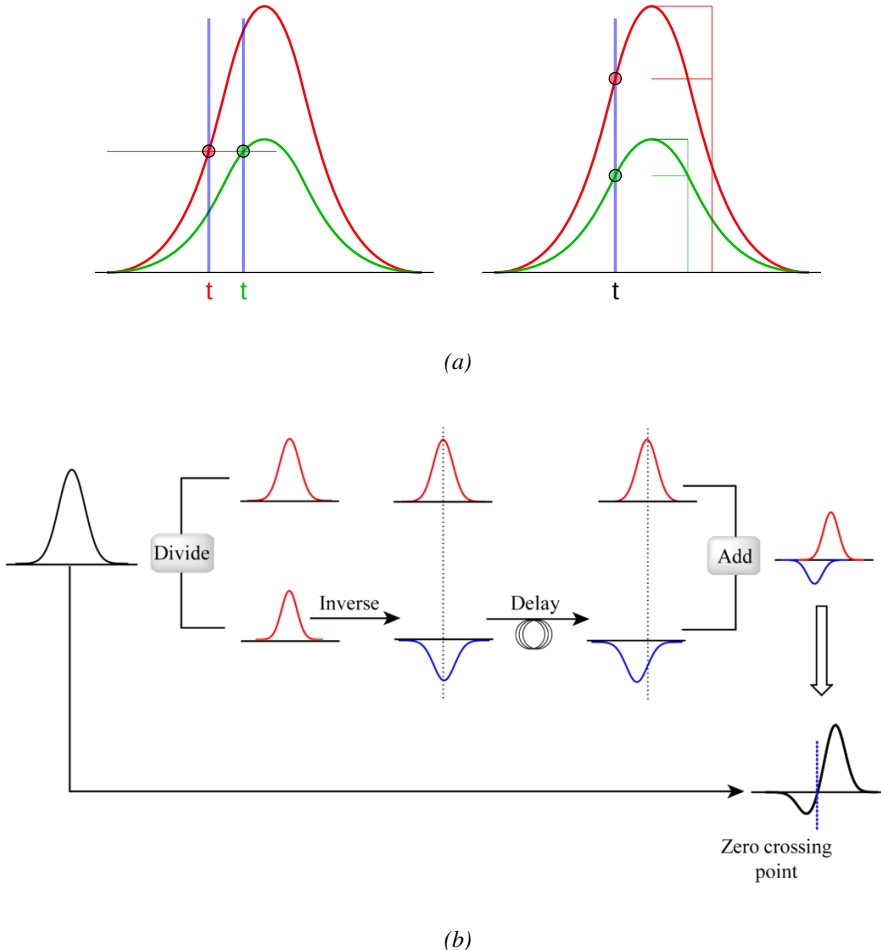


Figure 5.2: Description of the principle of a CFD. A comparison of threshold triggering (left) and constant fraction triggering (right) is shown in Figure 5.2a. Constant fraction triggering is obtained thanks to zero-crossing technique as explained in Figure 5.2b. The signal arriving at the input of the CFD is split into three components. A first one is delayed and connected to the inverting input of a first comparator. A second component is connected to the noninverting input of this first comparator. A third component is connected to the noninverting input of another comparator along with a threshold value connected to the inverting input. Finally, the output of both comparators is fed through an AND gate.

2086 5.2 Testing detectors under extreme conditions

2087 The upgrade from LHC to HL-LHC will increase the peak luminosity from $10^{34} \text{ cm}^{-2} \text{ s}^{-1}$ to reach
 2088 $5 \times 10^{34} \text{ cm}^{-2} \text{ s}^{-1}$, increasing in the same way the total expected background to which the RPC
 2089 system will be subjected to. Composed of low energy gammas and neutrons from $p\text{-}p$ collisions, low
 2090 momentum primary and secondary muons, puch-through hadrons from calorimeters, and particles
 2091 produced in the interaction of the beams with collimators, the background will mostly affect the
 2092 regions of CMS that are the closest to the beam line, i.e. the RPC detectors located in the endcaps.
 2093 [To update.]

2094

2095 The 2016 data allowed to study the values of the background rate in all RPC system. In Figure 2096 5.3, the distribution of the chamber background hit rate per unit area is shown at a luminosity 2097 of $5 \times 10^{34} \text{ cm}^{-2} \cdot \text{s}^{-1}$ linearly extrapolating from data collected in 2016 [ref mentioning the linear 2098 dependency of rate vs lumi]. The maximum rate per unit area at HL-LHC conditions is expected to 2099 be of the order of 600 Hz/cm^2 (including a safety factor 3). Nevertheless, Fluka simulations have 2100 conducted in order to understand the background at HL-LHC conditions. The comparison to the 2101 data has shown, in Figure 5.4, a discrepancy of a factor 2 even though the order of magnitude is 2102 consistent. [Understand mismatch.]

2103

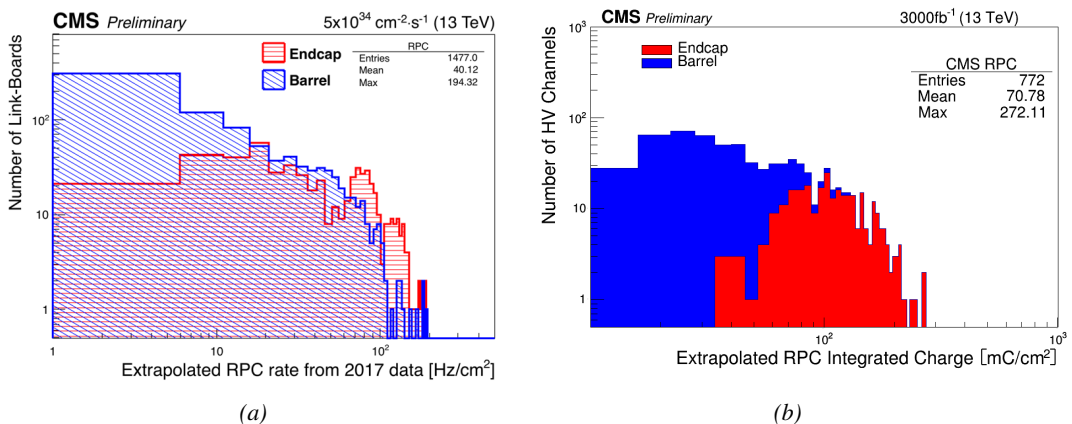


Figure 5.3: Figure 5.3a: The integrated charge per region (Barrel, Endcap) is extrapolated to HL-LHC integrated luminosity (3000 fb^{-1}) using the data accumulated in 2016 in every HV channels. Figure 5.3b: The hit rate per region (Barrel, Endcap) is linearly extrapolated to HL-LHC highest instantaneous luminosity ($5 \times 10^{34} \text{ cm}^{-2} \text{s}^{-1}$) using the rate as a function of instantaneous luminosity recorded by RPCs in 2017 showing a linear dependence.

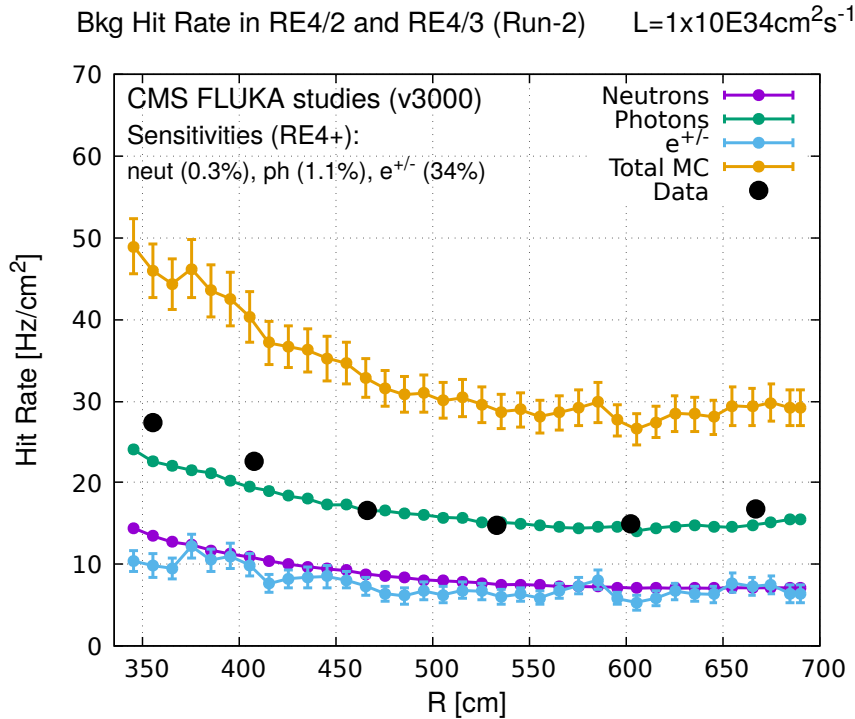


Figure 5.4: Background Fluka simulation compared to 2016 Data at $L = 10^{34} \text{ cm}^{-2} \cdot \text{s}^{-1}$ in the fourth endcap disk region. A mismatch in between simulation and data can be observed. [\[To be understood.\]](#)

In the past, extensive long-term tests were carried out at several gamma and neutron facilities certifying the detector performance. Both full size and small prototype RPCs have been irradiated with photons up to an integrated charge of $\sim 0.05 \text{ C}/\text{cm}^2$ and $\sim 0.4 \text{ C}/\text{cm}^2$, respectively [61, 62]. During Run-I, the RPC system provided stable operation and excellent performance and did not show any aging effects for integrated charge of the order of $0.01 \text{ C}/\text{cm}^2$. Projections on currents from 2016 Data, has allowed to determine that the total integrated charge, by the end of HL-LHC, would be of the order of $1 \text{ C}/\text{cm}^2$ (including a safety factor 3). [\[Corresponding figure needed.\]](#)

2111

2112 5.2.1 The Gamma Irradiation Facilities

2113 5.2.1.1 GIF

2114 Located in the SPS West Area at the downstream end of the X5 test beam, the Gamma Irradiation
 2115 Facility (GIF) was a test area in which particle detectors were exposed to a particle beam in presence
 2116 of an adjustable gamma background [63]. Its goal was to reproduce background conditions these
 2117 detectors would suffer in their operating environment at LHC. GIF layout is shown in Figure 5.5.
 2118 Gamma photons are produced by a strong ^{137}Cs source installed in the upstream part of the zone
 2119 inside a lead container. The source container includes a collimator, designed to irradiate a $6 \times 6 \text{ m}^2$
 2120 area at 5 m maximum to the source. A thin lens-shaped lead filter helps providing with a uniform
 2121 outcoming flux in a vertical plane, orthogonal to the beam direction. The principal collimator hole
 2122 provides a pyramidal aperture of $74^\circ \times 74^\circ$ solid angle and provides a photon flux in a pyramidal vol-

2123 ume along the beam axis. The photon rate is controled by further lead filters allowing the maximum
 2124 rate to be limited and to vary within a range of four orders of magnitude. Particle detectors under test
 2125 are then placed within the pyramidal volume in front of the source, perpendicularly to the beam line
 2126 in order to profit from the homogeneous photon flux. Adjusting the background flux of photons can
 2127 then be done by using the filters and choosing the position of the detectors with respect to the source.
 2128

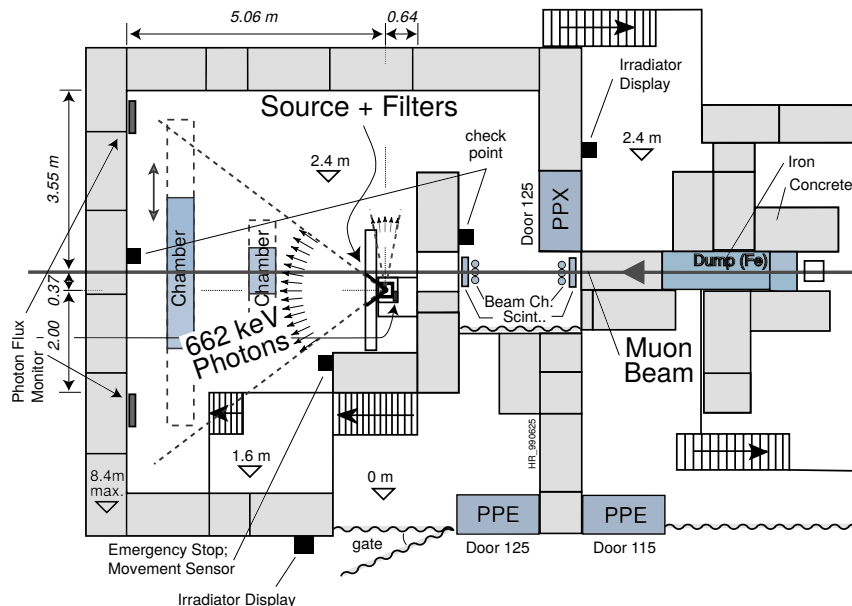


Figure 5.5: Layout of the test beam zone called X5c GIF at CERN. Photons from the radioactive source produce a sustained high rate of random hits over the whole area. The zone is surrounded by 8 m high and 80 cm thick concrete walls. Access is possible through three entry points. Two access doors for personnel and one large gate for material. A crane allows installation of heavy equipment in the area.

2129 As described on Figure 5.6, the ^{137}Cs source emits a 662 keV photon in 85% of the decays. An
 2130 activity of 740 GBq was measured on the 5th March 1997. To estimate the strength of the flux in
 2131 2014, it is necessary to consider the nuclear decay through time assiciated to the Cesium source
 2132 whose half-life is well known ($t_{1/2} = (30.05 \pm 0.08)$ y). The GIF tests where done in between the
 2133 20th and the 31st of August 2014, i.e. at a time $t = (17.47 \pm 0.02)$ y resulting in an attenuation of
 2134 the activity from 740 GBq in 1997 to 494 GBq in 2014.
 2135

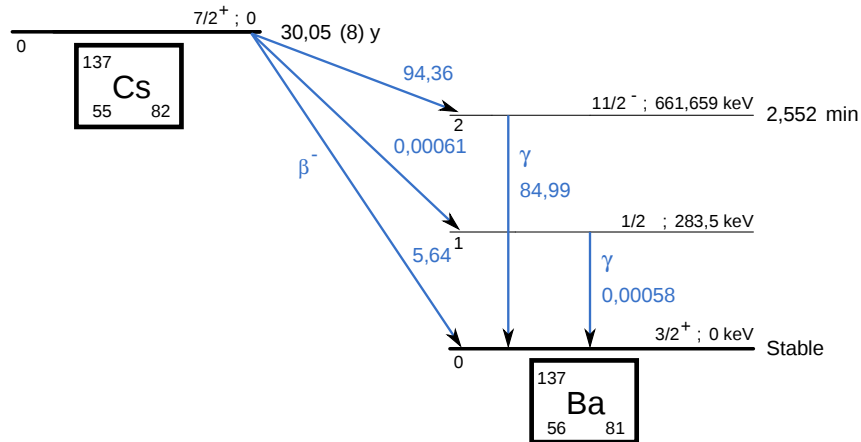


Figure 5.6: ^{137}Cs decays by β^- emission to the ground state of ^{137}Ba ($\text{BR} = 5.64\%$) and via the 662 keV isomeric level of ^{137}Ba ($\text{BR} = 94.36\%$) whose half-life is 2.55 min.

2136 5.2.1.2 GIF++

2137 The new Gamma Irradiation Facility (GIF++), located in the SPS North Area at the downstream end
 2138 of the H4 test beam, has replaced its predecessor during LS1 and has been operational since spring
 2139 2015 [64]. Like GIF, GIF++ features a ^{137}Cs source of 662 keV gamma photons, their fluence being
 2140 controlled with a set of filters of various attenuation factors. The source provides two separated large
 2141 irradiation areas for testing several full-size muon detectors with continuous homogeneous irradiation,
 2142 as presented in Figure 5.7.

2143

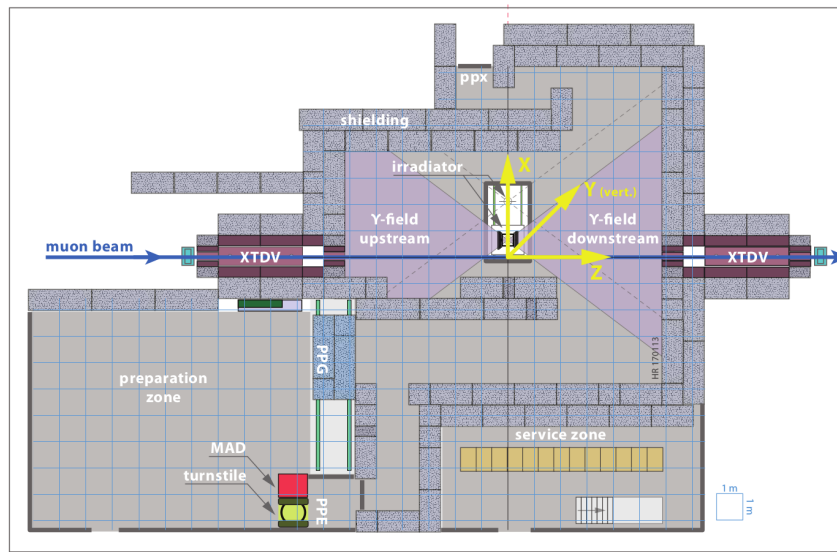


Figure 5.7: Floor plan of the GIF++ facility. When the facility downstream of the GIF++ takes electron beam, a beam pipe is installed along the beam line (z -axis). The irradiator can be displaced laterally (its center moves from $x = 0.65 \text{ m}$ to 2.15 m), to increase the distance to the beam pipe.

2144 The source activity was measured to be about 13.5 TBq in March 2016. The photon flux being
 2145 far greater than HL-LHC expectations, GIF++ provides an excellent facility for accelerated aging
 2146 tests of muon detectors.

2147

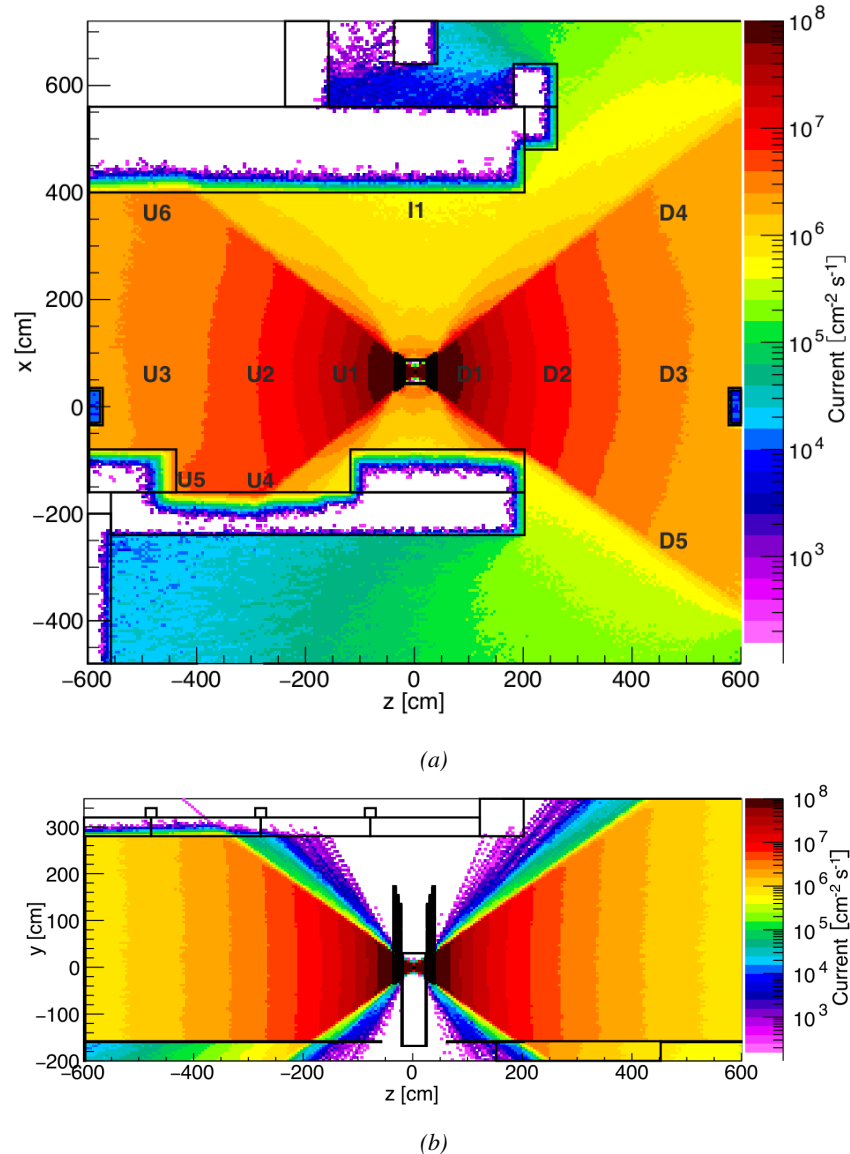


Figure 5.8: Simulated unattenuated current of photons in the xz plane (Figure 5.8a) and yz plane (Figure 5.8b) through the source at $x = 0.65$ m and $y = 0$ m. With angular correction filters, the current of 662 keV photons is made uniform in xy planes.

2148 The source is situated in the muon beam line with the muon beam being available a few times a
 2149 year. The H4 beam, composed of muons with a momentum of about 150 GeV/c, passes through the
 2150 GIF++ zone and is used to study the performance of the detectors. Its flux is of 104 particles/ cm^2

2151 focused in an area similar to $10 \times 10 \text{ cm}^2$. Therefore, with properly adjusted filters, one can imitate
 2152 the HL-LHC background and study the performance of muon detectors with their trigger/readout
 2153 electronics in HL-LHC environment.

2154

2155 5.3 Preliminary tests at GIF

2156 5.3.1 Resistive Plate Chamber test setup

2157 During summer 2014, preliminary tests have been conducted in the GIF area on a newly produced
 2158 RE4/2 chamber labelled RE-4-2-BARC-161. This chamber has been placed into a trolley covered
 2159 with a tent. The position of the RPC inside the tent and of the tent related to the source is described
 2160 in Figure 5.9. To test this CMS RPC, three different absorber settings were used. First of all,
 2161 measurements were done with fully opened source. Then, to complete this preliminary study, the
 2162 gamma flux has been attenuated from a factor 2 and a factor 5. The expected gamma flux at the level
 2163 of our detector will be discussed in subsection ??.

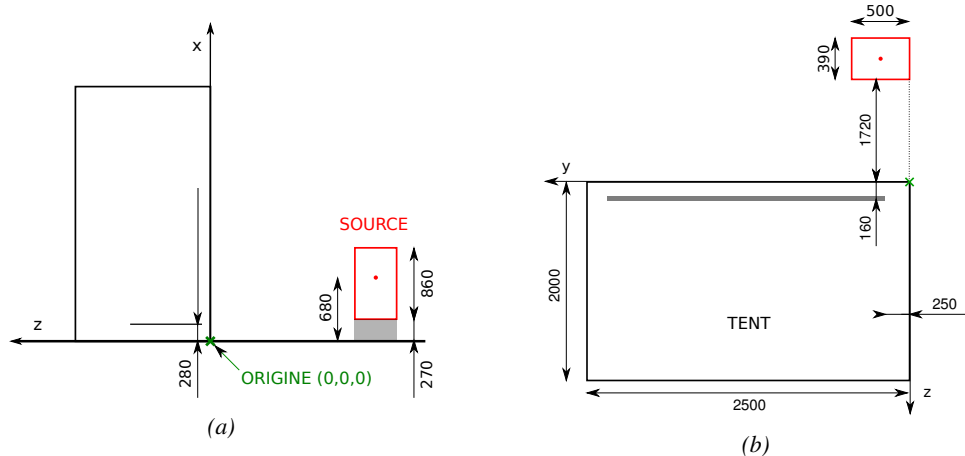


Figure 5.9: Description of the RPC setup. Dimensions are given in mm. A tent containing RPCs is placed at 1720 mm from the source container. The source is situated in the center of the container. RE-4-2-BARC-161 chamber is 160 mm inside the tent. This way, the distance between the source and the chambers plan is 2060 mm. Figure 5.9a provides a side view of the setup in the xz plane while Figure 5.9b shows a top view in the yz plane.



Figure 5.10: RE-4-2-BARC-I61 chamber is inside the tent as described in Figure 5.9. In the top right, the two scintillators used as trigger can be seen. This trigger system has an inclination of 10° relative to horizontal and is placed above half-partition B2 of the RPCs. PMT electronics are shielded thanks to lead blocks placed in order to protect them without stopping photons from going through the scintillators and the chamber.

2164 At the time of the tests, the beam not being operational anymore, a trigger composed of 2 plastic
2165 scintillators has been placed in front of the setup with an inclination of 10 deg with respect to the
2166 detector plane in order to look at cosmic muons. Using this particular trigger layout, shown on Fig-
2167 ure 5.10, leads to a cosmic muon hit distribution into the chamber similar to the one in Figure 5.11.
2168 Measured without gamma irradiation, two peaks can be seen on the profile of partition B, centered
2169 on strips 52 and 59. Section ?? will help us understand that these two peaks are due respectively to
2170 forward and backward coming cosmic particles where forward coming particles are first detected by
2171 the scintillators and then the RPC while the backward coming muons are first detected in the RPC.

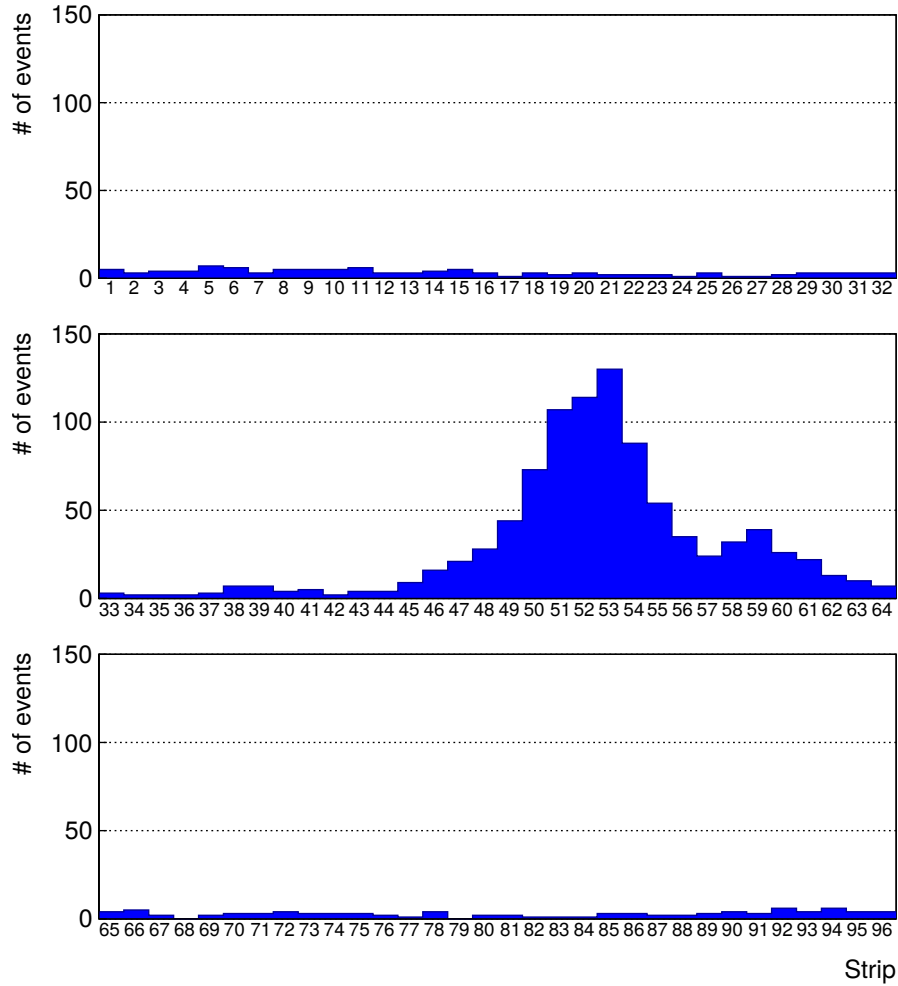


Figure 5.11: Hit distributions over all 3 partitions of RE-4-2-BARC-161 chamber is showed on these plots. Top, middle and bottom figures respectively correspond to partitions A, B, and C. These plots show that some events still occur in other half-partitions than B2, which corresponds to strips 49 to 64, in front of which the trigger is placed, contributing to the inefficiency of detection of cosmic muons. In the case of partitions A and C, the very low amount of data can be interpreted as noise. On the other hand, it is clear that a little portion of muons reach the half-partition B1, corresponding to strips 33 to 48.

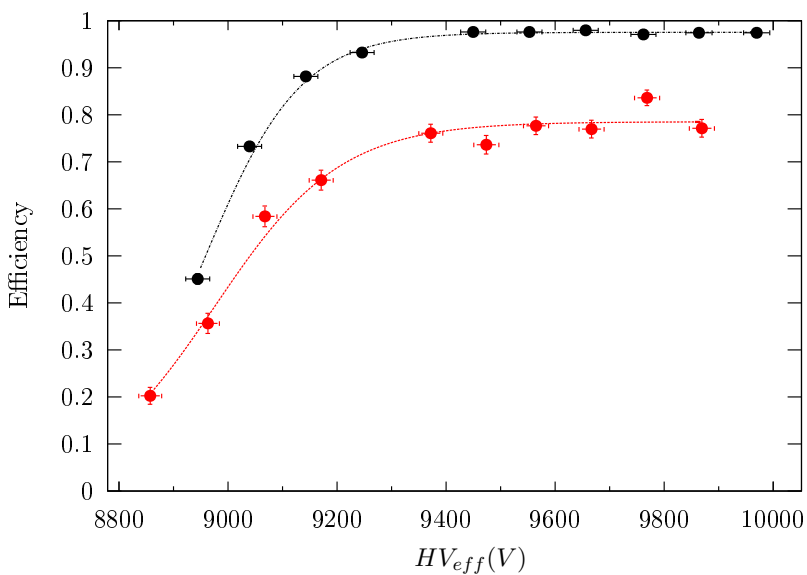
5.3.2 Data Acquisition

5.3.3 Geometrical acceptance of the setup layout to cosmic muons

In order to profit from a constant gamma irradiation, the detectors inside of the GIF bunker need to be placed in a plane orthogonal to the beam line. The muon beam that used to be available was meant to test the performance of detectors under test. This beam not being active anymore, another solution to test detector performance had to be used. Thus, it has been decided to use cosmic muons detected through a telescope composed of two scintillators. Lead blocks were used as shielding to

2179 protect the photomultipliers from gammas as can be seen from Figure 5.10.

2180 An inclination has been given to the cosmic telescope to maximize the muon flux. A good com-
 2181 promise had to be found between good enough muon flux and narrow enough hit distribution to
 2182 be sure to contain all the events into only one half partitions as required from the limited available
 2183 readout hardware. Nevertheless, a consequence of the misplaced trigger, that can be seen as a loss
 2184 of events in half-partition B1 in Figure 5.11, is an inefficiency. Nevertheless, the inefficiency of ap-
 2185 proximately 20 % highlighted in Figure 5.12 by comparing the performance of chamber BARC-161
 2186 in 904 and at GIF without irradiation seems too important to be explained only by the geometri-
 2187 cal acceptance of the setup itself. Simulations have been conducted to show how the setup brings
 2188 inefficiency.



2189 *Figure 5.12: Results are derived from data taken on half-partition B2 only. On the 18th of June 2014, data
 2190 has been taken on chamber RE-2-BARC-161 at building 904 (Prevessin Site) with cosmic muons providing us a
 2191 reference efficiency plateau of $(97.54 \pm 0.15)\%$ represented by a black curve. A similar measurement has been
 2192 done at GIF on the 21st of July with the same chamber giving a plateau of $(78.52 \pm 0.94)\%$ represented by a
 2193 red curve.*

2189 5.3.3.1 Description of the simulation layout

2190 The layout of GIF setup has been reproduced and incorporated into a Monte Carlo (MC) simulation
 2191 to study the influence of the disposition of the telescope on the final distribution measured by the
 2192 RPC. A 3D view of the simulated layout is given into Figure 5.13. Muons are generated randomly
 2193 in a horizontal plane located at a height corresponding to the lowest point of the PMTs. This way,
 2194 the needed size of the plane in order to simulate events happening at very big azimuthal angles (i.e.
 2195 $\theta \approx \pi$) can be kept relatively small. The muon flux is designed to follow the usual $\cos^2\theta$ distribution
 2196 for cosmic particle. The goal of the simulation is to look at muons that pass through the muon
 2197 telescope composed of the two scintillators and define their distribution onto the RPC plane. During
 2198 the reconstruction, the RPC plane is then divided into its strips and each muon track is assigned to a
 2199 strip.

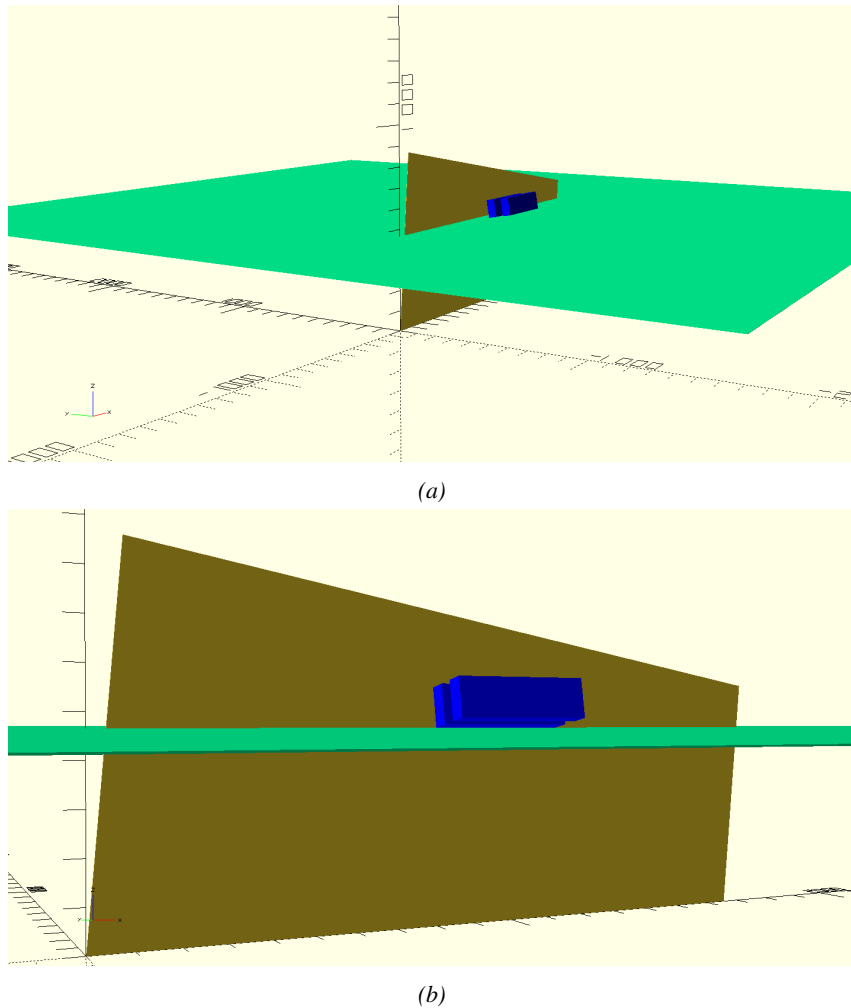


Figure 5.13: Representation of the layout used for the simulations of the test setup. The RPC is represented as a yellow trapezoid while the two scintillators as blue cuboids looking at the sky. A green plane corresponds to the muon generation plane within the simulation. Figure 5.9a shows a global view of the simulated setup. Figure 5.9b shows a zoomed view that allows to see the 2 scintillators as well as the full RPC plane.

2200 In order to further refine the quality of the simulation and understand deeper the results the
 2201 dependance of the distribution has been studied for a range of telescope inclinations. Moreover,
 2202 the threshold applied on the PMT signals has been included into the simulation in the form of a
 2203 cut. In the approximation of uniform scintillators, it has been considered that the threshold can be
 2204 understood as the minimum distance particles need to travel through the scintillating material to give
 2205 a strong enough signal. Particles that travel a distance smaller than the set "threshold" are thus not
 2206 detected by the telescope and cannot trigger the data taking. Finally, the FEE threshold also has
 2207 been considered in a similar way. The mean momentum of horizontal cosmic rays is higher than
 2208 those of vertical ones but the stopping power of matter for momenta ranging from 1 GeV to 1 TeV
 2209 stays comparable. It is then possible to assume that the mean number of primary e^- /ion pairs per
 2210 unit length will stay similar and thus, depending on the applied discriminator threshold, muons with

2211 the shortest path through the gas volume will deposit less charge and induce a smaller signal on the
 2212 pick-up strips that could eventually not be detected. These two thresholds also restrain the overall
 2213 geometrical acceptance of the system.

2214 **5.3.3.2 Simulation procedure**

2215 The simulation software has been designed using C++ and the output data is saved into ROOT
 2216 histograms. Simulations start for a threshold T_{scint} varying in a range from 0 to 45 mm in steps
 2217 of 5 mm, where $T_{scint} = 0$ mm corresponds to the case where there isn't any threshold apply on
 2218 the input signal while $T_{scint} = 45$ mm, which is the scintillator thickness, is the case where muons
 2219 cannot arrive orthogonally onto the scintillator surface. For a given T_{scint} , a set of RPC thresholds
 2220 are considered. The RPC threshold, T_{RPC} varies from 2 mm, the thickness of the gas volume, to
 2221 3 mm in steps of 0.25 mm. For each $(T_{scint}; T_{RPC})$ pair, $N_\mu = 10^8$ muons are randomly generated
 2222 inside the muon plane described in the previous paragraph with an azimuthal angle θ chosen to follow
 2223 a $\cos^2\theta$ distribution.

2224 Planes are associated to each surface of the scintillators. Knowing muon position into the muon
 2225 plane and its direction allows us, by assuming that muons travel in a straight line, to compute the
 2226 intersection of the muon track with these planes. Applying conditions to the limits of the surfaces
 2227 of the scintillator faces then gives us an answer to whether or not the muon passed through the
 2228 scintillators. In the case the muon has indeed passed through the telescope, the path through each
 2229 scintillator is computed and muons whose path was shorter than T_{scint} are rejected and are thus
 2230 considered as having not interacted with the setup.

2231 On the contrary, if the muon is labeled as good, its position within the RPC plane is computed
 2232 and the corresponding strip, determined by geometrical tests in the case the distance through the
 2233 gas volume was enough not to be rejected because of T_{RPC} , gets a hit and several histograms
 2234 are filled in order to keep track of the generation point on the muon plane, the intersection points
 2235 of the reconstructed muons within the telescope, or on the RPC plane, the path traveled through
 2236 each individual scintillator or the gas volume, as well as other histograms. Moreover, muons fill
 2237 different histograms whether they are forward or backward coming muons. They are discriminated
 2238 according to their direction components. When a muon is generated, an (x, y, z) position is assigned
 2239 into the muon plane as well as a $(\theta; \phi)$ pair that gives us the direction it's coming from. This way,
 2240 muons satisfying the condition $0 \leq \phi < \pi$ are designated as backward coming muons while muons
 2241 satisfying $\pi \leq \phi < 2\pi$ as forward coming muons.

2242 This simulation is then repeated for different telescope inclinations ranging in between 4 and 20°
 2243 and varying in steps of 2°. Due to this inclination and to the vertical position of the detector under
 2244 test, the muon distribution reconstructed in the detector plane is asymmetrical. The choice as been
 2245 made to chose a skew distribution formula to fit the data built as the multiplication of gaussian and
 2246 sigmoidal curves together. A typical gaussian formula is given as 5.1 and has three free parameters
 2247 as A_g , its amplitude, \bar{x} , its mean value and σ , its root mean square. Sigmoidal curves as given by
 2248 formula 5.2 are functions converging to 0 and A_s as x diverges. The inflection point is given as x_i
 2249 and λ is proportional to the slope at $x = x_i$. In the limit where $\lambda \rightarrow \infty$, the sigmoid becomes a
 2250 step function.

$$g(x) = A_g e^{-\frac{(x-\bar{x})^2}{2\sigma^2}} \quad (5.1)$$

$$s(x) = \frac{A_s}{1 + e^{-\lambda(x-x_i)}} \quad (5.2)$$

Finally, a possible representation of a skew distribution is given by formula 5.3 and is the product of 5.1 and 5.2. Naturally, here $A_{sk} = A_g \times A_s$ and represents the theoretical maximum in the limit where the skew tends to a gaussian function.

$$sk(x) = g(x) \times s(x) = A_{sk} \frac{e^{\frac{-(x-\bar{x})^2}{2\sigma^2}}}{1 + e^{-\lambda(x-x_i)}} \quad (5.3)$$

5.3.3.3 Results

Influence of T_{scint} on the muon distribution

Influence of T_{RPC} on the muon distribution

Influence of the telescope inclination on the muon distribution

Comparison to data taken at GIF without irradiation

5.3.4 Photon flux at GIF

5.3.4.1 Expectations from simulations

In order to understand and evaluate the γ flux in the GIF area, simulations had been conducted in 1999 and published by S. Agosteo et al [63]. Table 5.1 presented in this article gives us the γ flux for different distances D to the source. This simulation was done using GEANT and a Monte Carlo N-Particle (MCNP) transport code, and the flux F is given in number of γ per unit area and unit time along with the estimated error from these packages expressed in %.

Nominal ABS	Photon flux F [$s^{-1}cm^{-2}$]			
	at $D = 50$ cm	at $D = 155$ cm	at $D = 300$ cm	at $D = 400$ cm
1	$0.12 \cdot 10^8 \pm 0.2\%$	$0.14 \cdot 10^7 \pm 0.5\%$	$0.45 \cdot 10^6 \pm 0.5\%$	$0.28 \cdot 10^6 \pm 0.5\%$
2	$0.68 \cdot 10^7 \pm 0.3\%$	$0.80 \cdot 10^6 \pm 0.8\%$	$0.25 \cdot 10^6 \pm 0.8\%$	$0.16 \cdot 10^6 \pm 0.6\%$
5	$0.31 \cdot 10^7 \pm 0.4\%$	$0.36 \cdot 10^6 \pm 1.2\%$	$0.11 \cdot 10^6 \pm 1.2\%$	$0.70 \cdot 10^5 \pm 0.9\%$

Table 5.1: Total photon flux ($E\gamma \leq 662$ keV) with statistical error predicted considering a ^{137}Cs activity of 740 GBq at different values of the distance D to the source along the x -axis of irradiation field [63].

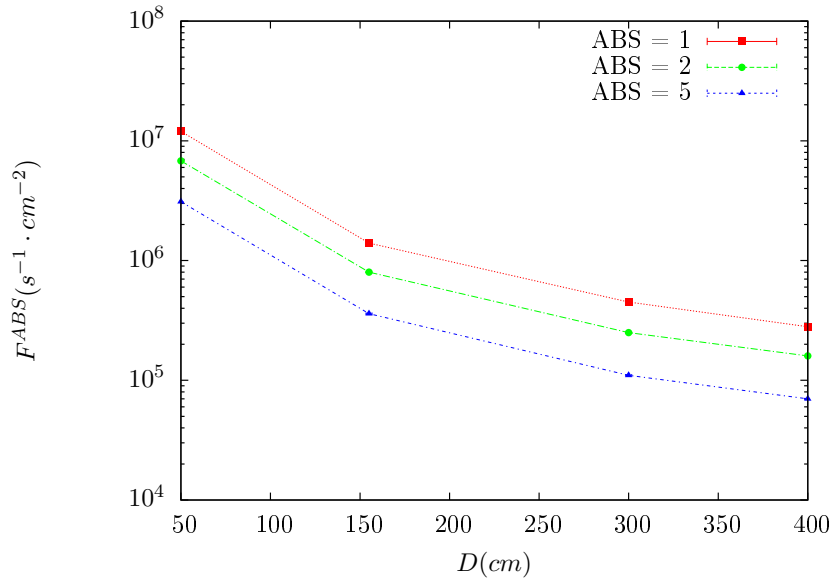


Figure 5.14: γ flux $F(D)$ is plot using values from table 5.1. As expected, the plot shows similar attenuation behaviours with increasing distance for each absorption factors.

The simulation doesn't directly provides us with an estimated flux at the level of our RPC. First of all, it is needed to extract the value of the flux from the available data contained in the original paper and then to estimate the flux in 2014 at the time the experimentation took place. Figure 5.14 that contains the data from Table 5.1. In the case of a pointlike source emitting isotropic and homogeneous gamma radiations, the gamma flux F at a distance D to the source with respect to a reference point situated at D_0 where a known flux F_0 is measured will be expressed like in Equation 5.4, assuming that the flux decreases as $1/D^2$, where c is a fitting factor.

$$F^{ABS} = F_0^{ABS} \times \left(\frac{cD_0}{D} \right)^2 \quad (5.4)$$

By rewriting Equation 5.4, it comes that :

$$c = \frac{D}{D_0} \sqrt{\frac{F^{ABS}}{F_0^{ABS}}} \quad (5.5)$$

$$\Delta c = \frac{c}{2} \left(\frac{\Delta F^{ABS}}{F^{ABS}} + \frac{\Delta F_0^{ABS}}{F_0^{ABS}} \right) \quad (5.6)$$

Finally, using Equation 5.5 and the data in Table 5.1 with $D_0 = 50$ cm as reference point, we can build Table 5.2. It is interesting to note that c for each value of D doesn't depend on the absorption factor.

Nominal ABS	Correction factor c		
	at $D = 155$ cm	at $D = 300$ cm	at $D = 400$ cm
1	$1.059 \pm 0.70\%$	$1.162 \pm 0.70\%$	$1.222 \pm 0.70\%$
2	$1.063 \pm 1.10\%$	$1.150 \pm 1.10\%$	$1.227 \pm 0.90\%$
5	$1.056 \pm 1.60\%$	$1.130 \pm 1.60\%$	$1.202 \pm 1.30\%$

Table 5.2: Correction factor c is computed thanks to formulae 5.5 taking as reference $D_0 = 50$ cm and the associated flux F_0^{ABS} for each absorption factor available in table 5.1.

2277 For the range of D/D_0 values available, it is possible to use a simple linear fit to get the evolution
 2278 of c . The linear fit will then use only 2 free parameters, a and b , as written in Equation 5.7. This gives
 2279 us the results showed in Figure 5.15. Figure 5.15b confirms that using only a linear fit to extract c is
 2280 enough as the evolution of the rate that can be obtained superimposes well on the simulation points.

$$c \left(\frac{D}{D_0} \right) = a \frac{D}{D_0} + b \quad (5.7)$$

$$F^{ABS} = F_0^{ABS} \left(a + \frac{bD_0}{D} \right)^2 \quad (5.8)$$

$$\Delta F^{ABS} = F^{ABS} \left[\frac{\Delta F_0^{ABS}}{F_0^{ABS}} + 2 \frac{\Delta a + \Delta b \frac{D_0}{D}}{a + \frac{bD_0}{D}} \right] \quad (5.9)$$

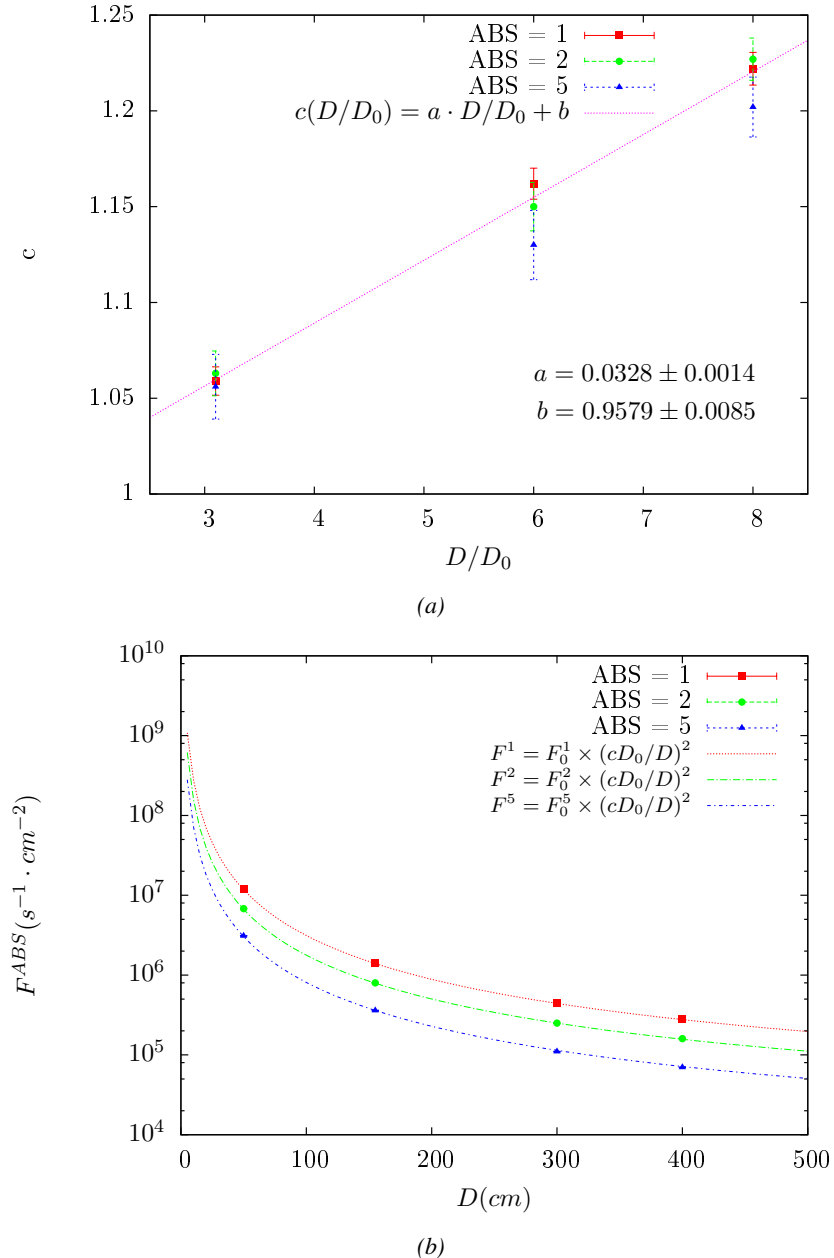


Figure 5.15: Figure 5.15a shows the linear approximation fit done via formulae 5.7 on data from table 5.2. Figure 5.15b shows a comparison of this model with the simulated flux using a and b given in figure 5.15a in formulae 5.4 and the reference value $D_0 = 50\text{cm}$ and the associated flux for each absorption factor F_0^{ABS} from table 5.1

In the case of the 2014 GIF tests, the RPC plane is located at a distance $D = 206\text{ cm}$ to the source. Moreover, to estimate the strength of the flux in 2014, it is necessary to consider the nuclear decay through time associated to the Cesium source whose half-life is well known ($t_{1/2} = (30.05 \pm 0.08)\text{ y}$). The very first source activity measurement has been done on the 5th of March 1997 while the GIF

2285 tests were done in between the 20th and the 31st of August 2014, i.e. at a time $t = (17.47 \pm 0.02)$ y
 2286 resulting in an attenuation of the activity from 740 GBq in 1997 to 494 GBq in 2014. All the needed
 2287 information to extrapolate the flux through our detector in 2014 has now been assembled, leading
 2288 to the Table 5.3. It is interesting to note that for a common RPC sensitivity to γ of $2 \cdot 10^{-3}$, the
 2289 order of magnitude of the estimated hit rate per unit area is of the order of the kHz for the fully
 2290 opened source. Moreover, taking profit of the two working absorbers, it will be possible to scan
 2291 background rates at 0 Hz, ~ 300 Hz as well as ~ 600 Hz. Without source, a good estimate of the
 2292 intrinsic performance will be available. Then at 300 Hz, the goal will be to show that the detectors
 2293 fulfill the performance certification of CMS RPCs. Then a first idea of the performance of the
 2294 detectors at higher background will be provided with absorption factors 2 (~ 600 Hz) and 1 (no
 2295 absorption). *[Here I will also put a reference to the plot showing the estimated background rate at
 2296 the level of RE3/1 in the case of HL-LHC but this one being in another chapter, I will do it later.]*

Nominal ABS	Photon flux F [$s^{-1}cm^{-2}$]			Hit rate/unit area [$Hz cm^{-2}$] at $D^{2014} = 206$ cm
	at $D_0^{1997} = 50$ cm	at $D^{1997} = 206$ cm	at $D^{2014} = 206$ cm	
1	$0.12 \cdot 10^8 \pm 0.2\%$	$0.84 \cdot 10^6 \pm 0.3\%$	$0.56 \cdot 10^6 \pm 0.3\%$	1129 ± 32
2	$0.68 \cdot 10^7 \pm 0.3\%$	$0.48 \cdot 10^6 \pm 0.3\%$	$0.32 \cdot 10^6 \pm 0.3\%$	640 ± 19
5	$0.31 \cdot 10^7 \pm 0.4\%$	$0.22 \cdot 10^6 \pm 0.3\%$	$0.15 \cdot 10^6 \pm 0.3\%$	292 ± 9

Table 5.3: The data at D_0 in 1997 is taken from [63]. In a second step, using Equations 5.8 and 5.9, the flux at D can be estimated in 1997. Then, taking into account the attenuation of the source activity, the flux at D can be estimated at the time of the tests in GIF in 2014. Finally, assuming a sensitivity of the RPC to γ $s = 2 \cdot 10^{-3}$, an estimation of the hit rate per unit area is obtained.

²²⁹⁷ **5.3.4.2 Dose measurements**

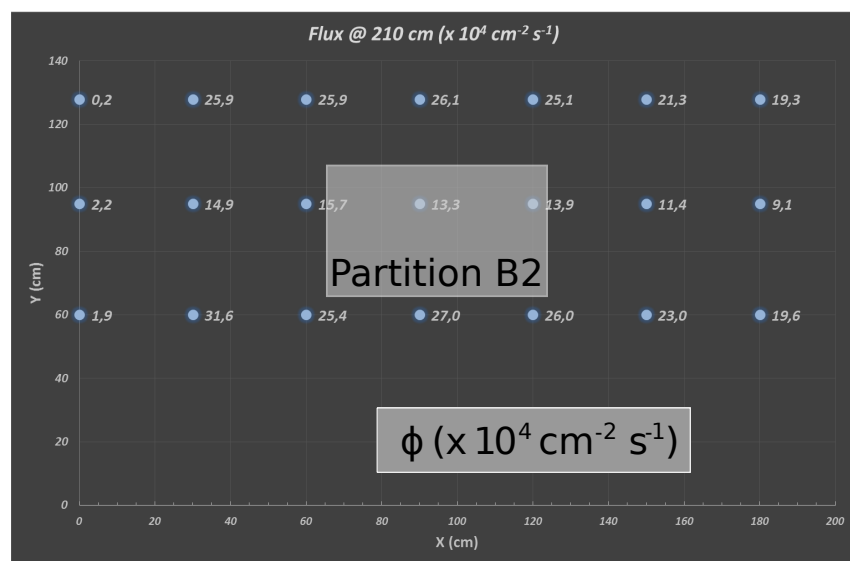


Figure 5.16: Dose measurements has been done in a plane corresponding to the tents front side. This plan is 1900 mm away from the source. As explained in the first chapter, a lens-shaped lead filter provides a uniform photon flux in the vertical plan orthogonal to the beam direction. If the second line of measured fluxes is not taken into account because of lower values due to experimental equipments in the way between the source and the tent, the uniformity of the flux is well showed by the results.

²²⁹⁸ **5.3.5 Results and discussions**

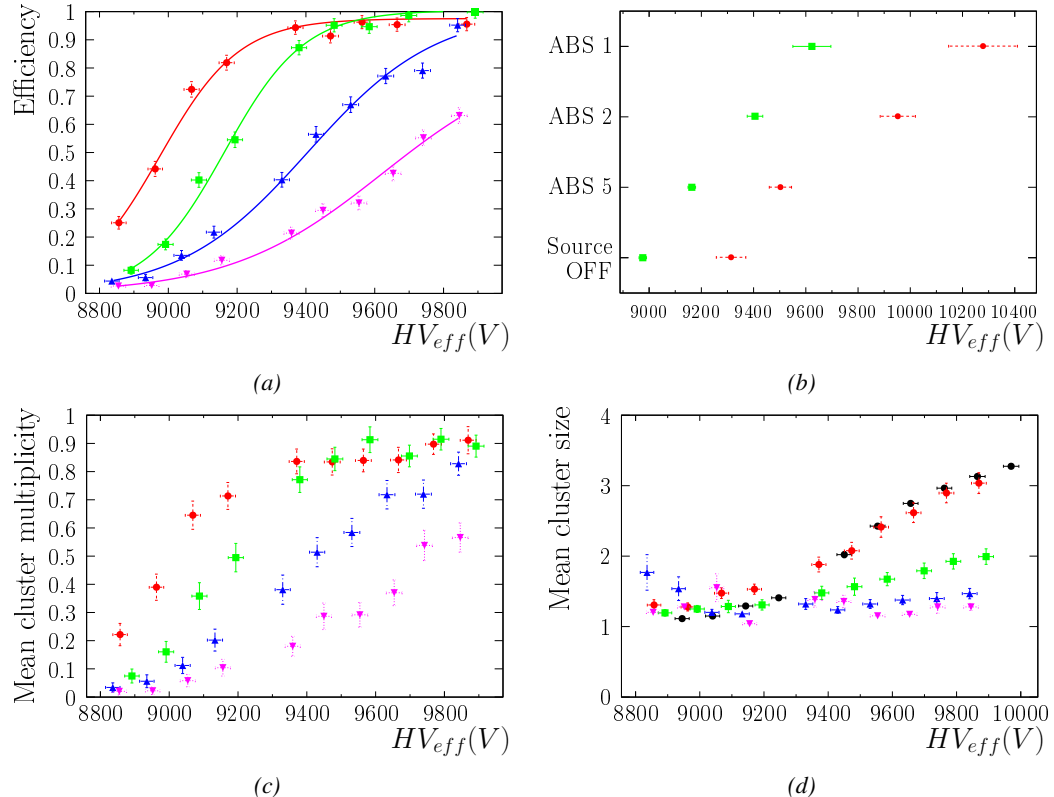


Figure 5.17

2299 5.4 Longevity tests at GIF++

2300 Longevity studies imply a monitoring of the performance of the detectors probed using a high inten-
2301 sity muon beam in a irradiated environment by periodically measuring their rate capability, the dark
2302 current running through them and the bulk resistivity of the Bakelite composing their electrodes.
2303 GIF++, with its very intense ^{137}Cs source, provides the perfect environment to perform such kind
2304 of tests. Assuming a maximum acceleration factor of 3, it is expected to accumulate the equivalent
2305 charge in 1.7 years.

2306 As the maximum background is found in the endcap, the choice naturally was made to focus the
2307 GIF++ longevity studies on endcap chambers. Most of the RPC system was installed in 2007. Nev-
2308 ertheless, the large chambers in the fourth endcap (RE4/2 and RE4/3) have been installed during
2309 LS1 in 2014. The Bakelite of these two different productions having different properties, four spare
2310 chambers of the present system were selected, two RE2,3/2 spares and two RE4/2 spares. Having
2311 two chambers of each type allows to always keep one of them non irradiated as reference, the per-
2312 formance evolution of the irradiated chamber being then compared through time to the performance
2313 of the non irradiated one.

2314 The performance of the detectors under different level of irradiation is measured periodically dur-
2315 ing dedicated test beam periods using the H4 muon beam. In between these test beam periods, the
2316 two RE2,3/2 and RE4/2 chambers selected for this study are irradiated by the ^{137}Cs source in order
2317 to accumulate charge and the gamma background is monitored, as well as the currents. The two
2318 remaining chambers are kept non-irradiated as reference detectors. Due to the limited gas flow in
2319 GIF++, the RE4 chamber remained non-irradiated until end of November 2016 where a new mass
2320 flow controller has been installed allowing for bigger volumes of gas to flow in the system.

2321 Figures 5.18 and 5.19 give us for different test beam periods, and thus for increasing integrated
2322 charge through time, a comparison of the maximum efficiency, obtained using a sigmoid-like func-
2323 tion, and of the working point of both irradiated and non irradiated chambers [52]. No aging is yet
2324 to see from this data, the shifts in γ rate per unit area in between irradiated and non irradiated detec-
2325 tors and RE2 and RE4 types being easily explained by a difference of sensitivity due to the various
2326 Bakelite resistivities of the HPL electrodes used for the electrode production.

2327 Collecting performance data at each test beam period allows us to extrapolate the maximum effi-
2328 ciency for a background hit rate of 300 Hz/cm² corresponding to the expected HL-LHC conditions.
2329 Aging effects could emerge from a loss of efficiency with increasing integrated charge over time,
2330 thus Figure 5.20 helps us understand such degradation of the performance of irradiated detectors in
2331 comparison with non irradiated ones. The final answer for an eventual loss of efficiency is given in
2332 Figure 5.21 by comparing for both irradiated and non irradiated detectors the efficiency sigmoids
2333 before and after the longevity study. Moreover, to complete the performance information, the Bake-
2334 lite resistivity is regularly measured thanks to Ag scans (Figure 5.22) and the noise rate is monitored
2335 weekly during irradiation periods (Figure 5.23). At the end of 2016, no signs of aging were observed
2336 and further investigation is needed to get closer to the final integrated charge requirements proposed
2337 for the longevity study of the present CMS RPC sub-system.

2338

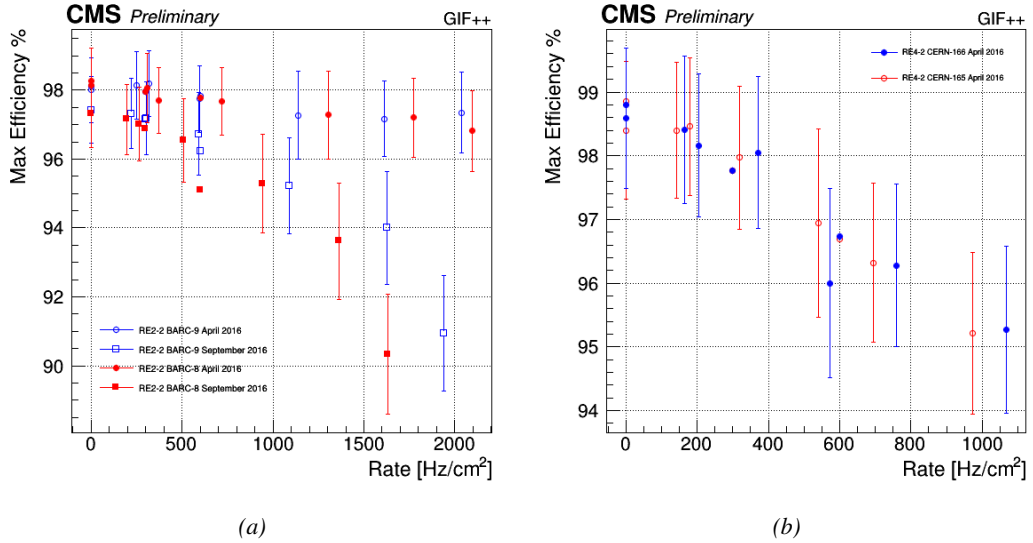


Figure 5.18: Evolution of the maximum efficiency for RE2 (5.18a) and RE4 (5.18b) chambers with increasing extrapolated γ rate per unit area at working point. Both irradiated (blue) and non irradiated (red) chambers are shown.

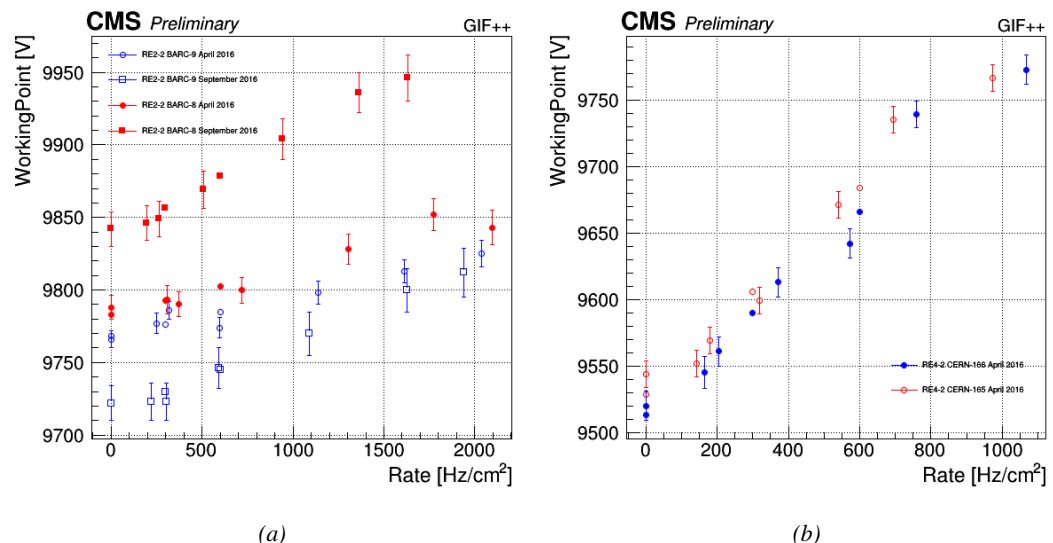


Figure 5.19: Evolution of the working point for RE2 (5.19a) and RE4 (5.19b) with increasing extrapolated γ rate per unit area at working point. Both irradiated (blue) and non irradiated (red) chambers are shown.

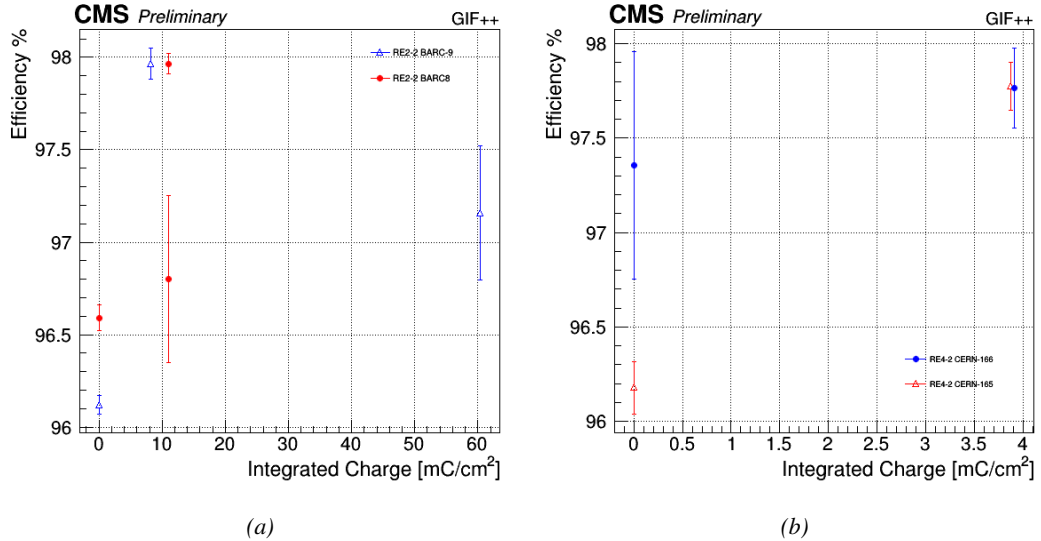


Figure 5.20: Evolution of the maximum efficiency at HL-LHC conditions, i.e. a background hit rate per unit area of 300 Hz/cm², with increasing integrated charge for RE2 (5.20a) and RE4 (5.20b) detectors. Both irradiated (blue) and non irradiated (red) chambers are shown. The integrated charge for non irradiated detectors is recorded during test beam periods and stays small with respect to the charge accumulated in irradiated chambers.

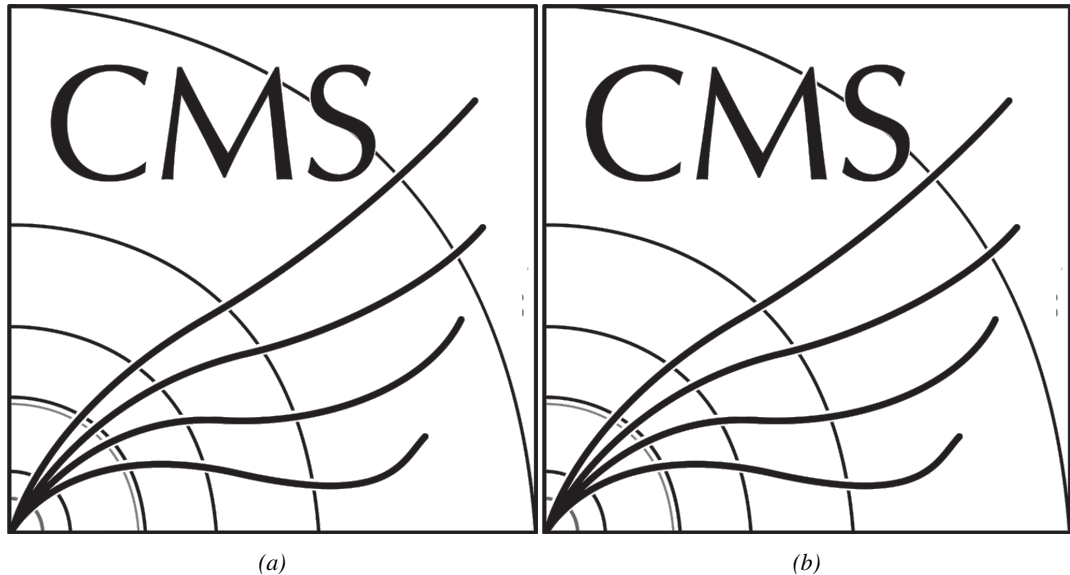


Figure 5.21: Comparison of the efficiency sigmoid before (triangles) and after (circles) irradiation for RE2 (5.21a) and RE4 (5.21b) detectors. Both irradiated (blue) and non irradiated (red) chambers are shown.

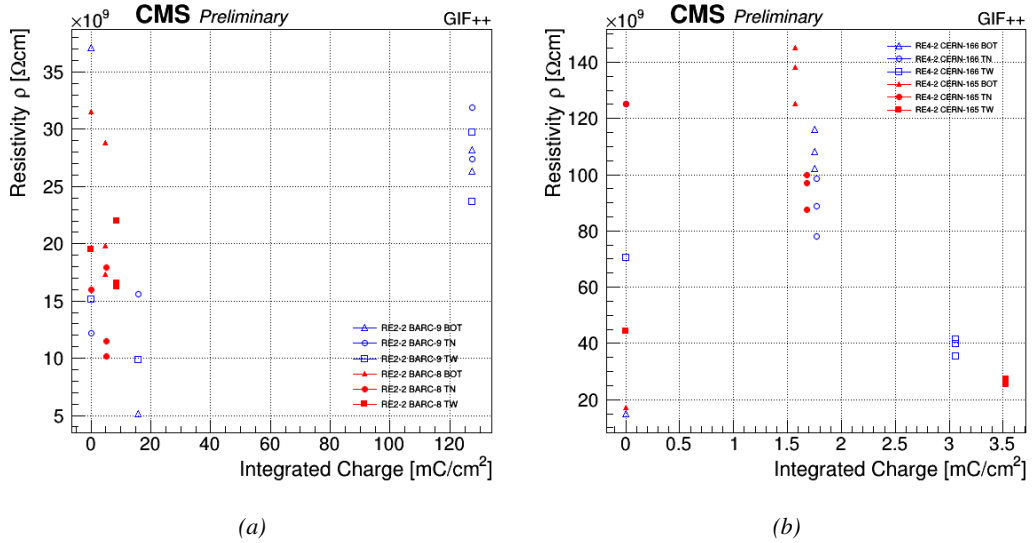


Figure 5.22: Evolution of the Bakelite resistivity for RE2 (5.22a) and RE4 (5.22b) detectors. Both irradiated (blue) and non-irradiated (red) chambers are shown.

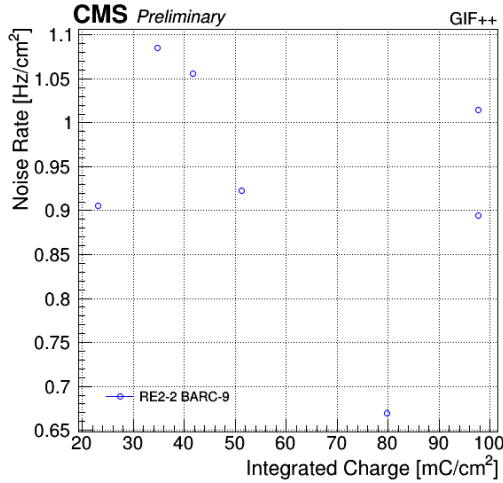


Figure 5.23: Evolution of the noise rate per unit area for the irradiated chamber RE2-2-BARC-9 only.

5.4.1 Description of the Data Acquisition

For the longevity studies, four spare chambers of the present system are used. Two spare RPCs of the RE2,3 stations as well as two spare RPCs from the new RE4 stations have been mounted in a Trolley. Six RE4 gaps are also placed in the trolley. The trolley is placed inside the GIFT++ in the upstream region of the bunker, taking the cesium source as a reference. The trolley is oriented for the detection surface of the chambers to be orthogonal to the beam line. The system can be moved along the orthogonal plane in order to have the beam in all η -partitions. For the aging the trolley is

2346 moved outside the beam line and is placed in a distance of 5.2 m to the source, which irradiates the
 2347 bunker using an attenuation filter of 2.2 which corresponds to a fluence of 10^7 gamma/cm^2 .

2348 During GIF++ operation, the data collected can be divided into different categories as several
 2349 parameters are monitored in addition to the usual RPC performance data. On one hand, to know
 2350 the performance of a chamber, it is need to measure its efficiency and to know the background
 2351 conditions in which it is operated. To do this, the hit signals from the chamber are recorded and
 2352 stored in a ROOT file via a Data Acquisition (DAQ) software. On the other hand, it is also very
 2353 important to monitor parameters such as environmental pressure and temperature, gas temperature
 2354 and humidity, RPC HV, LV, and currents, or even source and beam status. This is done through the
 2355 GIF++ web Detector Control Software (DCS) that stores this information in a database.

2356 Two different types of tests are conducted on RPCs via the DAQ. Indeed, the performance of the
 2357 detectors is measured periodically during dedicated test beam periods using the H4 muon beam. In
 2358 between these test beam periods, when the beam is not available, the chambers are irradiated by the
 2359 ^{137}Cs in order to accumulate deposited charge and the gamma background is measured.

2360 RPCs under test are connected through LVDS cables to V1190A Time-to-Digital Converter
 2361 (TDC) modules manufactured by CAEN. These modules, located in the rack area outside of the
 2362 bunker, get the logic signals sent by the chambers and save them into their buffers. Due to the
 2363 limited size of the buffers, the collected data is regularly erased and replaced. A trigger signal is
 2364 needed for the TDC modules to send the useful data to the DAQ computer via a V1718 CAEN USB
 2365 communication module.

2366 In the case of performance test, the trigger signal used for data acquisition is generated by the
 2367 coincidence of three scintillators. A first one is placed upstream outside of the bunker, a second one
 2368 is placed downstream outside of the bunker, while a third one is placed in front of the trolley, close by
 2369 the chambers. Every time a trigger is sent to the TDCs, i.e. every time a muon is detected, knowing
 2370 the time delay in between the trigger and the RPC signals, signals located in the right time window
 2371 are extracted from the buffers and saved for later analysis. Signals are taken in a time window of
 2372 400 ns centered on the muon peak (here we could show a time spectrum). On the other hand, in the
 2373 case of background rate measurement, the trigger signal needs to be "random" not to measure muons
 2374 but to look at gamma background. A trigger pulse is continuously generated at a rate of 300 Hz using
 2375 a dual timer. To integrate an as great as possible time, all signals contained within a time window of
 2376 10us prior to the random trigger signal are extracted form the buffers and saved for further analysis
 2377 (here another time spectrum to illustrate could be useful, maybe even place both spectrum together
 2378 as a single Figure).

2379 The signals sent to the TDCs correspond to hit collections in the RPCs. When a particle hits
 2380 a RPC, it induce a signal in the pickup strips of the RPC readout. If this signal is higher than the
 2381 detection threshold, a LVDS signal is sent to the TDCs. The data is then organised into 4 branches
 2382 keeping track of the event number, the hit multiplicity for the whole setup, and the time and channel
 2383 profile of the hits in the TDCs.

2384 **5.4.2 RPC current, environmental and operation parameter monitoring**

2385 In order to take into account the variation of pressure and temperature between different data taking
 2386 periods the applied voltage is corrected following the relationship :

$$2387 \quad HV_{eff} = HV_{app} \times \left(0.2 + 0.8 \cdot \frac{P_0}{P} \times \frac{T}{T_0} \right) \quad (5.10)$$

2387 where T_0 (=293 K) and P_0 (=990 mbar) are the reference values.

2388 **5.4.3 Measurement procedure**

2389 Insert a short description of the online tools (DAQ, DCS, DQM).

2390 Insert a short description of the offline tools : tracking and efficiency algorithm.

2391 Identify long term aging effects we are monitoring the rates per strip.

2392 **5.4.4 Longevity studies results**

6

2393

2394

Investigation on high rate RPCs

2395 **6.1 Rate limitations and ageing of RPCs**

2396 **6.1.1 Low resistivity electrodes**

2397 **6.1.2 Low noise front-end electronics**

2398 **6.2 Construction of prototypes**

2399 **6.3 Results and discussions**

7

2400

2401

Conclusions and outlooks

2402 **7.1 Conclusions**

2403 **7.2 Outlooks**

A

2404

2405

A data acquisition software for CAEN VME TDCs

2406

2407 Certifying detectors in the perspective of HL-LHC required to develop tools for the GIF++ expe-
2408 riment. Among them was the C++ Data Acquisition (DAQ) software that allows to make the com-
2409 munications in between a computer and TDC modules in order to retrieve the RPC data [65]. In this
2410 appendix, details about this software, as of how the software was written, how it functions and how
2411 it can be exported to another similar setup, will be given.

2412 A.1 GIF++ DAQ file tree

2413 GIF++ DAQ source code is fully available on github at [https://github.com/afagot/GIF_](https://github.com/afagot/GIF_DAQ)
2414 DAQ. The software requires 3 non-optional dependencies:

- 2415 • CAEN USB Driver, to mount the VME hardware,
2416 • CAEN VME Library, to communicate with the VME hardware, and
2417 • ROOT, to organize the collected data into a TTree.

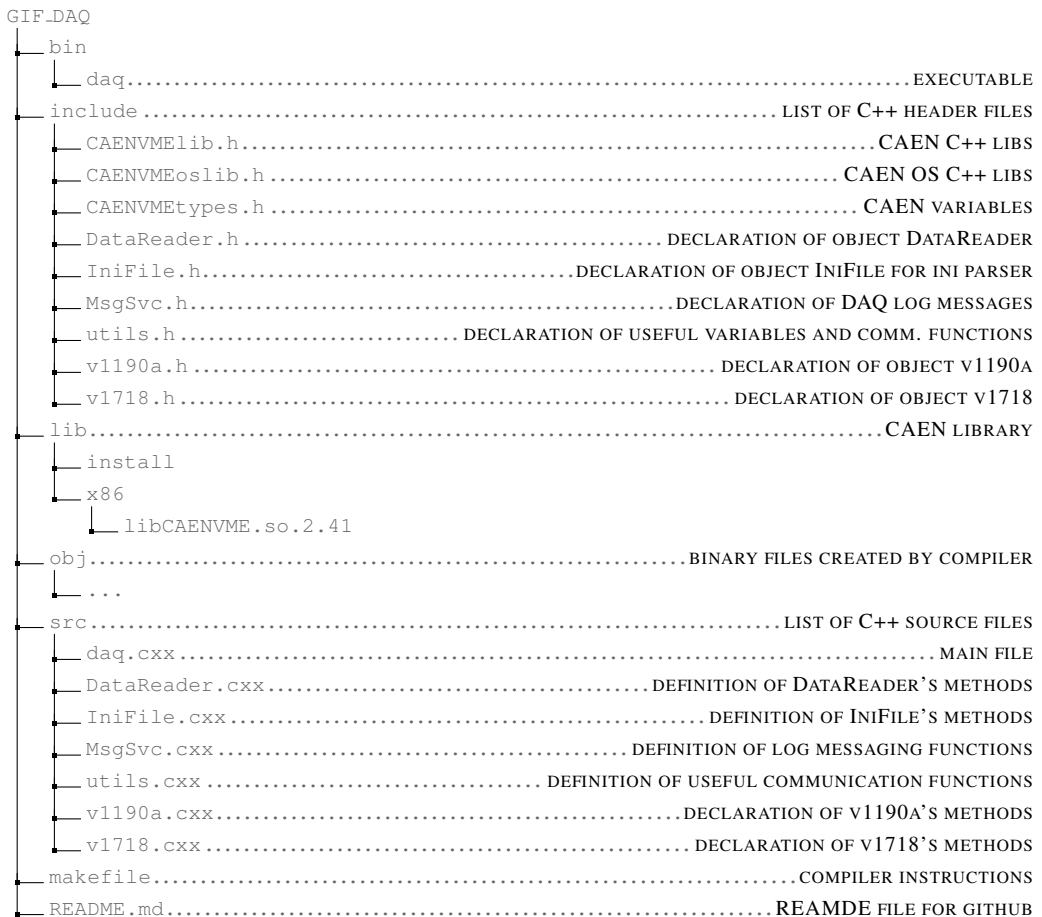
2418 The CAEN VME library will not be packaged by distributions and will need to be installed man-
2419 ually. To compile the GIF++ DAQ project via a terminal, from the DAQ folder use the command:

2420

```
2421     make
```

2422 The source code tree is provided below along with comments to give an overview of the files' con-
2423 tent. The different objects created for this project (`v1718`, `v1190a`, `IniFile` & `DataReader`) will be
2424 described in details in the following sections.

2425



2426 A.2 Usage of the DAQ

2427 GIF++ DAQ, as used in GIF++, is not a standalone software. Indeed, the system being more com-
 2428 plex, the DAQ only is a sub-layer of the software architecture developed to control and monitor
 2429 the RPCs that are placed into the bunker for performance study in an irradiated environment. The top
 2430 layer of GIF++ is a Web Detector Control System (webDCS) application. The DAQ is only called
 2431 by the webDCS when data needs to be acquired. The webDCS operates the DAQ through command
 2432 line. To start the DAQ, the webDCS calls:

2433

2434 bin/daq /path/to/the/log/file/in/the/output/data/folder

2435 where /path/to/the/log/file/in/the/output/data/folder is the only argument required. This
 2436 log file is important for the webDCS as this file contains all the content of the communication of the
 2437 webDCS and the different systems monitored by the webDCS. Its content is constantly displayed
 2438 during data taking for the users to be able to follow the operations. The communication messages
 2439 are normally sent to the webDCS log file via the functions declared in file `MsgSvc.h`, typically
 2440 `MSG_INFO(string message)`.

2441

2442 A.3 Description of the readout setup

2443 The CMS RPC setup at GIF++ counts 5 V1190A Time-to-Digital Converter (TDC) manufactured
 2444 by CAEN [66]. V1190A are VME units accepting 128 independent Multi-Hit/Multi-Event TDC
 2445 channels whose signals are treated by 4 100 ps high performance TDC chips developed by CERN
 2446 / ECP-MIC Division. The communication between the computer and the TDCs to transfer data is
 2447 done via a V1718 VME master module also manufactured by CAEN and operated from a USB
 2448 port [67]. These VME modules are all hosted into a 6U VME 6021 powered crate manufactured by
 2449 W-Ie-Ne-R than can accommodate up to 21 VME bus cards [68]. These 3 components of the DAQ
 2450 setup are shown in Figure A.1.

2451

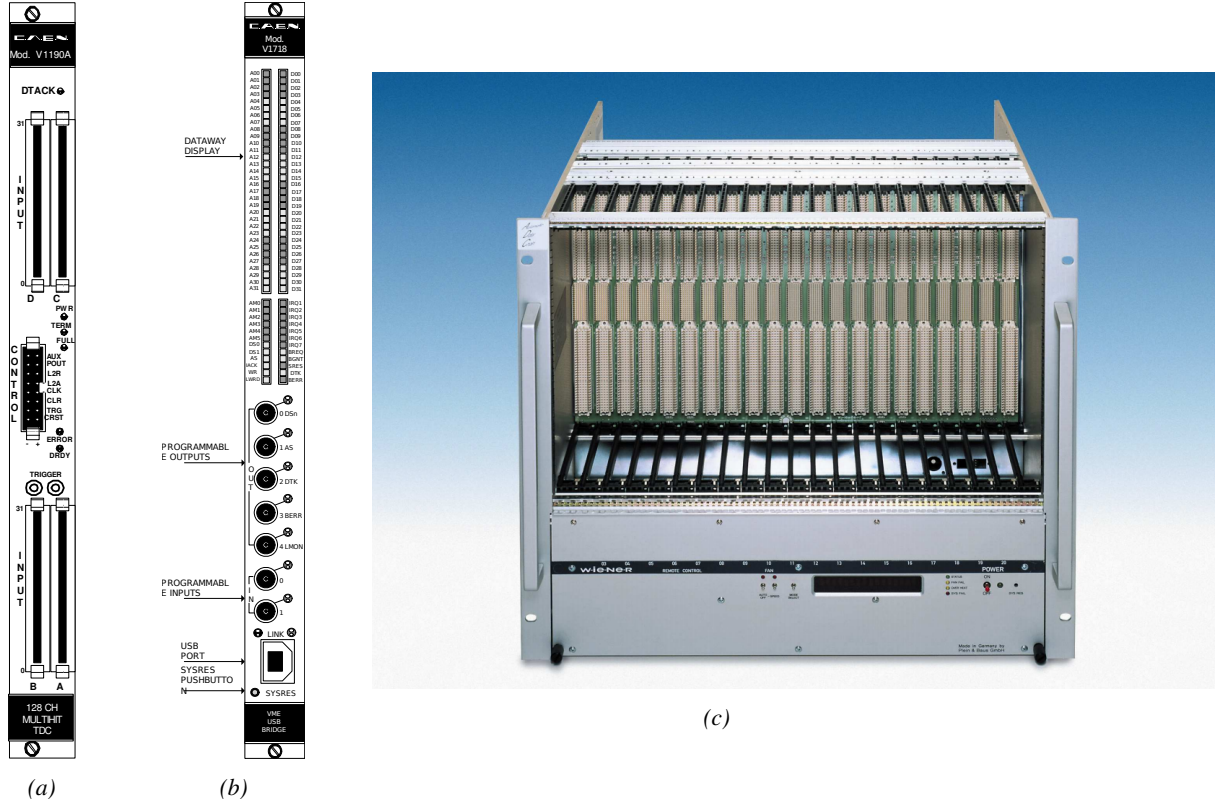


Figure A.1: (A.1a) View of the front panel of a V1190A TDC module [66]. (A.1b) View of the front panel of a V1718 Bridge module [67]. (A.1c) View of the front panel of a 6U 6021 VME crate [68].

2452

A.4 Data read-out

2453 To efficiently perform a data readout algorithm, C++ objects to handle the VME modules (TDCs
 2454 and VME bridge) have been created along with objects to store data and read the configuration file

2455 that comes as an input of the DAQ software.

2456

2457 A.4.1 V1190A TDCs

2458 The DAQ used at GIF takes profit of the *Trigger Matching Mode* offered by V1190A modules.
 2459 This setting is enabled through the method `v1190a::SetTrigMatching (int ntdcs)` where `ntdcs`
 2460 is the total number of TDCs in the setup this setting needs to be enabled for (Source Code A.1). A
 2461 trigger matching is performed in between a trigger time tag, a trigger signal sent into the TRIGGER
 2462 input of the TDC visible on Figure A.1a, and the channel time measurements, signals recorded from
 2463 the detectors under test in our case. Control over this data acquisition mode, explained through
 2464 Figure A.2, is offered via 4 programmable parameters:

- 2465 • **match window:** the matching between a trigger and a hit is done within a programmable time
 2466 window. This is set via the method

2467 `void v1190a::SetTrigWindowWidth(Uint windowHeight, int ntdcs)`

- 2468 • **window offset:** temporal distance between the trigger tag and the start of the trigger matching
 2469 window. This is set via the method

2470 `void v1190a::SetTrigWindowWidth(Uint windowHeight, int ntdcs)`

- 2471 • **extra search margin:** an extended time window is used to ensure that all matching hits are
 2472 found. This is set via the method

2473 `void v1190a::SetTrigSearchMargin(Uint searchMargin, int ntdcs)`

- 2474 • **reject margin:** older hits are automatically rejected to prevent buffer overflows and to speed
 2475 up the search time. This is set via the method

2476 `void v1190a::SetTrigRejectionMargin(Uint rejectMargin, int ntdcs)`

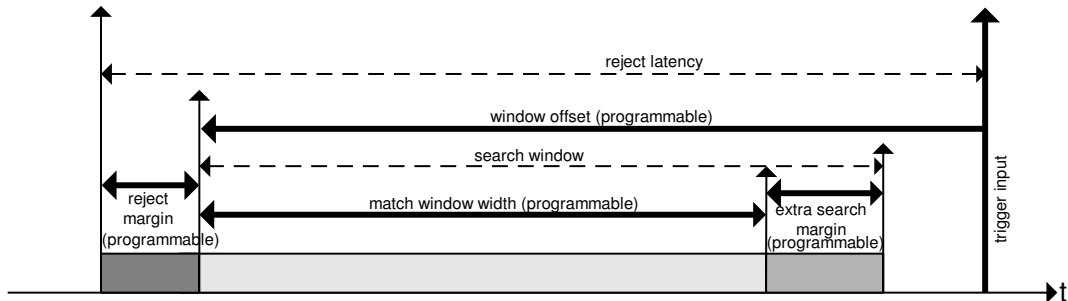


Figure A.2: Module V1190A Trigger Matching Mode timing diagram [66].

2477 Each of these 4 parameters are given in number of clocks, 1 clock being 25 ns long. It is easy to
 2478 understand at this level that there are 3 possible functioning settings:

- 2479 • **1:** the match window is entirely contained after the trigger signal,

- 2480 • **2:** the match window overlaps the trigger signal, or

- 2481 • **3:** the match window is entirely contained before the trigger signal as displayed on Figure A.2.

2482 In both the first and second cases, the sum of the window width and of the offset can be set to
2483 a maximum of 40 clocks, which corresponds to 1 μ s. Evidently, the offset can be negative, allowing
2484 for a longer match window, with the constraint of having the window ending at most 1 μ s after the
2485 trigger signal. In the third case, the maximum negative offset allowed is of 2048 clocks (12 bit) cor-
2486 responding to 51.2 μ s, the match window being strictly smaller than the offset. In the case of GIF++,
2487 the choice has been made to use this last setting by delaying the trigger signal. During the studies
2488 performed in GIF++, both the efficiency of the RPCs, probed using a muon beam, and the noise or
2489 gamma background rate are monitored. The extra search and reject margins are left unused.
2490 To probe the efficiency of RPC detectors, the trigger time tag is provided by the coïncidence of
2491 scintillators when a bunch of muons passes through GIF++ area is used to trigger the data acquisi-
2492 tion. For this measurement, it is useful to reduce the match window width only to contain the muon
2493 information. Indeed, the delay in between a trigger signal and the detection of the corresponding
2494 muon in the RPC being very contant (typically a few tens of ns due to jitter and cable length), the
2495 muon signals are very localised in time. Thus, due to a delay of approximalety 325 ns in between
2496 the muons and the trigger, the settings where chosen to have a window width of 24 clocks (600 ns)
2497 centered on the muon peak thanks to a negative offset of 29 clocks (725 ns).
2498 On the otherhand, monitoring the rates don't require for the DAQ to look at a specific time window.
2499 It is important to integrate enough time to have a robust measurement of the rate as the number of
2500 hits per time unit. The triggerring signal is provided by a pulse generator at a frequency of 300 Hz
2501 to ensure that the data taking occurs in a random way, with respect to beam physics, to probe only
2502 the irradiation spectrum on the detectors. The match window is set to 400 clocks (10 μ s) and the
2503 negative offset to 401 clocks as it needs to exceed the value of the match window.

```

2504
class v1190a
{
    private :
        long             Handle;
        vector<Data32>   Address;
        CVDataWidth      DataWidth;
        CVAddressModifier AddressModifier;

    public:

        v1190a(long handle, IniFile *inifile, int ntdcs);
        ~v1190a();
        Data16 write_op_reg(Data32 address, int code, string error);
        Data16 read_op_reg(Data32 address, string error);
        void Reset(int ntdcs);
        void Clear(int ntdcs);
        void TestWR(Data16 value,int ntdcs);
        void CheckTDCStatus(int ntdcs);
        void CheckCommunication(int ntdcs);
        void SetTDCTestMode(Data16 mode,int ntdcs);
        void SetTrigMatching(int ntdcs);
        void SetTrigTimeSubtraction(Data16 mode,int ntdcs);
        void SetTrigWindowWidth(Uint windowHeight,int ntdcs);
        void SetTrigWindowOffset(Uint windowOffset,int ntdcs);
        void SetTrigSearchMargin(Uint searchMargin,int ntdcs);
        void SetTrigRejectionMargin(Uint rejectMargin,int ntdcs);
        void GetTrigConfiguration(int ntdcs);
        void SetTrigConfiguration(IniFile *inifile,int ntdcs);
        void SetTDCDetectionMode(Data16 mode,int ntdcs);
        void SetTDCResolution(Data16 lsb,int ntdcs);
        void SetTDCDeadTime(Data16 time,int ntdcs);
        void SetTDCHeadTrailer(Data16 mode,int ntdcs);
        void SetTDCEventSize(Data16 size,int ntdcs);
        void SwitchChannels(IniFile *inifile,int ntdcs);
        void SetIRQ(Data32 level, Data32 count,int ntdcs);
        void SetBlockTransferMode(Data16 mode,int ntdcs);
        void Set(IniFile *inifile,int ntdcs);
        void CheckStatus(CVErrorCodes status) const;
        int ReadBlockD32(Uint tdc, const Data16 address,
                         Data32 *data, const Uint words, bool ignore_berr);
        Uint Read(RAWData *DataList,int ntdcs);
};

2505

```

2506 *Source Code A.1: Description of C++ object v1190a.*

2507 The v1190a object, defined in the DAQ software as in Source Code A.1, offers the possibility to
 2508 concatenate all TDCs in the readout setup into a single object containing a list of hardware addresses
 2509 (addresses to access the TDCs' buffer through the VME crate) and each constructor and method acts
 2510 on the list of TDCs.

2511

2512 A.4.2 DataReader

2513 Enabled thanks to v1190a::SetBlockTransferMode(Data16 mode, int ntdcs), the data transfer
 2514 is done via Block Transfer (BLT). Using BLT allows to tranfer a fixed number of events called a
 2515 *block*. This is used together with an Almost Full Level (AFL) of the TDCs' output buffers, defined

2516 through `v1190a::SetIRQ(Data32 level, Data32 count, int ntdcs)`. This AFL gives the maxi-
 2517 mum amount of 32735 words (16 bits, corresponding to the depth of a TDC output buffer) that can
 2518 write in a buffer before an Interrupt Request (IRQ) is generated and seen by the VME Bridge,
 2519 stopping the data acquisition to transfer the content of each TDC buffers before resuming. For each
 2520 trigger, 6 words or more are written into the TDC buffer:

- 2521 • a **global header** providing information of the event number since the beginning of the data
 acquisition,
- 2523 • a **TDC header**,
- 2524 • the **TDC data** (*if any*), 1 for each hit recorded during the event, providing the channel and the
 time stamp associated to the hit,
- 2526 • a **TDC error** providing error flags,
- 2527 • a **TDC trailer**,
- 2528 • a **global trigger time tag** that provides the absolute trigger time relatively to the last reset,
 and
- 2530 • a **global trailer** providing the total word count in the event.

2531 As previously described in Section ??, CMS RPC FEEs provide us with 100 ns long LVDS out-
 2532 put signals that are injected into the TDCs' input. Any avalanche signal that gives a signal above the
 2533 FEEs threshold is thus recorded by the TDCs as a hit within the match window. Each hit is assigned
 2534 to a specific TDC channel with a time stamp, with a precision of 100 ps. The reference time, $t_0 = 0$,
 2535 is provided by the beginning of the match window. Thus for each trigger, coming from a scintillator
 2536 coïncidence or the pulse generator, a list of hits is stored into the TDCs' buffers and will then be
 2537 transferred into a ROOT Tree.

2538 When the BLT is used, it is easy to understand that the maximum number of words that have
 2539 been set as ALF will not be a finite number of events or, at least, the number of events that would
 2540 be recorded into the TDC buffers will not be a multiple of the block size. In the last BLT cycle to
 2541 tranfer data, the number of events to transfer will most probably be lower than the block size. In that
 2542 case, the TDC can add fillers at the end of the block but this option requires to send more data to the
 2543 computer and is thus a little slower. Another solution is to finish the transfer after the last event by
 2544 sending a bus error that states that the BLT reached the last event in the pile. This method has been
 2545 chosen in GIF++.

2547 Due to irradiation, an event in GIF++ can count up to 300 words per TDC. A limit of 4096 words
 2548 (12 bits) has been set to generate IRQ which represent from 14 to almost 700 events depending on
 2549 the average of hits collected per event. Then the block size has been set to 100 events with enabled
 2550 bus errors. When an AFL is reached for one of the TDCs, the VME bridge stops the acquisition by
 2552 sending a BUSY signal.

2553

```

2554     The data is then transferred one TDC at a time into a structure called RAWData (Source Code A.2).
2555
2556 struct RAWData{
2557     vector<int>           *EventList;
2558     vector<int>           *NHitsList;
2559     vector<int>           *QFlagList;
2560     vector<vector<int>> >   *Channellist;
2561     vector<vector<float>> > *TimeStampList;
2562 };

```

2557 *Source Code A.2: Description of data holding C++ structure `RAWData`.*

2558 In order to organize the data transfer and the data storage, an object called `DataReader` was
2559 created (Source Code A.3). On one hand, it has `v1718` and `v1190a` objects as private members for
2560 communication purposes, such as VME modules settings via the configuration file `*iniFile` or data
2561 read-out through `v1190a::Read()` and on the other hand, it contains the structure `RAWData` that allows
2562 to organise the data in vectors reproducing the tree structure of a ROOT file.

```

2563
2564 class DataReader
2565 {
2566     private:
2567     bool      StopFlag;
2568     IniFile  *iniFile;
2569     Data32    MaxTriggers;
2570     v1718    *VME;
2571     int       nTDCs;
2572     v1190a   *TDCs;
2573     RAWData  TDCData;
2574
2575     public:
2576     DataReader();
2577     virtual ~DataReader();
2578     void      SetIniFile(string inifilename);
2579     void      SetMaxTriggers();
2580     Data32    GetMaxTriggers();
2581     void      SetVME();
2582     void      SetTDC();
2583     int       GetQFlag(Uint it);
2584     void      Init(string inifilename);
2585     void      FlushBuffer();
2586     void      Update();
2587     string   GetFileName();
2588     void      WriteRunRegistry(string filename);
2589     void      Run();
2590 };

```

2565 *Source Code A.3: Description of C++ object `DataReader`.*

2566 Each event is transferred from `TDCData` and saved into branches of a ROOT `TTree` as 3 integers
2567 that represent the event ID (`EventCount`), the number of hits read from the TDCs (`nHits`), and the
2568 quality flag that provides information for any problem in the data transfer (`qflag`), and 2 lists of
2569 `nHits` elements containing the fired TDC channels (`TDCCh`) and their respective time stamps (`TDCTS`),
2570 as presented in Source Code A.4. The ROOT file file is named using information contained into
2571 the configuration file, presented in section A.5.2. The needed information is extracted using method
2572 `DataReader::GetFileName()` and allow to build the output filename format `ScanXXXXXX_HVX_DAQ.root`

2573 where ScanXXXXXX is a 6 digit number representing the scan number into GIFT++ database and HVX
 2574 the HV step within the scan that can be more than a single digit. An example of ROOT data file is
 2575 provided with Figure A.3.

```
2576
RAWData TDCData;
TFile *outputFile = new TFile(outputFileName.c_str(),"recreate");
TTree *RAWDataTree = new TTree("RAWData","RAWData");

int EventCount = -9;
int nHits = -8;
int qflag = -7;
vector<int> TDCCh;
vector<float> TDCTS;

RAWDataTree->Branch("EventNumber",&EventCount, "EventNumber/I");
RAWDataTree->Branch("number_of_hits",&nHits,"number_of_hits/I");
RAWDataTree->Branch("Quality_flag",&qflag,"Quality_flag/I");
RAWDataTree->Branch("TDC_channel",&TDCCh);
RAWDataTree->Branch("TDC_TimeStamp",&TDCTS);

2577
//...
//Here read the TDC data using v1190a::Read() and place it into
//TDCData for as long as you didn't collect the requested amount
//of data.
//...

for(Uint i=0; i<TDCData.EventList->size(); i++){
    EventCount = TDCData.EventList->at(i);
    nHits = TDCData.NHitsList->at(i);
    qflag = TDCData.QFlagList->at(i);
    TDCCh = TDCData.ChannelList->at(i);
    TDCTS = TDCData.TimeStampList->at(i);
    RAWDataTree->Fill();
}
```

2578 *Source Code A.4: Highlight of the data transfer and organisation within DataReader::Run() after the data has been collected into TDCData.*

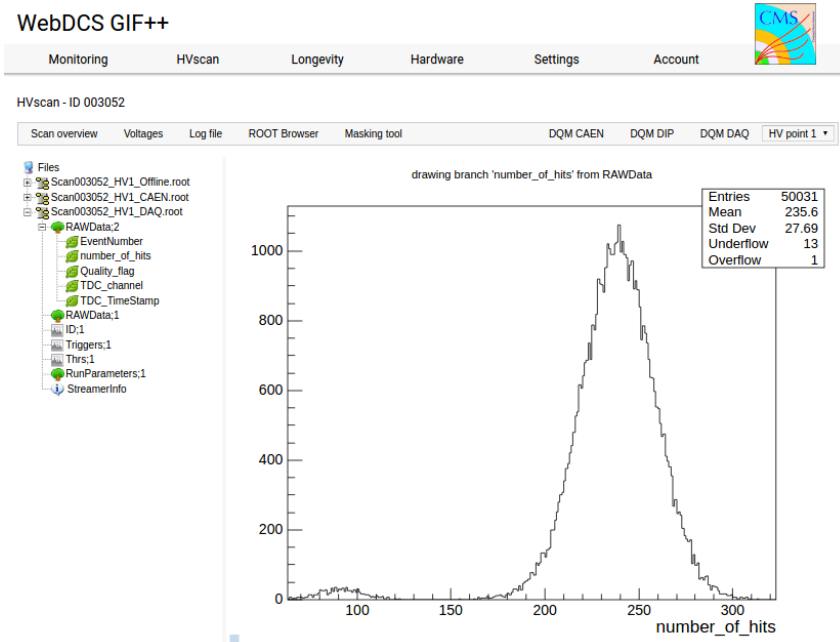


Figure A.3: Structure of the ROOT output file generated by the DAQ. The 5 branches (EventNumber, number_of_hits, Quality_flag, TDC_channel and TDC_TimeStamp) are visible on the left panel of the ROOT browser. On the right panel is visible the histogram corresponding to the variable nHits. In this specific example, there were approximately 50k events recorded to measure the gamma irradiation rate on the detectors. Each event is stored as a single entry in the TTree.

2579 A.4.3 Data quality flag

2580 Among the parameters that are recorded for each event, the quality flag, defined in Source Code A.5,
 2581 is determined on the fly by checking the data recorded by every single TDC. From method `v1190a::Read()`,
 2582 it can be understood that the content of each TDC buffer is readout one TDC at a time. Entries are
 2583 created in the data list for the first TDC and then, when the second buffer is readout, events corre-
 2584 sponding to entries that have already been created to store data for the previous TDC are added to
 2585 the existing list element. On the contrary, when an event entry has not been yet created in the data
 2586 list, a new entry is created.

```
2587
  typedef enum _QualityFlag {
    GOOD      = 1,
    CORRUPTED = 0
} QualityFlag;
```

2589 *Source Code A.5: Definition of the quality flag `enum`.*

2590 It is possible that each TDC buffer contains a different number of events. In cases where the first
 2591 element in the buffer list is an event for corresponds to a new entry, the difference in between the
 2592 entry from the buffer and the last entry in the data list is recorded and checked. If it is greater than 1,
 2593 what should never be the case, the quality flag is set to CORRUPTED for this TDC and an empty entry
 2594 is created in the place of the missing ones. Missing entries are believe to be the result of a bad hold

2595 on the TDC buffers at the moment of the readout. Indeed, the software hold is effective only on 1
 2596 TDC at a time and no solution as been found yet to completely block the writting in the buffers when
 2597 an IRQ is received.

2598 At the end of each BLT cycle, the ID of the last entry stored for each TDC buffer is not recorded.
 2599 When starting the next cycle, if the first entry in the pile corresponds to an event already existing
 2600 in the list, the readout will start from this list element and will not be able to check the difference
 2601 in between this entry's ID and the one of the last entry that was recorded for this TDC buffer in
 2602 the previous cycle. In the case events were missing, the flag stays at its initial value of 0, which is
 2603 similar to CORRUPTED and it is assumed that then this TDC will not contribute to `number_of_hits`,
 2604 `TDC_channel` or `TDC_TimeStamp`.

2605 Finally, since there will be 1 `RAWData` entry per TDC for each event (meaning `nTDCs` entries,
 2606 referring to `DataReader` private attribute), the individual flags of each TDC will be added together.
 2607 The final format is an integer composed `nTDCs` digits where each digit is the flag of a specific TDC.
 2608 This is constructed using powers of 10 like follows:

```
2609 TDC 0: QFlag = 100 × _QualityFlag
2610 TDC 1: QFlag = 101 × _QualityFlag
2611 ...
2612 TDC N: QFlag = 10N × _QualityFlag
```

2613 and the final flag to be with N digits:

```
2614 QFlag = n....3210
```

2615 each digit being 1 or 0. Below is given an example with a 4 TDCs setup.

```
2616 If all TDCs were good : QFlag = 1111,
2617 but if TDC 2 was corrupted : QFlag = 1011.
```

2618 When data taking is over and the data contained in the dynamical `RAWData` structure is transferred
 2619 to the ROOT file, all the 0s are changed into 2s by calling the method `DataReader::GetQFlag()`.
 2620 This will help translating the flag without knowing the number of TDCs beforehand. Indeed, a flag
 2621 111 could be due to a 3 TDC setup with 3 good individual TDC flags or to a more than 3 TDC setup
 2622 with TDCs those ID is greater than 2 being CORRUPTED, thus giving a 0.

2623 The quality flag has been introduced quite late, in October 2017 only, to the list of GIFT++ DAQ
 2624 parameters to be recorded into the output ROOT file. Before this addition, the missing data, corrupting
 2625 the quality for the offline analysis, was contributing to artificially fill data with lower multiplicity.
 2626 Looking at `TBranch number_of_hits` provides an information about the data of the full GIFT++
 2627 setup. When a TDC is not able to transfer data for a specific event, the effect is a reduction of the
 2628 total number of hits recorded in the full setup, this is what can be seen from Figure A.4. After offline
 2629 reconstruction detector by detector, the effect of missing events can be seen in the artificially filled
 2630 bin at multiplicity 0 shown in Figure A.5. Nonetheless, for data with high irradiation levels, as it is
 2631 the case for Figure A.5a, discarding the fake multiplicity 0 data can be done easily during the offline
 2632 analysis. At lower radiation, the missing events contribution becomes more problematic as the mul-
 2633 tiplicity distribution overlaps the multiplicity 0 and that in the same time the proportion of missing

events decreases. Attempts to fit the distribution with a Poisson or skew distribution function were not conclusive and this very problem has been at the origin of the quality flag that allows to give a non ambiguous information about each event quality.

2637

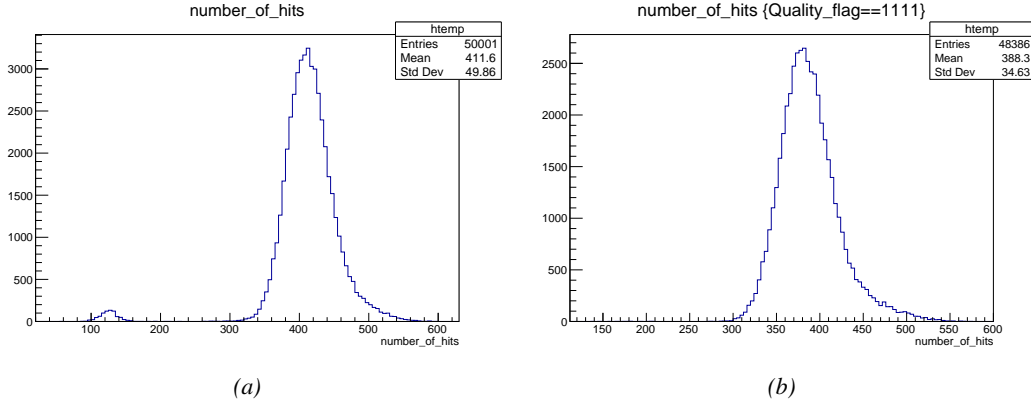


Figure A.4: The effect of the quality flag is explained by presenting the content of TBranch `number_of_hits` of a data file without `Quality_flag` in Figure A.4a and the content of the same TBranch for data corresponding to a `Quality_flag` where all TDCs were labelled as `GOOD` in Figure A.4b taken with similar conditions. It can be noted that the number of entries in Figure A.4b is slightly lower than in Figure A.4a due to the excluded events.

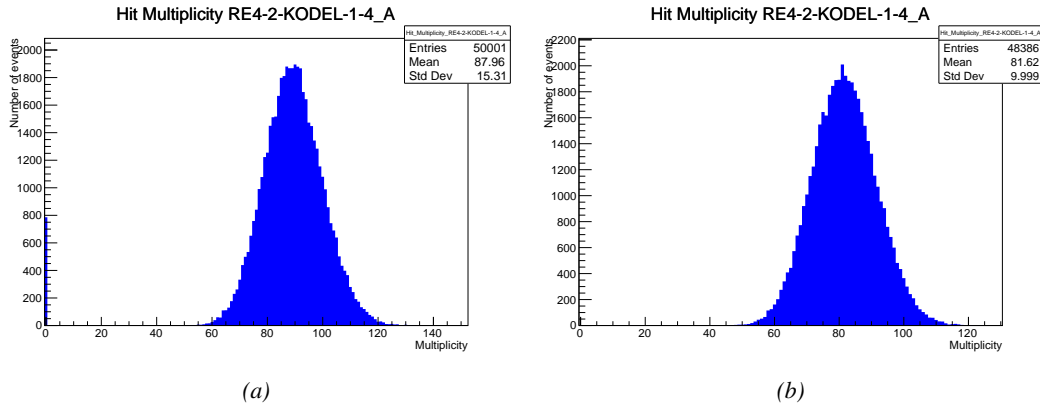


Figure A.5: Using the same data as previously showed in Figure A.4, the effect of the quality flag is explained by presenting the reconstructed hit multiplicity of a data file without `Quality_flag` in Figure A.5a and the reconstructed content of the same RPC partition for data corresponding to a `Quality_flag` where all TDCs were labelled as `GOOD` in Figure A.5b taken with similar conditions. The artificial high content of bin 0 is completely suppressed.

A.5 Communications

2638 To ensure data readout and dialog in between the machine and the TDCs or in between the webDCS
2640 and the DAQ, different communication solutions were used. First of all, it is important to have a

2641 module to allow the communication in between the TDCs and the computer from which the DAQ
 2642 operates. When this communication is effective, shifters using the webDCS to control data taking
 2643 can thus send instructions to the DAQ.

2644

2645 A.5.1 V1718 USB Bridge

2646 In the previous section, the data transfer has been discussed. The importance of the `v1718` object
 2647 (Source Code A.6), used as private member of `DataReader`, was not explicated. VME master
 2648 modules are used for communication purposes as they host the USB port that connects the pow-
 2649 ered crate buffer to the computer where the DAQ is installed. From the source code point of view,
 2650 this object is used to control the communication status, by reading the returned error codes with
 2651 `v1718::CheckStatus()`, or to check for IRQs coming from the TDCs through `v1718::CheckIRQ()`.
 2652 Finally, to ensure that triggers are blocked at the hardware level, a NIM pulse is sent out of one of the
 2653 5 programmable outputs (`v1718::SendBUSY()`) to the VETO of the coincidence module where the
 2654 trigger signals originate from. As long as this signal is ON, no trigger can reach the TDCs anymore.
 2655

```
2656
2657 class v1718{
2658     private:
2659         int Handle;
2660         Data32 Data;           // Data
2661         CVIRQLevels Level;    // Interrupt level
2662         CVAddressModifier AM;   // Addressing Mode
2663         CVDataWidth dataSize; // Data Format
2664         Data32 BaseAddress;   // Base Address
2665
2666     public:
2667         v1718(IniFile *inifile);
2668         ~v1718();
2669         long GetHandle(void) const;
2670         int SetData(Data16 data);
2671         Data16 GetData(void);
2672         int SetLevel(CVIRQLevels level);
2673         CVIRQLevels GetLevel(void);
2674         int SetAM(CVAddressModifier am);
2675         CVAddressModifier GetAM(void);
2676         int SetDatasize(CVDataWidth datasize);
2677         CVDataWidth GetDataSize(void);
2678         int SetBaseAddress(Data16 baseaddress);
2679         Data16 GetBaseAddress(void);
2680         void CheckStatus(CVErrorCodes status) const;
2681         void CheckIRQ();
2682         void SetPulsers();
2683         void SendBUSY(BusyLevel level);
2684     };
2685
2686
2687
2688
2689
2690
2691
2692
2693
2694
2695
2696
2697
2698
2699
2700
2701
2702
2703
2704
2705
2706
2707
2708
2709
2710
2711
2712
2713
2714
2715
2716
2717
2718
2719
2720
2721
2722
2723
2724
2725
2726
2727
2728
2729
2730
2731
2732
2733
2734
2735
2736
2737
2738
2739
2740
2741
2742
2743
2744
2745
2746
2747
2748
2749
2750
2751
2752
2753
2754
2755
2756
2757
2758
2759
2760
2761
2762
2763
2764
2765
2766
2767
2768
2769
2770
2771
2772
2773
2774
2775
2776
2777
2778
2779
2780
2781
2782
2783
2784
2785
2786
2787
2788
2789
2790
2791
2792
2793
2794
2795
2796
2797
2798
2799
2800
2801
2802
2803
2804
2805
2806
2807
2808
2809
2810
2811
2812
2813
2814
2815
2816
2817
2818
2819
2820
2821
2822
2823
2824
2825
2826
2827
2828
2829
2830
2831
2832
2833
2834
2835
2836
2837
2838
2839
2840
2841
2842
2843
2844
2845
2846
2847
2848
2849
2850
2851
2852
2853
2854
2855
2856
2857
2858
2859
2860
2861
2862
2863
2864
2865
2866
2867
2868
2869
2870
2871
2872
2873
2874
2875
2876
2877
2878
2879
2880
2881
2882
2883
2884
2885
2886
2887
2888
2889
2890
2891
2892
2893
2894
2895
2896
2897
2898
2899
2900
2901
2902
2903
2904
2905
2906
2907
2908
2909
2910
2911
2912
2913
2914
2915
2916
2917
2918
2919
2920
2921
2922
2923
2924
2925
2926
2927
2928
2929
2930
2931
2932
2933
2934
2935
2936
2937
2938
2939
2940
2941
2942
2943
2944
2945
2946
2947
2948
2949
2950
2951
2952
2953
2954
2955
2956
2957
2958
2959
2960
2961
2962
2963
2964
2965
2966
2967
2968
2969
2970
2971
2972
2973
2974
2975
2976
2977
2978
2979
2980
2981
2982
2983
2984
2985
2986
2987
2988
2989
2990
2991
2992
2993
2994
2995
2996
2997
2998
2999
3000
3001
3002
3003
3004
3005
3006
3007
3008
3009
3010
3011
3012
3013
3014
3015
3016
3017
3018
3019
3020
3021
3022
3023
3024
3025
3026
3027
3028
3029
3030
3031
3032
3033
3034
3035
3036
3037
3038
3039
3040
3041
3042
3043
3044
3045
3046
3047
3048
3049
3050
3051
3052
3053
3054
3055
3056
3057
3058
3059
3060
3061
3062
3063
3064
3065
3066
3067
3068
3069
3070
3071
3072
3073
3074
3075
3076
3077
3078
3079
3080
3081
3082
3083
3084
3085
3086
3087
3088
3089
3090
3091
3092
3093
3094
3095
3096
3097
3098
3099
3100
3101
3102
3103
3104
3105
3106
3107
3108
3109
3110
3111
3112
3113
3114
3115
3116
3117
3118
3119
3120
3121
3122
3123
3124
3125
3126
3127
3128
3129
3130
3131
3132
3133
3134
3135
3136
3137
3138
3139
3140
3141
3142
3143
3144
3145
3146
3147
3148
3149
3150
3151
3152
3153
3154
3155
3156
3157
3158
3159
3160
3161
3162
3163
3164
3165
3166
3167
3168
3169
3170
3171
3172
3173
3174
3175
3176
3177
3178
3179
3180
3181
3182
3183
3184
3185
3186
3187
3188
3189
3190
3191
3192
3193
3194
3195
3196
3197
3198
3199
3200
3201
3202
3203
3204
3205
3206
3207
3208
3209
3210
3211
3212
3213
3214
3215
3216
3217
3218
3219
3220
3221
3222
3223
3224
3225
3226
3227
3228
3229
3230
3231
3232
3233
3234
3235
3236
3237
3238
3239
3240
3241
3242
3243
3244
3245
3246
3247
3248
3249
3250
3251
3252
3253
3254
3255
3256
3257
3258
3259
3260
3261
3262
3263
3264
3265
3266
3267
3268
3269
3270
3271
3272
3273
3274
3275
3276
3277
3278
3279
3280
3281
3282
3283
3284
3285
3286
3287
3288
3289
3290
3291
3292
3293
3294
3295
3296
3297
3298
3299
3300
3301
3302
3303
3304
3305
3306
3307
3308
3309
3310
3311
3312
3313
3314
3315
3316
3317
3318
3319
3320
3321
3322
3323
3324
3325
3326
3327
3328
3329
3330
3331
3332
3333
3334
3335
3336
3337
3338
3339
3340
3341
3342
3343
3344
3345
3346
3347
3348
3349
3350
3351
3352
3353
3354
3355
3356
3357
3358
3359
3360
3361
3362
3363
3364
3365
3366
3367
3368
3369
3370
3371
3372
3373
3374
3375
3376
3377
3378
3379
3380
3381
3382
3383
3384
3385
3386
3387
3388
3389
3390
3391
3392
3393
3394
3395
3396
3397
3398
3399
3400
3401
3402
3403
3404
3405
3406
3407
3408
3409
3410
3411
3412
3413
3414
3415
3416
3417
3418
3419
3420
3421
3422
3423
3424
3425
3426
3427
3428
3429
3430
3431
3432
3433
3434
3435
3436
3437
3438
3439
3440
3441
3442
3443
3444
3445
3446
3447
3448
3449
3450
3451
3452
3453
3454
3455
3456
3457
3458
3459
3460
3461
3462
3463
3464
3465
3466
3467
3468
3469
3470
3471
3472
3473
3474
3475
3476
3477
3478
3479
3480
3481
3482
3483
3484
3485
3486
3487
3488
3489
3490
3491
3492
3493
3494
3495
3496
3497
3498
3499
3500
3501
3502
3503
3504
3505
3506
3507
3508
3509
3510
3511
3512
3513
3514
3515
3516
3517
3518
3519
3520
3521
3522
3523
3524
3525
3526
3527
3528
3529
3530
3531
3532
3533
3534
3535
3536
3537
3538
3539
3540
3541
3542
3543
3544
3545
3546
3547
3548
3549
3550
3551
3552
3553
3554
3555
3556
3557
3558
3559
3560
3561
3562
3563
3564
3565
3566
3567
3568
3569
3570
3571
3572
3573
3574
3575
3576
3577
3578
3579
3580
3581
3582
3583
3584
3585
3586
3587
3588
3589
3590
3591
3592
3593
3594
3595
3596
3597
3598
3599
3599
3600
3601
3602
3603
3604
3605
3606
3607
3608
3609
3610
3611
3612
3613
3614
3615
3616
3617
3618
3619
3620
3621
3622
3623
3624
3625
3626
3627
3628
3629
3630
3631
3632
3633
3634
3635
3636
3637
3638
3639
3640
3641
3642
3643
3644
3645
3646
3647
3648
3649
3649
3650
3651
3652
3653
3654
3655
3656
3657
3658
3659
3659
3660
3661
3662
3663
3664
3665
3666
3667
3668
3669
3669
3670
3671
3672
3673
3674
3675
3676
3677
3678
3679
3679
3680
3681
3682
3683
3684
3685
3686
3687
3688
3689
3689
3690
3691
3692
3693
3694
3695
3696
3697
3698
3699
3699
3700
3701
3702
3703
3704
3705
3706
3707
3708
3709
3709
3710
3711
3712
3713
3714
3715
3716
3717
3718
3719
3719
3720
3721
3722
3723
3724
3725
3726
3727
3728
3729
3729
3730
3731
3732
3733
3734
3735
3736
3737
3738
3739
3739
3740
3741
3742
3743
3744
3745
3746
3747
3748
3749
3749
3750
3751
3752
3753
3754
3755
3756
3757
3758
3759
3759
3760
3761
3762
3763
3764
3765
3766
3767
3768
3769
3769
3770
3771
3772
3773
3774
3775
3776
3777
3778
3778
3779
3779
3780
3781
3782
3783
3784
3785
3786
3787
3788
3789
3789
3790
3791
3792
3793
3794
3795
3796
3797
3798
3799
3799
3800
3801
3802
3803
3804
3805
3806
3807
3808
3809
3809
3810
3811
3812
3813
3814
3815
3816
3817
3818
3819
3819
3820
3821
3822
3823
3824
3825
3826
3827
3828
3829
3829
3830
3831
3832
3833
3834
3835
3836
3837
3838
3839
3839
3840
3841
3842
3843
3844
3845
3846
3847
3848
3849
3849
3850
3851
3852
3853
3854
3855
3856
3857
3858
3859
3859
3860
3861
3862
3863
3864
3865
3866
3867
3868
3869
3869
3870
3871
3872
3873
3874
3875
3876
3877
3878
3879
3879
3880
3881
3882
3883
3884
3885
3886
3887
3888
3889
3889
3890
3891
3892
3893
3894
3895
3896
3897
3898
3898
3899
3899
3900
3901
3902
3903
3904
3905
3906
3907
3908
3909
3909
3910
3911
3912
3913
3914
3915
3916
3917
3918
3919
3919
3920
3921
3922
3923
3924
3925
3926
3927
3928
3929
3929
3930
3931
3932
3933
3934
3935
3936
3937
3938
3939
3939
3940
3941
3942
3943
3944
3945
3946
3947
3948
3949
3949
3950
3951
3952
3953
3954
3955
3956
3957
3958
3959
3959
3960
3961
3962
3963
3964
3965
3966
3967
3968
3969
3969
3970
3971
3972
3973
3974
3975
3976
3977
3978
3979
3979
3980
3981
3982
3983
3984
3985
3986
3987
3988
3989
3989
3990
3991
3992
3993
3994
3995
3996
3997
3998
3998
3999
3999
4000
4001
4002
4003
4004
4005
4006
4007
4008
4009
4009
4010
4011
4012
4013
4014
4015
4016
4017
4018
4019
4019
4020
4021
4022
4023
4024
4025
4026
4027
4028
4029
4029
4030
4031
4032
4033
4034
4035
4036
4037
4038
4039
4039
4040
4041
4042
4043
4044
4045
4046
4047
4048
4049
4049
4050
4051
4052
4053
4054
4055
4056
4057
4058
4059
4059
4060
4061
4062
4063
4064
4065
4066
4067
4068
4069
4069
4070
4071
4072
4073
4074
4075
4076
4077
4078
4079
4079
4080
4081
4082
4083
4084
4085
4086
4087
4088
4089
4089
4090
4091
4092
4093
4094
4095
4096
4097
4098
4098
4099
4099
4100
4101
4102
4103
4104
4105
4106
4107
4108
4109
4109
4110
4111
4112
4113
4114
4115
4116
4117
4118
4119
4119
4120
4121
4122
4123
4124
4125
4126
4127
4128
4129
4129
4130
4131
4132
4133
4134
4135
4136
4137
4138
4139
4139
4140
4141
4142
4143
4144
4145
4146
4147
4148
4149
4149
4150
4151
4152
4153
4154
4155
4156
4157
4158
4159
4159
4160
4161
4162
4163
4164
4165
4166
4167
4168
4169
4169
4170
4171
4172
4173
4174
4175
4176
4177
4178
4179
4179
4180
4181
4182
4183
4184
4185
4186
4187
4188
4189
4189
4190
4191
4192
4193
4194
4195
4196
4197
4198
4198
4199
4199
4200
4201
4202
4203
4204
4205
4206
4207
4208
4209
4209
4210
4211
4212
4213
4214
4215
4216
4217
4218
4219
4219
4220
4221
4222
4223
4224
4225
4226
4227
4228
4229
4229
4230
4231
4232
4233
4234
4235
4236
4237
4238
4239
4239
4240
4241
4242
4243
4244
4245
4246
4247
4248
4249
4249
4250
4251
4252
4253
4254
4255
4256
4257
4258
4259
4259
4260
4261
4262
4263
4264
4265
4266
4267
4268
4269
4269
4270
4271
4272
4273
4274
4275
4276
4277
4278
4279
4279
4280
4281
4282
4283
4284
4285
4286
4287
4288
4289
4289
4290
4291
4292
4293
4294
4295
4296
4297
4298
4298
4299
4299
4300
4301
4302
4303
4304
4305
4306
4307
4308
4309
4309
4310
4311
4312
4313
4314
4315
4316
4317
4318
4319
4319
4320
4321
4322
4323
4324
4325
4326
4327
4328
4329
4329
4330
4331
4332
4333
4334
4335
4336
4337
4338
4339
4339
4340
4341
4342
4343
4344
4345
4346
4347
4348
4349
4349
4350
4351
4352
4353
4354
4355
4356
4357
4358
4359
4359
4360
4361
4362
4363
4364
4365
4366
4367
4368
4369
4369
4370
4371
4372
4373
4374
4375
4376
4377
4378
4379
4379
4380
4381
4382
4383
4384
4385
4386
4387
4388
4389
4389
4390
4391
4392
4393
4394
4395
4396
4397
4398
4398
4399
4399
4400
4401
4402
4403
4404
4405
4406
4407
4408
4409
4409
4410
4411
4412
4413
4414
4415
4416
4417
4418
4419
4419
4420
4421
4422
4423
4424
4425
4426
4427
4428
4429
4429
4430
4431
4432
4433
4434
4435
4436
4437
4438
4439
4439
4440
4441
4442
4443
4444
4445
4446
4447
4448
4449
4449
4450
4451
4452
4453
4454
4455
4456
4457
4458
4459
4459
4460
4461
4462
4463
4464
4465
4466
4467
4468
4469
4469
4470
4471
4472
4473
4474
4475
4476
4477
4478
4479
4479
4480
4481
4482
4483
4484
4485
4486
4487
4488
4489
4489
4490
4491
4492
4493
4494
4495
4496
4497
4498
4498
4499
4499
4500
4501
4502
4503
4504
4505
4506
4507
4508
4509
4509
4510
4511
4512
4513
4514
4515
4516
4517
4518
4519
4519
4520
4521
4522
4523
4524
4525
4526
4527
4528
4529
4529
4530
4531
4532
4533
4534
4535
4536
4537
4538
4539
4539
4540
4541
4542
4543
4544
4545
4546
4547
4548
4549
4549
4550
4551
4552
4553
4554
4555
4556
4557
4558
4559
4559
4560
4561
4562
4563
4564
4565
4566
4567
4568
4569
4569
4570
4571
4572
4573
4574
4575
4576
4577
4578
4579
4579
4580
4581
4582
4583
4584
4585
4586
4587
4588
4589
4589
4590
4591
4592
4593
4594
4595
4596
4597
4598
4598
4599
4599
4600
4601
4602
4603
4604
4605
4606
4607
4608
4609
4609
4610
4611
4612
4613
4614
4
```

2662 be stored in the ROOT file that contains the DAQ data as can be seen from Figure A.3. Indeed,
 2663 another `TTree` called `RunParameters` as well as the 2 histograms `ID`, containing the scan number,
 2664 start and stop time stamps, and `Triggers`, containing the number of triggers requested by the shifter,
 2665 are available in the data files. Moreover, `ScanID` and `HV` are then used to construct the file name
 2666 thanks to the method `DataReader::GetFileName()`.

WebDCS GIF++

Monitoring HVscan Longevity Hardware Settings Account CMS

DAQ High Voltage Scan

Type scan: Rate Scan Comments:

Source configuration: Source OFF U 333 D 333 HV after scan: Turn off

Beam configuration: Beam OFF

Waiting time: 1 (min)

Trigger mode: External Internal Random

Minimal measure time: 10 (min)

Chamber	RE2-2-NPD-BARC-8	RE4-2-CERN-106	RE2-2-NPD-BARC-9	RE4-2-CERN-105	RE4-2-KODEL-1-4	Max triggers
H _{Veff} 1	8600	8500	8600	8500	6500	
H _{Veff} 2	8700	8600	8700	8600	6600	
H _{Veff} 3	8800	8700	8800	8700	6700	
H _{Veff} 4	8900	8800	8900	8800	6800	
H _{Veff} 5	9000	8900	9000	8900	6900	
H _{Veff} 6	9100	9000	9100	9000	7000	
H _{Veff} 7	9200	9100	9200	9100	7100	
H _{Veff} 8	9300	9200	9300	9200	7200	
H _{Veff} 9	9400	9300	9400	9300	7300	
H _{Veff} 10	9500	9400	9500	9400	7400	

Start HV scan

Figure A.6: WebDCS DAQ scan page. On this page, shifters need to choose the type of scan (Rate, Efficiency or Noise Reference scan), the gamma source configuration at the moment of data taking, the beam configuration, and the trigger mode. These information will be stored in the DAQ ROOT output. Are also given the minimal measurement time and waiting time after ramping up of the detectors is over before starting the data acquisition. Then, the list of HV points to scan and the number of triggers for each run of the scan are given in the table underneath.

2667 The rest of the information is written beforehand in the configuration file template, as explicated
 2668 in Source Code A.7, and contains the hardware addresses to the different VME modules in the
 2669 setup as well as settings for the TDCs. As the TDC settings available in the configuration file are not
 2670 supposed to be modified, an improvement would be to remove them from the configuration file and
 2671 to hardcode them inside of the DAQ code itself or to place them into a different INI file that would
 2672 host only the TDC settings to lower the probability for a bad manipulation of the configuration file
 2673 that can be modified from one of webDCS' menus.

2674

```
[General]
TdcS=4
ScanID=$scanid
HV=$HV
RunType=$runtype
MaxTriggers=$maxtriggers
Beam=$beam
[VMEInterface]
Type=V1718
BaseAddress=0xFF0000
Name=VmeInterface
[TDC0]
Type=V1190A
BaseAddress=0x00000000
Name=Tdc0
StatusA00-15=1
StatusA16-31=1
StatusB00-15=1
StatusB16-31=1
StatusC00-15=1
StatusC16-31=1
StatusD00-15=1
StatusD16-31=1
[TDC1]
Type=V1190A
BaseAddress=0x11110000
Name=Tdc1
StatusA00-15=1
StatusA16-31=1
StatusB00-15=1
StatusB16-31=1
StatusC00-15=1
StatusC16-31=1
StatusD00-15=1
StatusD16-31=1
[TDC2]
Type=V1190A
BaseAddress=0x22220000
Name=Tdc2
StatusA00-15=1
StatusA16-31=1
StatusB00-15=1
StatusB16-31=1
StatusC00-15=1
StatusC16-31=1
StatusD00-15=1
StatusD16-31=1
[TDC3]
Type=V1190A
BaseAddress=0x44440000
Name=Tdc3
StatusA00-15=1
StatusA16-31=1
StatusB00-15=1
StatusB16-31=1
StatusC00-15=1
StatusC16-31=1
StatusD00-15=1
StatusD16-31=1
[TDCSettings]
TriggerExtraSearchMargin=0
TriggerRejectMargin=0
TriggerTimeSubtraction=0b1
TdcDetectionMode=0b01
TdcResolution=0b10
TdcDeadTime=0b00
TdcHeadTrailer=0b1
TdcEventSize=0b1001
TdcTestMode=0b0
BLTMode=1
```

2675

Source Code A.7: INI configuration file template for 4 TDCs. In section [General], the number of TDCs is explicitated and information about the ongoing run is given. Then, there are sections for each and every VME modules. There buffer addresses are given and for the TDCs, the list of channels to enable is given. Finally, in section [TDCSettings], a part of the TDC settings are given.

2677 In order to retrieve the information of the configuration file, the object `IniFile` has been developed
 2678 to provide an INI parser, presented in Source Code A.8. It contains private methods returning a
 2679 boolean to check the type of line written in the file, whether a comment, a group header or a key line
 2680 (`IniFile::CheckIfComment()`, `IniFile::CheckIfGroup()` and `IniFile::CheckIfToken()`). The
 2681 key may sometimes be referred to as *token* in the source code. Moreover, the private element
 2682 `FileData` is a map of `const string` to `string` that allows to store the data contained inside the
 2683 configuration file via the public method `IniFile::GetFileData()` following the formatting (see
 2684 method `IniFile::Read()`):

```
2685
  2686     string group, token, value;
  // Get the field values for the 3 strings.
  // Then concatenate group and token together as a single string
  // with a dot separation.
  token = group + "." + token;
  FileData[token] = value;
```

2687 More methods have been written to translate the different keys into the right variable format
 2688 when used by the DAQ. For example, to get a `float` value out of the configuration file data, knowing
 2689 the group and the key needed, the method `IniFile::floatType()` can be used. It takes 3 arguments
 2690 being the group name and key name (both `string`), and a default `float` value used as exception in
 2691 the case the expected combination of group and key cannot be found in the configuration file. This
 2692 default value is then used and the DAQ continues on working after sending an alert in the log file for
 2693 further debugging.

```

2694 typedef map< const string, string > IniFileData;
2695
class IniFile{
    private:
        bool          CheckIfComment (string line);
        bool          CheckIfGroup(string line, string& group);
        bool          CheckIfToken(string line, string& key, string& value);
        string         FileName;
        IniFileData   FileData;
        int           Error;

    public:
        IniFile();
        IniFile(string filename);
        virtual      ~IniFile();

        // Basic file operations
        void          SetFileName(string filename);
        int           Read();
        int           Write();
        IniFileData GetFileData();

        // Data readout methods
        Data32         addressType (string groupname, string keyname, Data32
→     defaultvalue);
        long          intType     (string groupname, string keyname, long
→     defaultvalue);
        long long    longType    (string groupname, string keyname, long long
→     defaultvalue );
        string         stringType  (string groupname, string keyname, string
→     defaultvalue );
        float         floatType   (string groupname, string keyname, float
→     defaultvalue );

        // Error methods
        string         GetErrorMsg();
    };

```

2696 *Source Code A.8: Description of C++ object `IniFile` used as a parser for INI file format.*

A.5.3 WebDCS/DAQ intercommunication

2697 When shifters send instructions to the DAQ via the configuration file, it is the webDCS itself that
 2698 gives the start command to the DAQ and then the 2 softwares use inter-process communication
 2700 through file to synchronise themselves. This communication file is represented by the variable **const**
 2701 **string** __runstatuspath.

2702 On one side, the webDCS sends commands or status that are readout by the DAQ:

- 2703 ● INIT, status sent when launching a scan and read via function `CtrlRunStatus(...)`,
- 2704 ● START, command to start data taking and read via function `CheckSTART()`,
- 2705 ● STOP, command to stop data taking at the end of the scan and read via function `CheckSTOP()`,
 2706 and
- 2707 ● KILL, command to kill data taking sent by user and read via function `CheckKILL()`

2708 and on the other, the DAQ sends status that are controled by the webDCS:

- 2709 ● `DAQ_RDY`, sent with `SendDAQReady()` to signify that the DAQ is ready to receive commands
2710 from the webDCS,
- 2711 ● `RUNNING`, sent with `SendDAQRunning()` to signify that the DAQ is taking data,
- 2712 ● `DAQ_ERR`, sent with `SendDAQError()` to signify that the DAQ didn't receive the expected com-
2713 mand from the webDCS or that the launch command didn't have the right number of argu-
2714 ments,
- 2715 ● `RD_ERR`, sent when the DAQ wasn't able to read the communication file, and
- 2716 ● `WR_ERR`, sent when the DAQ wasn't able to write into the communication file.

2717 **A.5.4 Example of inter-process communication cycle**

2718 Under normal conditions, the webDCS and the DAQ processes exchange commands and status via
2719 the file hosted at the address `__runstatuspath`, as explained in subsection A.5.3. An example of
2720 cycle is given in Table A.1. In this example, the steps 3 to 5 are repeated as long as the webDCS tells
2721 the DAQ to take data. A data taking cycle is the equivalent as what is called a *Scan* in GIFT++ jargon,
2722 referring to a set a runs with several HV steps. Each repetition of steps 3 to 5 is then equivalent to a
2723 single *Run*.

2724

2725 At any moment during the data taking, for any reason, the shifter can decide that the data taking
2726 needs to be stopped before it reached the end of the scheduled cycle. Thus at any moment on the
2727 cycle, the content of the inter-process communication file will be changed to `KILL` and the DAQ will
2728 shut down right away. The DAQ checks for `KILL` signals every 5s after the TDCs configuration is
2729 over. So far, the function `CheckKILL()` has been used only inside of the data taking loop of method
2730 `DataReader::Run()` and thus, if the shifter decides to KILL the data taking during the TDC con-
2731 figuration phase or the HV ramping in between 2 HV steps, the DAQ will not be stopped smoothly
2732 and a *force kill* command will be sent to stop the DAQ process that is still awake on the computer.
2733 Improvements can be brought on this part of the software to make sure that the DAQ can safely
2734 shutdown at any moment.

2735

2736 **A.6 Software export**

2737 In section A.2 was discussed the fact that the DAQ as written in its last version is not a standalone
2738 software. It is possible to make it a standalone program that could be adapted to any VME setup
2739 using V1190A and V1718 modules by creating a GUI for the software or by printing the log mes-
2740 sages that are normally printed in the webDCS through the log file, directly into the terminal. This
2741 method was used by the DAQ up to version 3.0 moment where the webDCS was completed. Also, it
2742 is possible to check branches of DAQ v2.X to have example of communication through a terminal.

2743

2744 DAQ v2.X is nonetheless limited in it's possibilities and requires a lot of offline manual interven-
2745 tions from the users. Indeed, there is no communication of the software with the detectors' power
2746 supply system that would allow for a user a predefine a list of voltages to operate the detectors at

step	actions of webDCS	status of DAQ	<code>__runstatuspath</code>
1	launch DAQ ramp voltages ramping over wait for currents stabilization	readout of IniFile configuration of TDCs	INIT
2		configuration done send DAQ ready wait for START signal	DAQ_RDY
3	waiting time over send START		START
4	wait for run to end monitor DAQ run status	data taking ongoing check for KILL signal	RUNNING
5		run over send DAQ_RDY wait for next DCS signal	DAQ_RDY
6	ramp voltages ramping over wait for currents stabilization		DAQ_RDY
3	waiting time over send START		START
4	wait for run to end monitor DAQ run status	update IniFile information data taking ongoing check for KILL signal	RUNNING
5		run over send DAQ_RDY wait for next DCS signal	DAQ_RDY
7	send command STOP	DAQ shuts down	STOP

Table A.1: Inter-process communication cycles in between the webDCS and the DAQ through file string signals.

2747 and loop over to take data without any further manual intervention. In v2.X, the data is taken for a
2748 single detector setting and at the end of each run, the softwares asks the user if he intends on taking
2749 more runs. If so, the software invites the user to set the operating voltages accordingly to what is
2750 necessary and to manual update the configuration file in consequence. This working mode can be a
2751 very first approach before an evolution and has been successfully used by colleagues from different
2752 collaborations.

2753
2754 For a more robust operation, it is recommended to develop a GUI or a web application to inter-
2755 face the DAQ. Moreover, to limit the amount of manual interventions, and thus the probability to
2756 make mistakes, it is also recommended to add an extra feature into the DAQ by installing the HV
2757 Wrapper library provided by CAEN of which an example of use in a similar DAQ software devel-
2758 opped by a master student of UGent, and called TinyDAQ, is provided on UGent's github. Then, this
2759 HV Wrapper will help you communicating with and give instructions to a CAEN HV powered crate
2760 and can be added into the DAQ at the same level where the communication with the user was made
2761 in DAQ v2.X. In case you are using another kind of power system for your detectors, it is stringly
2762 adviced to use HV modules or crates that can be remotely controled via a using C++ libraries.
2763

B

2764

2765

Details on the offline analysis package

2766 The data collected in GIF++ thanks to the DAQ described in Appendix A is difficult to interpret by
2767 a human user that doesn't have a clear idea of the raw data architecture of the ROOT data files. In
2768 order to render the data human readable, a C++ offline analysis tool was designed to provide users
2769 with detector by detector histograms that give a clear overview of the parameters monitored during
2770 the data acquisition [70]. In this appendix, details about this software in the context of GIF++, as of
2771 how the software was written and how it functions will be given.

2772 B.1 GIF++ Offline Analysis file tree

2773 GIF++ Offline Analysis source code is fully available on github at https://github.com/afagot/GIF_OfflineAnalysis. The software requires ROOT as non-optionnal dependency
2774 as it takes ROOT files in input and write an output ROOT file containing histograms. To compile the
2775 GIF++ Offline Analysis project is compiled with cmake. To compile, first a build/ directory must
2776 be created to compile from there:
2777

```
2778 mkdir build
2779 cd build
2780 cmake ..
2781 make
2782 make install
```

2780 To clean the directory and create a new build directory, the bash script cleandir.sh can be used:

```
2781
2782 ./cleandir.sh
```

2783 The source code tree is provided below along with comments to give an overview of the files' con-
2784 tent. The different objects created for this project (`Infrastructure`, `Trolley`, `RPC`, `Mapping`, `RPCHit`,
2785 `RPCCluster` and `Inifile`) will be described in details in the following sections.

2786

```

GIF_OfflineAnalysis
├── bin
│   └── offlineanalysis ..... EXECUTABLE
├── build..... CMAKE COMPILATION DIRECTORY
└── ...
    ├── include..... LIST OF C++ HEADER FILES
    │   ├── Cluster.h..... DECLARATION OF OBJECT RPCCLUSTER
    │   ├── Current.h..... DECLARATION OF GETCURRENT ANALYSIS MACRO
    │   ├── GIFTrolley.h..... DECLARATION OF OBJECT TROLLEY
    │   ├── Infrastructure.h..... DECLARATION OF OBJECT INFRASTRUCTURE
    │   ├── IniFile.h..... DECLARATION OF OBJECT INI FILE FORINI PARSER
    │   ├── Mapping.h..... DECLARATION OF OBJECT MAPPING
    │   ├── MsgSvc.h..... DECLARATION OF OFFLINE LOG MESSAGES
    │   ├── OfflineAnalysis.h..... DECLARATION OF DATA ANALYSIS MACRO
    │   ├── RPCTracker.h..... DECLARATION OF OBJECT RPC
    │   ├── RPCHit.h..... DECLARATION OF OBJECT RPCHIT
    │   ├── types.h..... DEFINITION OF USEFUL VARIABLE TYPES
    │   └── utils.h..... DECLARATION OF USEFUL FUNCTIONS
    ├── obj..... BINARY FILES CREATED BY COMPILER
    └── ...
        ├── src..... LIST OF C++ SOURCE FILES
        │   ├── Cluster.cc..... DEFINITION OF OBJECT RPCCLUSTER
        │   ├── Current.cc .....

```

2787

B.2 Usage of the Offline Analysis

2788

In order to use the Offline Analysis tool, it is necessary to know the Scan number and the HV Step of the run that needs to be analysed. This information needs to be written in the following format:

2790

2791

```
Scan00XXXX_HVY
```

2792

2793

where XXXX is the scan ID and Y is the high voltage step (in case of a high voltage scan, data will be taken for several HV steps). This format corresponds to the base name of data files in the database

2794 of the GIF++ webDCS. Usually, the offline analysis tool is automatically called by the webDCS at
 2795 the end of data taking or by a user from the webDCS panel if an update of the tool was brought.
 2796 Nonetheless, an expert can locally launch the analysis for tests on the GIF++ computer, or a user can
 2797 get the code on its local machine from github and download data from the webDCS for its own anal-
 2798 ysis. To launch the code, the following command can be used from the `GIF_OfflineAnalysis` folder:

2799
 2800 `bin/offlineanalysis /path/to/Scan00XXXX_HVY`

2801 where, `/path/to/Scan00XXXX_HVY` refers to the local data files. Then, the offline tool will by itself
 2802 take care of finding all available ROOT data files present in the folder, as listed below:

- 2803
 - 2804 ● `Scan00XXXX_HVY_DAQ.root` containing the TDC data as described in Appendix ?? (events, hit
 and timestamp lists), and
 - 2805 ● `Scan00XXXX_HVY_CAEN.root` containing the CAEN mainframe data recorded by the monitor-
 ing tool webDCS during data taking (HVs and currents of every HV channels). This file is
 created independently of the DAQ.

2808 **B.2.1 Output of the offline tool**

2809 **B.2.1.1 ROOT file**

2810 The analysis gives in output ROOT datafiles that are saved into the data folder and called using the
 2811 naming convention `Scan00XXXX_HVY_Offline.root`. Inside those, a list of `TH1` histograms can be
 2812 found. Its size will vary as a function of the number of detectors in the setup as each set of histograms
 2813 is produced detector by detector. For each partition of each chamber, can be found:

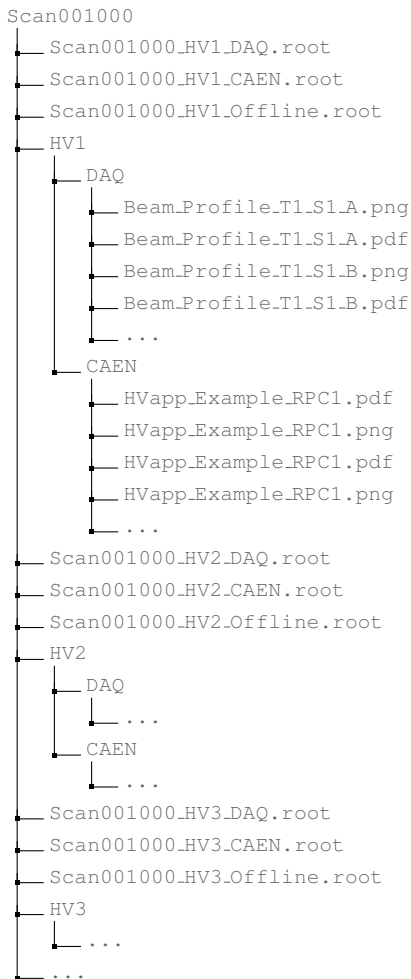
- 2814
 - 2815 ● `Time_Profile_Tt_Sc_p` shows the time profile of all recorded events (number of events per
 time bin),
 - 2816 ● `Hit_Profile_Tt_Sc_p` shows the hit profile of all recorded events (number of events per chan-
 nel),
 - 2818 ● `Hit_Multiplicity_Tt_Sc_p` shows the hit multiplicity (number of hits per event) of all recorded
 events (number of occurrences per multiplicity bin),
 - 2820 ● `Strip_Mean_Noise_Tt_Sc_p` shows noise/gamma rate per unit area for each strip in a se-
 lected time range. After filters are applied on `Time_Profile_Tt_Sc_p`, the filtered version
 of `Hit_Profile_Tt_Sc_p` is normalised to the total integrated time and active detection area
 of a single channel,
 - 2824 ● `Strip_Activity_Tt_Sc_p` shows noise/gamma activity for each strip (normalised version of
 previous histogram - strip activity = strip rate / average partition rate),
 - 2826 ● `Strip_Homogeneity_Tt_Sc_p` shows the *homogeneity* of a given partition ($\text{homogeneity} = \exp(-\text{strip rates standard deviation(strip rates in partition/average partition rate)})$),
 - 2828 ● `mask_Strip_Mean_Noise_Tt_Sc_p` shows noise/gamma rate per unit area for each masked
 strip in a selected time range. Offline, the user can control the noise/gamma rate and decide to
 mask the strips that are judged to be noisy or dead. This is done via the *Masking Tool* provided
 by the webDCS,

- 2832 ● `mask_Strip_Activity_Tt_Sc_p` shows noise/gamma activity per unit area for each masked
2833 strip with respect to the average rate of active strips,
- 2834 ● `NoiseCSize_H_Tt_Sc_p` shows noise/gamma cluster size, a cluster being constructed out of
2835 adjacent strips giving a signal at the *same time* (hits within a time window of 25 ns),
- 2836 ● `NoiseCMult_H_Tt_Sc_p` shows noise/gamma cluster multiplicity (number of reconstructed
2837 clusters per event),
- 2838 ● `Chip_Mean_Noise_Tt_Sc_p` shows the same information than `Strip_Mean_Noise_Tt_Scp` us-
2839 ing a different binning (1 chip corresponds to 8 strips),
- 2840 ● `Chip_Activity_Tt_Sc_p` shows the same information than `Strip_Activity_Tt_Scp` using
2841 chip binning,
- 2842 ● `Chip_Homogeneity_Tt_Sc_p` shows the homogeneity of a given partition using chip binning,
- 2843 ● `Beam_Profile_Tt_Sc_p` shows the estimated beam profile when taking efficiency scan. This
2844 is obtained by filtering `Time_Profile_Tt_Sc_p` to only consider the muon peak where the
2845 noise/gamma background has been subtracted. The resulting hit profile corresponds to the
2846 beam profile on the detector channels,
- 2847 ● `L0_Efficiency_Tt_Sc_p` shows the level 0 efficiency that was estimated **without** muon track-
2848 ing,
- 2849 ● `MuonCSize_H_Tt_Sc_p` shows the level 0 muon cluster size that was estimated **without** muon
2850 tracking, and
- 2851 ● `MuonCMult_H_Tt_Sc_p` shows the level 0 muon cluster multiplicity that was estimated **without**
2852 muon tracking.

2853 In the histogram labels, *t* stands for the trolley number (1 or 3), *c* for the chamber slot label in
2854 trolley *t* and *p* for the partition label (A, B, C or D depending on the chamber layout) as explained
2855 in Chapter 5.4.

2856 In the context of GIF++, an extra script called by the webDCS is called to extract the histograms
2857 from the ROOT files. The histograms are then stored in PNG and PDF formats into the correspond-
2858 ing folder (a single folder per HV step, so per ROOT file). the goal is to then display the histograms
2859 on the Data Quality Monitoring (DQM) page of the webDCS in order for the users to control the
2860 quality of the data taking at the end of data taking. An example of histogram organisation is given
2861 below:

2862



2864 *Here can put some screens from the webDCS to show the DQM and the plots available to users.*
 2865

2866 **B.2.1.2 CSV files**

2867 Moreover, up to 3 CSV files can be created depending on which ones of the 3 input files were in the
 2868 data folder:

- 2869 ● `Offline-Corrupted.csv` , is used to keep track of the amount of data that was corrupted and
 2870 removed from old data format files that don't contain any data quality flag.
- 2871 ● `Offline-Current.csv` , contains the summary of the currents and voltages applied on each
 2872 RPC HV channel.
- 2873 ● `Offline-L0-EffC1.csv` , is used to write the efficiencies, cluster size and cluster multiplicity
 2874 of efficiency runs. Note that `L0` refers here to *Level 0* and means that the results of efficiency and
 2875 clusterization are a first approximation calculated without performing any muon tracking in

2876 between the different detectors. This offline tool provides the user with a preliminar calculation
 2877 of the efficiency and of the muon event parameters. Another analysis software especially
 2878 dedicated to muon tracking is called on selected data to retrieve the results of efficiency and
 2879 muon clusterization using a tracking algorithm to discriminate noise or gamma from muons
 2880 as muons are the only particles that pass through the full setup, leaving hits than can be used
 2881 to reconstruct their tracks.

- 2882 • `Offline-Rate.csv`, is used to write the noise or gamma rates measured in the detector readout
 2883 partitions.

2884 Note that these 4 CSV files are created along with their *headers* (`Offline-[...]-Header.csv`
 2885 containing the names of each data columns) and are automatically merged together when the offline
 2886 analysis tool is called from the webDCS, contrary to the case where the tool is runned locally from
 2887 the terminal as the merging bash script is then not called. Thus, the resulting files, used to make
 2888 official plots, are:

- 2889 • `Corrupted.csv`,
 2890 • `Current.csv`,
 2891 • `L0-EffCl.csv`.
 2892 • `Rate.csv`.

2893 B.3 Analysis inputs and information handling

2894 The usage of the Offline Analysis tool as well as its output have been presented in the previous section.
 2895 It is now important to dig further and start looking at the source code and the inputs necessary
 2896 for the tool to work. Indeed, other than the raw ROOT data files that are analysed, more information
 2897 needs to be imported inside of the program to perform the analysis such as the description of the
 2898 setup inside of GIFT++ at the time of data taking (number of trolleys, of RPCs, dimensions of the
 2899 detectors, etc...) or the mapping that links the TDC channels to the coresponding RPC channels in
 2900 order to translate the TDC information into human readable data. 2 files are used to transmit all this
 2901 information:
 2902

- 2903 • `Dimensions.ini`, that provides the necessary setup and RPC information, and
 2904 • `ChannelsMapping.csv`, that gives the link between the TDC and RPC channels as well as the
 2905 *mask* for each channel (masked or not?).

2906 B.3.1 Dimensions file and InFile parser

2907 This input file, present in every data folder, allows the analysis tool to know of the number of active
 2908 trolleys, the number of active RPCs in those trolleys, and the details about each RPCs such as
 2909 the number of RPC gaps, the number of pseudo-rapidity partitions (for CMS-like prototypes), the
 2910 number of strips per partion or the dimensions. To do so, there are 3 types of groups in the INI file
 2911 architecture. A first general group, appearing only once at the head of the document, gives information
 2912 about the number of active trolleys as well as their IDs, as presented in Source Code B.1. For

2913 each active trolley, a group similar to Source Code B.2 can be found containing information about
 2914 the number of active detectors in the trolley and their IDs. Each trolley group as a `Tt` name format,
 2915 where `t` is the trolley ID. Finally, for each detector stored in slots of an active trolley, there is a group
 2916 providing information about their names and dimensions, as shown in Source Code B.3. Each slot
 2917 group as a `TtSs` name format, where `s` is the slot ID of trolley `t` where the active RPC is hosted.

```
2918 [General]
2919 nTrolleys=2
TrolleysID=13
```

2920 *Source Code B.1: Example of `[General]` group as might be found in `Dimensions.ini`. In Gif++, only 2 trolleys are available to hold RPCs and place them inside of the bunker for irradiation. The IDs of the trolleys are written in a single string as "13" and then read character by character by the program.*

```
2921 [T1]
nSlots=4
SlotsID=1234
```

2922 *Source Code B.2: Example of trolley group as might be found in `Dimensions.ini`. In this example, the file tells that there are 4 detectors placed in the holding slots of the trolley `T1` and that their IDs, written as a single string variable, are 1, 2, 3 and 4.*

```
2923 [T1S1]
Name=RE2-2-NPD-BARC-8
Partitions=3
Gaps=3
Gap1=BOT
Gap2=TN
Gap3=TW
AreaGap1=11694.25
AreaGap2=6432
AreaGap3=4582.82
Strips=32
ActiveArea-A=157.8
ActiveArea-B=121.69
ActiveArea-C=93.03
```

2924 *Source Code B.3: Example of slot group as might be found in `Dimensions.ini`. In this example, the file provides information about a detector named `RE2-2-NPD-BARC-8`, having 3 pseudo-rapidity readout partitions and stored in slot `S1` of trolley `T1`. This is a CMS RE2-2 type of detector. This information will then be used for example to compute the rate per unit area calculation.*

2925 This information is readout and stored in a C++ object called `IniFile`, that parses the information
 2926 in the INI input file and stores it into a local buffer for later use. This INI parser is the exact same
 2927 one that was previously developed for the Gif++ DAQ and described in Appendix A.5.2.

2928 B.3.2 TDC to RPC link file and Mapping

2929 The same way the INI dimension file information is stored using `map`, the channel mapping and mask
 2930 information is stored and accessed through `map`. First of all, the mapping CSV file is organised into
 2931 3 columns separated by tabulations (and not by commas, as expected for CSV files as it is easier using
 2932 streams to read tab or space separated data using C++):

2933

2934 RPC_channel TDC_channel mask

2935 using as formatting for each field:

2936

2937	TSCCC	TCCC	M
------	-------	------	---

2938 TSCCC is a 5-digit integer where τ is the trolley ID, s the slot ID in which the RPC is held insite
 2939 the trolley τ and ccc is the RPC channel number, or *strip* number, that can take values up to
 2940 3-digits depending on the detector,

2941 TCCC is a 4 digit integer where τ is the TDC ID, ccc is the TDC channel number that can take values
 2942 in between 0 and 127, and

2943 M is a 1-digit integer indicating if the channel should be considered ($M = 1$) or discarded ($M = 0$)
 2944 during analysis.

2945 This mapping and masking information is readout and stored thanks to the object `Mapping`, pre-
 2946 sented in Source Code B.4. Similarly to `IniFile` objects, this class has private methods. The first
 2947 one, `Mapping::CheckIfNewLine()` is used to find the newline character '`\n`' or return character
 2948 '`\r`' (depending on which kind of operating system interacted with the file). This is used for the
 2949 simple reason that the masking information has been introduced only during the year 2017 but the
 2950 channel mapping files exist since 2015 and the very beginning of data taking at GIF++. This means
 2951 that in the older data folders, before the upgrade, the channel mapping file only had 2 columns, the
 2952 RPC channel and the TDC channel. For compatibility reasons, this method helps controling the
 2953 character following the readout of the 2 first fields of a line. In case any end of line character is
 2954 found, no mask information is present in the file and the default $M = 1$ is used. On the contrary, if
 2955 the next character was a tabulation or a space, the mask information is present.

2956 Once the 3 fields have been readout, the second private method `Mapping::CheckIfTDCCh()` is
 2957 used to control that the TDC channel is an existing TDC channel. Finally, the information is stored
 2958 into 3 different maps (`Link`, `ReverseLink` and `Mask`) thanks to the public method `Mapping::Read()`.
 2959 `Link` allows to get the RPC channel by knowing the TDC channel while `ReverseLink` does the op-
 2960 posite by returning the TDC channel by knowing the RPC channel. Finally, `Mask` returns the mask
 2961 associated to a given RPC channel.

```

2962 typedef map<Uint,Uint> MappingData;
2963
2964 class Mapping {
2965     private:
2966         bool          CheckIfNewLine(char next);
2967         bool          CheckIfTDCCh(Uint channel);
2968         string        FileName;
2969         MappingData  Link;
2970         MappingData  ReverseLink;
2971         MappingData  Mask;
2972         int           Error;
2973
2974     public:
2975         Mapping();
2976         Mapping(string baseName);
2977         ~Mapping();
2978
2979         void SetFileName(const string filename);
2980         int  Read();
2981         Uint GetLink(Uint tdcchannel);
2982         Uint GetReverse(Uint rpcchannel);
2983         Uint GetMask(Uint rpcchannel);
2984     };

```

2964 *Source Code B.4: Description of C++ object Mapping used as a parser for the channel mapping and mask file.*

2965 B.4 Description of GIF++ setup within the Offline Analysis tool

2966 In the previous section, the tool input files have been discussed. The dimension file information is
 2967 stored in a map hosted by the `IniFile` object. But this information is then used to create a series of
 2968 new objects that helps defining the GIF++ infrastructure directly into the Offline Analysis. Indeed,
 2969 from the `RPC`, to the more general `Infrastructure`, every element of the GIF++ infrastrucutre is
 2970 recreated for each data analysis based on the information provided in input. All this information
 2971 about the infrastructure will be used to assign each hit signal to a specific strip channel of a specific
 2972 detector, and having a specific active area. This way, rate per unit area calculation is possible.
 2973

2974 B.4.1 RPC objects

2975 `RPC` objects have been developped to represent physical active detectors in GIF++ at the moment
 2976 of data taking. Thus, there are as many `RPC` objects created during the analysis than there were
 2977 active `RPCs` tested during a run. Each `RPC` hosts the information present in the corresponding INI
 2978 slot group, as shown in B.3, and organises it using a similar architecture. This can be seen from
 2979 Source B.5.

2980 To make the object more compact, the lists of gap labels, of gap active areas and strip active
 2981 areas are stored into `vector` dynamical containers. `RPC` objects are always contructed thanks to the
 2982 dimension file information stored into the `IniFILE` and their ID, using the format `TtSs`. Using the
 2983 `RPC` ID, the constructor calls the methods of `IniFILE` to initialise the `RPC`. The other constructors
 2984 are not used but exist in case of need. Finally, some getters have been written to access the different
 2985 private parameters storing the detector information.

```

2986
class RPC{
    private:
        string      name;           //RPC name as in webDCS database
        Uint        nGaps;          //Number of gaps in the RPC
        Uint        nPartitions;    //Number of partitions in the RPC
        Uint        nStrips;         //Number of strips per partition
        vector<string> gaps;       //List of gap labels (BOT, TOP, etc...)
        vector<float>  gapGeo;        //List of gap active areas
        vector<float>  stripGeo;      //List of strip active areas

    public:
        RPC();
        RPC(string ID, IniFile* geofile);
        RPC(const RPC& other);
        ~RPC();
        RPC& operator=(const RPC& other);

        string GetName();
        Uint GetNGaps();
        Uint GetNPartitions();
        Uint GetNStrips();
        string GetGap(Uint g);
        float GetGapGeo(Uint g);
        float GetStripGeo(Uint p);
};

2987

```

2988 *Source Code B.5: Description of C++ objects RPC that describe each active detectors used during data taking.*

2989 B.4.2 Trolley objects

2990 Trolley objects have been developped to represent physical active trolleys in GIFT++ at the moment
 2991 of data taking. Thus, there are as many trolley objects created during the analysis than there were
 2992 active trolleys hosting tested RPCs during a run. Each Trolley hosts the information present in the
 2993 corresponding INI trolley group, as shown in B.2, and organises it using a similar architecture. In
 2994 addition to the information hosted in the INI file, these object have a dynamical container of RPC
 2995 objects, representing the active detectors the active trolley was hosting at the time of data taking.
 2996 This can been seen from Source Code B.6.

2997 Trolley objects are always contructed thanks to the dimension file information stored into the
 2998 IniFILE and their ID, using the format Tt. Using the Trolley ID, the constructor calls the methods
 2999 of IniFILE to initialise the Trolley. Retrieving the information of the RPC IDs via SlotsID, a new
 3000 RPC is constructed and added to the container RPCs for each character in the ID string. The other
 3001 constructors are not used but exist in case of need. Finally, some getters have been written to access
 3002 the different private parameters storing the trolley and detectors information.

```

3003 class Trolley{
3004     private:
3005         Uint           nSlots; //Number of active RPCs in the considered trolley
3006         string        SlotsID; //Active RPC IDs written into a string
3007         vector<RPC*> RPCs;   //List of active RPCs
3008
3009     public:
3010         //Constructors, destructor and operator =
3011         Trolley();
3012         Trolley(string ID, IniFile* geofile);
3013         Trolley(const Trolley& other);
3014         ~Trolley();
3015         Trolley& operator=(const Trolley& other);
3016
3017         //Get GIFTrolley members
3018         Uint    GetNSlots();
3019         string  GetSlotsID();
3020         Uint    GetSlotID(Uint s);
3021
3022         //Manage RPC list
3023         RPC*   GetRPC(Uint r);
3024         void   DeleteRPC(Uint r);
3025
3026         //Methods to get members of RPC objects stored in RPCs
3027         string  GetName(Uint r);
3028         Uint    GetNGaps(Uint r);
3029         Uint    GetNPartitions(Uint r);
3030         Uint    GetNStrips(Uint r);
3031         string  GetGap(Uint r, Uint g);
3032         float   GetGapGeo(Uint r, Uint g);
3033         float   GetStripGeo(Uint r, Uint p);
3034     };

```

Source Code B.6: Description of C++ objects Trolley that describe each active trolley used during data taking.

3006 B.4.3 Infrastructure object

3007 The `Infrastructure` object has been developped to represent the GIFT++ bunker area dedicated to
 3008 CMS RPC experiments. With this very specific object, all the information about the CMS RPC
 3009 setup within GIFT++ at the moment of data taking is stored. It hosts the information present in the
 3010 corresponding INI general group, as shown in B.1, and organises it using a similar architecture. In
 3011 addition to the information hosted in the INI file, this object have a dynamical container of `Trolley`
 3012 objects, representing the active tolleys in GIFT++ area. This can be seen from Source Code B.7.

3013 The `Infrastructure` object is always contructed thanks to the dimension file information stored
 3014 into the `IniFILE`. Retrieving the information of the trolley IDs via `TrolleysID`, a new `Trolley` is
 3015 constructed and added to the container `Trolleys` for each character in the ID `string`. By extension,
 3016 it is easy to understand that the process described in Section B.4.2 for the construction of RPCs
 3017 takes place when a trolley is constructed. The other constructors are not used but exist in case of
 3018 need. Finally, some getters have been written to access the different private parameters storing the
 3019 infrastructure, tolleys and detectors information.

```

3020
class Infrastructure {
    private:
        Uint             nTrolleys;   //Number of active Trolleys in the run
        string          TrolleysID;  //Active trolley IDs written into a string
        vector<Trolley*> Trolleys;  //List of active Trolleys (struct)

    public:
        //Constructors and destructor
        Infrastructure();
        Infrastructure(IniFile* geofile);
        Infrastructure(const Infrastructure& other);
        ~Infrastructure();
        Infrastructure& operator=(const Infrastructure& other);

        //Get Infrastructure members
        Uint  GetNTrolleys();
        string GetTrolleysID();
        Uint   GetTrolleyID(Uint t);

3021
        //Manage Trolleys
        Trolley* GetTrolley(Uint t);
        void     DeleteTrolley(Uint t);

        //Methods to get members of GIFTrolley objects stored in Trolleys
        Uint  GetNSlots(Uint t);
        string GetSlotsID(Uint t);
        Uint   GetSlotID(Uint t, Uint s);
        RPC*  GetRPC(Uint t, Uint r);

        //Methods to get members of RPC objects stored in RPCs
        string GetName(Uint t, Uint r);
        Uint   GetNGaps(Uint t, Uint r);
        Uint   GetNPartitions(Uint t, Uint r);
        Uint   GetNStrips(Uint t, Uint r);
        string GetGap(Uint t, Uint r, Uint g);
        float  GetGapGeo(Uint t, Uint r, Uint g);
        float  GetStripGeo(Uint t, Uint r, Uint p);
    };

```

Source Code B.7: Description of C++ object *Infrastructure* that contains the full information about CMS RPC experiment in GIF++.

3023 B.5 Handeling of data

3024 As discussed in Appendix A.4.2, the raw data as a `TTree` architecture where every entry is related to
 3025 a trigger signal provided by a muon or a random pulse, whether the goal of the data taking was to
 3026 measure the performance of the detector or the noise/gamma background respectively. Each of these
 3027 entries, referred also as events, contain a more or less full list of hits in the TDC channels to which
 3028 the detectors are connected. To this list of hits corresponds a list of time stamps, marking the arrival
 3029 of the hits within the TDC channel.

3030 The infrastructure of the CMS RPC experiment within GIF++ being defined, combining the
 3031 information about the raw data with the information provided by both the mapping/mask file and the
 3032 dimension file allows to build new physical objects that will help in computing efficiency or rates.

3033 B.5.1 RPC hits

3034 The raw data stored in the ROOT file as output of the GIFT++ DAQ, is readout by the analysis tool
 3035 using the structure `RAWData` presented in Source Code B.9 that differs from the structure presented
 3036 in Appendix A.4.2 as it is not meant to hold all of the data contained in the ROOT file. In this sense,
 3037 this structure is in the case of the offline analysis tool not a dynamical object and will only be storing
 3038 a single event contained in a single entry of the `TTree`.

```
3039
  class RPCHit {
    private:
      Uint Channel;      //RPC channel according to mapping (5 digits)
      Uint Trolley;     //0, 1 or 3 (1st digit of the RPC channel)
      Uint Station;     //Slot where is held the RPC in Trolley (2nd digit)
      Uint Strip;       //Physical RPC strip where the hit occurred (last 3
→   digits)
      Uint Partition;   //Readout partition along eta segmentation
      float TimeStamp; //Time stamp of the arrival in TDC

    public:
      //Constructors, destructor & operator =
      RPCHit();
      RPCHit(Uint channel, float time, Infrastructure* Infra);
      RPCHit(const RPCHit& other);
      ~RPCHit();
      RPCHit& operator=(const RPCHit& other);

      //Get RPCHit members
      Uint GetChannel();
      Uint GetTrolley();
      Uint GetStation();
      Uint GetStrip();
      Uint GetPartition();
      float GetTime();
    };

    typedef vector<RPCHit> HitList;
    typedef struct GIFHitList { HitList rpc[NTROLLEYS][NSLOTS][NPARTITIONS]; }
→   GIFHitList;

    bool SortHitbyStrip(RPCHit h1, RPCHit h2);
    bool SortHitbyTime(RPCHit h1, RPCHit h2);
  
```

3041 *Source Code B.8: Description of C++ object `RPCHit`.*

```
3042
  struct RAWData{
    int iEvent;        //Event i
    int TDCNHits;    //Number of hits in event i
    int QFlag;         //Quality flag list (1 flag digit per TDC)
    vector<Uint> *TDCCh; //List of channels giving hits per event
    vector<float> *TDCTS; //List of the corresponding time stamps
  };

```

3043 *Source Code B.9: Description of C++ structure `RAWData`.*

3044 Each member of the structure is then linked to the corresponding branch of the ROOT data tree,
 3045 as shown in the example of Source Code B.10, and using the method `GetEntry(int i)` of the ROOT
 3046 class `TTree` will update the state of the members of `RAWData`.

```

3047   TTree* dataTree = (TTree*)dataFile.Get("RAWData");
3048   RAWData data;
3049
3050   dataTree->SetBranchAddress("EventNumber", &data.iEvent);
3051   dataTree->SetBranchAddress("number_of_hits", &data.TDCNHits);
3052   dataTree->SetBranchAddress("Quality_flag", &data.QFlag);
3053   dataTree->SetBranchAddress("TDC_channel", &data.TDCCh);
3054   dataTree->SetBranchAddress("TDC_TimeStamp", &data.TDCTS);

```

3049 *Source Code B.10: Example of link in between RAWData and TTree.*

3050 The data is then analysed entry by entry and to each element of the TDC channel list, a `RPCHit` is
 3051 constructed by linking each TDC channel to the corresponding RPC channel thanks to the `Mapping`
 3052 object. The information carried by the RPC channel format allows to easily retrieve the trolley and
 3053 slot from which the hit was recorded (see section B.3.2). Using these 2 values, the readout partition
 3054 can be found by knowing the strip channel and comparing it with the number of partitions and strips
 3055 per partition stored into the `Infrastructure` object.

3056 Thus `RPCHit` objects are then stored into 3D dynamical list called `GIFHitList` (Source Code B.9)
 3057 where the 3 dimensions refer to the 3 layers of the readout in `GIF++` : in the bunker there are *trolleys*
 3058 (τ) holding detectors in *slots* (s) and each detector readout is divided into 1 or more pseudo-rapidity
 3059 *partitions* (p). Using these 3 information allows to assign an address to each readout partition and
 3060 this address will point to a specific hit list.

3061

3062 **B.5.2 Clusters of hits**

3063 All the hits contained in the ROOT file have been sorted into the different hit lists through the
 3064 `GIFHitList`. At this point, it is possible to start looking for clusters. A cluster is a group of adjacent
 3065 strips getting hits within a time window of 25 ns. These strips are then assumed to be part of the same
 3066 physical avalanche signal generated by a muon passing through the chamber or by the interaction of
 3067 a gamma stopping into the electrodes of the RPCs.

3068 To keep the cluster information, `RPCCluster` objects have been defined as shown in Source
 3069 Code B.11. Using the information of each individual `RPCHit` taken out of the hit list, it stores
 3070 the cluster size (number of adjacent strips composing the cluster), the first and last hit, the center for
 3071 spatial reconstruction and finally the start and stop time stamps as well as te time spread in between
 3072 the first and last hit.

```

3073
class RPCCluster{
    private:
        Uint ClusterSize; //Size of cluster #ID
        Uint FirstStrip; //First strip of cluster #ID
        Uint LastStrip; //Last strip of cluster #ID
        float Center; //Center of cluster #ID ((first+last)/2)
        float StartStamp; //Time stamp of the earliest hit of cluster #ID
        float StopStamp; //Time stamp of the latest hit of cluster #ID
        float TimeSpread; //Time difference between earliest and latest hits
                           //of cluster #ID

    public:
        //Constructors, destructor & operator =
        RPCCluster();
        RPCCluster(HitList List, Uint cID, Uint cSize, Uint first, Uint firstID);
        RPCCluster(const RPCCluster& other);
        ~RPCCluster();
        RPCCluster& operator=(const RPCCluster& other);

        //Get Cluster members
        Uint GetID();
        Uint GetSize();
        Uint GetFirstStrip();
        Uint GetLastStrip();
        float GetCenter();
        float GetStart();
        float GetStop();
        float GetSpread();
    };

typedef vector<RPCCluster> ClusterList;

//Other functions to build cluster lists out of hit lists
void BuildClusters(HitList &cluster, ClusterList &clusterList);
void Clusterization(HitList &hits, TH1 *hcSize, TH1 *hcMult);

```

Source Code B.11: Description of C++ object cluster.

To investigate the hit list of a given detector partition, the function `Clusterization()` defined in `include/Cluster.h` needs the hits in the list to be time sorted. This is achieved by calling function `sort()` of library `<algorithm>` using the comparator `SortHitbyTime(RPCHit h1, RPCHit h2)` defined in `include/RPCHit.h` that returns `true` if the time stamp of hit `h1` is lower than that of `h2`. A first isolation of strips is made only based on time information. All the hits within the 25 ns window are taken separately from the rest. Then, this sub-list of hits is sorted this time by ascending strip number, using this time the comparator `SortHitbyStrip(RPCHit h1, RPCHit h2)`. Finally, the groups of adjacent strips are used to construct `RPCCluster` objects that are then stored in a temporary list of clusters that is at the end of the process used to know how many clusters were reconstructed and to fill their sizes into an histogram that will allows to know the mean size of muon or gamma clusters.

3088 B.6 DAQ data Analysis

All the ingredients to analyse GIF++ data have been defined. This section will focus on the different part of the analysis performed on the data, from determining the type of data the tool is dealing with

3091 to calculating the rate in each detector or reconstructing muon or gamma clusters.

3092 B.6.1 Determination of the run type

3093 In GIF++, both the performance of the detectors in detecting muons in an irradiated environment and
 3094 the gamma background can be independantly measured. These corresponds to different run types
 3095 and thus, to different TDC settings giving different data to look at.

3096 In the case of performance measurements, the trigger for data taking is provided by the coïncidence
 3097 of several scintillators when muons from the beam passing through the area are detected. Data
 3098 is collected in a 600 ns wide window around the arrival of muons in the RPCs. The expected time
 3100 distribution of hits is shown in Figure B.1a. The muon peak is clearly visible in the center of the
 3101 distribution and is to be extracted from the gamma background that composes the flat part of the
 3102 distribution.

3103 On the other hand, gamma background or noise measurements are focussed on the non muon
 3104 related physics and the trigger needs to be independant from the muons to give a good measurement
 3105 of the gamma/noise distribution as seen by the detectors. The trigger is then provided by a pulse
 3106 generator at a frequency of 300 Hz whose pulse is not likely to be on time with a muon. In order
 3107 to increase the integrated time without increasing the acquisition time too much, the width of the
 3108 acquisition windows are increased to 10 μ s. The time distribution of the hits is expected to be flat, as
 3109 shown by Figure B.1b.

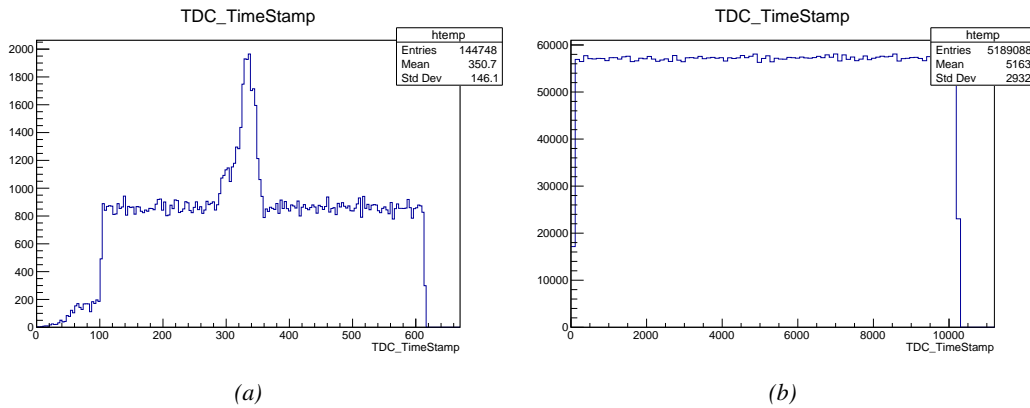


Figure B.1: Example of expected hit time distributions in the cases of efficiency (Figure B.1a) and noise/gamma rate per unit area (Figure B.1b) measurements as extracted from the raw ROOT files. The unit along the x-axis corresponds to ns. The fact that "the" muon peak is not well defined in Figure B.1a is due to the contribution of all the RPCs being tested at the same time that don't necessarily have the same signal arrival time. Each individual peak can have an offset with the ones of other detectors. The inconsistency in the first 100 ns of both time distributions is an artefact of the TDCs and are systematically rejected during the analysis.

3110 The ROOT files include a TTree called RunParameters containing, among other things, the in-
 3111 formation related to the type of run. The run type can then be accessed as described by Source
 3112 Code B.12 and the function IsEfficiencyRun() is then used to determine if the run file is an effi-
 3113 ciency run or, on the contrary, another type of run (noise or gamma measurement).

```

3114
3115     TTree* RunParameters = (TTree*)dataFile.Get("RunParameters");
3116     TString* RunType = new TString();
3117     RunParameters->SetBranchAddress("RunType", &RunType);
3118     RunParameters->GetEntry(0);

```

3116 *Source Code B.12: Access to the run type contained in TTree* RunParameters.*

3117 Finally, the data files will have a slightly different content whether it was collected before or after
 3118 October 2017 and the upgrade of the DAQ software that brought a new information into the ROOT
 3119 output. This is discussed in Appendix A.4.3 and implies that the analysis will differ a little depending
 3120 on the data format. Indeed, as no information on the data quality is stored, in older data files, the cor-
 3121 rections for missing events has to be done at the end of the analysis. The information about the type
 3122 of data format is stored in the variable **bool** `isNewFormat` by checking the list of branches contained
 3123 in the data tree via the methods `TTree::GetListOfBranches()` and `TCollection::Contains()`.

3124 **B.6.2 Beam time window calculation for efficiency runs**

3125 Knowing the run type is important first of all to know the width of the acquisition window to be used
 3126 for the rate calculation and finally to be able to seek for muons. Indeed, the peak that appears in the
 3127 time distribution for each detectors is then fitted to extract the most probable time window in which
 3128 the tool should look for muon hits. The data outside of this time window is then used to evaluate the
 3129 noise or gamma background the detector was subjected to during the data taking. Computing the
 3130 position of the peak is done calling the function `SetBeamWindow()` defined in file `src/RPCHit.cc` that
 3131 loops a first time on the data. The data is first sorted in a 3D array of 1D histograms (`GIFH1Array`, see
 3132 `include/types.h`). Then the location of the highest bin is determined using `TH1::GetMaximumBin()`
 3133 and is used to define a window in which a gaussian fit will be applied to compute the peak width.
 3134 This window is a 80 ns defined by Formula B.1 around the central bin.

$$t_{center}(ns) = \text{bin} \times \text{width}_{\text{bin}}(ns) \quad (\text{B.1a})$$

$$[t_{low}; t_{high}] = [t_{center} - 40; t_{center} + 40] \quad (\text{B.1b})$$

3135 Before the fit is performed, the average number of noise/gamma hits per bin is evaluated using
 3136 the data outside of the fit window. Excluding the first 100 ns, the average number of hits per bin
 3137 due to the noise or gamma is defined by Formula B.2 after extracting the amount of hits in the time
 3138 windows $[100; t_{low}]$ and $[t_{high}; 600]$ thanks to the method `TH1::Integral()`. This average number
 3139 of hits is then subtracted to every bin of the 1D histogram, in order to *clean* it from the noise or
 3140 gamma contribution as much as possible to improve the fit quality. Bins where $\langle n_{\text{hits}} \rangle$ is greater
 3141 than the actual bin content are set to 0.

$$\Delta t_{noise}(ns) = 600 \overbrace{-t_{high} + t_{low}}^{-80ns} - 100 = 420ns \quad (\text{B.2a})$$

$$\langle n_{\text{hits}} \rangle = \text{width}_{\text{bin}}(ns) \times \frac{\sum_{t=100}^{t_{low}} + \sum_{t=t_{high}}^{600}}{\Delta t_{noise}(ns)} \quad (\text{B.2b})$$

3142 Finally, the fit parameters are extracted and saved for each detector in 3D arrays of **float**
 3143 (`muonPeak`, see `include/types.h`), a first one for the mean arrival time of the muons, `PeakTime`,

3144 and a second one for the width of the peak, `PeakWidth`. The width is defined as 6σ of the gaussian
 3145 fit. The same settings are applied to every partitions of the same detector. To determine which one
 3146 of the detector's partitions is directly illuminated by the beam, the peak height of each partition is
 3147 compared and the highest one is then used to define the peak settings.

3148 **B.6.3 Data loop and histogram filling**

3149 3D arrays of histogram are created to store the data and display it on the DQM of G4F++ webDCS
 3150 for the use of shifters. These histograms, presented in section B.2.1.1, are filled while looping on
 3151 the data. Before starting the analysis loop, it is necessary to control the entry quality for the new
 3152 file formats featuring `QFlag`. If the `QFlag` value for this entry shows that 1 TDC or more have a
 3153 `CORRUPTED` flag, then this event is discarded. The loss of statistics is low enough to be neglected.
 3154 `QFlag` is controlled using the function `IsCorruptedEvent()` defined in `src/utils.cc`. As explained
 3155 in Appendix A.4.3, each digit of this integer represents a TDC flag that can be 1 or 2. Each 2 is
 3156 the sign of a `CORRUPTED` state. Then, the data is accessed entry by entry in the ROOT `TTree` using
 3157 `RAWData` and each hit in the hit list is assigned to a detector channel and saved in the corresponding
 3158 histograms. In the first part of the analysis, in which the loop over the ROOT file's content is
 3159 performed, the different steps are:

3160 **1- RPC channel assignment and control:** a check is done on the RPC channel extracted thanks
 3161 to the mapping via the method `Mapping::GetLink()`. If the channel is not initialised and is 0, or if
 3162 the TDC channel was greater than 5127, the hit is discarded. This means there was a problem in the
 3163 mapping. Often a mapping problem leads to the crash of the offline tool.

3164 **2- Creation of a `RPCHit` object:** to easily get the trolley, slot and partition in which the hit has
 3165 been assigned, this object is particularly helpful.

3166 **3- General histograms are filled:** the hit is filled into the time distribution and the general hit
 3167 distribution histograms, and if the arrival time is within the first 100 ns, it is discarded and nothing
 3168 else happens and the loop proceeds with the next hit in the list.

3169 **4- Multiplicity counter:** the hit multiplicity counter of the corresponding detectors incremented.

3170 **5-a- Efficiency runs - Is the hit within the peak window? :** if the peak is contained in the peak
 3171 window previously defined in section B.6.2, the hit is filled into the beam hit profile histogram of
 3172 the corresponding chamber, added into the list of muon hits and increments the counter of *in time*
 3173 hits. The term *in time* here refers to the hits that are likely to be muons by arriving in the expected
 3174 time window. If the hit is outside of the peak window, it is filled into the noise profile histogram
 3175 of the corresponding detector, added into the list of noise/gamma hits and increments the counter of
 3176 noise/gamma hits.

3177 **5-b- Noise/gamma rate runs - Noise histograms are filled:** the hit is filled into the noise profile
 3178 histogram of the corresponding detector, added into the list of noise/gamma hits and increments the
 3179 counter of noise/gamma hits.

After the loop on the hit list of the entry is over, the next step is to clusterize the 3D lists filled in the previous steps. A 3D loop is then started over the active trolley, slot and RPC partitions to access these objects. Each `NoiseHitList` and `MuonHitList`, in case of efficiency run, are clusterized as described in section B.5.2. There corresponding cluster size and multiplicity histograms are filled at the end of the clustering process. Then, the efficiency histogram is filled in case of efficiency run. The selection is simply made by checking whether the RPC detected signals in the peak window during this event. Nevertheless, it is useful to highlight that at this level, it is not possible yet to discriminate in between a muon hit and noise or gamma hit. Thus, `MuonCSize_H`, `MuonCMult_H` and `Efficiency0_H` are subjected to noise and gamma contamination. This contamination will be estimated and corrected at the moment the results will be written into output CSV files. Finally, the loop ends on the filling of the general hit multiplicity histogram.

B.6.4 Results calculation

As mentioned in section B.2.1, the analysis of DAQ data provides the user with 3 CSV files and a ROOT file associated to each and every ROOT data file. The fourth CSV file is provided by the extraction of the CEAN main frame data monitored during data taking and will be discussed later. After looping on the data in the previous part of the analysis macro, the output files are created and a 3D loop on each RPC readout partitions is started to extract the histograms parameters and compute the final results.

3199

B.6.4.1 Rate normalisation

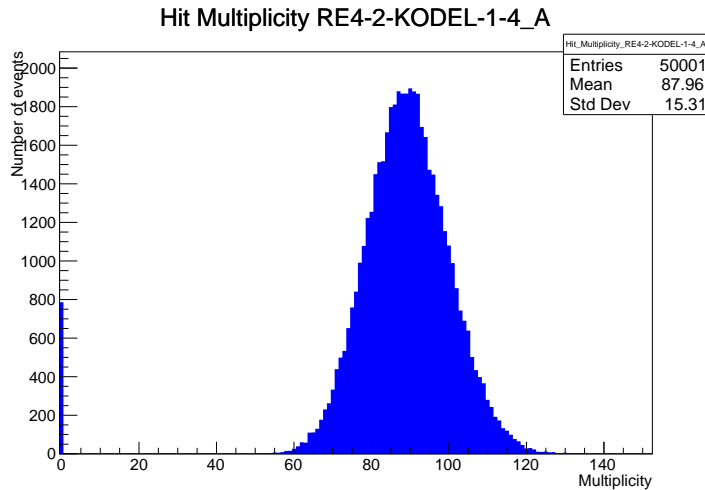


Figure B.2: The effect of the quality flag is explained by presenting the reconstructed hit multiplicity of a data file without `Quality_flag`. The artificial high content of bin 0 is the effect of corrupted data.

To analyse old data format files, not containing any quality flag, it is needed to estimate the amount of corrupted data via a fit as the corrupted data will always fill events with a fake "0 multiplicity". Indeed, as no hits were stored in the DAQ ROOT files, these events artificially contribute to fill the bin corresponding to a null multiplicity, as shown in Figure B.2. In the case the mean of the

3201
3202
3203
3204

3205 hit multiplicity distribution is high, the contribution of the corrupted data can easily be evaluated
 3206 for later correction by comparing the level of the bin at multiplicity 0 and of a skew fit curve that
 3207 should indicate a value consistent with 0. A skew fit has been chosen over a Poisson fit as it was
 3208 giving better results for lower mean multiplicity values. Nevertheless, for low irradiation cases,
 3209 as explained in Appendix A.4.3, the hit multiplicity distribution mean is, on the contrary, rather
 3210 small and the probability to record events without hits can't be considered small anymore, leading
 3211 to a difficult and non-reliable estimation of the corruption. As can be seen in Source Code B.13,
 3212 conditions have been applied to prevent bad fits and wrong corruption estimation in cases where :

3213 • The difference in between the data for multiplicity 1 and the corresponding fit value should be
 3214 lower than 1% of the total amount of data : $\frac{|n_{m=1} - sk(1)|}{N_{tot}} < 0.01$ where $n_{m=1}$ is the number
 3215 of entries with multiplicity 1, $sk(1)$ the value of the skew fit, as defined by Formula 5.3, for
 3216 multiplicity 1 and N_{tot} the total number of entries.

3217 • The amount of data contained in the multiplicity 0 bin should not exceed 40% : $\frac{n_{m=0}}{N_{tot}} \leq 0.4$
 3218 where $n_{m=0}$ is the number of entries with multiplicity 0. This number has been determined
 3219 to be the maximum to be able to separate the excess of data due to corruption from the hit
 3220 multiplicity distribution.

3221 Those 2 conditions need to be fulfilled to estimate the corruption of old data format files. If the
 3222 fit was successful, the level of corruption is written in `Offline-Corrupted.csv` and the number of
 3223 corrupted entries, refered as the integer `nEmptyEvent`, is subtracted from the total number of entries
 3224 when the rate normalisation factor is computed as explicit in Source Code B.13. Note that for new
 3225 data format files, the number of corrupted entries being set to 0, the definition of `rate_norm` stays
 3226 valid.

```

3227
if(!isNewFormat){
    TF1* GaussFit = new TF1("gaussfit","[0]*exp(-0.5*((x-[1])/[2])**2)",0,Xmax);
    GaussFit->SetParameter(0,100);
    GaussFit->SetParameter(1,10);
    GaussFit->SetParameter(2,1);
    HitMultiplicity_H.rpc[T][S][p]->Fit(GaussFit,"LIQR","",0.5,Xmax);

    TF1* SkewFit = new TF1("skewfit","[0]*exp(-0.5*((x-[1])/[2])**2) / (1 +
→ exp(-[3]*(x-[4])))",0,Xmax);
    SkewFit->SetParameter(0,GaussFit->GetParameter(0));
    SkewFit->SetParameter(1,GaussFit->GetParameter(1));
    SkewFit->SetParameter(2,GaussFit->GetParameter(2));
    SkewFit->SetParameter(3,1);
    SkewFit->SetParameter(4,1);
    HitMultiplicity_H.rpc[T][S][p]->Fit(SkewFit,"LIQR","",0.5,Xmax);

    double fitValue = SkewFit->Eval(1,0,0,0);
    double dataValue = (double)HitMultiplicity_H.rpc[T][S][p]->GetBinContent(2);
    double difference = TMath::Abs(dataValue - fitValue);
    double fitTOdataVSentries_ratio = difference / (double)nEntries;
    bool isFitGOOD = fitTOdataVSentries_ratio < 0.01;

3228
    double nSinglehit = (double)HitMultiplicity_H.rpc[T][S][p]->GetBinContent(1);
    double lowMultRatio = nSinglehit / (double)nEntries;
    bool isMultLOW = lowMultRatio > 0.4;

    if(isFitGOOD && !isMultLOW){
        nEmptyEvent = HitMultiplicity_H.rpc[T][S][p]->GetBinContent(1);
        nPhysics = (int)SkewFit->Eval(0,0,0,0);
        if(nPhysics < nEmptyEvent)
            nEmptyEvent = nEmptyEvent-nPhysics;
    }
}

double corrupt_ratio = 100.*(double)nEmptyEvent / (double)nEntries;
outputCorrCSV << corrupt_ratio << '\t';

float rate_norm = 0.;
float stripArea = GIFIInfra->GetStripGeo(tr,sl,p);

if(IsEfficiencyRun(RunType)){
    float noiseWindow = BMTDCWINDOW - TIMEREJECT - 2*PeakWidth.rpc[T][S][p];
    rate_norm = (nEntries-nEmptyEvent)*noiseWindow*1e-9*stripArea;
} else
    rate_norm = (nEntries-nEmptyEvent)*RDMNOISEWDW*1e-9*stripArea;

```

Source Code B.13: Definition of the rate normalisation variable. It takes into account the number of non corrupted entries and the time window used for noise calculation, to estimate the total integrated time, and the strip active area to express the result as rate per unit area.

3230 B.6.4.2 Rate and activity

3231 At this point, the strip rate histograms, StripNoiseProfile_H.rpc[T][S][p], only contain an in-
3232 formation about the total number of noise or rate hits each channel received during the data taking.
3233 As described in Source Code B.14, a loop on the strip channels will be used to normalise the content
3234 of the rate distribution histogram for each detector partitions. The initial number of hits recorded for
3235 a given bin will be extracted and 2 values will be computed:

- 3236 ● the strip rate, defined as the number of hits recorded in the bin normalised like described in
 3237 the previous section, using the variable `rate_norm`, and

- 3238 ● the strip activity, defined as the number of hits recorded in the bin normalised to the average
 3239 number of hits per bin contained in the partition histogram, using the variable `averageNhit`.
 3240 This value provides an information on the homogeneity of the detector response to the gamma
 3241 background or of the detector noise. An activity of 1 corresponds to an average response.
 3242 Above 1, the channel is more active than the average and bellow 1, the channel is less active.

```

int nNoise = StripNoiseProfile_H.rpc[T][S][p]->GetEntries();
float averageNhit = (nNoise>0) ? (float)(nNoise/nStripsPart) : 1.;

for(Uint st = 1; st <= nStripsPart; st++) {
    float stripRate =
        StripNoiseProfile_H.rpc[T][S][p]->GetBinContent(st)/rate_norm;
    float stripAct =
        StripNoiseProfile_H.rpc[T][S][p]->GetBinContent(st)/averageNhit;

    StripNoiseProfile_H.rpc[T][S][p]->SetBinContent(st,stripRate);
    StripActivity_H.rpc[T][S][p]->SetBinContent(st,stripAct);
}

```

3244 *Source Code B.14: Description of the loop that allows to set the content of each strip rate and strip activity
 channel for each detector partition.*

3245 On each detector partitions, which are readout by a single FEE, all the channels are not processed
 3246 by the same chip. Each chip can give a different noise response and thus, histograms using a chip
 3247 binning are used to investigate chip related noise behaviours. The average values of the strip rate
 3248 or activity grouped into a given chip are extracted using the using the function `GetChipBin()` and
 3249 stored in dedicated histograms as described in Source Codes B.15 and B.16 respectively.

```

float GetChipBin(TH1* H, Uint chip){
    Uint start = 1 + chip*NSTRIPSCHIP;
    int nActive = NSTRIPSCHIP;
    float mean = 0.;

    for(Uint b = start; b <= (chip+1)*NSTRIPSCHIP; b++) {
        float value = H->GetBinContent(b);
        mean += value;
        if(value == 0.) nActive--;
    }

    if(nActive != 0) mean /= (float)nActive;
    else mean = 0.;

    return mean;
}

```

3252 *Source Code B.15: Function used to compute the content of a bin for an histogram using chip binning.*

```

3253   for(UInt ch = 0; ch < (nStripsPart/NSTRIPSCHIP); ch++) {
3254     ChipMeanNoiseProf_H.rpc[T][S][p]->
3255       SetBinContent(ch+1,GetChipBin(StripNoiseProfile_H.rpc[T][S][p],ch));
3256     ChipActivity_H.rpc[T][S][p]->
3257       SetBinContent(ch+1,GetChipBin(StripActivity_H.rpc[T][S][p],ch));
3258   }

```

Source Code B.16: Description of the loop that allows to set the content of each chip rate and chip activity bins for each detector partition knowing the information contained in the corresponding strip distribution histograms.

The activity variable is used to evaluate the homogeneity of the detector response to background or of the detector noise. The homogeneity h_p of each detector partition can be evaluated using the formula $h_p = \exp(-\sigma_p^R / \langle R \rangle_p)$, where $\langle R \rangle_p$ is the partition mean rate and σ_p^R is the rate standard deviation calculated over the partition channels. The more homogeneously the rates are distributed and the smaller will σ_p^R be, and the closer to 1 will h_p get. On the contrary, if the standard deviation of the channel's rates is large, h_p will rapidly get to 0. This value is saved into histograms as shown in Source Code B.17 and could in the future be used to monitor through time, once extracted, the evolution of every partition homogeneity. This could be of great help to understand the apparition of eventual hot spots due to ageing of the chambers subjected to high radiation levels. The monitored homogeneity information could then be combined with a monitoring of the activity of each individual channel in order to have a finer information. Monitoring tools have been suggested and need to be developed for this purpose.

```

3267   float MeanPartSDev = GetTH1StdDev(StripNoiseProfile_H.rpc[T][S][p]);
3268   float strip_homog = (MeanPartRate==0)
3269     ? 0.
3270     : exp(-MeanPartSDev/MeanPartRate);
3271   StripHomogeneity_H.rpc[T][S][p]->Fill("exp -#left(#frac{\#sigma_{Strip}
3272     \rightarrow Rate}{\#mu_{Strip Rate}}\#right)",strip_homog);
3273   StripHomogeneity_H.rpc[T][S][p]->GetYaxis()->SetRangeUser(0.,1.);
3274
3275   float ChipStDevMean = GetTH1StdDev(ChipMeanNoiseProf_H.rpc[T][S][p]);
3276   float chip_homog = (MeanPartRate==0)
3277     ? 0.
3278     : exp(-ChipStDevMean/MeanPartRate);
3279   ChipHomogeneity_H.rpc[T][S][p]->Fill("exp -#left(#frac{\#sigma_{Chip}
3280     \rightarrow Rate}{\#mu_{Chip Rate}}\#right)",chip_homog);
3281   ChipHomogeneity_H.rpc[T][S][p]->GetYaxis()->SetRangeUser(0.,1.);

```

Source Code B.17: Storage of the homogeneity into dedicated histograms.

3270 B.6.4.3 Strip masking tool

The offline tool is automatically called at the end of each data taking to analyse the data and offer the shifter DQM histograms to control the data quality. After the histograms have been published online in the DQM page, the shifter can decide to mask noisy or dead channels that will contribute to bias the final rate calculation by editing the mask column of `ChannelsMapping.csv` as can be seen in Figure B.3.

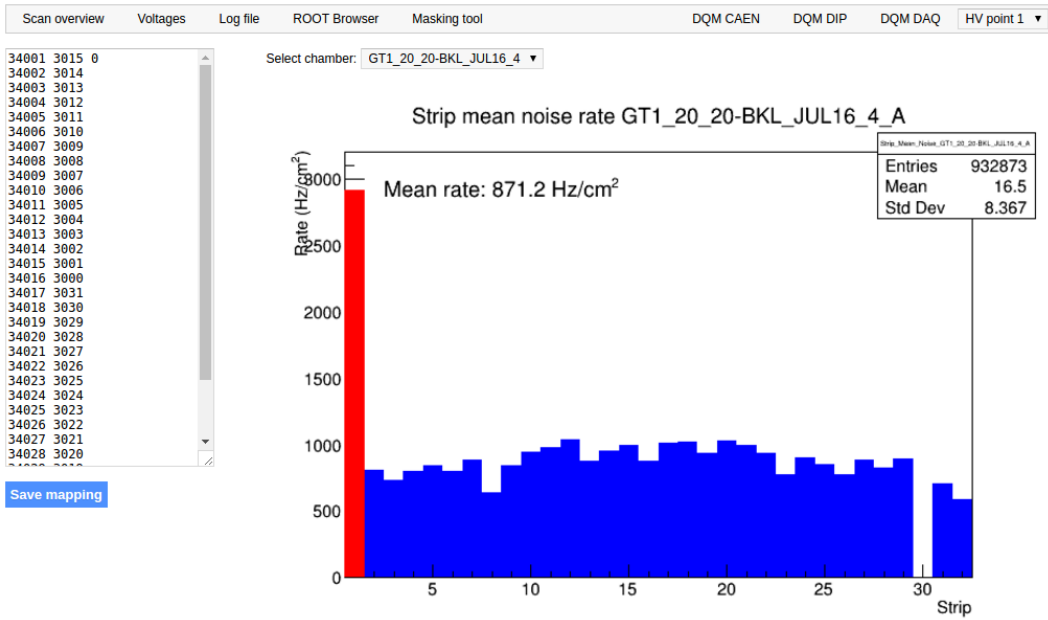


Figure B.3: Display of the masking tool page on the webDCS. The window on the left allows the shifter to edit ChannelsMapping.csv. To mask a channel, it only is needed to set the 3rd field corresponding to the strip to mask to 0. It is not necessary for older mapping file formats to add a 1 for each strip that is not masked as the code is versatile and the default behaviour is to consider missing mask fields as active strips. The effect of the mask is directly visible for noisy channels as the corresponding bin turns red. The global effect of masking strips will be an update of the rate value showed on the histogram that will take into consideration the rejected channels.

3276 From the code point of view, the function `GetTH1Mean()` is used to retrieve the mean rate par-
 3277 tition by partition after the rates have been calculated strip by strip and filled into the histograms
 3278 `StripNoiseProfile_H.rpc[T][S][p]`, as described through Source Code B.18.

3279 Once the mask for each rejected channel has been updated, the shifter can manually run the of-
 3280 fline tool again to update the DQM plots, now including the masked strips, as well the rate results
 3281 written in the output CSV file `Offline-Rate.csv`. If not done during the shifts, the strip masking
 3282 procedure needs to be carefully done by the person in charge of data analysis on the scans that were
 3283 selected to produce the final results.

```

3284   float GetTH1Mean(TH1* H) {
3285     int nBins = H->GetNbinsX();
3286     int nActive = nBins;
3287     float mean = 0.;
3288
3289     for(int b = 1; b <= nBins; b++) {
3290       float value = H->GetBinContent(b);
3291       mean += value;
3292       if(value == 0.) nActive--;
3293     }
3294
3295     if(nActive != 0) mean /= (float)nActive;
3296     else mean = 0.;
3297
3298     return mean;
3299   }

```

Source Code B.18: The function `GetTH1Mean()` is used to return the mean along the y-axis of `TH1` histograms containing rate information. In order to take into account masked strips whose rate is set to 0, the function looks for masked channels and decrement the number of active channels for each null value found.

3287 B.6.4.4 Output CSV files filling

3288 All the histograms have been filled. Parameters will then be extracted from them to compute the
 3289 final results that will later be used to produce plots. Once the results have been computed, the very
 3290 last step of the offline macro is to write these values into the corresponding CSV outputs. Aside of
 3291 the file `Offline-Corrupted.csv`, 2 CSV files are being written by the macro `offlineAnalysis()`,
 3292 `Offline-Rates.csv` and `Offline-L0-EffCl.csv` that respectively contain information about noise
 3293 or gamma rates, cluster size and multiplicity, and about level 0 reconstruction of the detector effi-
 3294 ciency, muon cluster size and multiplicity. Details on the computation and file writing are respec-
 3295 tively given in Sources Codes B.19 and B.20.

3296 **Noise/gamma background variables** are computed and written in the output file for each detector
 3297 partitions. A detector average of the hit and cluster rate is also provided, as shown through Sources
 3298 Code B.19. The variables that are written for each partition are:

- 3299 • The mean partition hit rate per unit area, `MeanPartRate`, that is extracted from the histogram
 3300 `StripNoiseProfile_H` as the mean value along the y-axis, as described in section B.6.4.3. No
 3301 error is recorded for the hit rate as this is considered a single measurement. No statistical error
 3302 can be associated to it and the systematics are unknown.
- 3303 • The mean cluster size, `cSizePart`, is extracted from the histogram `NoiseCSize_H` and it's
 3304 statistical error, `cSizePartErr`, is taken to be 2σ of the total distribution.
- 3305 • The mean cluster multiplicity per trigger, `cMultPart`, is extracted from the histogram `NoiseCMult_H`
 3306 and it's statistical error, `cMultPartErr`, is taken to be 2σ of the total distribution. It is impor-
 3307 tant to point to the fact that this variable gives an information that is dependent on the buffer
 3308 window width used for each trigger for the calculation.
- 3309 • The mean cluster rate per unit area, `ClustPartRate`, is defined as the mean hit rate normalised

3310 to the mean cluster size and it's statistical error, `ClustPartRateErr`, is then obtained using the
 3311 relative statistical error on the mean cluster size.

```

for (UInt tr = 0; tr < GIFInfra->GetNTrolleys(); tr++) {
  UInt T = GIFInfra->GetTrolleyID(tr);

  for (UInt sl = 0; sl < GIFInfra->GetNSlots(tr); sl++) {
    UInt S = GIFInfra->GetSlotID(tr,sl) - 1;

    float MeanNoiseRate = 0.;
    float ClusterRate = 0.;
    float ClusterSDev = 0.;

    for (UInt p = 0; p < GIFInfra->GetNPartitions(tr,sl); p++) {
      float MeanPartRate = GetTH1Mean(StripNoiseProfile_H.rpc[T][S][p]);
      float cSizePart = NoiseCSIZE_H.rpc[T][S][p]->GetMean();
      float cSizePartErr = (NoiseCSIZE_H.rpc[T][S][p]->GetEntries()==0)
        ? 0.
        : 2*NoiseCSIZE_H.rpc[T][S][p]->GetStdDev() /
          sqrt(NoiseCSIZE_H.rpc[T][S][p]->GetEntries());
      float cMultPart = NoiseCMult_H.rpc[T][S][p]->GetMean();
      float cMultPartErr = (NoiseCMult_H.rpc[T][S][p]->GetEntries()==0)
        ? 0.
        : 2*NoiseCMult_H.rpc[T][S][p]->GetStdDev() /
          sqrt(NoiseCMult_H.rpc[T][S][p]->GetEntries());
      float ClustPartRate = (cSizePart==0) ? 0.
        : MeanPartRate/cSizePart;
      float ClustPartRateErr = (cSizePart==0) ? 0.
        : ClustPartRate * cSizePartErr/cSizePart;

      outputRateCSV << MeanPartRate << '\t'
        << cSizePart << '\t' << cSizePartErr << '\t'
        << cMultPart << '\t' << cMultPartErr << '\t'
        << ClustPartRate << '\t' << ClustPartRateErr << '\t';

      RPCarea += stripArea * nStripsPart;
      MeanNoiseRate += MeanPartRate * stripArea * nStripsPart;
      ClusterRate += ClustPartRate * stripArea * nStripsPart;
      ClusterSDev += (cSizePart==0)
        ? 0.
        : ClusterRate*cSizePartErr/cSizePart;
    }

    MeanNoiseRate /= RPCarea;
    ClusterRate /= RPCarea;
    ClusterSDev /= RPCarea;

    outputRateCSV << MeanNoiseRate << '\t'
      << ClusterRate << '\t' << ClusterSDev << '\t';
  }
}

```

Source Code B.19: Description of rate result calculation and writing into the CSV output `Offline-Rate.csv`. Are saved into the file for each detector, the mean partition rate, cluster size and cluster mutiplicity, along with their errors, for each partition and as well as a detector average.

3314 **Muon performance variables** are computed and written in the output file for each detector parti-
 3315 tions as shown through Sources Code B.20. The variables that are written for each partition are:

- 3316 ● The muon efficiency, `eff`, extracted from the histogram `Efficiency0_H`. It is reminded that
3317 this offline tool doesn't include any tracking algorithm to identify muons from the beam and
3318 only relies on the hits arriving in the time window corresponding to the beam time. The con-
3319 tent of the efficiency histogram is thus biased by the noise/gamma background contribution
3320 into this window and is thus corrected by estimating the muon data content in the peak re-
3321 gion knowing the noise/gamma content in the rate calculation region. Both time windows
3322 being different, the choice was made to normalise the noise/gamma background calculation
3323 window to it's equivalent beam window in order to have comparable values using the variable
3324 `windowRatio`. Finally, to estimate the data ratio in the peak region, the variable `DataRatio`
3325 is defined as the ratio in between the estimated mean cluster multiplicity of the muons in the
3326 peak region, `MuonCM`, and of the total mean cluster multiplicity in the peak region, `PeakCM`.
3327 `MuonCM` is itself defined as the difference in between the total mean cluster multiplicity in the
3328 peak region and the normalised mean noise/gamma cluster multiplicity calculated outside of
3329 the peak region. The statistical error related to the efficiency, `eff_err`, is computed using a
3330 binomial distribution, as the efficiency measure the probability of "success" and "failure" to
3331 detect muons.
- 3332 ● The mean muon cluster size, `MuonCS`, is calculated using the total mean cluster size and multi-
3333 plicity in the peak region, respectively extracted from histograms `MuonCSize_H` and `MuonCMult_H`,
3334 the noise/gamma background mean cluster size and normalised multiplicity, extracted from
3335 `NoiseCSize_H` and `NoiseCMult_H`, and of the estimated muon cluster multiplicity `MuonCM` pre-
3336 viously explicated. The associated statistical error, `MuonCM_err`, is calculated using the propa-
3337 gation of errors of the mentioned variables.
- 3338 ● The mean muon cluster multiplicity in the peak region, `MuonCM`, explicated above whose sta-
3339 tistical error, `MuonCM_err`, is the sum of statistical error associated to the total mean clus-
3340 ter multiplicity in the peak reagion, `PeakCM_err`, and of the mean noise/gamma cluster size,
3341 `NoiseCM_err`.

3342 In addition to these 2 CSV files, the histograms are saved in ROOT file `Scan00XXXX_HVY_Offline.root`
3343 as explained in section B.2.1.1.

3344

```

for (UInt tr = 0; tr < GIFInfra->GetNTrolleys(); tr++) {
    UInt T = GIFInfra->GetTrolleyID(tr);
    for (UInt sl = 0; sl < GIFInfra->GetNSlots(tr); sl++) {
        UInt S = GIFInfra->GetSlotID(tr,sl) - 1;
        for (UInt p = 0; p < GIFInfra->GetNPartitions(tr,sl); p++) {
            float noiseWindow =
                BMTDCWINDOW - TIMEREJECT - 2*PeakWidth.rpc[T][S][p];
            float peakWindow = 2*PeakWidth.rpc[T][S][p];
            float windowRatio = peakWindow/noiseWindow;

            float PeakCM = MuonCMult_H.rpc[T][S][p]->GetMean();
            float PeakCS = MuonCSize_H.rpc[T][S][p]->GetMean();
            float NoiseCM = NoiseCMult_H.rpc[T][S][p]->GetMean() *windowRatio;
            float NoiseCS = NoiseCSize_H.rpc[T][S][p]->GetMean();
            float MuonCM = (PeakCM<NoiseCM) ? 0. : PeakCM-NoiseCM;
            float MuonCS = (MuonCM==0 || PeakCM*PeakCS<NoiseCM*NoiseCS)
                ? 0.
                : (PeakCM*PeakCS-NoiseCM*NoiseCS) / MuonCM;
            float PeakCM_err = (MuonCMult_H.rpc[T][S][p]->GetEntries()==0.)
                ? 0.
                : 2*MuonCMult_H.rpc[T][S][p]->GetStdDev() /
                    sqrt(MuonCMult_H.rpc[T][S][p]->GetEntries());
            float PeakCS_err = (MuonCSize_H.rpc[T][S][p]->GetEntries()==0.)
                ? 0.
                : 2*MuonCSize_H.rpc[T][S][p]->GetStdDev() /
                    sqrt(MuonCSize_H.rpc[T][S][p]->GetEntries());
            float NoiseCM_err = (NoiseCMult_H.rpc[T][S][p]->GetEntries()==0.)
                ? 0.
                : windowRatio*2*NoiseCMult_H.rpc[T][S][p]->GetStdDev() /
                    sqrt(NoiseCMult_H.rpc[T][S][p]->GetEntries());
            float NoiseCS_err = (NoiseCSize_H.rpc[T][S][p]->GetEntries()==0.)
                ? 0.
                : 2*NoiseCSize_H.rpc[T][S][p]->GetStdDev() /
                    sqrt(NoiseCSize_H.rpc[T][S][p]->GetEntries());
            float MuonCM_err = (MuonCM==0) ? 0. : PeakCM_err+NoiseCM_err;
            float MuonCS_err = (MuonCS==0 || MuonCM==0) ? 0.
                : (PeakCS*PeakCM_err + PeakCM*PeakCS_err +
                    NoiseCS*NoiseCM_err + NoiseCM*NoiseCS_err +
                    MuonCS*MuonCM_err) / MuonCM;

            float DataRatio = MuonCM/PeakCM;
            float DataRatio_err = (MuonCM==0) ? 0.
                : DataRatio*(MuonCM_err/MuonCM + PeakCM_err/PeakCM);
            float eff = DataRatio*Efficiency0_H.rpc[T][S][p]->GetMean();
            float eff_err = DataRatio*2*Efficiency0_H.rpc[T][S][p]->GetStdDev() /
                sqrt(Efficiency0_H.rpc[T][S][p]->GetEntries()) +
                Efficiency0_H.rpc[T][S][p]->GetMean()*DataRatio_err;

            outputEffCSV << eff << '\t' << eff_err << '\t'
                << MuonCS << '\t' << MuonCS_err << '\t'
                << MuonCM << '\t' << MuonCM_err << '\t';
        }
    }
}

```

3345

Source Code B.20: Description of efficiency result calculation and writing into the CSV output Offline-L0-EffCl.csv. Are saved into the file for each detector, the efficiency, corrected taking into account the background in the peak window of the time profile, muon cluster size and muon cluster multiplicity, along with their errors, for each partition and as well as a detector average.

3346

3347 B.7 Current data Analysis

3348 Detectors under test at GIF++ are connected both to a CAEN HV power supply and to a CAEN
3349 ADC that reads the currents inside of the RPC gaps bypassing the supply cable. During data tak-
3350 ing, the webDCS records into a ROOT file called `Scan00XXXX_HVY_CAEN.root` histograms with the
3351 monitored parameters of both CAEN devices. Are recorded for each RPC channels (in most cases,
3352 a channel corresponds to an RPC gap):

- 3353 • the effective voltage, HV_{eff} , set by the webDCS using the PT correction on the CAEN power
3354 supply,
- 3355 • the applied voltage, HV_{app} , monitored by the CAEN power supply, and the statistical error
3356 related to the variations of this value through time to follow the variation of the environmental
3357 parameters defined as the RMS of the histogram divided by the square root of the number of
3358 recorded points,
- 3359 • the monitored current, I_{mon} , monitored by the CAEN power supply, and the statistical error
3360 related to the variations of this value through time to follow the variation of the environmental
3361 parameters defined as the RMS of the histogram divided by the square root of the number of
3362 recorded points,
- 3363 • the corresponding current density, J_{mon} , defined as the monitored current per unit area,
3364 $J_{mon} = I_{mon}/A$, where A is the active area of the corresponding gap,
- 3365 • the ADC current, I_{ADC} , recorded through the CAEN ADC module that monitors the dark
3366 current in the gap itself. First of all, the resolution of such a module is better than that of
3367 CAEN power supplies and moreover, the current is not read-out through the HV supply line
3368 but directly at the chamber level giving the real current inside of the detector. The statistical
3369 error is defined as the RMS of the histogram distribution divided by the square root of the
3370 number of recorded points.

3371 Once extracted through a loop over the element of GIF++ infrastructure via the C++ macro
3372 `GetCurrent()`, these parameters, organised in 9 columns per detector HV supply line, are written in
3373 the output CSV file `Offline-Current.csv`. The macro can be found in the file `Current.cc`.

References

- 3375 [1] T. Massam et al. “Experimental observation of antideuteron production”. In: *Il Nuovo Cimento A* 63 (1965), pp. 10–14.
- 3376
- 3377 [2] UA1 Collaboration. “Experimental observation of isolated large transverse energy electrons with associated missing energy at $s = 540 \text{ GeV}$ ”. In: *Physics Letters B* 122 (1983), pp. 103–116.
- 3378
- 3379
- 3380 [3] UA2 Collaboration. “Observation of single isolated electrons of high transverse momentum in events with missing transverse energy at the CERN pp collider”. In: *Physics Letters B* 122 (1983), pp. 476–485.
- 3381
- 3382
- 3383 [4] UA1 Collaboration. “Experimental observation of lepton pairs of invariant mass around $95 \text{ GeV}/c^2$ at the CERN SPS collider”. In: *Physics Letters B* 126 (1983), pp. 398–410.
- 3384
- 3385 [5] UA2 Collaboration. “Evidence for $Z_0 \rightarrow e^+e^-$ at the CERN pp collider”. In: *Physics Letters B* 129 (1983), pp. 130–140.
- 3386
- 3387 [6] ALEPH Collaboration. “Determination of the number of light neutrino species”. In: *Physics Letters B* 231 (1989), pp. 519–529.
- 3388
- 3389 [7] CERN, ed. (1985).
- 3390 [8] CERN, ed. (1986).
- 3391 [9] CERN, ed. (1994).
- 3392 [10] CERN, ed. (1998).
- 3393 [11] CERN, ed. (1999).
- 3394 [12] CERN. Geneva. LHC Experiments Committee. *Letter of Intent for A Large Ion Collider Experiment [ALICE]*, note = CERN-LHCC-93-016. Tech. rep. ALICE Collaboration, 1993.
- 3395
- 3396 [13] CERN. Geneva. LHC Experiments Committee. *ATLAS : technical proposal for a general-purpose pp experiment at the Large Hadron Collider at CERN*, note = CERN-LHCC-94-43. Tech. rep. ATLAS Collaboration, 1994.
- 3397
- 3398
- 3399 [14] CERN. Geneva. LHC Experiments Committee. *CMS : letter of intent by the CMS Collaboration for a general purpose detector at LHC*, note = CERN-LHCC-92-003. Tech. rep. CMS Collaboration, 1992.
- 3400
- 3401
- 3402 [15] CERN. Geneva. LHC Experiments Committee. *LHCb : letter of intent*. Tech. rep. CERN-LHCC-95-5. LHCb Collaboration, 1995.
- 3403
- 3404 [16] L. Evans and P. Bryant. “LHC Machine”. In: *JINST* 3 (2008). S08001.
- 3405 [17] CMS Collaboration ATLAS Collaboration. “Combined Measurement of the Higgs Boson Mass in pp Collisions at $\sqrt{s} = 7$ and 8 TeV with the ATLAS and CMS Experiments”. In: *Physical Review Letters* 114 (2015). 191803.
- 3406
- 3407
- 3408 [18] LHCb Collaboration. “Observation of $J/\psi p$ Resonances Consistent with Pentaquark States in $\Lambda_b^0 \rightarrow J/\psi K^- p$ Decays”. In: *Physical Review Letters* 115 (2015). 072001.
- 3409

- 3410 [19] LHCb Collaboration. “Observation of $J/\psi\phi$ Structures Consistent with Exotic States from
3411 Amplitude Analysis of $B^+ \rightarrow J/\psi\phi K^+$ Decays”. In: *Physical Review Letters* 118 (2017).
3412 022003.
- 3413 [20] CERN. Geneva. *High-Luminosity Large Hadron Collider (HL-LHC) Technical Design Report V. 0.1*. Tech. rep. CERN-2017-007-M. 2017.
- 3415 [21] CERN. Geneva. LHC Experiments Committee. *The CMS muon project : Technical Design Report*. Tech. rep. CERN-LHCC-97-032. CMS Collaboration, 1997.
- 3417 [22] CERN. Geneva. LHC Experiments Committee. *CMS, the Compact Muon Solenoid : technical proposal*. Tech. rep. CERN-2015-005. 2015.
- 3419 [23] CERN. Geneva. LHC Experiments Committee. *The Phase-2 Upgrade of the CMS Muon Detectors*. Tech. rep. CERN-LHCC-2017-012, CMS-TDR-016. CMS Collaboration, 2017.
- 3421 [24] CERN. Geneva. LHC Experiments Committee. *High-Luminosity Large Hadron Collider (HL-LHC) Preliminary Design Report*. Tech. rep. CERN-LHCC-94-38. CMS Collaboration, 1994.
- 3424 [25] CERN. Geneva. LHC Experiments Committee. *The Phase-2 Upgrade of the CMS Level-1 Trigger - Interim Report to the LHCC*. Tech. rep. CERN-LHCC-2017-013, CMS-TDR-017. CMS Collaboration, 2017.
- 3427 [26] CERN. Geneva. LHC Experiments Committee. *Technical Proposal for the Phase-II Upgrade of the CMS Detector*. Tech. rep. CERN-LHCC-2015-010, CMS-TDR-15-02. CMS Collaboration, 2015.
- 3430 [27] A. Gelmi. *CMS iRPC at HL-LHC: background study*. 2018. URL: https://indico.cern.ch/event/732794/contributions/3021836/attachments/1657792/2654574/iRPC_bkg_study_Upgrade29_05_18.pdf.
- 3433 [28] F.Sauli. “GEM: A new concept for electron amplification in gas detectors”. In: *Nucl. Instr. Meth. Phys. Res.* 386 (1997), pp. 531–534.
- 3435 [29] CERN. Geneva. LHC Experiments Committee. *CMS Technical Design Report for the Muon Endcap GEM Upgrade*. Tech. rep. CERN-LHCC-2015-012, CMS-TDR-013. CMS Collaboration, 2015.
- 3438 [30] The CMS collaboration. “The performance of the CMS muon detector in proton-proton collisions at $\sqrt{s} = 7$ TeV at the LHC”. In: *JINST* 8 (2013). P11002.
- 3440 [31] P.Bortignon. “Design and performance of the upgrade of the CMS L1 muon trigger”. In: *Nucl. Instr. Meth. Phys. Res.* 824 (2016), pp. 256–257.
- 3442 [32] R. Santonico and R. Cardarelli. “Development of resistive plate counters”. In: *Nucl. Instr. Meth. Phys. Res.* 187 (1981), pp. 377–380.
- 3444 [33] Yu.N. Pestov and G.V. Fedotovich. *A picosecond time-of-flight spectrometer for the VEPP-2M based on local-discharge spark counter*. Tech. rep. SLAC-TRANS-0184. SLAC, 1978.
- 3446 [34] W.W. Ash, ed. *Spark Counter With A Localized Discharge*. Vol. SLAC-R-250. 1982, pp. 127–131.
- 3448 [35] I. Crotty et al. “The non-spark mode and high rate operation of resistive parallel plate chambers”. In: *NIMA* 337 (1993), pp. 370–381.
- 3450 [36] I. Crotty et al. “Further studies of avalanche mode operation of resistive parallel plate chambers”. In: *NIMA* 346 (1994), pp. 107–113.
- 3452 [37] R. Cardarelli et al. “Avalanche and streamer mode operation of resistive plate chambers”. In: *NIMA* 382 (1996), pp. 470–474.

BIBLIOGRAPHY

- [3454] [38] E. Cerron Zeballos et al. “A new type of resistive plate chamber: The multigap RPC”. In: *NIMA* 374 (1996), pp. 132–135.
- [3455]
- [3456] [39] M.C.S. Williams. “The development of the multigap resistive plate chamber”. In: *Nucl. Phys. B* 61 (1998), pp. 250–257.
- [3457]
- [3458] [40] H. Czirkowski et al. “New developments on resistive plate chambers for high rate operation”. In: *NIMA* 419 (1998), pp. 490–496.
- [3459]
- [3460] [41] P. Camarri et al. “Streamer suppression with SF₆ in RPCs operated in avalanche mode”. In: *NIMA* 414 (1998), pp. 317–324.
- [3461]
- [3462] [42] E. Cerron Zeballos et al. “Effect of adding SF₆ to the gas mixture in a multigap resistive plate chamber”. In: *NIMA* 419 (1998), pp. 475–478.
- [3463]
- [3464] [43] CERN. Geneva. LHC Experiments Committee. *ATLAS muon spectrometer: Technical design report*. Tech. rep. CERN-LHCC-97-22. ATLAS Collaboration, 1997.
- [3465]
- [3466] [44] CERN. Geneva. LHC Experiments Committee. *ALICE Time-Of-Flight system (TOF) : Technical Design Report*. Tech. rep. CERN-LHCC-2000-012. ALICE Collaboration, 2000.
- [3467]
- [3468] [45] The CALICE collaboration. “First results of the CALICE SDHCAL technological prototype”. In: *JINST* 11 (2016).
- [3469]
- [3470] [46] PoS, ed. *Density Imaging of Volcanoes with Atmospheric Muons using GRPCs*. International Europhysics Conference on High Energy Physics - HEP 2011. 2011.
- [3471]
- [3472] [47] C. Lippmann. “Detector Physics of Resistive Plate Chambers”. PhD thesis. Johann Wolfgang Goethe-Universität, 2003.
- [3473]
- [3474] [48] M. Abbrescia et al. “Properties of C2H₂F₄-based gas mixture for avalanche mode operation of resistive plate chambers”. In: *NIMA* 398 (1997), pp. 173–179.
- [3475]
- [3476] [49] G. Battistoni et al. “Sensitivity of streamer mode to single ionization electrons”. In: *NIMA* 235 (1985), pp. 91–97.
- [3477]
- [3478] [50] W. Riegler. “Induced signals in resistive plate chambers”. In: *NIMA* 491 (2002), pp. 258–271.
- [3479]
- [3480] [51] E. Cerron Zeballos et al. “A comparison of the wide gap and narrow gap resistive plate chamber”. In: *NIMA* 373 (1996), pp. 35–42.
- [3481]
- [3482] [52] M. Abbrescia et al. “Cosmic ray tests of double-gap resistive plate chambers for the CMS experiment”. In: *NIMA* 550 (2005), pp. 116–126.
- [3483]
- [3484] [53] ALICE Collaboration. “A study of the multigap RPC at the gamma irradiation facility at CERN”. In: *NIMA* 490 (2002), pp. 58–70.
- [3485]
- [3486] [54] B. Bonner et al. “A multigap resistive plate chamber prototype for time-of-flight for the STAR experiment at RHIC”. In: *NIMA* 478 (2002), pp. 176–179.
- [3487]
- [3488] [55] S. Yang et al. “Test of high time resolution MRPC with different readout modes for the BESIII upgrade”. In: *NIMA* 763 (2014), pp. 190–196.
- [3489]
- [3490] [56] A. Akindinov et al. “RPC with low-resistive phosphate glass electrodes as a candidate for the CBM TOF”. In: *NIMA* 572 (2007), pp. 676–681.
- [3491]
- [3492] [57] JINST, ed. *Development of the MRPC for the TOF system of the MultiPurpose Detector. RPC2016: XII Workshop on Resistive Plate Chambers and Related Detectors*. 2016.
- [3493]
- [3494] [58] M.C.S. Williams. “Particle identification using time of flight”. In: *Journal of Physics G* 39 (2012).
- [3495]
- [3496] [59] A. Alici et al. “Aging and rate effects of the Multigap RPC studied at the Gamma Irradiation Facility at CERN”. In: *NIMA* 579 (2007), pp. 979–988.
- [3497]

- 3497 [60] M. Abbrescia et al. “The simulation of resistive plate chambers in avalanche mode: charge
3498 spectra and efficiency”. In: *NIMA* 431 (1999), pp. 413–427.
- 3499 [61] M. Abbrescia et al. “Study of long-term performance of CMS RPC under irradiation at the
3500 CERN GIF”. In: *NIMA* 533 (2004), pp. 102–106.
- 3501 [62] H.C. Kim et al. “Quantitative aging study with intense irradiation tests for the CMS forward
3502 RPCs”. In: *NIMA* 602 (2009), pp. 771–774.
- 3503 [63] S. Agosteo et al. “A facility for the test of large-area muon chambers at high rates”. In: *NIMA*
3504 452 (2000), pp. 94–104.
- 3505 [64] PoS, ed. *CERN GIF ++ : A new irradiation facility to test large-area particle detectors for*
3506 *the high-luminosity LHC program*. Vol. TIPP2014. 2014, pp. 102–109.
- 3507 [65] A. Fagot. *GIF++ DAQ v4.0*. 2017. URL: https://github.com/afagot/GIF_DAQ.
- 3508 [66] CAEN. *Mod. V1190-VX1190 A/B, 128/64 Ch Multihit TDC*. 14th ed. 2016.
- 3509 [67] CAEN. *Mod. V1718 VME USB Bridge*. 9th ed. 2009.
- 3510 [68] W-Ie-Ne-R. *VME 6021-23 VXI*. 5th ed. 2016.
- 3511 [69] Wikipedia. *INI file*. 2017. URL: https://en.wikipedia.org/wiki/INI_file.
- 3512 [70] S. Carrillo A. Fagot. *GIF++ Offline Analysis v6*. 2017. URL: https://github.com/afagot/GIF_OfflineAnalysis.